

UNIVERSITÉ DU QUÉBEC À MONTRÉAL

SCANNING PROBE TECHNIQUES APPLICABLE TO BATTERIES

DISSERTATION

PRESENTED

AS PARTIAL FULFILLMENT FOR THE DEGREE OF

DOCTOR OF PHILOSOPHY IN CHEMISTRY

BY

ANJANA RAJ RAJU

JANUARY 2025

UNIVERSITÉ DU QUÉBEC À MONTRÉAL

LES TECHNIQUES DE SONDE ELECTROCHIMIQUE A BALAYAGE APPLIQUE AUX
PILES

THÈSE

PRÉSENTÉE

COMME EXIGENCE PARTIELLE

DU DOCTORAT EN CHIMIE

PAR

ANJANA RAJ RAJU

JANVIER 2025

UNIVERSITÉ DU QUÉBEC À MONTRÉAL
Service des bibliothèques

Avertissement

La diffusion de cette thèse se fait dans le respect des droits de son auteur, qui a signé le formulaire *Autorisation de reproduire et de diffuser un travail de recherche de cycles supérieurs* (SDU-522 – Rév.12-2023). Cette autorisation stipule que «conformément à l'article 11 du Règlement no 8 des études de cycles supérieurs, [l'auteur] concède à l'Université du Québec à Montréal une licence non exclusive d'utilisation et de publication de la totalité ou d'une partie importante de [son] travail de recherche pour des fins pédagogiques et non commerciales. Plus précisément, [l'auteur] autorise l'Université du Québec à Montréal à reproduire, diffuser, prêter, distribuer ou vendre des copies de [son] travail de recherche à des fins non commerciales sur quelque support que ce soit, y compris l'Internet. Cette licence et cette autorisation n'entraînent pas une renonciation de [la] part [de l'auteur] à [ses] droits moraux ni à [ses] droits de propriété intellectuelle. Sauf entente contraire, [l'auteur] conserve la liberté de diffuser et de commercialiser ou non ce travail dont [il] possède un exemplaire.»

UNIVERSITÉ DU QUÉBEC À MONTRÉAL

Service des bibliothèques

Avertissement

La diffusion de cette thèse se fait dans le respect des droits de son auteur, qui a signé le formulaire Autorisation de reproduire et de diffuser un travail de recherche de cycles supérieurs (SDU-522 – Rév.04-2020). Cette autorisation stipule que «conformément à l'article 11 du Règlement no 8 des études de cycles supérieurs, [l'auteur] concède à l'Université du Québec à Montréal une licence non exclusive d'utilisation et de publication de la totalité ou d'une partie importante de [son] travail de recherche pour des fins pédagogiques et non commerciales. Plus précisément, [l'auteur] autorise l'Université du Québec à Montréal à reproduire, diffuser, prêter, distribuer ou vendre des copies de [son] travail de recherche à des fins non commerciales sur quelque support que ce soit, y compris l'Internet. Cette licence et cette autorisation n'entraînent pas une renonciation de [la] part [de l'auteur] à [ses] droits moraux ni à [ses] droits de propriété intellectuelle. Sauf entente contraire, [l'auteur] conserve la liberté de diffuser et de commercialiser ou non ce travail dont [il] possède un exemplaire.»

ACKNOWLEDGMENTS

I began my PhD journey amid the unprecedented challenges and uncertainties of the COVID-19 pandemic, a time that tested the resilience and adaptability of the entire global community. Pursuing a PhD is never a solitary endeavor. Along the way, many people join in, offering their support directly and indirectly. I am indebted to all those people who helped me successfully complete this rigorous academic journey.

First and foremost, I want to thank my research director, Prof. Steen B. Schougaard, for his guidance and support throughout this arduous journey. As he always emphasizes, it had its fair share of difficult years and better days. Thank you for motivating me during tough times, constantly challenging me with thought-provoking scientific questions, and guiding me toward becoming an independent researcher.

At this point, I would also like to acknowledge Prof. Janine Mauzeroll from McGill University, with whom I got a chance to write my first review. Thank you for extending the invitation, guiding me throughout the writing process along with Prof. Schougaard, and providing access to your lab facilities at McGill.

Next, I would like to acknowledge all the support and inspiration that I received from my colleagues in the Schougaard lab. Thanks to Dr. Laurence Savignac, who helped me get acquainted with the lab and fostered a welcoming atmosphere in the group. I extend my gratitude to Dr. Jeremy Dawkins for training me to build coin cells and motivating me when the experiments did not work as planned. I am grateful to Dr. Andrew Danis, a mentor to me, for being available to discuss my scientific inquiries. I would also like to express my gratitude to Dr. Bastian Krueger, who was instrumental in designing all the 3D-printed setups for my project. Additionally, a big thank you to Dr. Jonathan Adsetts for all the guidance and help during my proposal exams.

Extending the acknowledgment to the current group members, starting with Brittany, a colleague who always encouraged me and whom I can rely on for assistance in the lab, Marie-Claude, a helpful colleague whom I could clarify my doubts in French, Maddison, a dear colleague who always has fascinating stories to share, and Elliot, who helped with my first publication in the group. I also want to thank all the past and current undergraduates and interns with whom I had the opportunity to work or share the office space. You all are talented people who surprised me with your competence and scientific inquisitiveness. Thank you, everyone, for creating a workspace where we could laugh, learn, and grow.

I want to also extend my gratitude to Isabelle, who is a bridge between the Schougaard and Mauzeroll groups, for responding quickly to any queries I had. Many thanks to the Mauzeroll group members, especially Changyue and Meijing, for training me in the preparation of microelectrodes.

Many thanks to Gwenael Chamoulaud for all his support with the NanoQAM facilities. I am also acknowledging the assistance I received from Luc, Chanel, and Marie-Claude at the chemical stores.

Finally, I would like to express my gratitude to my parents, who have unfailingly supported me throughout my life, never questioning my decisions. A special thank you to my mother, who always stood by me. Next, I want to thank my brother, Athul, who is a strong pillar in my life. Thank you for always having my back no matter what adventure I embark on. I am also grateful to Geethu, my sister-in-law, who is equally as supportive as my brother. Additionally, I want to extend my thanks to my in-laws for their support.

Last but not least, I must express my deepest gratitude to my significant other, Navathej, whose unwavering support has been indispensable on this journey. Thank you for always standing up for me, challenging me with your scientific questions about batteries, and showcasing your wonderful culinary skills, especially throughout my writing phase.

DEDICATION

To my grandparents, Viswanathan, and Savithri.

TABLE OF CONTENTS

| | |
|---|-------|
| LIST OF FIGURES | xii |
| LIST OF ABBREVIATIONS | xix |
| LIST OF SYMBOLS AND UNITS | xxi |
| RÉSUMÉ | xxiv |
| ABSTRACT..... | xxvii |
| CHAPTER I..... | 1 |
| INTRODUCTION..... | 1 |
| 1.0. Renewable Energy: Fueling A Sustainable Future | 1 |
| 1.0.1. Climate change: A Global Concern..... | 1 |
| 1.0.2. Mitigation Measures..... | 2 |
| 1.0.3. Renewable Energy: Challenges & Solutions..... | 3 |
| 1.1. Lithium-ion Batteries (LIBs) | 3 |
| 1.1.1. Working Principle..... | 3 |
| 1.2. Motivation for the Dissertation | 5 |
| 1.2.1. LIBs: Challenges in Storing Renewable Energy Efficiently | 5 |
| 1.3. Mass Transport in Composite Electrodes | 6 |
| 1.3.1. Mass Transport/ Concentration Overpotential..... | 8 |
| 1.3.2. Regulating Mass Transport in Electrodes | 10 |
| 1.3.2.1. Role of Electrode Architecture..... | 10 |
| 1.3.2.2. Strategies for Optimizing Mass Transport in Electrode Architecture..... | 15 |
| 1.3.2.3. Effective Mass Transport Parameters in Composite Electrodes | 17 |
| 1.4. Multiscale Techniques Applicable to Batteries | 18 |
| 1.4.1. Cyclic Voltammetry (CV) | 19 |
| 1.4.1.1. Working Principle | 19 |
| 1.4.1.2. Effect of Transport on CV Shape..... | 22 |
| 1.4.1.3. Planar and Hemispherical Diffusion..... | 23 |
| 1.4.2. Electrochemical Impedance Spectroscopy (EIS)..... | 24 |
| 1.4.2.1. Working Principle | 24 |
| 1.4.2.2. Understanding EIS Spectra..... | 26 |
| 1.4.3. Galvanostatic & Potentiostatic Intermittent Titration Technique (GITT & PITT)..... | 28 |

| | |
|--|----|
| 1.4.3.1. Working Principle | 28 |
| 1.4.4. Scanning Electrochemical Microscopy..... | 30 |
| 1.4.4.1. Principles of Operation | 30 |
| 1.4.4.1. Battery Relevant Operating Modes of SECM | 32 |
| 1.4.4.2. Probes in SECM..... | 35 |
| 1.4.4.3. SECM Modeling..... | 37 |
| 1.4.5. Scanning Ion Conductance Microscopy (SICM) | 39 |
| 1.4.5.1. Working Principle | 39 |
| 1.4.5.2. Probe Fabrication and Equivalent Circuit..... | 41 |
| 1.4.5.3. SICM Operating Modes..... | 44 |
| 1.4.5.4. SICM Modeling Studies | 45 |
| 1.5. Outline of Dissertation | 46 |
| CHAPTER II..... | 48 |
| CURRENT TRENDS IN SECM FOR ENERGY STORAGE DEVICES: REACHING THE MICROSTRUCTURE LEVEL TO TUNE DEVICES AND PERFORMANCE..... | 48 |
| 2.1. Abstract..... | 48 |
| 2.2. Introduction..... | 49 |
| 2.3. LIBs | 50 |
| 2.3.1. Solid Electrolyte Interphase (SEI)..... | 50 |
| 2.3.2. Cathode Electrolyte Interphase (CEI)..... | 52 |
| 2.3.3. Ion Transport and Detection | 53 |
| 2.4. Fuel Cells..... | 54 |
| 2.4.1. Oxygen Reduction Reaction (ORR)..... | 54 |
| 2.4.2. Hydrogen Oxidation Reaction (HOR)..... | 56 |
| 2.4.3. Membranes | 57 |
| 2.5. Supercapacitors | 57 |
| 2.6. Conclusion and Perspectives..... | 57 |
| 2.7. Acknowledgments | 58 |
| CHAPTER III | 59 |
| INVESTIGATING MASS TRANSPORT IN LI-ION BATTERY ELECTRODES USING SECM AND SICM | 59 |
| 3.1. Abstract..... | 60 |
| 3.2. Introduction..... | 60 |

| | |
|---|----|
| 3.3. Experimental | 63 |
| 3.3.1. Preparation of Partially Delithiated LiFePO ₄ (pd-LFP) Electrodes | 63 |
| 3.3.2. Preparation of Micropipettes | 63 |
| 3.3.3. Preparation of Microelectrodes | 64 |
| 3.3.4. SICM and SECM Measurements | 64 |
| 3.3.5. Data Analysis | 66 |
| 3.4. Results and Discussion | 66 |
| 3.4.1. SICM: Ion Current Measurement | 66 |
| 3.4.2. SECM: Faradaic Current Measurement | 71 |
| 3.4.3. 2D Surface Mapping and MacMullin Number | 74 |
| 3.5. Conclusion and Perspectives | 75 |
| 3.6. Acknowledgment | 76 |
| CHAPTER IV | 77 |
| MICROPOROUS SUBSTRATE EFFECT ON SECM STEADY STATE CURRENTS – A 3D MODELING STUDY CRITICAL TO BATTERY ELECTRODE PERFORMANCE | 77 |
| 4.1. Abstract | 78 |
| 4.2. Introduction | 78 |
| 4.3. Methods | 80 |
| 4.4. Results and Discussion | 83 |
| 4.4.1. Effect of Substrate Thickness (h) | 83 |
| 4.4.2. Impact of Porosity (ϵ) | 84 |
| 4.4.3. MacMullin Number of Modeled Substrates | 85 |
| 4.4.4. Effect of RG | 87 |
| 4.4.5. Concentration Profiles | 87 |
| 4.5. Conclusion | 88 |
| 4.6. Acknowledgment | 89 |
| CHAPTER V | 90 |
| INVESTIGATING THE IMPACT OF SURFACE ROUGHNESS ON MASS TRANSPORT IN POROUS SUBSTRATES | 90 |
| 5.1. Abstract | 90 |
| 5.2. Introduction | 91 |
| 5.3. Methods | 93 |
| 5.4. Results And Discussion | 95 |

| | |
|---|-----|
| 5.4.1. Steady State Concentration Map of Anthracene | 95 |
| 5.4.2. Impact of Porosity and Surface Roughness..... | 96 |
| 5.4.3. Comparing the Diffusion Profile of Anthracene | 97 |
| 5.4.4. Determining MacMullin Number | 98 |
| 5.5. Conclusion and Perspectives..... | 100 |
| 5.6. Acknowledgment..... | 101 |
| CHAPTER VI..... | 102 |
| CONCLUSIONS & PERSPECTIVES..... | 102 |
| 6.1. Summary..... | 102 |
| 6.2. Outlook..... | 105 |
| APPENDIX A | 109 |
| SUPPORTING INFORMATION TO INVESTIGATING MASS TRANSPORT IN LI-ION BATTERY ELECTRODES USING SECM AND SICM..... | 109 |
| A.1. Porosity Calculation..... | 114 |
| APPENDIX B | 116 |
| SUPPORTING INFORMATION TO MICROPOROUS SUBSTRATE EFFECT ON SECM STEADY STATE CURRENT-A 3D MODELING STUDY CRITICAL TO BATTERY ELECTRODE PERFORMANCE | 116 |
| B.1. Simulation Details..... | 116 |
| B.2. Boundary Conditions..... | 118 |
| B.3. Meshing | 119 |
| B.4. Post Processing..... | 120 |
| B.5. Dimensions of HF-1 and HF-2 Structures | 120 |
| B.6. Effect of Size (W_T) in HF-1 Substrate..... | 121 |
| APPENDIX C | 125 |
| SUPPORTING INFORMATION TO INVESTIGATING THE IMPACT OF SURFACE ROUGHNESS ON MASS TRANSPORT IN POROUS SUBSTRATES | 125 |
| C.1. SECM: 3D COMSOL Simulation..... | 125 |
| C.2. Boundary Conditions..... | 127 |
| C.3. Meshing | 127 |
| C.4. Calculating the Current..... | 128 |
| APPENDIX D..... | 129 |
| DEVELOPING GALLIUM-COATED MICROELECTRODE FOR LITHIUM-ION DETECTION IN SOLUTION | 129 |

| | |
|---|-----|
| D.1. Introduction..... | 129 |
| D.2. Experimental Methods | 130 |
| D.2.1. Fabrication of platinum (Pt) microelectrodes | 130 |
| D.2.2. Coating Pt ME with gallium | 130 |
| D.2.3. Experimental setup | 131 |
| D.3. Results and Discussion | 132 |
| D.4. Conclusion | 139 |
| BIBLIOGRAPHY..... | 140 |

LIST OF FIGURES

| | |
|---|----|
| Figure 1.1. a) Global land & ocean average temperature anomalies from 1850-2023 relative to 1901-2000 mean (data obtained from National Oceanic and Atmospheric Administration) b) Actual and projected global temperature change relative to 1850-1900 (IPCC, 2022)..... | 1 |
| Figure 1.2. Working of LIB during a) charge and b) discharge | 4 |
| Figure 1.3. a) Schematic of a composite electrode and b) different processes occurring at the electrode level (Zhu <i>et al.</i> , 2022)..... | 7 |
| Figure 1.4. Schematic showing the evolution of Li^+ concentration gradient in the solution-phase of LIB during charge..... | 10 |
| Figure 1.5. a) Schematic of electrode thickness effect on Li^+ transport during battery charging. The curve shows the Li^+ concentration for thick (red) and thin (black) electrodes (Liu <i>et al.</i> , 2019d), b) active material utilization in thick and thin electrodes (Weiss <i>et al.</i> , 2021) | 11 |
| Figure 1.6. Cross-sectional view of a) uncalendered (high porosity) and b) calendered (low porosity) graphite electrodes obtained using scanning electron microscopy. Carbon-binder domains (red box) and cracks in particles (green box) are marked (Robertson <i>et al.</i> , 2021)..... | 12 |
| Figure 1.7. a) Schematic showing the Li^+ ion transport through tortuous paths in thin and thick electrodes b) Faster ion transport in thick electrode with low tortuosity. The shortest paths for transport are indicated by red arrows (Kuang <i>et al.</i> , 2019) | 14 |
| Figure 1.8. a) Fe_3O_4 coated graphite flakes b) alignment of coated graphite flakes in the presence and absence of magnetic field creating different tortuous paths within the electrode (Billaud <i>et al.</i> , 2016)..... | 15 |
| Figure 1.9. a)-d) Different printing steps involved in the fabrication of interdigitated micro batteries using a 30 μm nozzle diameter e) scanning electron microscopy image of the 3D printed and annealed LTO/LFP battery (Sun <i>et al.</i> , 2013) | 16 |
| Figure 1.10. Mass transport processes in porous electrodes occur at different time scales and dimensions (Zhang <i>et al.</i> , 2021) | 18 |
| Figure 1.11. Commonly used multiscale techniques for analyzing and characterizing batteries, arranged based on their ability to provide information in different scales | 19 |
| Figure 1.12. Schematic of a) potential waveform, CV of b) reversible reaction, and c) irreversible reaction showing only oxidation peak, and d) change in concentration of redox species over time | 20 |
| Figure 1.13. Difference in the shape of cyclic voltammograms with different kinetic and mass transport parameters. a) rate of charge transfer \gg mass transport rate, b) very slow rate of charge | |

| | |
|---|----|
| transfer and mass transport, and c) rate of charge transfer \ll mass transport rate, red arrows indicate the increasing scan rate direction (Vassiliev <i>et al.</i> , 2016) | 22 |
| Figure 1.14. a) Planar diffusion in macroelectrode, b) hemispherical diffusion in microelectrode (dotted lines represent the diffusion profile and the arrows indicate the transport of diffusing species), and c) cyclic voltammogram of microelectrode | 23 |
| Figure 1.15. Schematic showing the relation between input and output signals over time (Redrawn from (Vadhva <i>et al.</i> , 2021))..... | 25 |
| Figure 1.16. a) Nyquist plot (Laschuk <i>et al.</i> , 2021), b) Bode plot (Vadhva <i>et al.</i> , 2021), and c) Randle's circuit for an electrochemical cell..... | 26 |
| Figure 1.17. a) Schematic showing the applied current pulse with a duration (τ) b) corresponding transient voltage change and c) transport of Li^+ ions during the single step of GITT (Kim <i>et al.</i> , 2022) | 29 |
| Figure 1.18. Schematic of SECM setup showing the various components (Polcari <i>et al.</i> , 2016) 31 | |
| Figure 1.19. Schematic of different operating modes in SECM with a redox mediator 'R' undergoing an oxidation reaction at the ME. a) hemispherical diffusion at steady state where microelectrode positioned away from the substrate, b) negative feedback near insulator, c) positive feedback near conductor, d) substrate generation-tip collection (SG/TC) mode, e) tip generation-substrate collection (TG/SC) mode, f) redox competition mode. Redrawn from Polcari <i>et al.</i> , 2016 | 32 |
| Figure 1.20. Representative approach curve of insulating and conducting substrates..... | 34 |
| Figure 1.21. Different probe geometries and sizes a) Pt disk microelectrode, b) Pt disk nanoelectrode, c) Hg hemispherical microelectrode, d) Au conical microelectrode, and e) Au ring microelectrode (Polcari <i>et al.</i> , 2016)..... | 36 |
| Figure 1.22. Different steps in the fabrication of microelectrodes using a) soda-lime glass capillary, b) laser heating and pulling capillaries c) pulled micropipettes, d) Adding active wire inside micropipette, e) heat sealing the tip and, f) assembled microelectrode (Danis <i>et al.</i> , 2015) | 37 |
| Figure 1.23. SICM setup with two-electrode configuration (QRCE: Quasi-reference counter electrode) (Page <i>et al.</i> , 2017) | 40 |
| Figure 1.24. a) Different steps in nanopipette fabrication using a laser puller (Stanley et Pourmand, 2020), b) SEM image of a nanopipette (Zhu <i>et al.</i> , 2021) | 41 |
| Figure 1.25. a) Equivalent circuit diagram of SICM, b) schematic of a nanopipette with the important geometric parameters (Zhu <i>et al.</i> , 2021) | 42 |
| Figure 1.26. Cyclic voltammetry of SICM pipette tip in 0.3 M LiPF_6 in propylene carbonate at a scan rate of 5 mVs^{-1} , WE and CE/RE: LiFePO_4 | 43 |

| | |
|---|----|
| Figure 1.27. Different operating modes in SICM (Leitão, 2015) | 44 |
| Figure 2.1. FB-SECM images at Li metal a) before and b), c), d) after charge-discharge cycles with protocols I), II), and III) respectively. Reproduced with permission from Krueger <i>et al.</i> , 2020. Copyright 2020 Wiley-VCH Verlag GmbH & Co. KGaA. CC-BY-NC 4.0..... | 52 |
| Figure 2.2. a) SECM schematic showing the manganese dissolution from LiMn_2O_4 b) Tip voltammograms obtained before (light color) and after (dark color) holding the LiMn_2O_4 substrate at 4.5V in various electrolytes at 1 V/s. Reproduced with permission from Huang <i>et al.</i> , 2021. Copyright 2021 American Chemical Society. CC-BY 4.0..... | 53 |
| Figure 2.3. a) RC-SECM schematic and b) the corresponding image of localized ORR activity of nitrogen containing carbon sphere catalyst spot in 0.1 M NaOH electrolyte. Potentials were converted to RHE scale. Reproduced with permission from Tiwari <i>et al.</i> , 2017. Copyright 2017 the Royal Society of Chemistry. SI-SECM analysis showing c) cyclic voltammograms of ORR in N_2 saturated KOH electrolyte and d) titrated gravimetric site density of monometallic and bimetallic catalysts. Reproduced with permission from Li <i>et al.</i> , 2019. Copyright 2019 American Chemical Society. | 55 |
| Figure 2.4. a) Image of electron backscatter diffraction inverse pole figure (IPF) b-k) SECM HOR current map at the corresponding grain boundaries of the polycrystalline platinum substrate biased at different potentials vs MSE in 10 mM H_2SO_4 + 0.1 M K_2SO_4 solution ($E_{\text{tip}} = -1.5$ V). Normal direction (ND) was represented by a color triangle whereas the transverse and rolling direction axes by TD and RD respectively. Reproduced with permission from Wang et Wipf, 2020. Copyright 2020 the Electrochemical Society..... | 56 |
| Figure 3.1. (a) Equivalent circuit for the electrochemical cell in SICM; (b) schematic of SICM set up when the micropipette is unaffected by an insulating or porous substrate (Arrows represent the ion current)..... | 67 |
| Figure 3.2. (a) Equivalent circuit diagram for the porous substrate; SICM schematic demonstrates the ion current due to migration (brown color arrows) (b) inside porous LTO films when the pipette is positioned on the LTO surface; (c) restricted current flow when the micropipette is near the insulator; (d) experimental SICM approach curves of LTO films (sample number 1-4) with different porosity (ϵ) | 69 |
| Figure 3.3. SECM schematic showing the Pt microelectrode detection of anthracene oxidation (a) in the bulk position; (b) near the insulator; (c) near the porous LTO film; (d) SECM experimental approach curves of LTO films (sample number 1-4) with various porosity (ϵ) (blue arrows represent the anthracene diffusion)..... | 71 |
| Figure 3.4. (a) SICM and (b) SECM 2D surface mapping of LTO film with a porosity, $\epsilon = 63.2 \pm 3.2$ % and thickness = 77.2 ± 3.9 μm ; (c) NM values calculated for porous LTO films tested with SECM and SICM | 74 |
| Figure 4.1. a) SECM 3D COMSOL model geometry, a zoomed-in view of porous substrates b) SP c) HF-1, d) HF-2 | 80 |

| | |
|--|-----|
| Figure 4.2. Approach curves show the effect of thickness in a) SP, b) HF-1 c) HF-2 substrates, and d) a comparison of thickness effect between HF-1 and SP substrates with $\epsilon = 63.3\%$ at $L = 0.008$ | 83 |
| Figure 4.3. Approach curves showing the effect of porosities in a) SP, b) HF-1 c) HF-2 substrates with $h = 40\ \mu\text{m}$, and d) comparison of normalized current obtained in all three models at $L = 0.008$ | 84 |
| Figure 4.4. a) Comparison of NM of three modeled substrates ($h = 40\ \mu\text{m}$) with Bruggeman relation, b) shows the effect of RG on current for various porosities of the SP substrate at $L = 0.008$ and inset shows the meshed geometry of the microelectrode with the surrounding glass sheath | 85 |
| Figure 4.5. Cross-sectional view of anthracene concentration profile showing the comparison between a) SP and HF-1, b) SP and HF-2 substrates with $h = 40\ \mu\text{m}$, $\epsilon = 63.3\%$, $RG = 3$ | 87 |
| Figure 5.1. Grid geometry of a) smooth substrate with the repeating unit (brown color) and b) rough substrate (iii) with the building units i) and ii) | 93 |
| Figure 5.2. 2D cross-sectional concentration map of anthracene in a, b, c, d) smooth and e, f, g, h) rough substrates with various porosities at a normalized tip-substrate distance, $L = 0.008$ | 95 |
| Figure 5.3. Approach curves showing the effect of porosities (ϵ) in a) smooth substrates, b) rough substrates with a thickness of $100\ \mu\text{m}$, and c) comparison of porosity effect in smooth and rough substrates at normalized tip substrate distance, $L = 0.008$ | 96 |
| Figure 5.4. a) Concentration map of anthracene shows the comparison of diffusion in smooth and rough substrates with a thickness of $100\ \mu\text{m}$ and porosity, $\epsilon = 40\%$, b) MacMullin number comparison of the modeled substrates with the Bruggeman's relation | 98 |
| Figure 6.1. Smooth substrate with 80% porosity imaged using a), b) scanning electron microscopy, and c), d) optical microscopy | 107 |
| Figure A.1. a) Measurement of open circuit potential of the pd-LFP coated Al wire showing its stability, b) chronoamperometry (applied potential = $3.5\ \text{V vs Li/Li}^+$) of the pd-LFP coated Al wire immersed within micropipette; Electrolyte: $0.1\ \text{M LiPF}_6$ in PC and QRCE: Li metal | 109 |
| Figure A.2. SEM images of the micropipette a) side view, b) top view; and optical microscopy images of the Pt microelectrode c) side view, d) top view | 109 |
| Figure A.3. SEM images of LTO films a, b) before and c, d) after calendaring | 110 |
| Figure A.4. Schematic of two-electrode configuration for SICM with the zoomed-in view of the electrochemical cell filled with electrolyte. A similar cell was used for SECM in three-electrode configuration with a microelectrode | 110 |
| Figure A.5. Cyclic voltammetry (CV) of anthracene using a) $25\ \mu\text{m}$ Pt microelectrode, b) $1.6\ \text{mm}$ diameter Pt macroelectrode at a scan rate = $100\ \text{mVs}^{-1}$ in $0.1\ \text{M TEABF}_4/\text{PC}$ | 111 |

| | |
|---|-----|
| Figure A.6. SECM approach curves on insulator and conductor showing the hindered diffusion using anthracene..... | 112 |
| Figure A.7. Cyclic voltammetry using partially delithiated LFP ($\text{Li}_{(1-x)}\text{FePO}_4$) at a scan rate of 0.1 mVs^{-1} in $0.1 \text{ M LiPF}_6/\text{PC}$, counter/ reference electrode: Li metal. The area under the oxidation/reduction curves is the same and equals $41 \mu\text{A V}$ | 112 |
| Figure A.8. SECM approach curves on the insulator repeated 25 times showing the reproducibility of the technique..... | 113 |
| Figure A.9. MacMullin number calculated from SECM and SICM measurements conducted on the same LTO films | 113 |
| Figure B.1. Model geometry with domains (A, B, C), boundaries of electrolyte (1-5), and microelectrode (6)..... | 116 |
| Figure B.2. Model geometry with tetrahedral mesh | 118 |
| Figure B.3. a) Schematic of rectangular pillars in HF-1 b) repeating units in HF-2 substrates.. | 119 |
| Figure B.4. Approach curves show the impact of the pillar size (w_T) of the HF-1 substrate on the current (inset shows the normalized current values at normalized tip-substrate distance = 0.008, for different pillar sizes)..... | 121 |
| Figure B.5. Diffusive flux visualization within HF-1 substrate ($h = 40 \mu\text{m}$ and $\epsilon = 63.3\%$) at a normalized tip-substrate distance, $L = 0.008$ for various lateral pillar sizes (w_T) | 122 |
| Figure B.6. Differences in diffusive flux visualized within HF-1 substrate at a normalized tip-substrate distance, $L = 0.008$ for pillar size, $w_T = 10 \mu\text{m}$ when the microelectrode center is positioned a) above the pillar and b) above the pore (Black arrows indicate the microelectrode centre) | 123 |
| Figure B.7. Shows the calculated effective diffusion coefficients for all modeled substrates from the normalized currents when the microelectrode is positioned at a normalized tip-substrate distance, $L = 0.008$ | 123 |
| Figure B.8. Diffusive flux visualization in a) SP, b) HF-1, and c) HF-2 substrates with $h=40 \mu\text{m}$, $\epsilon=63.3\%$, $\text{RG}=3$ | 124 |
| Figure C.1. a) Model geometry with domains (boundaries of electrolyte (1-5), and microelectrode (6), and b) with tetrahedral mesh | 125 |
| Figure D.1. Steps in the fabrication of gallium microelectrode..... | 131 |
| Figure D.2. Schematic of the experimental setup with Ga-coated ME as working electrode and partially delithiated $\text{Li}_{(1-x)}\text{FePO}_4$ film as quasi-reference counter electrode | 132 |

Figure D.3. a) Optical microscopy images of Ga-coated ME taken outside glove box, b) camera images of Ga-coated ME immersed in electrolyte taken inside the glove box, c) cyclic voltammogram for surface activation of Ga-coated ME, d) cyclic voltammogram during plating and stripping of Li^+ ions at 50 mVs^{-1} , e) the corresponding potential vs time plot, and f) current vs time plot 133

Figure D.4. a) Cyclic voltammogram during plating and stripping of Li^+ ions at 50 mVs^{-1} , b) the corresponding current vs time plot, and c) potential vs time plot at $40 \text{ }^\circ\text{C}$ 135

Figure D.5. a) Cyclic voltammogram of gallium tip with different concentrations of LiPF_6 in EC: DMC, and b) Variation of current at the gallium tip for the 0.1 M electrolyte before and after testing different concentrations, scan rate= 50 mVs^{-1} 136

Figure D.6. a) Cyclic voltammogram of Ga-coated macroelectrode during plating and stripping of Li^+ ions in 0.1 M LiPF_6 electrolyte at 50 mVs^{-1} , dinolite camera images of Ga-coated macroelectrode b) before and c) after 180 cycles 137

Figure D.7. a) Schematic of X-ray diffraction sample holder containing microelectrode with and without air-tight cover, b) sample holder in the diffraction set up, and c) comparison of XRD of the sample holder and Ga-coated ME containing lithium-gallium alloy 138

LIST OF TABLES

| | |
|--|-----|
| Table 3.1. LTO films used for SICM measurements (95 % confidence interval) | 69 |
| Table 3.2. LTO films used for SECM measurements (95 % confidence interval) | 71 |
| Table 4.1. Model parameters | 82 |
| Table 5.1. Geometric dimensions of smooth and rough grid porous structures | 93 |
| Table 5.2. Model parameters | 94 |
| Table A.1. The film parameters used for MacMullin number calculations in Figure A.9 | 114 |
| Table B.1. Shows the meshing parameters | 118 |
| Table B.2. Geometric dimensions of HF-1 structure | 120 |
| Table B.3. Geometric dimensions of HF-2 structure | 120 |
| Table C.1. Shows the meshing parameters used in the model | 128 |

LIST OF ABBREVIATIONS

| | |
|------|--|
| 2D | Two-dimensional |
| 3D | Three-dimensional |
| AC | Alternating current |
| AFM | Atomic force microscopy |
| CEI | Cathode electrolyte interphase |
| COP | Conference of Parties |
| CPE | Constant phase element |
| CV | Cyclic voltammetry |
| DC | Direct current |
| DMC | Dimethyl carbonate |
| EC | Ethylene carbonate |
| EESC | Electrochemical energy storage and conversion |
| EIS | Electrochemical impedance spectroscopy |
| EVs | Electric vehicles |
| FB | Feedback mode |
| FEM | Finite element method |
| GC | Generation-collection mode |
| GITT | Galvanostatic intermittent titration technique |
| HF | High-fidelity |
| HOR | Hydrogen oxidation reaction |
| IPCC | Intergovernmental Panel on Climate Change |
| LCO | Lithium cobalt oxide |
| LFP | Lithium iron phosphate |
| LIBs | Lithium-ion batteries |
| LTO | Lithium titanate |
| ME | Microelectrode |

| | |
|-------|---|
| MSE | Mercury-mercurous sulfate electrode |
| NCA | Lithium nickel cobalt aluminum oxide |
| ND | Normal direction |
| ORR | Oxygen reduction reaction |
| PITT | Potentiostatic intermittent titration technique |
| RC | Redox competition mode |
| RD | Rolling direction |
| SECM | Scanning electrochemical microscopy |
| SEI | Solid electrolyte interphase |
| SEM | Scanning electron microscopy |
| SG/TC | Substrate generation/ tip collection |
| SI | Surface interrogation mode |
| SICM | Scanning ion conductance microscopy |
| SOC | State of charge |
| SP | Superposition |
| SPMs | Scanning probe microscopies |
| TD | Transverse direction |
| TDS | Transport of diluted species in porous media |
| TEM | Transmission electron microscopy |
| TG/SC | Tip generation/ substrate collection |
| WE | Working electrode |
| XRD | X-ray diffraction |

LIST OF SYMBOLS AND UNITS

| | |
|--------------------|--|
| $^{\circ}\text{C}$ | Degree Celsius |
| s | Second |
| m | Meter |
| mol | Mole |
| $J_{D,i}$ | Flux of species i due to diffusion |
| ∇ | Gradient operator |
| C | Concentration when used as a symbol or Coulomb when used as a unit |
| D | Diffusion coefficient |
| $J_{M,i}$ | Flux of species i due to migration |
| F | Faraday constant |
| R | Universal gas constant |
| T | Temperature |
| ϕ | Electrostatic potential |
| u_i | Mobility of charged species i |
| $J_{C,i}$ | Flux of species i due to convection |
| v | Solution velocity |
| J_i | Net flux of species i |
| E | Electrode potential |
| E_{eq} | Thermodynamic equilibrium potential of the redox reaction |
| η | Total overpotential |
| η_c | Concentration overpotential |
| n | Number of electrons |
| h | Hour |
| min | Minute |
| A | Area when used as a symbol or Ampere when used as a unit |
| V | Volume when used as a symbol or Volt when used as a unit |
| ε | Porosity |
| τ | Tortuosity |

| | |
|---------------|---|
| d | Mass transport distance |
| L | Straight-line distance |
| κ | Ionic conductivity or Rate constant |
| N_M | MacMullin number |
| E^0 | Standard electrode potential |
| I | Electric current |
| v | Scan rate |
| f | Frequency |
| ϕ | Phase difference |
| Z | Impedance |
| C_{dl} | Double layer capacitance |
| R_{CT} | Charge transfer resistance |
| R_s | Solution resistance |
| m | Mass |
| M | Molar mass when used as symbol and mol dm ⁻³ when used as a unit |
| τ | Pulse time |
| τ_{diff} | Characteristic diffusion time |
| l | Characteristic diffusion length |
| L | Normalized tip-substrate distance |
| r | Radius |
| α | Cone angle |
| R_p | Pipette resistance |
| R_a | Access resistance |
| e | Charge of an electron or Euler's number |
| R_{por} | Resistance through the porous film |
| R_{gap} | Solution resistance in the gap between the pipette and the substrate |
| N_i | Normalized current |
| K | Kelvin |
| J | Joule |
| h | Thickness |
| ρ | Density |

| | |
|-----|----------------------|
| z | Dimensionless charge |
| ppm | Parts per million |

RÉSUMÉ

Les piles lithium-ion (LIB) ont émergées comme une solution prometteuse pour exploiter durablement les énergies renouvelables et électrifier les transports ainsi que les secteurs industriels afin de lutter contre le changement climatique. Toutefois, les performances des piles classiques ne sont pas suffisantes pour ces applications qui nécessitent des capacités de charge rapide ainsi qu'une densité énergétique, une durée de vie et une sécurité élevées. Le principal problème est la limitation de la densité de puissance des piles lithium-ion causée par la lenteur du transport des ions Li^+ à travers les pores remplis d'électrolyte (phase liquide) et à l'intérieur du matériau actif (phase solide) dans les électrodes composites.

Lorsque les électrodes atteignent une épaisseur significative, c'est le transport dans la phase liquide qui limite la puissance lors de l'application de densités de courant élevées. Le transport dans la phase liquide peut être grandement influencé par les paramètres architecturaux de l'électrode tels que la porosité, l'épaisseur et la tortuosité de celle-ci. L'optimisation de ces paramètres dans les électrodes de batterie de la prochaine génération peut améliorer le transport de masse en phase liquide et, par conséquent, améliorer leurs densités de puissance. Les techniques existantes utilisées pour étudier l'impact des paramètres architecturaux des électrodes sur le transport de masse ne permettent pas de distinguer les différences de transport dans les phases solide et liquide. De plus, puisque les paramètres architecturaux comme la porosité et la tortuosité, varient à l'échelle microscopique dans l'ensemble de l'électrode composite, il est crucial d'analyser leur effet sur le transport de masse à l'aide de techniques offrant une haute résolution spatiale. C'est la principale motivation de cette thèse. Par conséquent, cette thèse étudie l'impact des paramètres architecturaux de l'électrode sur le transport de masse en phase liquide, en particulier en utilisant des méthodes de microscopie à sonde locale (SPM) telles que la microscopie électrochimique à balayage (SECM) et la microscopie de conductance ionique à balayage (SICM).

La SECM étant l'une des principales techniques utilisées dans cette thèse, le deuxième chapitre a été consacré à un résumé de ses tendances récentes et démontre l'application étendue de divers modes de SECM pour étudier les cathodes, les anodes et les processus de transport d'ions dans

les piles ainsi que la réaction d'oxydation de l'hydrogène, la réaction de réduction de l'oxygène et le transport membranaire dans les piles à combustible et les supercondensateurs. Il met également en évidence les domaines qui doivent être explorés par la SECM.

Le troisième chapitre illustre comment la SICM et la SECM peuvent être utilisées dans des études expérimentales pour mesurer le transport en phase de liquide exclusivement dans les électrodes $\text{Li}_4\text{Ti}_5\text{O}_{12}$. La conclusion importante est la nature complémentaire de la SECM et de la SICM pour les mesures de transport de masse utilisant les nombres de MacMullin (N_M). En outre, ces techniques ont été utilisées pour étudier l'hétérogénéité des films grâce à la cartographie topographique 2D.

Le quatrième chapitre traite de l'importance des différences de géométrie des substrats sur le transport de masse. Une approche de modélisation SECM 3D est employée dans cette étude pour analyser l'effet géométrique sur le transport de masse dans trois types de substrats (SP, HF-1 et HF-2) ayant la même porosité et la même épaisseur. Notre étude démontre que, lorsque la complexité géométrique augmente, le transport devient plus lent à travers les pores, comme l'indiquent les faibles courants de sonde SECM et les valeurs N_M élevées.

Alors que les chapitres III et IV traitent de l'importance des paramètres architecturaux de base, notamment la porosité et l'épaisseur, ainsi que de la géométrie du substrat, le chapitre V s'intéresse à la rugosité de la surface, un autre paramètre qui influence le courant de sonde SECM. Cette étude numérique SECM 3D démontre que le courant de sonde est une combinaison de la rugosité de surface ainsi que de la porosité des substrats et est plus prononcée dans le cas des substrats rugueux. Ainsi, cette étude souligne la nécessité de mesurer la rugosité de la surface des substrats poreux avant de les utiliser pour des études de transport de masse par SECM.

Les études expérimentales et la modélisation numérique des SPM discutées dans cette thèse peuvent améliorer les connaissances existantes sur l'impact des différents paramètres architecturaux sur le transport de masse à l'échelle microscopique. En outre, ces études seront utiles pour la conception de futures piles à haute performance.

Mots-clés : piles lithium-ion, transport de masse, SECM, SICM, nombre de MacMullin, modèle 3D, coefficient de diffusion effectif, conductivité effective.

ABSTRACT

Lithium-ion batteries (LIBs) have emerged as a promising solution for sustainably harnessing renewable energy and electrifying transportation as well as industrial sectors to combat climate change. However, the performance of conventional LIBs is not sufficient for these applications, which require fast-charging capabilities along with high energy density, cycle life, and safety. The main issue is the LIBs' power density limitation caused by sluggish Li^+ ion transport through the electrolyte-filled pores (solution phase) and within the active material (solid-phase) in composite electrodes.

Solution-phase transport plays a critical role in determining the power performance of thick battery electrodes at high current densities and is influenced by electrode architectural parameters such as porosity, thickness, and tortuosity. Optimizing these parameters in next-generation battery electrodes can enhance the solution-phase mass transport and, thereby, improve their power densities. The existing techniques used to investigate the impact of the electrode architectural parameters on mass transport cannot distinguish the differences in transport through the solid and solution phases. Moreover, as architectural parameters, including the porosity and tortuosity, vary at the microscale throughout the composite electrode, it is crucial to analyze their effect on mass transport using techniques that offer high spatial resolution. This is the main motivation of this dissertation. Consequently, this dissertation investigates the impact of electrode architectural parameters on solution-phase mass transport, especially using scanning probe microscopies (SPMs) such as scanning electrochemical microscopy (SECM) and scanning ion conductance microscopy (SICM).

As SECM is one of the main techniques employed in this dissertation, the second chapter has been devoted to summarizing its recent trends and demonstrates the extensive application of various modes of SECM for studying the cathodes, anodes, and ion transport processes in batteries, hydrogen oxidation reaction, oxygen reduction reaction, and membrane transport in fuel cells and supercapacitors. It also highlights the areas that need further exploration with SECM.

The third chapter illustrates how SICM and SECM can be used in experimental studies to measure the solution-phase transport exclusively within $\text{Li}_4\text{Ti}_5\text{O}_{12}$ electrodes. The important finding is the complementary nature of SECM and SICM for mass transport measurements using MacMullin (N_M) numbers. In addition, these techniques have been used to investigate the heterogeneity of the films through 2D topography mapping.

The fourth chapter discusses the importance of the differences in substrate geometries on mass transport. A 3D SECM modeling approach is employed in this study to investigate the geometric effect on mass transport in three types of substrates (SP, HF-1, and HF-2) having the same porosity and thickness. Our study shows that as geometric complexity increases, the transport becomes more sluggish through the pores within them, indicated by the low SECM probe currents and high N_M values.

As Chapters III and IV discuss the importance of basic architectural parameters, including porosity and thickness, along with the substrate geometry, Chapter V is concerned with surface roughness, another parameter that affects the SECM probe current. This 3D SECM numerical study shows that the probe current is a combination of surface roughness and porosity of substrates, which is more pronounced in the case of rough substrates. As such, this study underscores the need for surface roughness measurement of porous substrates before using them for SECM mass transport studies.

The experimental studies and numerical modeling of SPMs discussed in this dissertation can enhance the existing knowledge about the impact of different architectural parameters on mass transport at the microscale. Furthermore, these studies will benefit the design of future high-performance battery designs.

Keywords: Lithium-ion batteries, Mass transport, SECM, SICM, MacMullin number, 3D Model, Effective diffusion coefficient, Effective conductivity

CHAPTER I

INTRODUCTION

1.0. Renewable Energy: Fueling A Sustainable Future

1.0.1. Climate change: A Global Concern

As the third decade of the 21st century dawns, climate change becomes a global concern. Although every year Earth is warming, the warming rate dramatically increased over the past decade (2014-2023), during which the top 10 warmest years occurred in the 174-year historical record (**Figure 1.1a**). Since the beginning of the Industrial Revolution, climate change has accelerated due to the emission of CO₂ and other greenhouse gases from the extensive use of fossil fuels like coal, gas, and oil for electricity, transportation, agriculture, *etc.* Consequently, the earth's surface temperature rises and melts the polar ice caps, disrupting the natural ecosystem and biodiversity. Furthermore, extreme weather events like intense heatwaves, drought, and heavy precipitation are being observed.

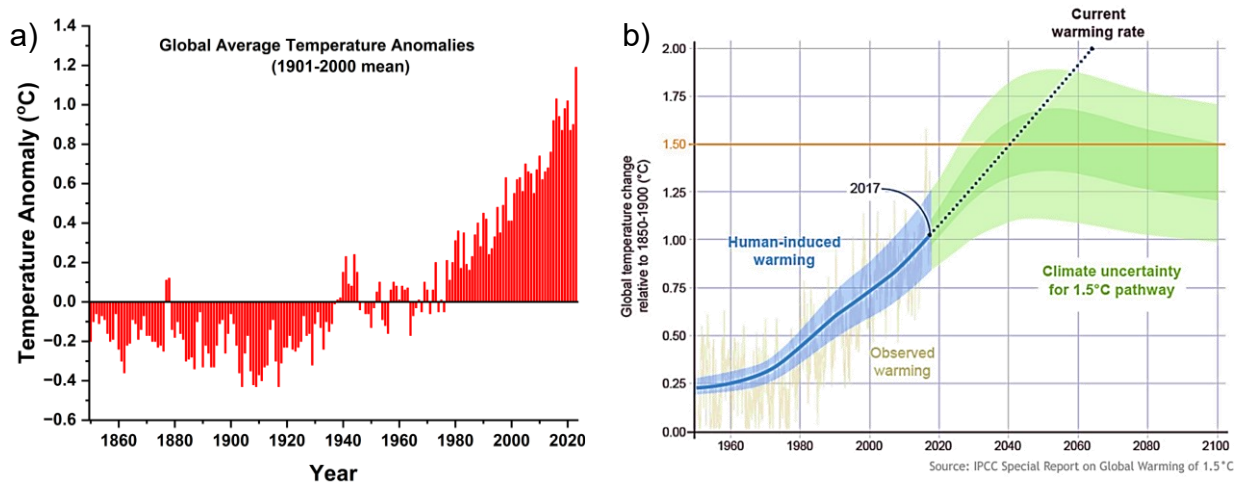


Figure 1.1. a) Global land & ocean average temperature anomalies from 1850-2023 relative to 1901-2000 mean (data obtained from National Oceanic and Atmospheric Administration) b) Actual and projected global temperature change relative to 1850-1900 (IPCC, 2022)

As energy is inevitable for sustaining life, we cannot suddenly stop using it to avoid the consequences including climate change. Therefore, the key questions are:

- 1) How can we mitigate climate change/global warming, ensuring a sustainable future without compromising energy usage?
- 2) How fast do we have to implement the mitigation measures to limit the temperature increase?

1.0.2. Mitigation Measures

The average global temperature change surpassed 1°C in 2017 compared to the pre-industrial level due to human activities, according to the 2018 special report from the Intergovernmental Panel on Climate Change (IPCC, 2022). If the current rate of warming continues, the global temperature change is projected to exceed 1.5 °C by around 2040 (**Figure 1.1b**). Therefore, strict action plans and alternatives to fossil fuel-based resources are required to reduce the current warming rate. The first global commitment, the Paris Agreement was signed in December 2015 at the 21st Conference of Parties (COP21) to mitigate climate change. As the earth's surface temperature is rising to alarming levels due to the burning of fossil fuels, the goal is to prevent the global temperature rise further to 1.5 °C and maintain it below 2 °C during this century compared to pre-industrial levels. Accomplishing this goal involves reducing fossil fuel usage, capturing and storing carbon emissions effectively, controlling population growth, and widely adopting renewable energies including solar, wind, hydropower, *etc.* Escalating energy requirements have led the world to focus on renewable energy sources. These energy sources are replenishable and most of them are “clean”, producing no greenhouse gas emissions, which helps alleviate climate change challenges. Consequently, the world is transitioning from traditional fossil fuels to sustainable renewable energy sources. Nevertheless, this transition is progressing very slowly, as remarked by the most recent COP28 summit in 2023. Hence, COP28 put forward the world's first ‘global stocktake’ aimed at accelerating this transition to achieve the Paris Agreement goals by 2030.

1.0.3. Renewable Energy: Challenges & Solutions

Renewable energy is a key weapon in our battle to mitigate climate change, however, their intermittent nature, along with high infrastructure and production costs makes the transition slow. Though policies are adopted to accelerate this transition, each country's technical, economic, and environmental capability to use renewables varies. Therefore, to use renewables as an alternative to fossil fuels in the long run and integrate them smoothly into the global energy market at low cost, they must be stored efficiently. At this stage, the development of efficient energy storage and conversion devices like batteries, supercapacitors, fuel cells, *etc.* are crucially required. When these devices are integrated into large-scale grids, they ensure energy security by storing energy during off-peak demand periods for use during peak consumption periods. Moreover, incorporating these energy storage devices in the transportation sector can significantly reduce greenhouse gas emissions. Among the existing energy storage devices, lithium-ion batteries (LIBs) have been widely used in everyday life to power electric vehicles (EVs) and electronic gadgets such as laptops, mobiles, digital cameras, *etc.* This is due to their unique advantages, such as high energy density, and long cycle life compared to other commercial energy storage devices like lead-acid and nickel-cadmium batteries. Given the significance of LIBs, it is crucial to study their working mechanism, and any pitfalls associated with them for designing next-generation batteries capable of storing store more energy and providing higher power. Therefore, the working principles of LIBs, current challenges, and techniques to improve and analyze their performance at the micro to mesoscale will be discussed in the following.

1.1. Lithium-ion Batteries (LIBs)

1.1.1. Working Principle

LIBs consist of three main components: a positive electrode, a negative electrode, and a separator with the electrolyte between them. The positive and negative electrodes are called cathode and anode by convention during the discharging process. However, these terms could be used interchangeably depending on whether the battery is in (dis)charged state. The active materials used in the positive electrode include lithium cobalt oxide (LCO), lithium iron phosphate (LFP), lithium nickel cobalt aluminum oxide (NCA), whereas for the negative electrode, graphite, lithium titanate (LTO), *etc.*, are used (Zubi *et al.*, 2018). The electrolyte could be either in solid or liquid form. As solid electrolytes which are still under development are

out of the scope of this dissertation, as such, we focus on the liquid electrolyte consisting of lithium salt and organic solvents. Lithium hexafluorophosphate (LiPF_6) is the commonly used salt in commercial LIBs due to its electrochemical stability and high lithium ion conductivity in organic carbonate solvents. To facilitate the mobility of the Li^+ ions, highly polar aprotic solvents including ethylene carbonate, dimethyl carbonate, diethyl carbonate, and propylene carbonate are used. As such, the electrolyte is ionically conducting and electronically insulating.

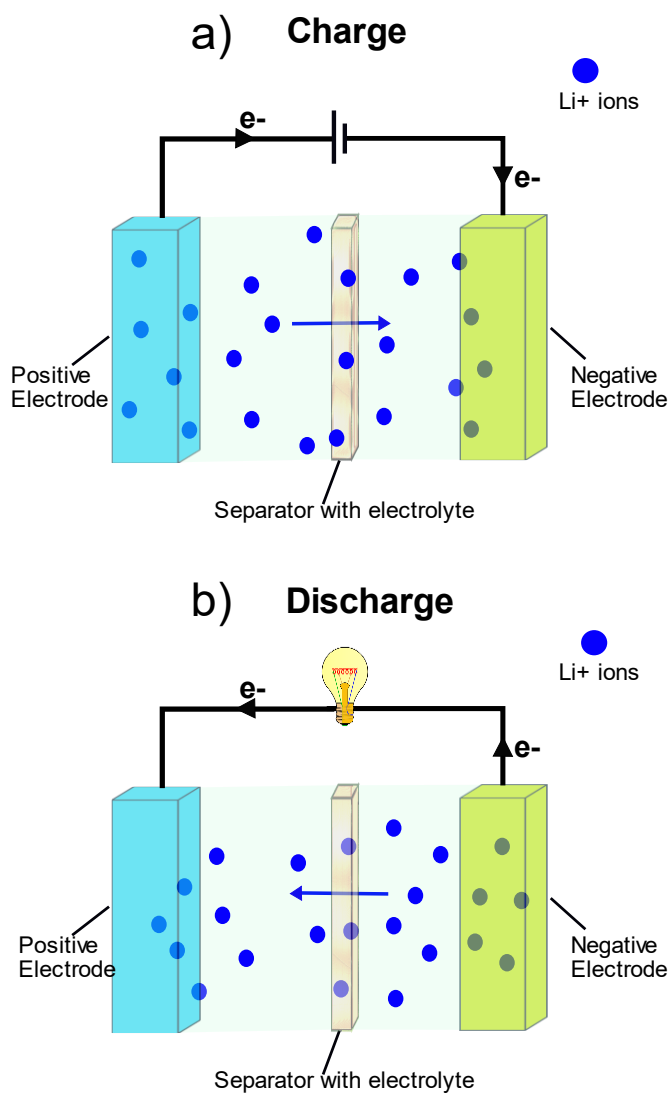
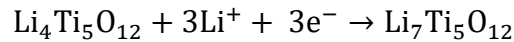
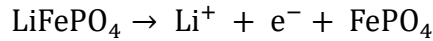


Figure 1.2. Working of LIB during a) charge and b) discharge

To explore the battery chemistry, LFP (LiFePO_4) and LTO ($\text{Li}_4\text{Ti}_5\text{O}_{12}$) are chosen as examples for positive and negative electrodes, respectively. During charge, LFP undergoes oxidation and releases Li^+ ions, and electrons (**Figure 1.2a**). These Li^+ ions travel through the electrolyte and intercalate into LTO, resulting in the reduction of LTO. On the other hand, the electrons move through the external circuit and reach LTO, thereby completing the circuit. The reverse process occurs during discharge *i.e.*, LTO oxidizes and releases Li^+ ions and electrons, which move into the LFP and reduce it (**Figure 1.2b**). This shuttling of solvated Li^+ ions between the two electrodes is called the “rocking chair” mechanism. The electrochemical reaction at LFP and LTO during charge are given as:



In general, the active materials used in battery electrodes have a low electronic conductivity, so conductive carbon additives are added to the electrode (Spahr, 2009). As such, positive and negative electrodes are composites comprising active material, carbon, and binder (*e.g.*: poly(vinylidene fluoride)) bound to a metallic current collector.

1.2. Motivation for the Dissertation

1.2.1. LIBs: Challenges in Storing Renewable Energy Efficiently

The use of LIBs in different industries relies on factors like energy density, power density, safety, cost, cycle life, and environmental impact (Manthiram, 2017). A trade-off between these factors is essential depending on the application as no battery technology has all the required aspects. In portable electronic device applications, a high energy density is imperative compared to power density. On the other hand, energy grid applications prioritize power density, safety, cost, and cycle life over energy density. Whereas in the case of EVs, power density, safety, cost, and cycle life are crucial along with energy density. For instance, the automotive application requires strict specifications including a 10-year calendar life, a 1000-cycle life, a temperature range of -30 to 50 °C, and a cost of less than \$100 per kilowatt-hour (Masias *et al.*, 2021). Consequently, the next-generation batteries must be able to store more energy and charge quickly. The goal of the

US Advanced Battery Consortium is to develop a battery technology that can achieve an 80% state of charge (SOC) in just 15 minutes (Deng *et al.*, 2020; Neubauer *et al.*, 2014). However, the properties of battery materials and cell chemistry are significant obstacles to reaching this fast-charging goal.

During the operation of LIBs, the internal resistance leads to overpotentials. These, in turn, cause limited charging speeds owing to the limited potential stability window of the electrolyte and excess heat generation as well as safety issues due to lithium plating. (Waldmann *et al.*, 2018). These issues prevent the battery from attaining its theoretical energy density. Therefore, reducing the overpotential is crucial to improving the battery performance. The factors contributing to overpotential include ion and electron transport within positive and negative electrodes, ion transport within the electrolyte, and charge transfer reactions at the electrode/electrolyte interface (Chen *et al.*, 2021). Among these, the Li^+ ion transport within the composite electrodes is the rate-determining step in attaining high power density (Cornut *et al.*, 2015 ; Heubner *et al.*, 2020a ; Ogihara *et al.*, 2015 ; Weiss *et al.*, 2021). Therefore, the scope of this dissertation revolves around the mass transport within porous electrodes.

1.3. Mass Transport in Composite Electrodes

Mass transport is used to describe the movement of Li^+ ions within a battery electrolyte and electrode material when the battery operates. Within the porous composite electrodes, two types of transport processes occur, such as:

- 1) Li^+ ion transport through the liquid electrolyte present in the electrode pores (solution-phase),
- 2) Li^+ ion transport within the active material (solid-state) (**Figure 1.3**).

Among these two processes, the solution-phase transport becomes the critical factor influencing the power performance of LIBs at high current densities, *i.e.*, the faster the Li^+ ion transport, the better the power of batteries (Cornut *et al.*, 2015 ; Ye *et al.*, 2015).

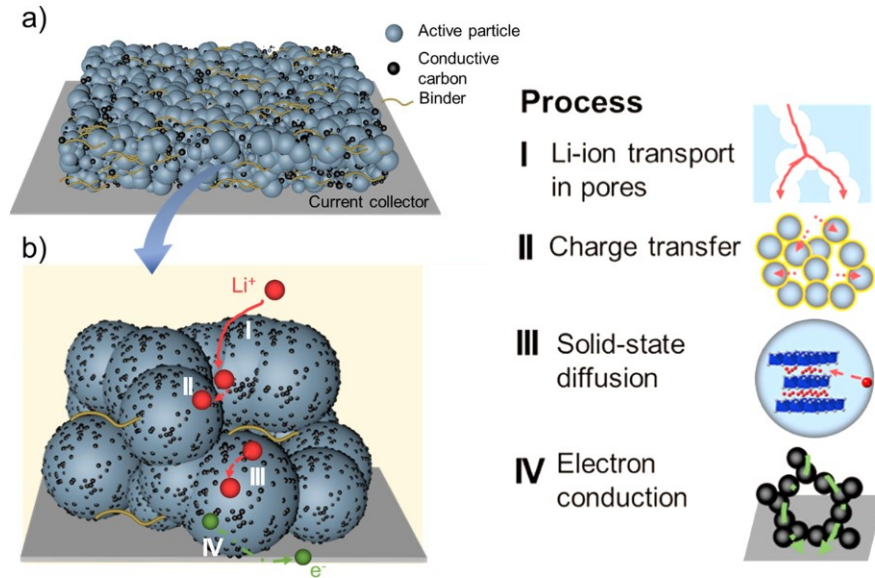


Figure 1.3. a) Schematic of a composite electrode and b) different processes occurring at the electrode level (Zhu *et al.*, 2022)

The transport of Li^+ ions can be expressed in terms of molar flux, which is the number of moles of ions traveling per unit time through a unit area ($\text{mol cm}^{-2} \text{s}^{-1}$). Depending on the driving force for transport, the three basic mechanisms of mass transport are:

1) Diffusion: Is the movement of species (i) from a high concentration to a low concentration, *i.e.*, diffusion is driven by a concentration gradient. Generally, the diffusion flux ($J_{D,i}$) is described by Fick's first law and in 3D it is expressed as follows with the help of a gradient operator (∇):

$$J_{D,i} = -D_i \nabla C_i \quad (1.0)$$

Where D_i is the diffusion coefficient, ∇C_i the concentration gradient, C_i the concentration of Li^+ ions.

2) Migration: Is the movement of a charged species in electrochemical processes due to the electric field. The flux due to migration ($J_{M,i}$) is:

$$J_{M,i} = -\frac{z_i F}{RT} D_i C_i \nabla \phi \quad (1.1)$$

Where z_i the dimensionless charge, F is the Faraday constant, R is the universal gas constant, T is the temperature and $\nabla \phi$ the electrostatic potential gradient. The coefficient $\frac{z_i F}{RT} D_i$ gives the mobility of charged species (u_i).

3) Convection: Movement of the species by bulk motion of a solution in response to a mechanical force. It could be either forced convection or natural convection generated by slight temperature, gravity, or density changes. The flux due to convection ($J_{C,i}$) is:

$$J_{C,i} = v C_i \quad (1.2)$$

Where v is the solution velocity. In the modeling studies of LIBs, it is often assumed that the contribution of convective transport is negligible (Latz et Zausch, 2011).

The total solution-phase mass transport to an electrode in LIBs is a combination of the above three mechanisms, which is governed by the Nernst-Planck equation as follows:

$$J_i = \underbrace{-D_i \nabla C_i}_{\text{Diffusion}} - \underbrace{\frac{z_i F}{RT} D_i C_i \nabla \phi}_{\text{Migration}} + \underbrace{v C_i}_{\text{Convection}} \quad (1.3)$$

Where J_i represents the net flux of species.

1.3.1. Mass Transport/ Concentration Overpotential

Overpotential has a huge impact on the performance of LIBs affecting both the energy and power densities. It is defined as the difference between the output potential (E) and the thermodynamic equilibrium potential of the redox reaction (E_{eq}) *i.e.*, total overpotential (η) is given as:

$$\eta = E - E_{eq} \quad (1.4)$$

The total overpotential in a battery is a combination of three overpotentials.

1) Ohmic overpotential: This refers to the voltage drop caused by the internal resistance of the battery. This internal resistance can be caused by various components within the battery, including electrolyte resistance, resistance within the electrode comprising the resistance contribution of the active material and conductive carbon. During the charge/discharge processes of the battery, the current flowing through the battery encounters this internal resistance, resulting in a voltage drop.

2) Charge transfer overpotential: This is the extra potential required to overcome the activation energy barrier of an electrochemical reaction. It arises from the electron/charge transfer reactions at the electrode-electrolyte interface.

3) Concentration overpotential: This is the additional voltage required to drive the electrochemical reaction due to the concentration gradient of Li^+ ions developed in the battery electrolytes. For instance, during the charging process, Li^+ ions are consumed at the negative electrode. To compensate for these Li^+ ions, and thereby maintain charge neutrality throughout the battery, Li^+ ions are released at the positive electrode. However, this release of Li^+ ions create a concentration gradient between the electrode surface and bulk electrolyte as anions are not electroactive. Moreover, owing to the low cation transference number of the conventional liquid electrolyte, it cannot counteract this concentration gradient, thus resulting in a concentration overpotential (Newman et Balsara, 2004). For example, the cation transference number (t^+) of LiPF_6 is approximately equal to 0.4 (Fong *et al.*, 2019). Therefore, to enhance mass transport in batteries, the cation (Li^+ ion) is preferable to have a higher transference number than the anion.

A representative example showing the evolution of the concentration gradient during the charging of a battery has been given in (**Figure 1.4**). When the battery is at rest (time, $t=0$), the initial Li^+ concentration throughout the solution phase is uniform. However, when the battery starts to (dis)charge, a concentration gradient develops slowly due to the sluggish transport of Li^+

ions through the solution phase of the positive and negative electrodes leading to concentration overpotentials (η_c), which is given as follows (Li, 2021):

$$\eta_c = \frac{RT}{nF} \ln \frac{C_B}{C_S} \quad (1.5)$$

Where C_B denotes the bulk Li^+ ion concentration of the electrolyte, C_S the Li^+ ion concentration of the electrode surface, and n the number of electrons. As the battery starts to (dis)charge at high C-rates, this concentration overpotential increases dramatically due to the limited mass transport.

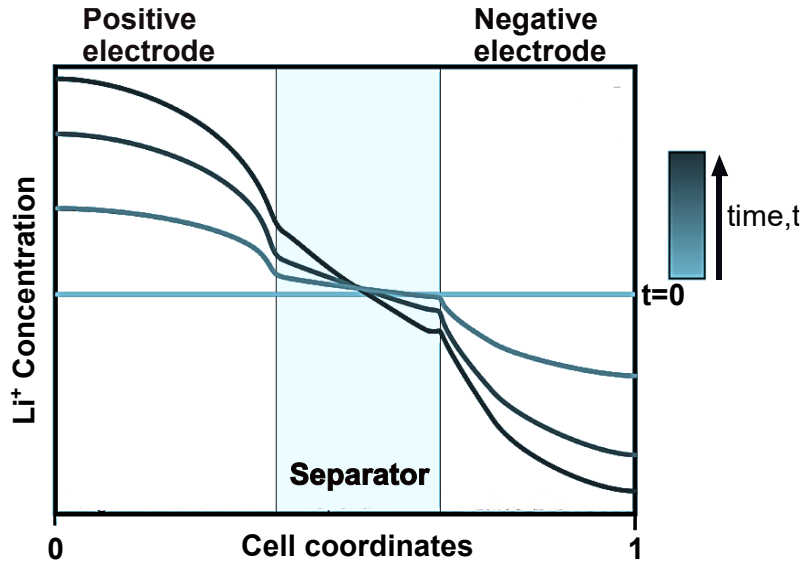


Figure 1.4. Schematic showing the evolution of Li^+ concentration gradient in the solution-phase of LIB during charge

1.3.2. Regulating Mass Transport in Electrodes

1.3.2.1. Role of Electrode Architecture

Controlling the architecture of both positive and negative electrodes is imperative to optimizing the mass transport within them. As such, the three important parameters, thickness, porosity, and tortuosity, have a significant effect on the Li^+ transport at the electrode level and, thereby the fast charging of batteries (Heubner *et al.*, 2020b ; Taleghani *et al.*, 2017 ; Yu *et al.*, 2006).

1) Electrode thickness

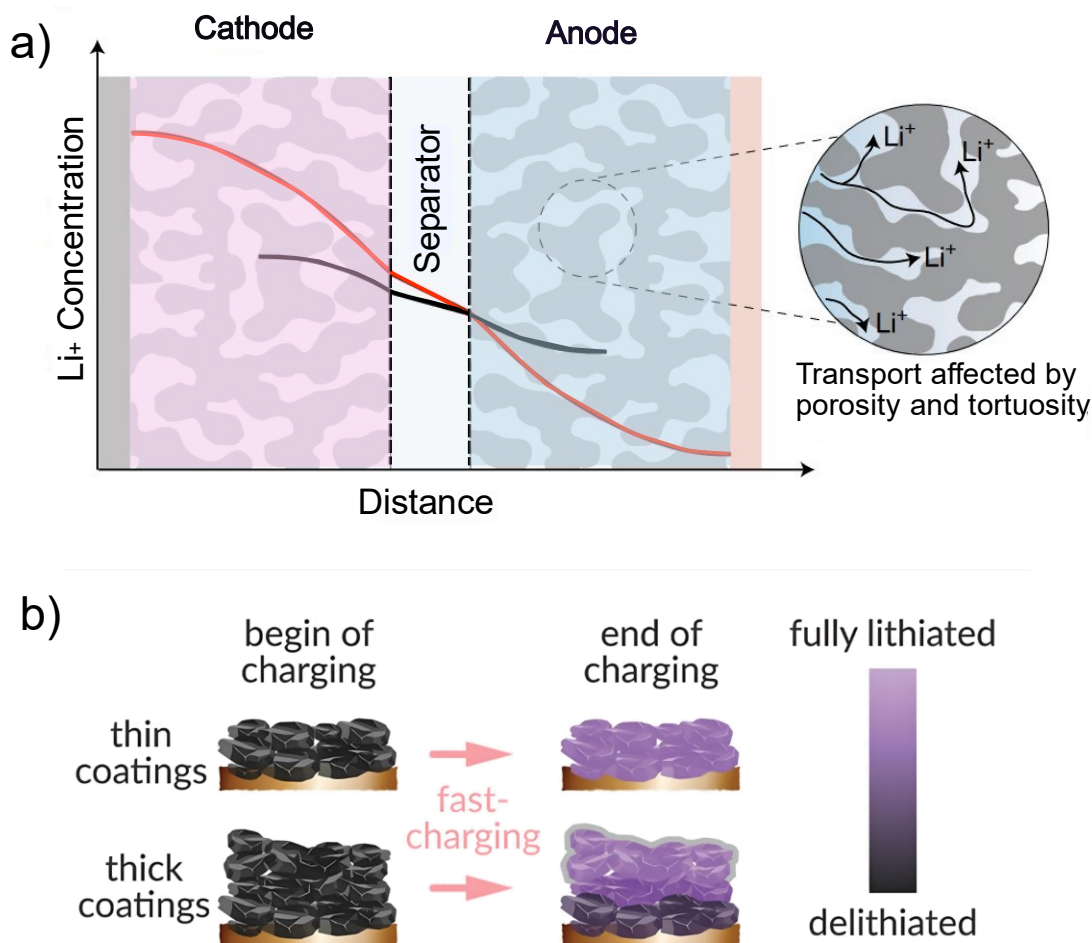


Figure 1.5. a) Schematic of electrode thickness effect on Li^+ transport during battery charging. The curve shows the Li^+ concentration for thick (red) and thin (black) electrodes (Liu et al., 2019d), b) active material utilization in thick and thin electrodes (Weiss et al., 2021)

The performance of batteries in terms of high power and energy densities is significantly affected by the thickness of the composite electrodes. An increased thickness can lead to enhanced mass transport limitations, impacting the power performance of batteries. When the electrode thickness increases, the diffusion paths for Li^+ ions become longer, leading to large concentration gradients within the solution phase of porous electrodes, which, in turn, increases concentration overpotential (**Figure 1.5a**) (Liu *et al.*, 2019d). Ultimately, this can lead to underutilization of active materials in the inner region of thick electrodes compared to thin ones (**Figure 1.5b**) (Li *et al.*, 2020a ; Weiss *et al.*, 2021).

On the other hand, in the case of thin electrodes, the concentration gradients developed within the electrodes are small due to the shorter diffusion length. Therefore, the solution phase mass transport of Li^+ ions is not limiting and can exhibit fast-charging capabilities. At high rates, the only factor restricting the performance of thin electrodes is the solid-state diffusion (Ju *et al.*, 2020). Although thin electrodes ($< 20 \mu\text{m}$) outperform thick electrodes ($>100 \mu\text{m}$) at high current densities in terms of the specific capacity (mAhg^{-1}) achieved, when a full-cell level is considered, the active-to-inactive material ratio is unfavorable to obtaining high energy densities and increases the cost of the battery (Heubner *et al.*, 2021). As a result, for optimum performance of LIBs, the current commercial electrodes have a thickness in the range of $50\text{-}100 \mu\text{m}$ (Zhu *et al.*, 2022).

2) Porosity

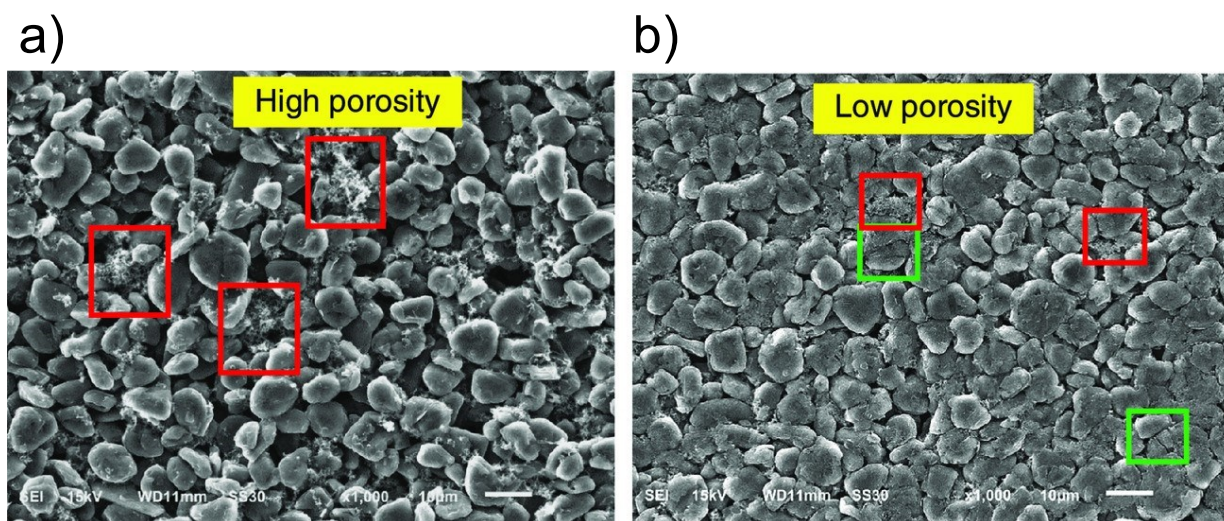


Figure 1.6. Cross-sectional view of a) uncalendered (high porosity) and b) calendered (low porosity) graphite electrodes obtained using scanning electron microscopy. Carbon-binder domains (red box) and cracks in particles (green box) are marked (Robertson *et al.*, 2021)

Porosity (ϵ) represents the volume fraction of the electrolyte-filled voids within the battery electrode *i.e.*,

$$\varepsilon = \frac{V_{void}}{V_T} \quad (1.6)$$

Where V_{void} is the volume of the voids and V_T the total volume constituting the volume of each component in the composite electrode and the volume of the voids.

Typically, the dry-processed electrodes with high porosity can enhance the wetting of the electrode, and thus facilitate the smooth transport of Li^+ ions through the electrode pores. This decreases the concentration overpotential and supports the fast charging in thick electrodes. Nevertheless, exceeding a certain value of porosity reduces the overall mass loading of active material per unit volume of the electrode, severely affecting the volumetric energy density (Parikh *et al.*, 2020). Moreover, high-porosity electrodes exhibit lower mechanical integrity and electronic conductivity than less porous ones (Antartis *et al.*, 2015). They are inhomogeneous due to the presence of a wide range of pore sizes and a non-uniform spatial distribution of carbon-binder domains (**Figure 1.6a**) (Robertson *et al.*, 2021). When these electrodes undergo a compaction process known as calendaring, particle-to-particle contact within them and the adhesion between the current collector and the electrode increases (Zheng *et al.*, 2012c). On the other hand, calendaring reduces the overall porosity (**Figure 1.6b**), resulting in decreased void spaces available for the Li^+ ions to travel within the electrode, leading to sluggish transport. Therefore, an optimum porosity is preferred for the performance of LIBs. In commercial battery electrodes, a porosity of 30% was used (Zhu *et al.*, 2022).

3) Tortuosity

Tortuosity (τ) plays an equally important role as porosity in determining the rate performance of LIBs. It is the ratio of the mass transport distance (d) between two points to the straight-line distance (L) within the porous composite electrodes (Sun *et al.*, 2024),

$$\tau = \frac{d}{L} \quad (1.7)$$

The above geometric definition of tortuosity characterizes the microstructure of porous electrodes. The concept of tortuosity has been defined in various ways in the literature. In this

dissertation, the definition of tortuosity will be based on the physical mass transport processes and will be described in relation to the effective ionic conductivity and diffusivity. This will be further discussed in the upcoming sections.

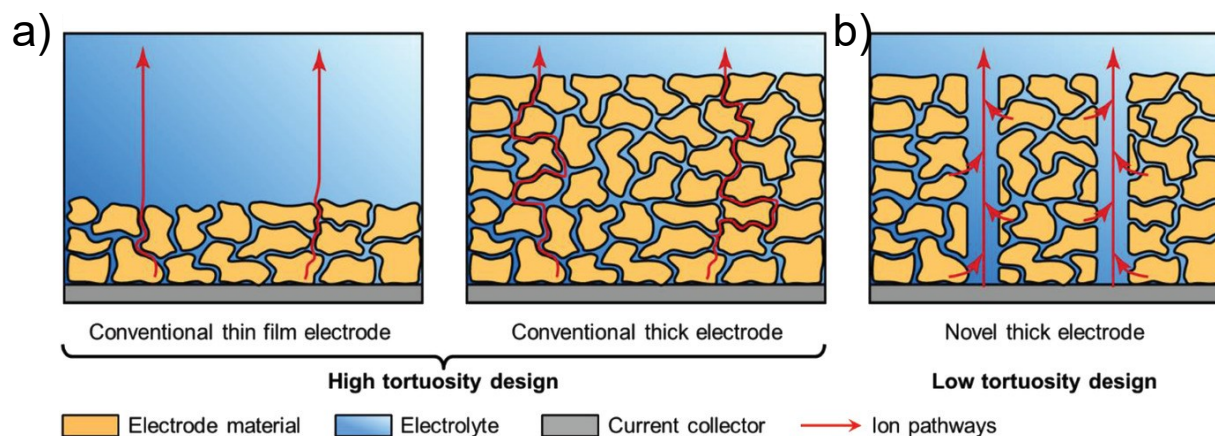


Figure 1.7. a) Schematic showing the Li^+ ion transport through tortuous paths in thin and thick electrodes b) Faster ion transport in thick electrode with low tortuosity. The shortest paths for transport are indicated by red arrows (Kuang *et al.*, 2019)

For an ideal electrode with a straight ion pathway, tortuosity is equal to one. In reality, the composite electrodes prepared with multicomponent slurry have tortuous paths through which the mass transport of Li^+ ions takes place. Generally, an electrode with high tortuosity experiences sluggish transport that results in poor rate performance. Compared to thin electrodes, the tortuous path for diffusion is longer in thick electrodes (**Figure 1.7a**) (Kuang *et al.*, 2019). This leads to severe concentration overpotential and affects the ability to maintain high cycling rates and power densities. Moreover, during fast charging, this causes Li^+ deposition on the negative electrode surface (close to the separator) (Wang *et al.*, 2016). Therefore, reducing the tortuosity is an effective way to facilitate mass transport in thick electrodes and achieve high rate capability (**Figure 1.7b**).

1.3.2.2. Strategies for Optimizing Mass Transport in Electrode Architecture

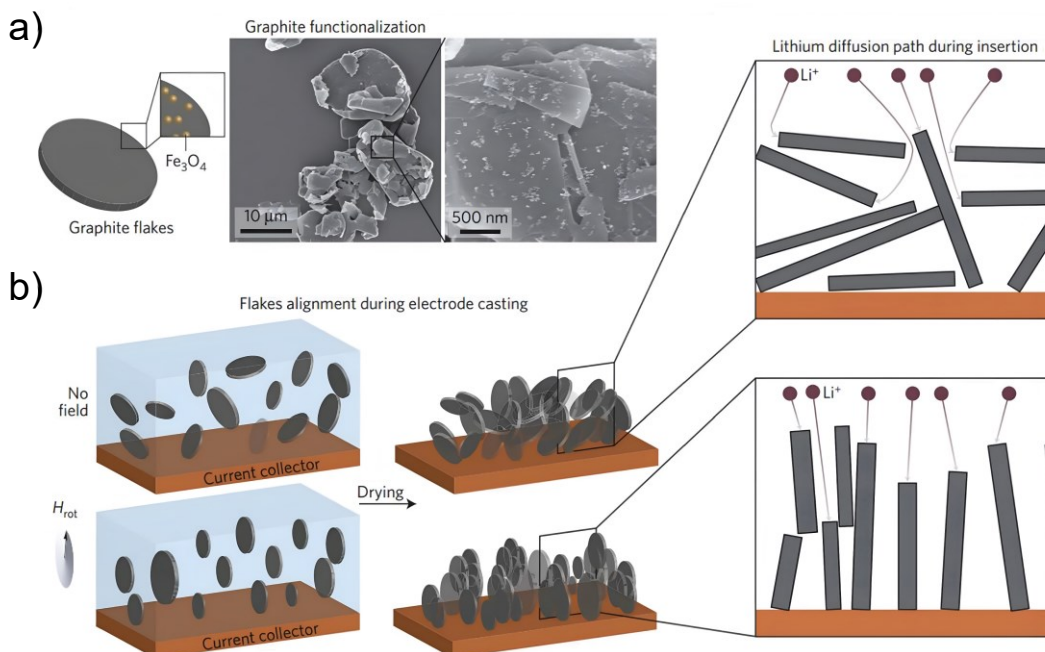


Figure 1.8. a) Fe_3O_4 coated graphite flakes b) alignment of coated graphite flakes in the presence and absence of magnetic field creating different tortuous paths within the electrode (Billaud *et al.*, 2016)

One common approach to optimizing electrode architecture and boosting mass transport is by reducing tortuosity. Several techniques have demonstrated high potential in designing thick electrodes with low tortuosity, such as salt templating (Elango *et al.*, 2018), ice templating (Amin *et al.*, 2018), wood templating (Lu *et al.*, 2018), and magnetic-assisted templating (Billaud *et al.*, 2016 ; Zhu *et al.*, 2022). Among these techniques, magnetic-assisted templating is a relatively slow process, however, it offers greater control over porosity, pore size, and shape. For example, in magnetic-assisted templating, graphite flakes coated with superparamagnetic Fe_3O_4 nanoparticles are aligned perpendicular to the current collector using an external magnetic field of strength 100 mT (**Figure 1.8**) (Billaud *et al.*, 2016). This alignment creates oriented pore channels, leading to less tortuous paths within the electrode and improving the rate performance of batteries.

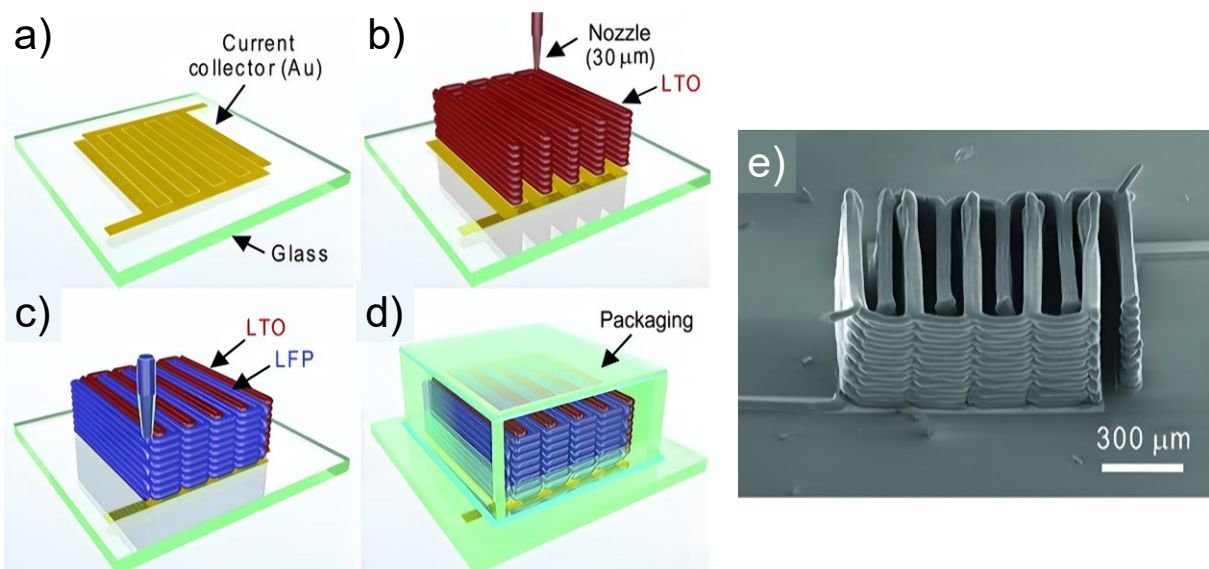


Figure 1.9. a)-d) Different printing steps involved in the fabrication of interdigitated micro batteries using a 30 μm nozzle diameter e) scanning electron microscopy image of the 3D printed and annealed LTO/LFP battery (Sun *et al.*, 2013)

An alternative method for creating low tortuosity electrodes involves 3D printing or direct ink writing (Fu *et al.*, 2017). This method allows for the printing of 3D electrodes using a slurry or ink in a layer-by-layer fashion and offers high precision and tunability. An example of this is the fabrication of a 3D microbattery, where a low tortuosity electrode of LFP and LTO in an interdigitated architecture was created by directly printing the slurry on top of a gold current collector (**Figure 1.9a-d**) (Sun *et al.*, 2013). Electrodes with low tortuosity can be attained after subsequent drying and annealing steps (**Figure 1.9e**). As the electronic conductivities of LFP and LTO are low, using graphene oxide-based inks can significantly improve the conductivity and thereby the energy and power densities of the battery (Fu *et al.*, 2016). Although 3D printing technology enables the fabrication of thick electrodes with low tortuosity, the high manufacturing cost and long printing time make it challenging for the large-scale production of thick electrodes at the industrial level.

In general, thin electrodes with high porosity and low tortuosity enhance the Li^+ ion transport within the electrode (Heubner *et al.*, 2019). However, the effect of electrode parameters such as thickness, porosity, and tortuosity on mass transport are interconnected. Therefore, rather than

focusing on the effect of a single parameter, it is imperative to consider the overall effect of these parameters to optimize the electrode architecture of LIBs in applications such as EVs where impressive energy and power density are required.

1.3.2.3. Effective Mass Transport Parameters in Composite Electrodes

Conventionally, the intrinsic transport parameters such as the ionic conductivity (κ_0) or diffusion coefficient (D_0) of the bulk electrolyte can be used to characterize the Li^+ transport kinetics. When Li^+ ions move through the porous electrodes, their facile transport can be obstructed by the arrangement of solid components, as indicated by the tortuosity. As the geometric definition of tortuosity (Eq.1.7) does not fully account for the constrictions and transport parameter changes at different locations within the porous electrodes, the effective transport parameters such as the effective diffusivity (D_{eff}) or effective conductivity (κ_{eff}) can be used to represent the overall mass transport (Tjaden *et al.*, 2018). These effective transport parameters take into account factors such as the porosity (ε) and tortuosity (τ) and the relation is given by (Thorat *et al.*, 2009):

$$\kappa_{eff} = \frac{\kappa_0 \varepsilon}{\tau} \quad (1.8)$$

$$D_{eff} = \frac{D_0 \varepsilon}{\tau} \quad (1.9)$$

The above equations show a relation between porosity and tortuosity in terms of the transport parameters. In porous structures, the direct correlation between the tortuosity and porosity is generally described by the Bruggeman relation ($\tau = \varepsilon^{-0.5}$) (Bruggeman, 1935). This relation is widely adopted to predict tortuosity assuming that the particles inside the porous structures are spherically shaped and monodispersed (Thorat *et al.*, 2009). However experimental studies have shown that these predictions can give inconsistent results (Hossain *et al.*, 2020). In battery studies, MacMullin number (N_M) is normally used to quantify the hindrance caused by the electrode geometry to the ion transport. This number provides the relationship between the electrolyte's porosity, tortuosity, intrinsic or bulk electrolyte transport properties, and the effective transport parameters in porous electrodes (Hossain *et al.*, 2020).

$$N_M = \frac{\kappa_0}{\kappa_{eff}} = \frac{D_0}{D_{eff}} = \frac{\tau}{\varepsilon} \quad (1.10)$$

If the transport parameters are known at a given porosity, either N_M or tortuosity can be determined. As such, it is vital to measure the effective transport parameters for regulating tortuosity and improving the mass transport in porous electrodes for fast charging. This is the key motivation of this dissertation, and the focus has been on localized probe-based techniques, which can offer localized information about the effective transport properties. Therefore, before exploring the probe-based techniques, the next section of the dissertation discusses the existing techniques for analyzing the mass transport parameters at the mesoscale and their challenges.

1.4. Multiscale Techniques Applicable to Batteries

In LIBs, mass transport processes occur at characteristic timescales ranging from microseconds to minutes while the electrode dimension in which these processes occur varies from the nanometer (nm) to millimeter (mm) scale (**Figure 1.10**) (Zhang *et al.*, 2021). Owing to the importance of mass transport in optimizing the design and overall performance of future batteries, developing multiscale techniques that accurately analyze the Li^+ ion transport in the length scale of nm to mm is an absolute requirement.

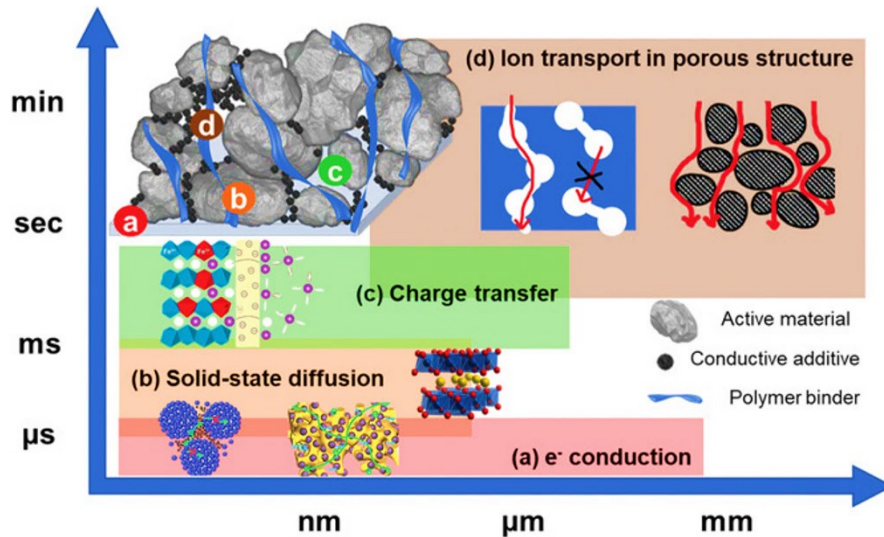


Figure 1.10. Mass transport processes in porous electrodes occur at different time scales and dimensions (Zhang *et al.*, 2021)

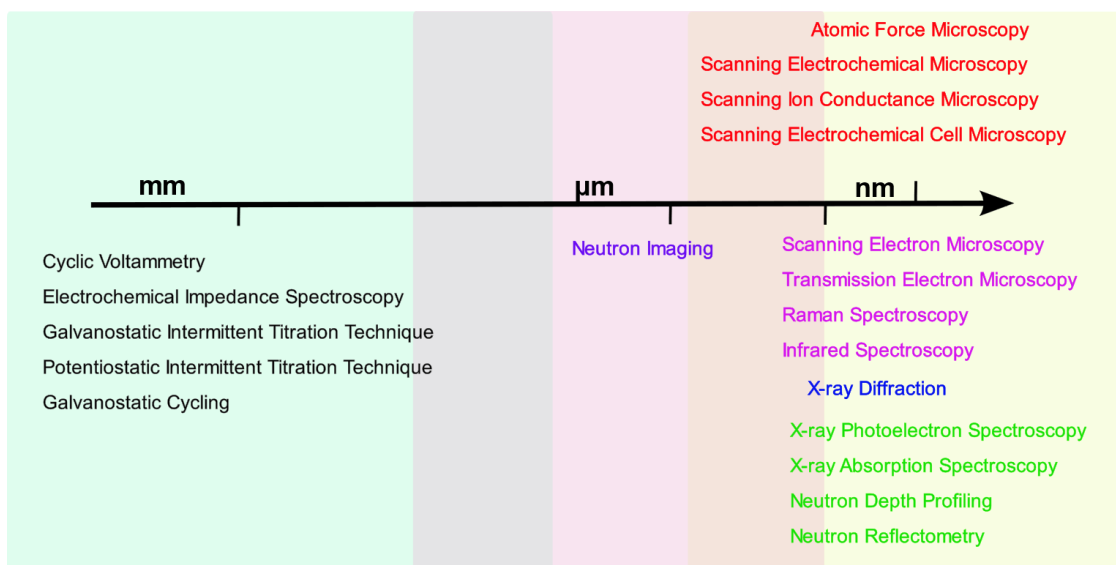


Figure 1.11. Commonly used multiscale techniques for analyzing and characterizing batteries, arranged based on their ability to provide information in different scales

A broad spectrum of techniques based on X-rays, neutrons, electrons, scanning probes, *etc.* are available for characterizing battery electrodes and evaluating their performance in various dimensions (**Figure 1.11**). As this dissertation primarily focuses on mass transport, it is imperative to discuss all the available multiscale techniques suitable for this purpose. Therefore, the initial discussion revolves around the well-established methods such as cyclic voltammetry, electrochemical impedance spectroscopy, and galvanostatic intermittent titration techniques that serve as alternatives to the microscale mass transport detection techniques. Subsequently, we will delve into microscale techniques such as scanning electrochemical microscopy (SECM) and scanning ion conductance microscopy (SICM), which are the core parts of this dissertation.

1.4.1. Cyclic Voltammetry (CV)

1.4.1.1. Working Principle

CV is a commonly used technique to study the bulk properties of electrochemical systems, including batteries. It provides information about mass transport and kinetics of electrochemical reactions. CV has been used in battery research to investigate their capacity fading (Zhang *et al.*, 2000), interfacial studies (Hui *et al.*, 2018 ; Yoo *et al.*, 2017), and electron and ion transport properties (Clancy et Rohan, 2018 ; Friedl et Stimming, 2017 ; Kim *et al.*, 2020).

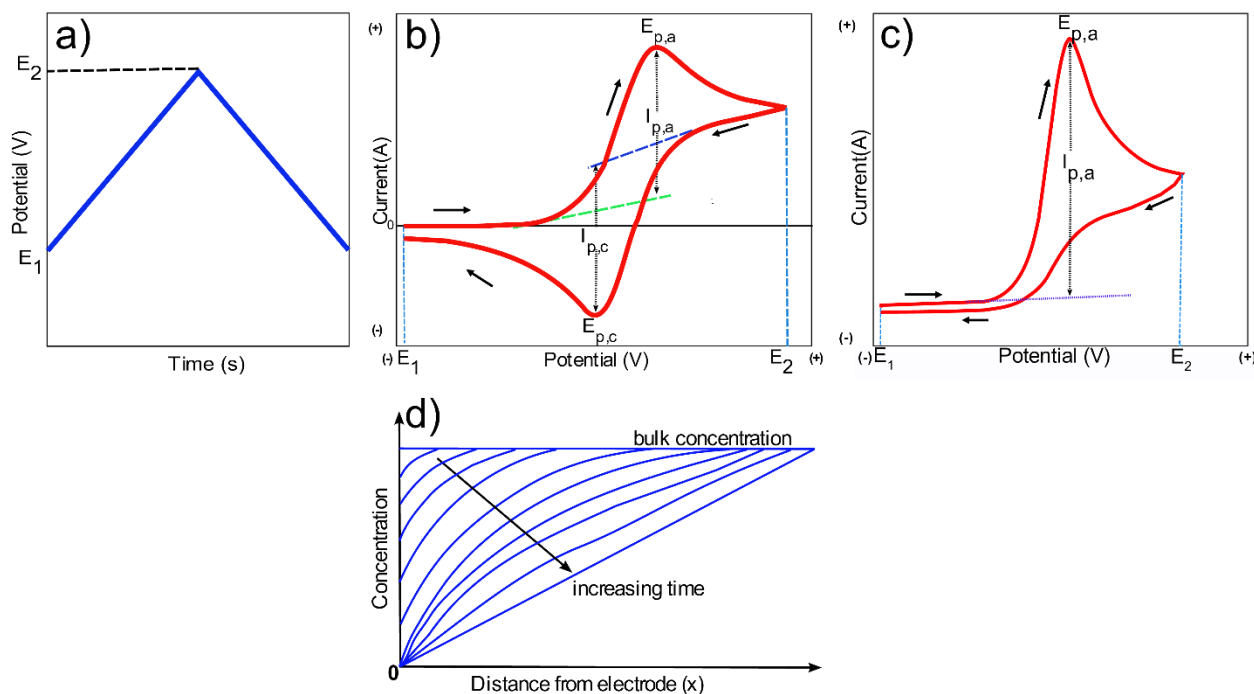


Figure 1.12. Schematic of a) potential waveform, CV of b) reversible reaction, c) irreversible reaction showing only oxidation peak, and d) change in concentration of redox species over time

Generally, a three-electrode cell consisting of a working, reference, and counter electrode is used in a CV measurement. A triangular potential waveform (**Figure 1.12a**) is swept linearly in the electrochemical cell at a specific scan rate, and the resulting current generated due to redox processes at the electrode-electrolyte interface is monitored, which enables the detection of the reversibility of the electrochemical reaction.

In an anodic or oxidative process, the applied potential (E) starts below the standard potential (E^0) of the redox material, while for the reductive process, E begins at a higher potential than E^0 . During the initial stages of both processes, only capacitive or non-faradaic currents are generated. For instance, in the case of an anodic process (oxidation), the potential sweep occurs in the positive direction, and the redox species in the vicinity of the working electrode begin to undergo oxidation. As the charge transfer rate increases, the faradaic current also increases, and gradually reaches a maximum current ($I_{p,a}$) at a specific potential ($E_{p,a}$) (**Figure 1.12b**). Over

time, the concentration of redox species in the surrounding area of the working electrode decreases, creating a concentration gradient between the electrode surface and the bulk electrolyte (**Figure 1.12d**). To maintain the oxidation rate, additional redox species must diffuse from the bulk electrolyte. However, as the diffusion layer expands, the faradaic current decreases to a minimum on increasing the potential due to the reduced concentration of the redox species.

After reaching the potential, E_2 , reversing the potential results in the reduction of oxidized species, and the current increases in the negative direction. After reaching its maximum ($I_{p,c}$), the current decreases due to the slow diffusion similar to the oxidative scan. Therefore, a duck-shaped cyclic voltammogram was formed in the case of a completely reversible system that includes both oxidation (anodic) and reduction (cathodic) peaks (**Figure 1.12b**). Moreover, as the charge transfer is faster, the current is limited only by the diffusional mass transport in a reversible process. On the other hand, for an irreversible system, either one peak corresponding to oxidation or reduction is present (**Figure 1.12c**).

The peak current (I_p) depends on the diffusion coefficient (D), concentration (C) of the species of interest, electroactive area (A) of the working electrode and the scan rate (v) with which the potential is swept. The relation between the peak current and these parameters for a reversible process at 298 K is given by the Randles-Sevcik equation:

$$I_p = 2.69 \times 10^5 n^{3/2} AC v^{1/2} D^{1/2} \quad (1.11)$$

Where n is the number of electrons involved in the electrochemical reaction. The linear relation between I_p and $v^{1/2}$ can be utilized to measure the diffusion coefficient. For example, Yu *et al.* conducted a systematic study of LiFePO₄ electrodes by CV and determined the apparent diffusion coefficient of Li⁺ ions (Yu *et al.*, 2007). In addition, the effect of electrode mass loading, scan rate, electrolytes, and temperature on the CV profile was also investigated. However, applying the Randles-Sevcik equation for analyzing battery electrodes requires careful consideration of electrode structure and their properties, as it is based on the assumption that the system contains only one diffusing species, the electrode surface is homogeneous, and exhibits planar diffusion. This limitation poses challenges when evaluating porous composite electrodes

in batteries, which possess diverse levels of porosity, tortuosity, and particle distribution, resulting in non-uniform and intricate diffusion pathways.

1.4.1.2. Effect of Transport on CV Shape

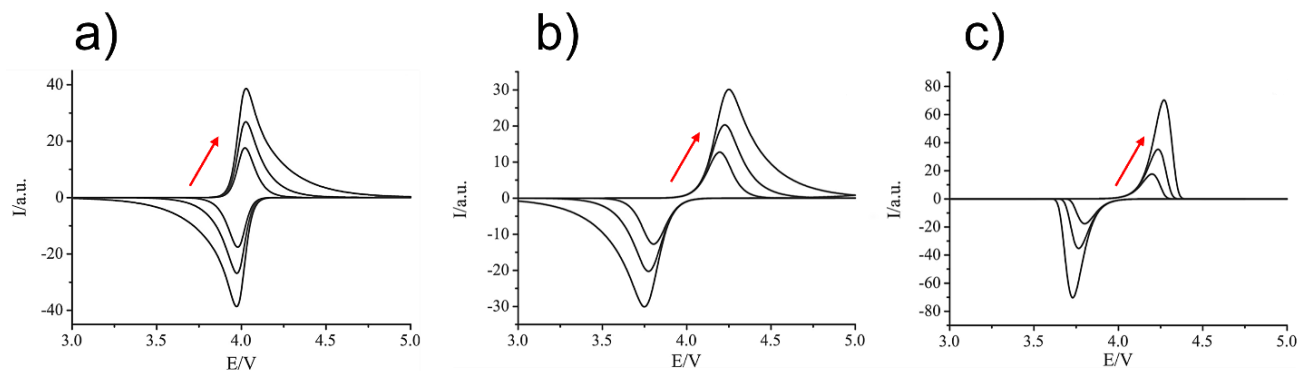


Figure 1.13. Difference in the shape of cyclic voltammograms with different kinetic and mass transport parameters. a) rate of charge transfer \gg mass transport rate, b) very slow rate of charge transfer and mass transport, and c) rate of charge transfer \ll mass transport rate, red arrows indicate the increasing scan rate direction (Vassiliev *et al.*, 2016)

The charge and discharge characteristics of batteries can be studied using the anodic and cathodic scans of CV, respectively. The shape of the cyclic voltammogram varies depending on the Li^+ (de)intercalation kinetics and mass transport limitation (Vassiliev *et al.*, 2016). When the intercalation or charge transfer rate is faster than the diffusional transport in the electrolyte, the current increases steeply, and the peak potential shifts in the direction of the potential scan. Furthermore, the region of CV where the decaying current's slope decreases with an increasing scan rate can be used to determine the diffusion coefficients (**Figure 1.13a**).

Conversely, if the rate of mass transport and charge transfer is slow, a broad peak is obtained at the beginning of CV due to sluggish charge transfer (**Figure 1.13b**). Increasing the scan rate shifts the oxidation and reduction peak potential to more anodic and cathodic values, leading to a higher peak-to-peak separation. Moreover, the peak current decreases slowly, predominantly due to diffusional transport. The final scenario is when the mass transport rate is significantly higher

compared to the charge transfer rate, in which the shape of the voltammogram is controlled by the charge transfer kinetics (**Figure 1.13c**).

1.4.1.3. Planar and Hemispherical Diffusion

The surface area of the working electrode plays an important role in CV measurements. The diffusion profile of the redox species could be planar or hemispherical between the bulk electrolyte and at the electrode/electrolyte interface depending on the surface area. The duck-shaped CV discussed in the previous sections is obtained as a result of semi-infinite linear diffusion (**Figure 1.14a**) towards the surface of a planar electrode also called macroelectrode, which has a surface area in the range of square millimeters (mm^2).

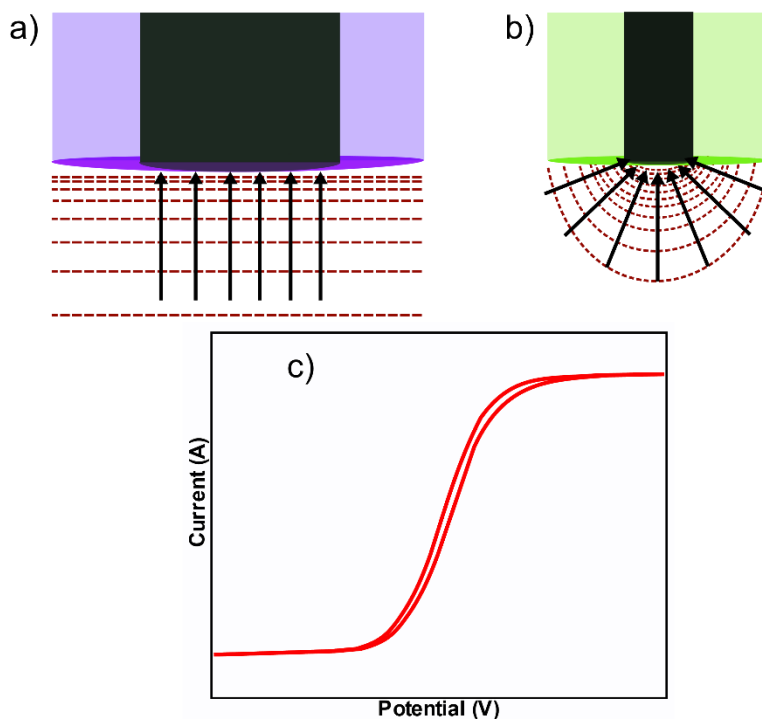


Figure 1.14. a) Planar diffusion in macroelectrode, b) hemispherical diffusion in microelectrode (dotted lines represent the diffusion profile and the arrows indicate the transport of diffusing species), and c) cyclic voltammogram of microelectrode

The electrode with at least one dimension in the range of $1\ \mu\text{m}$ to $25\ \mu\text{m}$ is called a microelectrode (ME). A hemispherical diffusion profile occurs in the case of ME and leads to a

sigmoid-shaped CV (**Figure 1.14b, c**). Owing to the micrometer dimension of ME, low currents in the range of pA-nA are detected. This minimizes the ohmic or voltage drop (IR) that arises due to the electrolyte resistance (R) between the working and reference electrodes when the current (I) flows. During CV at low scan rates, steady-state is achieved where the rate of oxidation or reduction is equal to the rate of diffusion due to the hemispherical diffusion at the ME. The steady-state current (I^0) at a disc-shaped ME is given by,

$$I^0 = 4nF\beta DCa \quad (1.12)$$

Where a is the radius of the electroactive area and β is a function of the RG (ratio of outer to inner radii) of the microelectrode (Bard et Faulkner, 2000 ; Lefrou et Cornut, 2010).

ME offers the advantage of conducting quick voltammetric studies and electrochemistry in confined spaces due to the faster response time and small size. The development of ME has led to the emergence of scanning probe microscopy techniques such as scanning electrochemical microscopy (SECM), which is the focal point of this dissertation.

1.4.2. Electrochemical Impedance Spectroscopy (EIS)

1.4.2.1. Working Principle

EIS is a powerful non-destructive, and rapid technique widely used in LIBs to analyze the bulk and interfacial transport phenomena over a range of time scales. In contrast to CV which employs a large potential perturbation to measure transient current response, EIS applies a small sinusoidal perturbation to an electrochemical cell at equilibrium across a wide frequency range and measures the characteristic response, which depends on the cell impedance at different time scales. Furthermore, EIS is, in favorable cases, capable of deconvoluting the potential drop due to ohmic, charge transfer, and concentration overpotentials and is instrumental in quantifying parameters such as diffusion coefficient, charge transfer resistance, and double layer capacitance (Hui *et al.*, 2019).

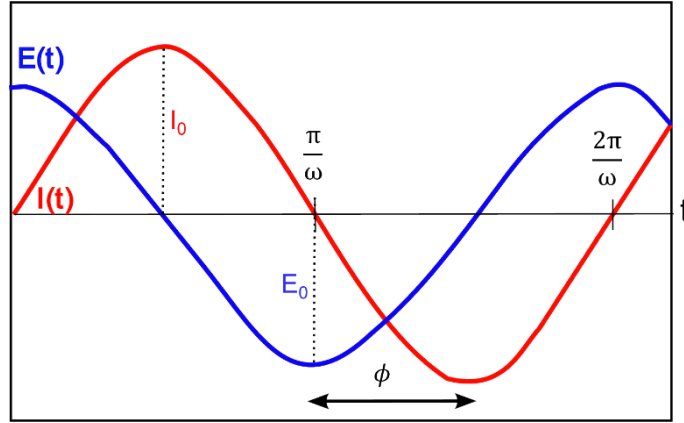


Figure 1.15. Schematic showing the relation between input and output signals over time
(Redrawn from (Vadhva *et al.*, 2021))

In EIS, the input sinusoidal signal can be potential (potentiodynamic) or current (galvanostatic). Typically, a sinusoidal potential, $E(t)$ at a frequency (f) is applied, and the resulting current, $I(t)$ is measured as output (**Figure 1.15**). While the output current has the same frequency as the input signal, its amplitude and phase may differ.

In potentiodynamic mode,

$$E(t) = E_0 \sin(\omega t) \quad (1.13)$$

$$I(t) = I_0 \sin(\omega t + \phi) \quad (1.14)$$

where $\omega = 2\pi f$ is the angular frequency, E_0 and I_0 are the amplitude of potential and current, t is the time, $\omega t + \phi$ is the phase angle and ϕ is the phase difference. The ratio of Eq. 2.4 and 2.5 gives an expression similar to Ohm's law for determining the impedance ($Z(\omega)$), which is the opposition to the flow of current in the system.

$$Z(\omega) = \frac{E(t)}{I(t)} = \frac{E_0 \sin(\omega t)}{I_0 \sin(\omega t + \phi)} = Z_0 \frac{\sin(\omega t)}{\sin(\omega t + \phi)} \quad (1.15)$$

As $E(t)$ and $I(t)$ consists of amplitude and phase difference, they can be represented by a complex number. As such, the impedance can also be represented as a complex number comprising of a real part (Z') and an imaginary (Z'') part.

$$Z(\omega) = |Z|[\cos(\phi) + j\sin(\phi)] = Z' + jZ'' \quad (1.16)$$

The modulus of Z and phase difference (ϕ) can be calculated as follows:

$$|Z| = \sqrt{Z'^2 + Z''^2} \quad (1.17)$$

$$\phi = \tan^{-1}\left(\frac{Z''}{Z'}\right) \quad (1.18)$$

1.4.2.2. Understanding EIS Spectra

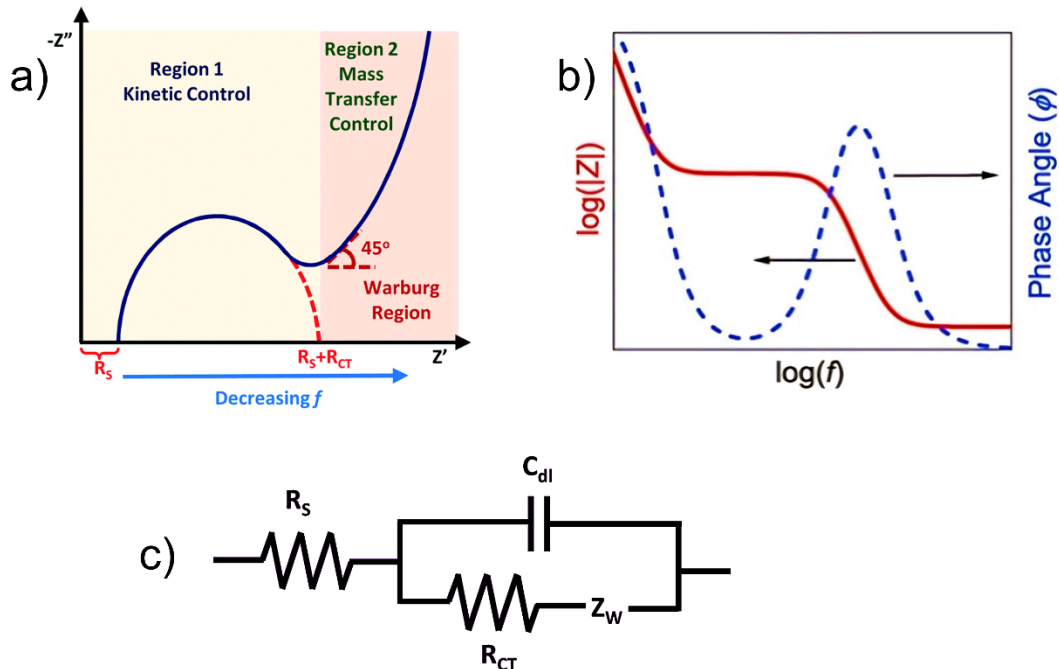


Figure 1.16. a) Nyquist plot (Laschuk *et al.*, 2021), b) Bode plot (Vadhva *et al.*, 2021), and c) Randle's circuit for an electrochemical cell

EIS spectra are represented in the form of either Nyquist or Bode plots. Nyquist plot (**Figure 1.16a**) provides the relation between the real and imaginary components of impedance, whereas Bode plot (**Figure 1.16b**) gives the relation of $\log |Z|$ vs $\log(f)$ and ϕ vs $\log(f)$. Among the two, the Nyquist plot is commonly used in LIBs analysis as the stability of the system, along with the solution (R_s) and charge transfer (R_{CT}) resistance values contributing to impedance, can be determined directly from the plot.

In general, the overall impedance of an electrochemical cell due to the electrolyte resistance, double-layer capacitance at the electrode-electrolyte interface, charge transfer kinetics, and mass transport can be represented with the help of resistors and capacitors. Therefore, the kinetic and mass transfer controlled regions in the Nyquist plot can be interpreted with the help of an equivalent circuit. One of the simplest and widely used equivalent circuits is Randle's circuit (**Figure 1.16c**), consisting of the solution resistance (R_s), in series to a parallelly connected combination of double layer capacitance (C_{dl}), charge transfer resistance (R_{CT}), and Warburg impedance (Z_w). In the low-frequency region of the spectrum, the overall impedance is controlled by the mass transfer or Warburg impedance and is given by

$$Z = R_s + R_{CT} + \sigma \omega^{-\frac{1}{2}}(1 - j) \quad (1.19)$$

Where $j = \sqrt{-1}$ and σ is the Warburg coefficient, which can be obtained from the slope of the linear relation between Z' or Z'' vs $\omega^{-\frac{1}{2}}$. The diffusion coefficient (D) can be calculated from σ using the relation (Lazanas et Prodromidis, 2023),

$$\sigma = \frac{2RT}{n^2 F^2 A C \sqrt{D} \sqrt{2}} \quad (1.20)$$

Where n is the number of electrons, A the electrochemical active area and C the bulk concentration of electroactive species. This relation has been utilized in EIS battery studies to quantify the mass transport in electrodes.

Although the Nyquist plot using Randle's circuit serves as a valuable tool for interpreting the EIS data, the experimental data can deviate from this model circuit due to the surface roughness of the electrodes and non-linear diffusion processes. As a result, the capacitance component in the circuit may be substituted by a constant phase element (CPE), to improve the numerical fitting of the circuit model to the experimental EIS data (Lasia, 2022). Despite the challenges associated with numerical fitting, the semi-circle region of the EIS spectrum at high-frequency offers valuable insights about R_{CT} , while the slope of the linear region at low frequency provides information about the mass transport parameters.

1.4.3. Galvanostatic & Potentiostatic Intermittent Titration Technique (GITT & PITT)

1.4.3.1. Working Principle

GITT and PITT are frequently used to assess the kinetic processes occurring in batteries. Many studies have used these techniques to determine the Li^+ diffusion coefficient in various electrodes, including graphite, LiFePO_4 , etc. (Aurbach *et al.*, 1998 ; Churikov *et al.*, 2010 ; Dees *et al.*, 2009 ; Markevich *et al.*, 2005). Unlike CV, which only offers an average diffusivity value, these techniques can effectively determine the lithium diffusion coefficient at various states of charge in LIBs. An electrochemical cell under equilibrium can be subjected to either a constant current (galvanostatic) pulse or a potential (potentiostatic) pulse. For instance in GITT, when a constant current pulse (I_0) is applied to a system under equilibrium at time t_0 , the equilibrium potential (E_1) changes to E_2 due to an IR drop originating from the internal resistance of the cell, including the electrolyte resistance (**Figure 1.17**) (Kim *et al.*, 2022). With a positive applied current, lithium ions deintercalate from the host material during the pulse duration (τ), resulting in a change in the potential to E_3 . Once the applied current pulse is stopped, the potential decreases due to the IR drop. This step is followed by a relaxation period during which no current flows. This allows the electrode composition to become homogeneous through the diffusion of Li^+ ions, and the system reaches a new equilibrium potential (E_4).

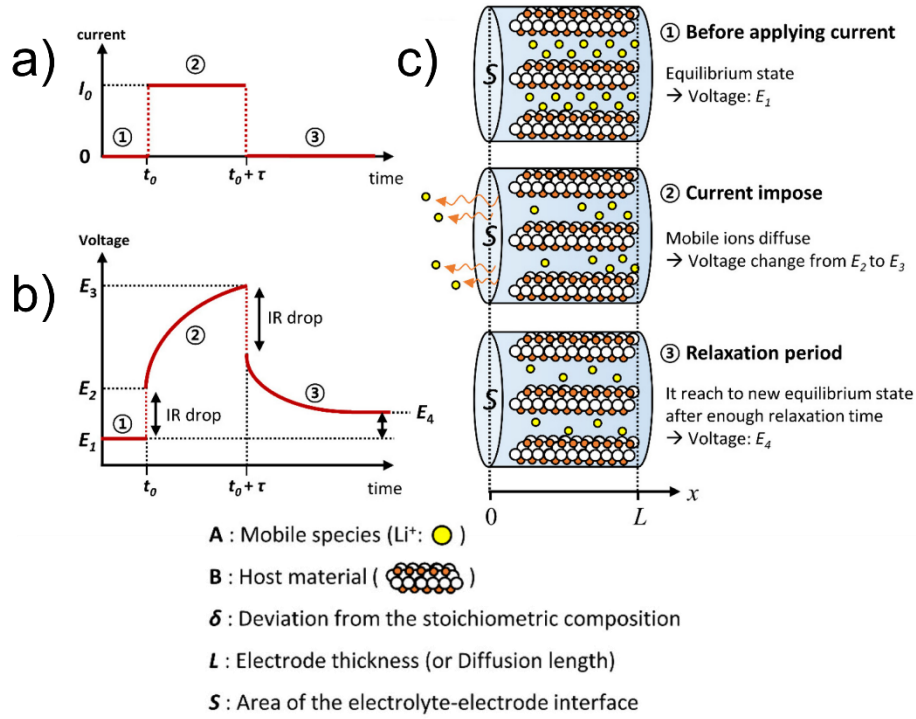


Figure 1.17. a) Schematic showing the applied current pulse with a duration (τ) b) corresponding transient voltage change and c) transport of Li^+ ions during the single step of GITT (Kim *et al.*, 2022)

Based on the current or voltage output, the diffusion coefficient of Li^+ ions (D) can be determined by a simplified equation derived from the combinations of Fick's first and second laws along with the Butler-Volmer equation as follows (Jia *et al.*, 2022 ; Kim *et al.*, 2022):

$$D = \frac{4}{\pi\tau} \left[\frac{m_B V_M}{M_B A} \right]^2 \left(\frac{\Delta E_s}{\Delta E_t} \right)^2 \quad (1.21)$$

Where m_B is the mass of host material in the electrode (g), M_B is the molar mass of the host material (g mol^{-1}), A is the electrode-electrolyte interface area (cm^2), V_M is the molar volume of the material ($\text{cm}^3 \text{mol}^{-1}$), $\Delta E_s = E_4 - E_1$ is the steady state voltage change and $\Delta E_t = E_3 - E_2$ is the total voltage change. The diffusion coefficient can be obtained using equation 1.21 when the pulse time (τ) is much smaller than the characteristic diffusion time (τ_{diff}), *i.e.*,

$$\tau \ll \tau_{diff} = \frac{l^2}{D} \quad (1.22)$$

Where l is the characteristic diffusion length that is assumed to be equal to the electrode thickness. Consequently, one drawback of GITT or PITT measurements is the long relaxation time required for the system to reach equilibrium, which can take up to a month or more depending on the experimental requirements (Gmitter *et al.*, 2010).

In summary, the electroanalytical techniques discussed in the preceding sections share the common characteristic of being able to determine diffusion coefficients within the composite battery electrodes at the mesoscale. Furthermore, they provide information about mass transport, encompassing both solid and solution phases in electrodes. Alongside this information, microscale and localized insights separately from these phases are also crucial for improving the power performance of LIBs as the range of ion transport processes within batteries occurs in nano to millimeter scale. As such, using techniques such as SECM and SICM is critical. The next section will discuss these two important scanning probe techniques.

1.4.4. Scanning Electrochemical Microscopy

Introduced simultaneously by Bard and Engstrom groups in 1989, SECM offers the unique advantage of investigating the electrode-electrolyte interface, degradation reactions, and electrode architectures with high spatial resolution (Bard *et al.*, 1989 ; Engstrom et Pharr, 1989). It is a powerful *in situ* technique that enables the monitoring of electrochemical processes in their actual environment and provides *transient* information at the micro to the nanoscale, which cannot be obtained with any of the macroscale techniques previously discussed.

1.4.4.1. Principles of Operation

A typical SECM instrument includes the following components (**Figure 1.18**):

1) A microelectrode (ME) with dimensions in the low micrometer or nanometer range, acting as a working electrode (WE1). The advantages of ME were already discussed in section 1.4.1.3.

- 2) A 3D positioning system consisting of stepper and piezo motors for controlling the movements in x, y, and z directions
- 3) A bipotentiostat for measuring and controlling potential and current
- 4) A data acquisition system to coordinate all components and record data

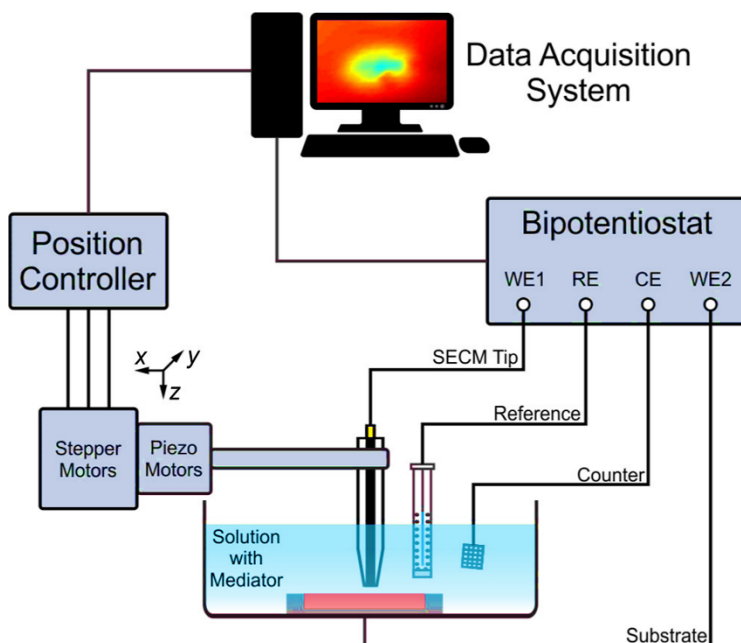


Figure 1.18. Schematic of SECM setup showing the various components (Polcari *et al.*, 2016)

When an electric potential corresponding to the redox potential of the mediator is applied between the WE1 and reference electrode, the mediator undergoes either oxidation or reduction, resulting in a faradaic current in the pA to nA range. SECM operates by measuring this faradaic current at the ME tip, allowing for analysis of the substrate immersed in the electrolyte solution. The substrate can serve as a second working electrode (WE2) if necessary or remain unbiased depending on the operating modes of SECM and specific requirements. The spatial resolution of SECM depends on the size of ME and the operating modes being used, which gives the benefit of monitoring features that are not observable in one mode to be noticeable in the other mode (Wang *et al.*, 2015). Moreover, SECM can identify well-separated features on the substrate if the

minimum feature size is 10 to 20 times smaller than the diameter of the ME *i.e.*, a 1 μm diameter ME can resolve 50 -100 nm sized features on the substrate (Bard *et al.*, 1992, p. 12).

1.4.4.1. Battery Relevant Operating Modes of SECM

There are several operating modes available in SECM. These include feedback, tip generation/ substrate collection (TG/SC), substrate generation/ tip collection (SG/TC), and redox competition, which are widely used in studying energy storage devices.

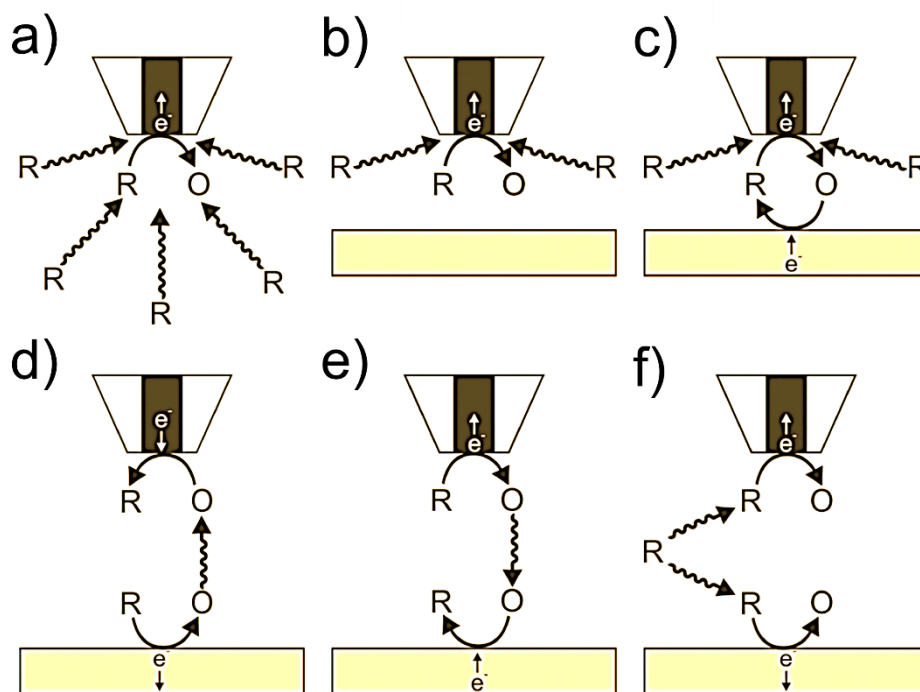


Figure 1.19. Schematic of different operating modes in SECM with a redox mediator ‘R’ undergoing an oxidation reaction at the ME. a) hemispherical diffusion at steady state where microelectrode positioned away from the substrate, b) negative feedback near insulator, c) positive feedback near conductor, d) substrate generation-tip collection (SG/TC) mode, e) tip generation- substrate collection (TG/SC) mode, f) redox competition mode. Redrawn from Polcari *et al.*, 2016

1) Feedback Mode

It is one of the first and commonly used modes in SECM. This mode is used in all SECM-related studies in this dissertation. Typically, in SECM, the faradaic current generated at the ME due to the oxidation or reduction reaction is recorded. For instance, consider the oxidation of a redox mediator R at the ME as follows:



As more R is used up at the ME, the difference in concentration of R between the center of ME and the remaining part of the electrochemical system generates a diffusion layer. As explained in section 1.4.1.3, the diffusion profile for a disk-shaped ME is hemispherical. When the ME/SECM tip is far from the substrate, *i.e.*, at a tip-substrate distance (d) 10 times greater than the radius of the tip (a), called the bulk position, the current corresponding to R oxidation (I^0) is detected at the ME (**Figure 1.19a**) and is given by equation 1.12. However, this faradaic current measured at the tip can significantly be affected by the presence of a substrate, depending on the substrate's topography and electrochemical activity.

In feedback mode, when the probe touches a substrate that is insulating, the oxidation reaction is impeded by its presence as the diffusion of R is hindered towards the tip, resulting in a net zero faradaic current (negative feedback) (**Figure 1.19b**). In contrast, when the tip makes contact with a conducting substrate, although the diffusion is hindered, the current measured at the substrate (I^*) is higher than the bulk current as R can be locally regenerated at the conducting substrate by receiving electrons from the substrate, creating positive feedback (**Figure 1.19c**). The results obtained from the feedback modes are represented with approach curves, which illustrate the relationship between the normalized current (I^*/I^0) and normalized tip-substrate distance ($L = d/a$) (**Figure 1.20**). The approach curves provide direct insight into the electrochemical nature of the substrate under study. The approach curve data for positive and negative feedback measurements can be quantitatively interpreted using approximate analytical expressions (Lefrou et Cornut, 2010). Chapter 3 discusses how this mode can be utilized to analyze the transport parameters for a porous substrate.

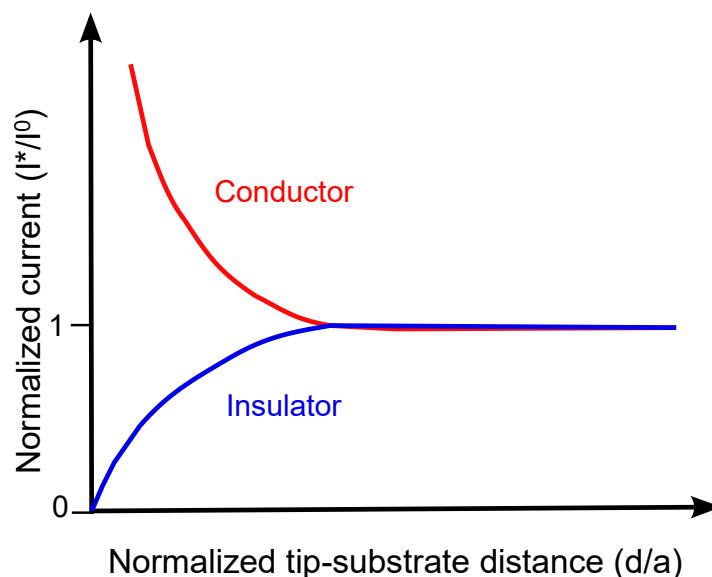


Figure 1.20. Representative approach curve of insulating and conducting substrates

2) Generation /Collection (GC) Mode

The generation /collection mode has two types: 1) substrate generation-tip collection (SG/TC) mode (**Figure 1.19d**), and 2) tip generation-substrate collection (TG/SC) mode (**Figure 1.19e**).

In SG/TC mode, R undergoes oxidation at the substrate generating an oxidized species that is being collected (reduced) by the biased tip. This approach has been effective in analyzing the concentration profile or chemical flux of species produced at the substrate. However, one drawback of this method is its inability to track larger substrates due to the non-steady state processes at the substrate. Moreover, larger substrate currents lead to a low collection efficiency (ratio of tip current and substrate current).

In TG/SC mode, R is oxidized at the tip and the oxidized species is collected by the substrate. Similar to SG/TC mode, the tip and substrate are biased in TG/SC mode, and the corresponding current at both the tip and substrate is measured. Upon biasing, the initial current at the tip is zero. However, oxidized species diffuses and reaches the tip, leading to a steady state current over time. When the normalized tip substrate distance, L is less than or equal to two, this mode

exhibits higher collection efficiency, unlike the TG/SC mode (Zhou *et al.*, 1992). As a result, the TG/SC mode is commonly employed for studying reaction kinetics.

3) Redox Competition (RC) Mode

While using RC mode, the tip and substrate are brought closer together and biased to the same potential, leading to competition between tip and substrate for the same redox species R (**Figure 1.19f**). The substrate is held at a reducing potential while a reducing potential pulse is applied to the tip to prevent the complete depletion of redox species in the gap between the tip and substrate. Here, only the current at the tip is measured which varies based on the activity of the substrate. For instance, the tip current remains constant over the electrochemically inactive area of the substrate, and it decreases when scanned over the electrochemically active area as the active area consumes the redox species faster than the tip. Compared to the other two modes of SECM, the RC mode is mostly useful in studying the substrate's electrocatalytic activity.

In addition to the three discussed basic modes, other operating modes such as direct, potentiometric modes, *etc.* are particularly useful in the fields beyond energy storage devices (Polcari *et al.*, 2016).

1.4.4.2. Probes in SECM

The probe or microelectrode, with at least one dimension less than 25 μm is the most important part of SECM. Common probe geometries include disk (Danis *et al.*, 2014), conical (Fan *et al.*, 1994), hemispherical (Mauzeroll *et al.*, 2003), ring disk (Nebel *et al.*, 2013), and inlaid ring (Takahashi *et al.*, 2010) (**Figure 1.21**). Among these, the disk geometry is the most prevalent due to its ease of fabrication. These probes are typically manufactured using electroactive wires such as platinum, gold, carbon, and silver as the core, which is then surrounded by a glass sheath. The SECM studies included in this dissertation use platinum disk microelectrodes.

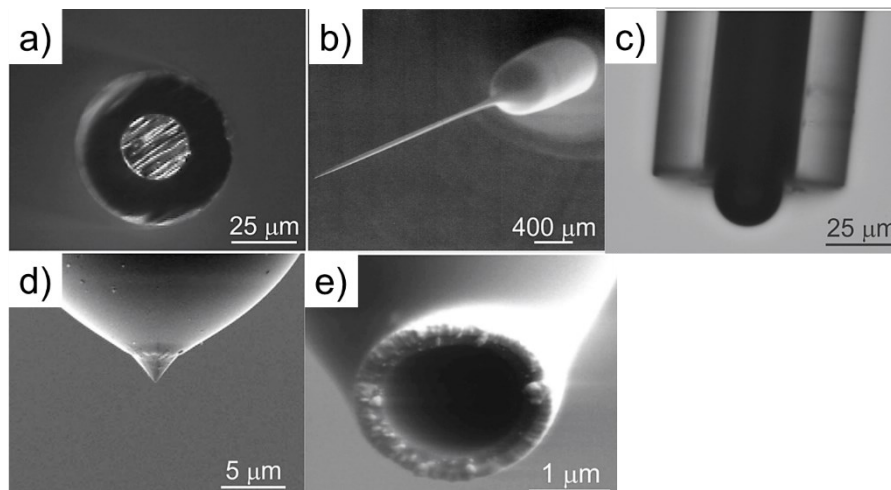


Figure 1.21. Different probe geometries and sizes a) Pt disk microelectrode, b) Pt disk nanoelectrode, c) Hg hemispherical microelectrode, d) Au conical microelectrode, and e) Au ring microelectrode (Polcari *et al.*, 2016)

The probe size is a critical factor in determining the spatial resolution of SECM. The ratio of the radius of the active core to the surrounding glass radius (RG) is an important geometric parameter that influences the quality of the microelectrode. A microelectrode with a smaller RG helps to attain minimum tip-substrate distance and enhances sensitivity by reducing the contact between the insulating glass sheath and the substrate. Although, MEs with diameters ranging from 5 to 25 μm are commercially available, the price per ME is very high. In contrast, probes in the micro to nanometer range with a reduced RG can be fabricated in-house using techniques such as laser pulling (Katemann et Schuhmann, 2002) and electrochemical etching (Sun *et al.*, 2001). For instance, the Mauzeroll group developed a simple, fast, and reproducible method using the laser pulling technique for fabricating disk microelectrodes with controlled geometries and an RG between 2.5 and 3.6 (**Figure 1.22**) (Danis *et al.*, 2015). This procedure is followed for the microelectrode fabrication in this dissertation.

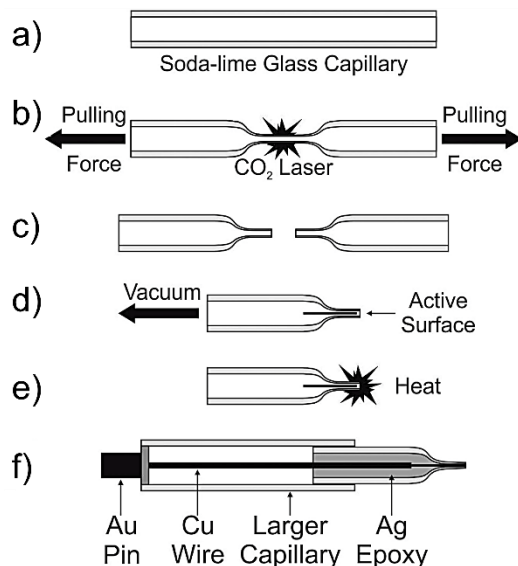


Figure 1.22. Different steps in the fabrication of microelectrodes using a) soda-lime glass capillary, b) laser heating and pulling capillaries c) pulled micropipettes, d) Adding active wire inside micropipette, e) heat sealing the tip and, f) assembled microelectrode (Danis *et al.*, 2015)

1.4.4.3. SECM Modeling

Modeling studies are often helpful in interpreting and quantifying SECM data especially when numerous factors including the probe geometry (Amphlett et Denuault, 1998), substrate's electrochemical activity (Mishra *et al.*, 2024 ; Xiong *et al.*, 2006), architecture (Hossain *et al.*, 2021), and topography (Li *et al.*, 2016), influence the faradaic current generated at the probe. Additionally, it offers precise control over intricate substrate geometries compared to experimental analysis.

Several numerical methods including the finite difference method (Bard *et al.*, 1992 ; Unwin et Bard, 1991), finite element method (Kwak et Bard, 1989 ; Xiong *et al.*, 2007), and boundary element method (Sklyar *et al.*, 2006 ; Sklyar et Wittstock, 2002), are available for SECM. Among these, the finite element method (FEM) is most commonly employed numerical method for feedback mode SECM as it offers the advantage of modeling irregular geometries and generating concentration profiles of diffusing species (Kwak et Bard, 1989). Moreover, the FEM modeling studies can easily be conducted using commercial computational software like COMSOL Multiphysics. In FEM studies of SECM, the first step involves defining a model

geometry that simulates the experimental setup, including domains such as bulk electrolyte, probe, and substrate. The model is then discretized into finite elements (mesh) to which the boundary conditions are applied, and the partial differential equations are solved. The model geometry could be two-dimensional (2D) axisymmetric or three-dimensional (3D). 2D-axisymmetric geometry is mostly suitable for modeling probe approach curves and flat substrates. On the other hand, 3D geometry, despite the higher computational cost, resembles the true experimental situation and can accommodate more complex diffusion patterns as there is no symmetry requirement (Filice *et al.*, 2015 ; Sklyar et Wittstock, 2002).

The Nernst-Planck equation (Eq.1.3) is useful for modeling the mass transport of redox mediators in SECM. The migration and convection terms in the Nernst-Planck equation can be neglected as the excess supporting electrolytes are added, and the approach curve measurements in the feedback mode are conducted with a slow speed that does not cause disturbance to the electrolyte. Consequently, equation 1.3 is reduced to Fick's diffusion equation. In SECM, as mass transport in the space between the probe and substrate is well-defined and assumed to be hemispherical, quantitative information about the substrate properties can be acquired by modeling the diffusive transport in this domain in stationary or time-dependent scenarios. As such, for stationary or steady-state study, Fick's first law (Eq.1.24) is followed, while for time-dependent study, Fick's second law (Eq.1.25) can be applied to calculate the flux (J).

$$J = -D\nabla C \quad (1.24)$$

$$\frac{\partial C}{\partial t} = -\nabla J \quad (1.25)$$

Where D is the diffusion coefficient and C is the concentration of the species.

The numerical modeling studies discussed in this dissertation focus on feedback mode SECM, where a 3D stationary modeling study is conducted. In brief, when the probe is away from the substrate, a steady state is achieved by the probe quickly, and the diffusive flux of molecules at the probe is maximum, which can be obtained using equation 1.24. If the substrates being investigated are porous, a second mass transport constraint arises from their porosity (ϵ) and

tortuosity (τ). This consequently reduces the diffusive flux near the substrate (J'), and is given by,

$$J' = -\frac{\varepsilon}{\tau} D \nabla C \quad (1.26)$$

After implementing the necessary boundary conditions for the system under investigation, the integration of the total normal flux across the probe's surface area (A) yields the probe current, a critical parameter in the SECM simulation that can be directly compared with the experimental results.

$$I = nFD \int_0^A \left[\frac{\partial C}{\partial z} \right]_{z=0} dA \quad (1.27)$$

Where $\left(\frac{\partial C}{\partial z} \right)$ is the concentration gradient normal to the microelectrode surface and $z = 0$ means the microelectrode-electrolyte interface. The current between the probe and the substrate at all tip-substrate distances can be determined easily using the above equation.

Furthermore, in SECM, 3D models are essential for simulating challenging situations involving the investigation of the tilt of the substrate or the probe, and surface roughness in porous substrates. Chapters 4 and 5 offer a comprehensive discussion of the 3D SECM geometries employed for analyzing the mass transport in various porous substrates, considering their geometric intricacies and surface roughness.

1.4.5. Scanning Ion Conductance Microscopy (SICM)

1.4.5.1. Working Principle

SICM is a nanopipette-based technique, introduced by Hansma *et al.* in 1989 (Hansma *et al.*, 1989). Traditionally, SICM is used for imaging topography. Another interesting application of SICM is in the field of biology, where nanopipettes are used to deliver species to the interface of living cells (Ivanov *et al.*, 2015 ; Korchev *et al.*, 1997 ; Page *et al.*, 2017). In SICM, typically, a nanopipette is used as a scanning probe and the instrumental setup resembles that of SECM, featuring stepping motors and piezoelectric actuators. It involves a two-electrode system, with

one electrode inserted into the nanopipette filled with electrolyte, and the other electrode in the bulk electrolyte solution (**Figure 1.23**) (Page *et al.*, 2017). A potential is applied between these two electrodes and the ion current generated is measured using a low-current amplifier. The sensitivity of this ion current at the tip increases when it is close to the substrate at a distance comparable to the order of the tip radius. Consequently, the tip current can be used as feedback to control the tip-substrate distance, allowing for contactless positioning of the tip relative to the substrate surface. Furthermore, in SICM, electrolytes with high ionic strength are commonly employed to minimize the formation of the diffuse double layer at the interface to less than 1 nm (Klenerman *et al.*, 2011). As a result, the nanopipette remains unaffected by surface charge effects, and the feedback current is exclusively dependent on the substrate's topography.

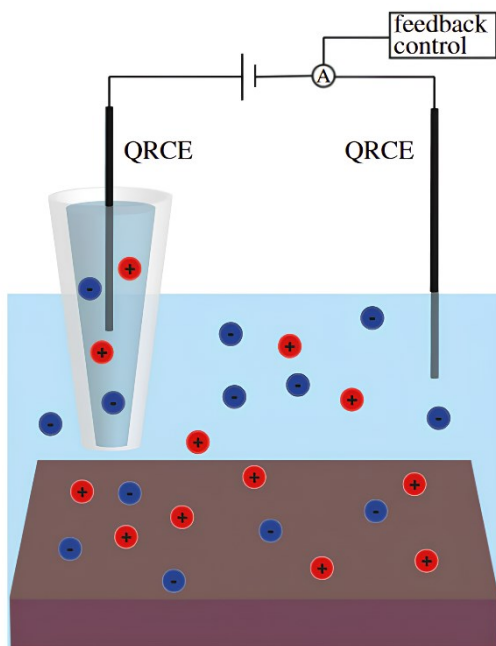


Figure 1.23. SICM setup with two-electrode configuration (QRCE: Quasi-reference counter electrode) (Page *et al.*, 2017)

Like SECM, the current and tip-substrate distance relationship in SICM can also be interpreted with the help of approach curves. In the bulk electrolyte *i.e.*, when the pipette is far from the substrate, owing to the unrestricted flow of ions towards the tip, the initial ion current generated is maximum and reaches a steady state. However, as the nanopipette approaches the substrate,

the ion flow toward the tip orifice is disrupted by the presence of the substrate, causing the net ion current to drop to zero. Since the working principle relies on the ion current flow between the nanopipette electrode and the electrode in the bulk electrolyte, the approach curve consistently shows negative feedback, regardless of whether the unbiased substrate being investigated is insulating or conducting.

1.4.5.2. Probe Fabrication and Equivalent Circuit

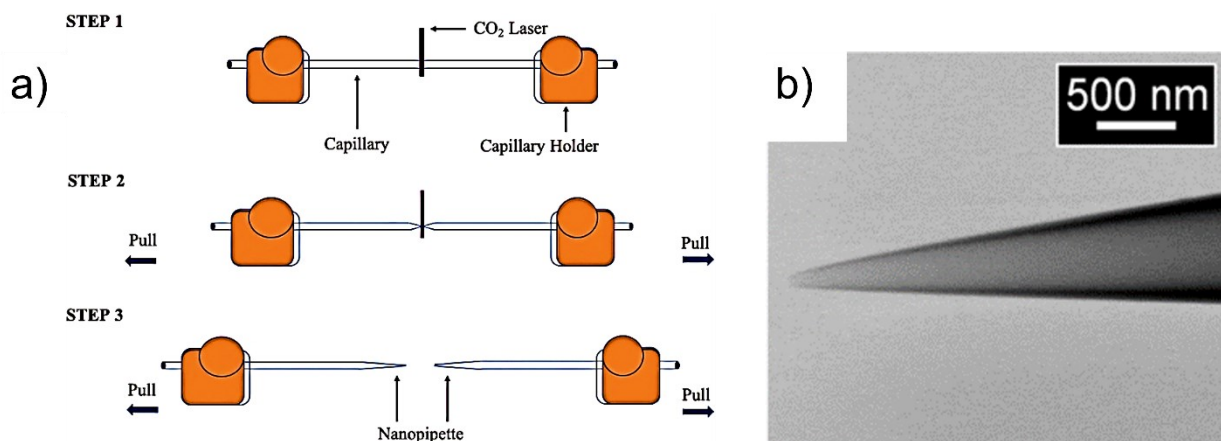


Figure 1.24. a) Different steps in nanopipette fabrication using a laser puller (Stanley et Pourmand, 2020), b) SEM image of a nanopipette (Zhu *et al.*, 2021)

The size and shape of SICM tips play a crucial role in determining the spatial resolution and sensitivity of the technique. Typically, borosilicate or quartz glass capillaries are used for the tip fabrication. With the help of a laser puller, these capillaries can be heated and melted at their center, producing two identical pipettes with a fine taper (**Figure 1.24a**). By choosing the appropriate laser pull parameters and glass capillary, reproducible pipettes with controlled geometry and tip sizes varying from nano to micrometers can be fabricated. As such, SICM offers a high spatial resolution in contrast to SECM. Moreover, the preparation of SICM probes is notably less complex, and the tip shape is generally conical. The fabricated tips can be imaged using characterization techniques like scanning electron microscopy (SEM) (**Figure 1.24b**) and transmission electron microscopy (TEM).

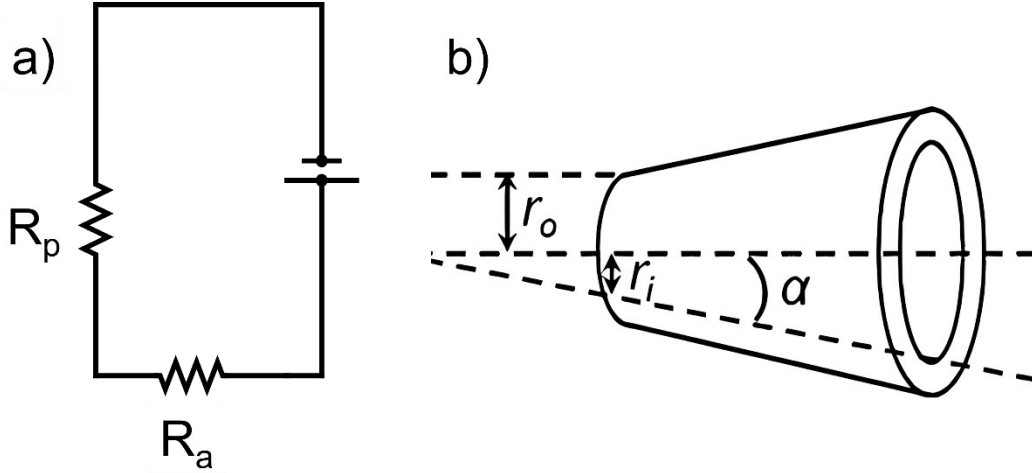


Figure 1.25. a) Equivalent circuit diagram of SICM, b) schematic of a nanopipette with the important geometric parameters (Zhu *et al.*, 2021)

In SICM, the different components are described by an equivalent circuit with resistors connected in series (**Figure 1.25a**). These include the pipette resistance R_p and access resistance R_a that denotes the solution resistance in the gap between the pipette tip and substrate. Both R_p and R_a depend on the conductivity of the electrolyte (κ), and the geometric parameters of the pipette such as the inner radius (r_i), outer radius (r_o), and cone angle (α) (**Figure 1.25b**), as given by (Zhu *et al.*, 2021):

$$R_p \approx \frac{1}{\kappa \pi r_i \tan \alpha} \quad (1.28)$$

$$R_a \approx \frac{\frac{3}{2} \ln \left(\frac{r_o}{r_i} \right)}{\kappa \pi d} \quad (1.29)$$

R_p is dominant in the bulk electrolyte whereas R_a is dominant in the presence of a substrate as it is the term that has a direct dependence on the tip-substrate distance (d). Hence, the total ion current ($I(d)$) generated in SICM is a combination of R_p and R_a , and shows a behavior similar to Ohm's law for an unbiased substrate given by (Zhu *et al.*, 2021):

$$I(d) = \frac{V}{R_p + R_a} \approx I^0 \left[1 + \frac{\frac{3}{2} \ln\left(\frac{r_o}{r_i}\right) r_i \tan(\alpha)}{d} \right]^{-1} \quad (1.30)$$

Where, $I^0 = \frac{V}{R_p}$ is the bulk current. The ratio of bulk current and current near the substrate can be used to determine the transport properties, which will be discussed in Chapter III.

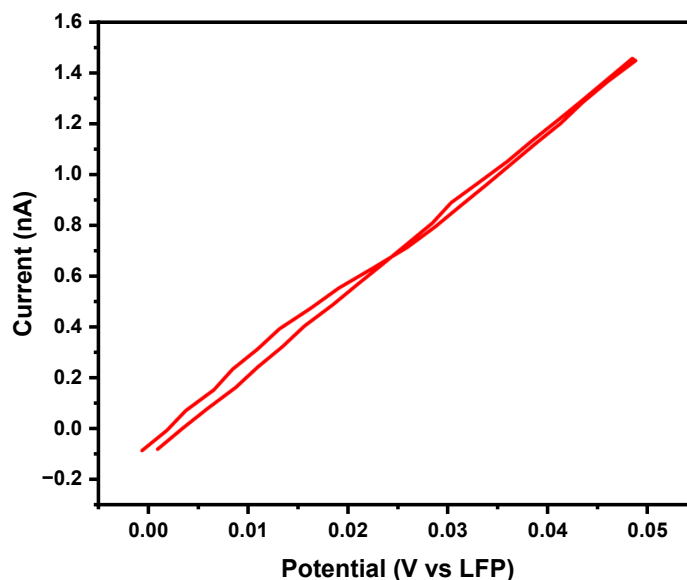


Figure 1.26. Cyclic voltammetry of SICM pipette tip in 0.3 M LiPF₆ in propylene carbonate at a scan rate of 5 mVs⁻¹, WE and CE/RE: LiFePO₄

Additionally, more accurate information about the tip geometric parameters discussed in the above equations can be achieved through ion conductance measurements (Edwards *et al.*, 2009). For instance, a cyclic voltammetry (**Figure 1.26**) can be conducted by positioning the SICM tip in the bulk position. The slope of the CV gives the value of pipette resistance (R_p). While the radius of the tip can be obtained using SEM or TEM, the conductivity of the solution can be obtained using a conductivity probe or from literature. For the example of the CV provided here (**Figure 1.26**), R_p is equal to 29.2 M Ω , r_i obtained from SEM is 1.5 μm and a conductivity of 4.5 mS cm⁻¹ taken from literature for 0.3 M LiPF₆ in propylene carbonate (Hwang *et al.*, 2018). Applying these values to equation (1.28) helps determine the value of the cone angle which is

approximately equal to 1° . However, the cone angle calculation is not critical for the methodology discussed in Chapter III.

1.4.5.3. SICM Operating Modes

The different types of operating modes in SICM include a) constant height (Z) mode, b) direct current (DC) mode c) alternating current (AC) mode, and d) hopping mode.

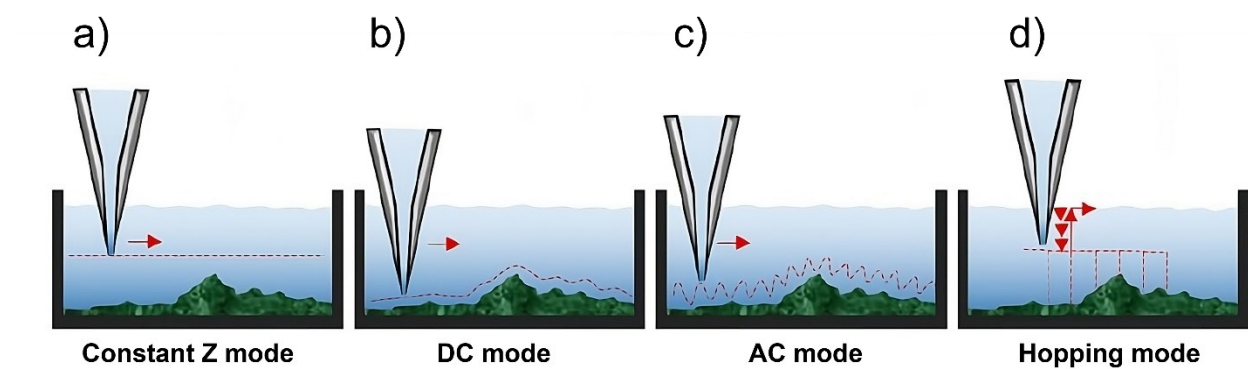


Figure 1.27. Different operating modes in SICM (Leitão, 2015)

1) Constant Z mode

In constant Z mode, the pipette is scanned laterally at a constant distance from the substrate to analyze its topography (**Figure 1.27a**). Although raster scanning patterns are commonly used in this mode, scanning can also be performed in spiral patterns (Momotenko *et al.*, 2016).

Moreover, this mode offers high temporal resolution. However, it is only suitable for studying the topography of extremely flat surfaces with minimal variation in surface features, as there is a risk of tip crashing.

2) DC mode

DC mode is one of the most fundamental and earliest modes developed. This mode utilizes the fluctuation in ion current to serve as a feedback loop for regulating the movement of the tip relative to the interface (**Figure 1.27b**). A predetermined current threshold, also known as the set point, is employed to approach the surface of the substrate. Once the tip has reached the specified set point, it is scanned across the substrate while continuously measuring the ion current. The Z

scanner adjusts the vertical position of the pipette based on the variation in current to maintain the given set point. However, during prolonged measurements, the current in DC mode can drift and result in the tip crashing into the surface.

3) AC mode

In AC mode, an AC signal is produced through either distance modulation or bias/phase/amplitude modulation. In the distance-modulated method, the Z-piezo experiences a minimal oscillation with a predetermined amplitude which is utilized to oscillate vertically the tip at a constant displacement (**Figure 1.27c**). This oscillation generates an AC component in the measured ion current as it approaches the surface, which can be examined using a lock-in amplifier for feedback control. Conversely, in bias/phase/amplitude-modulated methods, an additional voltage modulation is added to the pre-existing DC voltage, generating an AC component rather than physically oscillating the pipette. This mode offers advantages including enhanced temporal resolution, and the ability to investigate substrates with intricate topography. Additionally, it addresses the challenge of current drift during measurements.

4) Hopping mode

In hopping mode, the current records continuously while the pipette approaches the surface until a predetermined set point (**Figure 1.27d**). It is then retracted and relocated laterally to a new location, and the same approach to the surface is repeated. Hopping mode allows the mapping of substrates characterized by significant variations in surface features without damaging the tip. Nonetheless, the repetitive vertical movement of the tip reduces the overall scan speed.

1.4.5.4. SICM Modeling Studies

While not within the scope of this dissertation, it is worth noting that SICM modeling studies can effectively aid in interpreting data similar to SECM (Edwards *et al.*, 2009). Conducting FEM simulations can provide a thorough understanding of SICM experimental data, especially when the output ion current is influenced by multiple parameters such as substrate slope (Jiao *et al.*, 2020), surface charge (Sa *et al.*, 2013), ion permeability of the substrate (Payne *et al.*, 2019) and tip-substrate distance (Rheinlaender et Schäffer, 2017). The ionic flux towards the tip orifice and the electric potential in SICM can be modeled using Nernst-Planck and Poisson's equations,

respectively. The new advancements in SICM that enable surface charge mapping (McKelvey *et al.*, 2014 ; Zhu *et al.*, 2018) and quantifying electrochemical flux (Kang *et al.*, 2017 ; Lipson *et al.*, 2011), or both simultaneously (Chen *et al.*, 2019a), in addition to the topography mapping has resulted in a significantly increased number of numerical modeling studies.

1.5. Outline of Dissertation

This dissertation delves into the significance of mass transport processes in batteries and the multiscale techniques for detecting the transport parameters. Most importantly, the primary goal of the dissertation is to provide a comprehensive understanding of the impact of electrode architectural parameters on the solution phase mass transport in porous structures in the microscale using scanning probe microscopy techniques and numerical modeling studies.

Chapter I focuses on the necessity of energy storage devices in storing renewable energy, the factors limiting the application of LIBs, and the ability of different multiscale techniques to analyze the mass transport properties.

Chapter II is a mini-review that outlines the recent trends in SECM in the field of three important energy storage and conversion devices such as batteries, fuel cells, and supercapacitors. We particularly delve into recent literature to emphasize the crucial role of SECM in investigating the various processes inside these devices that lead to their performance deterioration.

Chapter III provides a comparative study between SICM and SECM to understand the mass transport process within porous $\text{Li}_4\text{Ti}_5\text{O}_{12}$ battery electrodes. We showed for the first time the complementary nature of these two techniques in investigating the mass transport in battery electrodes.

Chapter IV describes a 3D SECM modeling study of three porous substrates with different geometries. The effect of substrate geometry on the steady-state current arising due to the differences in mass transport within them was investigated. Most importantly, this chapter highlights the importance of modeling in transport studies of commercial battery electrodes.

Chapter V discusses the impact of surface roughness on mass transport in porous substrates. A 3D SECM simulation study was conducted to compare the transport in flat and rough substrates with identical porosity. It was found that surface roughness has a notable impact on transport measurements using the SECM probe, leading to an increased flow of molecules towards the partially covered probe due to the rough nature of the surface.

Chapter VI concludes Chapters I through V, focusing on the key findings. This chapter further discusses the perspectives of the research projects included in this dissertation.

CHAPTER II

CURRENT TRENDS IN SECM FOR ENERGY STORAGE DEVICES: REACHING THE MICROSTRUCTURE LEVEL TO TUNE DEVICES AND PERFORMANCE

The latest advancements in scanning electrochemical microscopy (SECM) regarding the three most important electrochemical energy storage and conversion (EESC) devices such as batteries, fuel cells, and supercapacitors are explored in this chapter. The significance of SECM as a powerful *in situ* probe technique to understand the electrochemical reactions at the electrode-electrolyte interface is mainly discussed. Additionally, this chapter gives an insight into the less studied areas in EESC devices, which is critical for their optimal performance. We anticipate the development of SECM hyphenated with other techniques to widen its scope in the energy research community. Therefore, this review comprises the recent articles published in the last decade relating to trends of SECM in EESC devices that appeal to electrochemists worldwide.

This chapter has been published as a review in the journal, [Current Opinion in Electrochemistry Volume 45](#), June 2024, 101522. Anjana Raj Raju, Prof. Steen Schougaard, and Prof. Janine Mauzeroll are co-authors of this article.

The contributions of the authors of the article are listed below:

- Anjana Raj Raju: Scope of the review, collected articles, redaction of manuscript
- Prof. Steen Schougaard: Discussion, supervision and redaction of manuscript.
- Prof. Janine Mauzeroll: Discussion, supervision and redaction of manuscript

2.1. Abstract

Increasing demand for sustainable energy resources necessitates the advancements of electrochemical energy storage and conversion (EESC) devices. For optimal device performance, it is imperative to have comprehensive insight into the multiple electrochemical processes occurring at the electrode-electrolyte interface from the atomic/molecular scale to the nanoscale. Scanning electrochemical microscopy (SECM), a powerful *in situ* technique, offers the unique

advantage of probing electrochemical processes and topography with nanoscale resolution. This review emphasizes the crucial role of SECM in providing localized information about surface heterogeneity, electrode reactions, and their kinetics that lead to performance deterioration in batteries, fuel cells, and supercapacitors.

2.2. Introduction

The development of electrochemical energy storage and conversion (EESC) devices is critical to meet the rising global energy demands and promote sustainable energy sources. Currently, the focus is on lithium-ion batteries (LIBs), fuel cells, and supercapacitor-related technologies. Each of these devices provides unique advantages and disadvantages. While LIBs have higher energy densities than supercapacitors, supercapacitors tend to have a higher power density [1]. In comparison, fuel cells show high energy density primarily due to the use of fuels *i.e.* mostly irreversible reactions where one of the reactants (O_2) is supplied from the atmosphere. However, the catalysts required for efficient conversion are expensive and the device requires a replenishable supply of fuels from sustainable sources like electrolysis of water (Ramachandran *et al.*, 2023). To improve the performance of the EESC devices, the electrochemical reactions occurring at the electrode-electrolyte interface, degradation mechanisms, and the influence of the electrode architectures must be explored.

To deepen our understanding of such reactions, interfaces, and architectures, we need *in situ* techniques with high spatial and temporal resolution that allow the redox reactions to be examined in their intended environment at the reaction site while providing information on *transient* events. SECM has a lot to offer in this area. As an *in situ* scanning probe technique, it enables the real-time monitoring of electrochemical reactions and topography with nanometer resolution (Bard *et al.*, 1989 ; Engstrom et Pharr, 1989). SECM operates by measuring the current generated at the poised microelectrode or nanoelectrode due to the electrochemical reaction of a redox mediator, enabling the analysis of insulating or conducting substrates immersed in electrolytes. Critically, this faradaic current, which is dependent on the probe geometry, probe-substrate distance, topography as well as the surface reactivity of the substrate, can be measured in a broad range of EESC electrolytes and under controlled atmosphere (Amphlett et Denuault, 1998 ; Bard *et al.*, 1991a ; Bülter *et al.*, 2014). State of the art

spatial resolution is intimately related to the probe geometry and its distance from the substrate (Bard *et al.*, 1991b). The SECM technique offers great flexibility in the experimental design due to the different operating modes such as feedback (FB), generation-collection (GC), surface interrogation (SI), and redox competition (RC) (Polcari *et al.*, 2016). In brief, FB mode provides positive or negative feedback based on the nature of the substrate (conductor/insulator), GC mode generates oxidized/reduced form of the mediator at the probe and collects them at the substrate or vice versa. RC mode involves both the substrate and probe competing for the same redox molecules and SI mode detects adsorbed species at the substrate using an electrogenerated titrant at the probe (Polcari *et al.*, 2016). This review highlights the significance of SECM in the realm of three critical EESC devices over the last decade (2013-2023). Specifically, we focus on the investigation of anodes and cathodes along with the ion transport in batteries, hydrogen oxidation, oxygen reduction reactions, and membrane transport in fuel cells as well as the electrochemical reactivity and kinetics of electrodes in supercapacitors.

2.3. LIBs

2.3.1. Solid Electrolyte Interphase (SEI)

SEI, a passive layer formed on the anode surface by the electrolyte reduction during the initial charging cycles plays an important role in the performance and degradation of LIBs (Verma *et al.*, 2010). The formation of SEI, its evolution, and degradation on the microscale are still not fully understood. SECM has been used substantially to explore the passivating properties of SEI on various electrodes such as graphite (Bülter *et al.*, 2014, 2016 ; T. Gossage *et al.*, 2019 ; Zampardi *et al.*, 2015b ; Zeng *et al.*, 2020a), Si-graphite (Jiyane *et al.*, 2023), graphene (Gossage *et al.*, 2020 ; Hui *et al.*, 2016 ; Schorr *et al.*, 2018 ; Zeng *et al.*, 2022), glassy carbon (Zampardi *et al.*, 2015a, 2015c), copper (Krumov *et al.*, 2023 ; Santos *et al.*, 2022), Li metal (Bülter *et al.*, 2015a ; Krueger *et al.*, 2020), silicon (Bülter *et al.*, 2015b ; dos Santos Sardinha *et al.*, 2019 ; Ventosa *et al.*, 2016), silicon clathrate (Tarnev *et al.*, 2020), and TiO₂ (Liu *et al.*, 2019a, 2019b ; Ventosa *et al.*, 2017 ; Zampardi *et al.*, 2013). As the SEI is delicate, spatially, and temporally dynamic in morphology and composition, it can easily get altered. Therefore, Zeng *et al.* used FB-SECM to investigate the electronically insulating SEI formed during the first lithiation and its partial decomposition in the subsequent delithiation on a graphite anode. Continued long-term cycling showed this SEI formation slowed and that the graphite surface was predominantly

covered with insulating components (Zeng *et al.*, 2020a). Krueger *et al.* studied the protecting properties of SEI on a Li metal using SECM directly within the cell between charge-discharge cycles (**Figure 2.1**) (Krueger *et al.*, 2020). Using three applied battery cycling protocols, the development of protruding lithium deposits that are significantly electrochemically active was monitored (**Figure 2.1d**) (Krueger *et al.*, 2020). The deposition of lithium can rupture SEI and expose fresh lithium that subsequently reacts with the electrolyte reforming the SEI (Wu *et al.*, 2021). This reformation entails a loss of mobile Li-ions in the electrolyte. The rupture of SEI during the lithium plating/stripping process and its heterogeneous nature towards electronic conductivity was demonstrated by SECM on a copper electrode, which showed a stable passivation at 0.5 V vs Li/Li⁺ (Krumov *et al.*, 2023). Ideally, SEI conducts Li⁺ ions and blocks electrons through them. Hence, understanding these two properties of the SEI quantitatively and qualitatively is critical for LIB performance. The combination of SECM FB and multi-frequency alternating current modes provided *in situ* and local quantitative information about the electronic and ionic properties of SEI for the first time by Santos *et al.* (Santos *et al.*, 2022). The impact of SEI formation protocols and the electrolyte composition on the resulting SEI properties were also reported (Santos *et al.*, 2022). In addition to these properties of SEI, topographic and interfacial reactivity information can be obtained by combining SECM with other techniques. For example, Schorr *et al.* coupled SECM with Raman to examine the localized charge transfer at the SEI of graphene (Schorr *et al.*, 2018) whereas Zampardi *et al.* used SECM with *in situ* atomic force microscopy (AFM) to explore the topography change on a glassy carbon electrode during SEI formation (Zampardi *et al.*, 2015a).

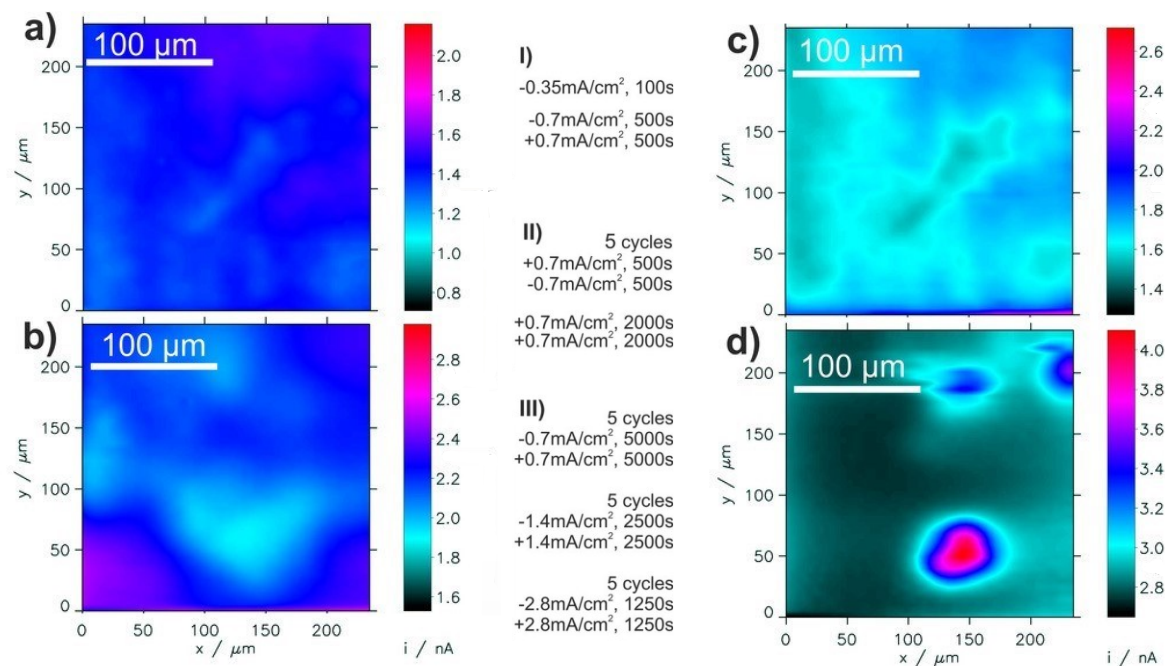


Figure 2.1. FB-SECM images at Li metal a) before and b), c), d) after charge-discharge cycles with protocols I), II), and III) respectively. Reproduced with permission from Krueger *et al.*, 2020. Copyright 2020 Wiley-VCH Verlag GmbH & Co. KGaA. [CC-BY-NC 4.0](https://creativecommons.org/licenses/by-nc/4.0/).

2.3.2. Cathode Electrolyte Interphase (CEI)

CEI, formed on the cathodes has been less explored than SEI. The high operating potential of cathodes comparable to the thermodynamic stability window of electrolytes, the presence of native surface oxides, transition metal dissolution into the electrolyte, oxygen evolution reaction, *etc.* pose challenges to CEI-related studies (Xu, 2014). Here, SECM was used to study electrodes such as LiMn_2O_4 (Huang *et al.*, 2021 ; Liu *et al.*, 2019c), $\text{LiNi}_{0.5}\text{Mn}_{1.5}\text{O}_4$ (Zampardi *et al.*, 2017), LiCoO_2 , and $\text{Li}_{1+x}(\text{Ni}_{1/3}\text{Mn}_{1/3}\text{Co}_{1/3})_{1-x}\text{O}_2$ (Mishra *et al.*, 2022). For LiMn_2O_4 (without binders and carbon additives), the SECM substrate generation/tip collection (SG/TC) mode was used to investigate the manganese dissolution in different lithium electrolytes (ClO_4^- , PF_6^- , and $(\text{CF}_3\text{SO}_2)_2\text{N}^-$) and the electrochemical activity of degradation products near CEI (**Figure 2.2**) (Huang *et al.*, 2021). The existence of multiple electrochemically active species after a 4.5 V vs. Li/Li^+ potential hold at the LiMn_2O_4 substrate (**Figure 2.2b**) and the detrimental effect of anions including ClO_4^- and PF_6^- on the manganese dissolution suspected to cause capacity decay was demonstrated (Huang *et al.*, 2021). Furthermore, the capacity fade can be accelerated by lattice

oxygen loss due to the structural changes inherent to the highly delithiated states. As such, a two-stage oxygen evolution was detected by SG/TC mode from LiCoO_2 , $\text{LiNi}_{0.33}\text{Mn}_{0.33}\text{Co}_{0.33}\text{O}_2$ and $\text{LiNi}_{0.8}\text{Mn}_{0.1}\text{Co}_{0.1}\text{O}_2$ (Mishra *et al.*, 2022). All the cathodes showed an unprecedented incipient release at a potential less than 3.3 V vs Li/Li^+ during the first charging cycle and the SECM mapping demonstrated spatial oxygen evolution heterogeneity (Mishra *et al.*, 2022).

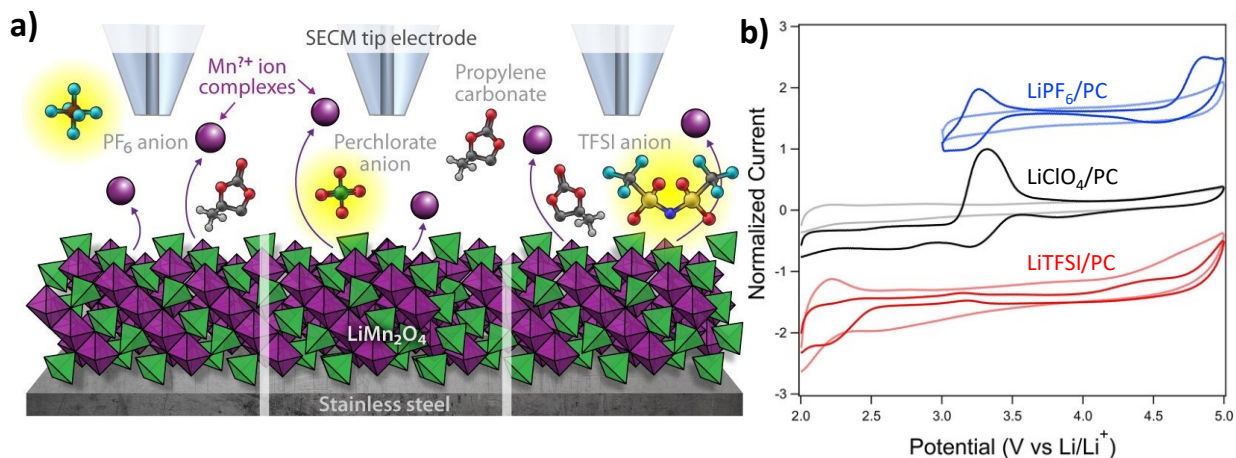


Figure 2.2. a) SECM schematic showing the manganese dissolution from LiMn_2O_4 b) Tip voltammograms obtained before (light color) and after (dark color) holding the LiMn_2O_4 substrate at 4.5V in various electrolytes at 1 V/s. Reproduced with permission from Huang *et al.*, 2021. Copyright 2021 American Chemical Society. [CC-BY 4.0](https://creativecommons.org/licenses/by/4.0/).

2.3.3. Ion Transport and Detection

Ion transport within the electrolyte-filled pores (solution-phase) in composite electrodes is critical to achieve higher rate performance in LIBs. SECM demonstrated the potential to deconvolute the effect of solution phase mass transport from the transport through the active materials. With the FB mode, the effective diffusion coefficient was directly measured using anthracene, an irreversible redox molecule, and the study showed a variation from the Bruggeman model for LiFePO_4 electrodes with porosities less than 60% (Hossain *et al.*, 2020). A mercury (Hg) capped platinum microelectrode was used in the redox SECM mode to get quantitative and spatially resolved information for the first time about the Li^+ ions and other alkali ions such as Na^+ and K^+ in non-aqueous environments (Barton et Rodríguez-López, 2014).

The anodic stripping voltammetry measurements obtained a limit of detection of 20 μM for Li^+ ions at the microelectrode and helped to identify the microscale surface features through the differences in local Li^+ flux (Barton et Rodríguez-López, 2014). However, the use of these Hg sphere-capped microelectrode was limited to rapid timescales and dilute solutions due to the irreversible Hg amalgam saturation. To tackle these shortcomings, a Hg disc well microelectrode was developed and showed an improved spatial and temporal resolution compared to a sphere-capped microelectrode (Barton et Rodríguez-López, 2017).

2.4. Fuel Cells

2.4.1. Oxygen Reduction Reaction (ORR)

SECM has gained attention in fuel cell research to screen electrocatalyst that boosts the anodic and cathodic reactions. The electrocatalytic activity for the cathode reaction, ORR was investigated in noble metal (Cho *et al.*, 2015 ; Nebel *et al.*, 2014) and non-precious metal catalysts (Dobrzaniecka *et al.*, 2016 ; Henrotte *et al.*, 2020 ; Li *et al.*, 2019, 2020b, 2023 ; Limani *et al.*, 2023 ; Seiffarth *et al.*, 2016 ; Silva *et al.*, 2016 ; Singh *et al.*, 2018). The Schumann group integrated the RC mode with the 4D shearforce-based constant-distance mode SECM to analyze the activity distribution of Pt/C catalyst separately by deconvoluting the topography effect (Nebel *et al.*, 2014). The Wittstock group utilized a similar approach to investigate the morphology and ORR activity of gas diffusion electrodes (Schulte *et al.*, 2017). The high cost of fuel cells is often attributed to the sluggish ORR kinetics at the cathode, which requires ten times more Pt catalyst compared to the anode (Gasteiger *et al.*, 2004 ; Jaouen *et al.*, 2011).

Consequently, tremendous efforts have been made to develop non-precious metal catalysts, and recent SECM studies have primarily focused on analyzing the ORR activity of these catalysts. For instance, Xin and colleagues demonstrated the good catalytic activity of $\text{MoSe}_2@\text{rGO}$ hybrid at both higher and lower potentials using RC-SECM (Xin *et al.*, 2016). The Nagaiah team visualized a nitrogen containing carbon sphere catalyst ORR activity in alkaline media for the first time without notable interference from viscous resistance during SECM imaging (**Figure 2.3a, b**) (Tiwari *et al.*, 2017). An SI-SECM approach showed that Co-Fe bimetallic subnanoclusters dispersed on a carbon matrix containing polypyrrole hydrogels have a higher active site density and faster binding rate to O_2 compared to their monometallic counterparts (**Figure 2.3c, d**) (Li *et al.*, 2019).

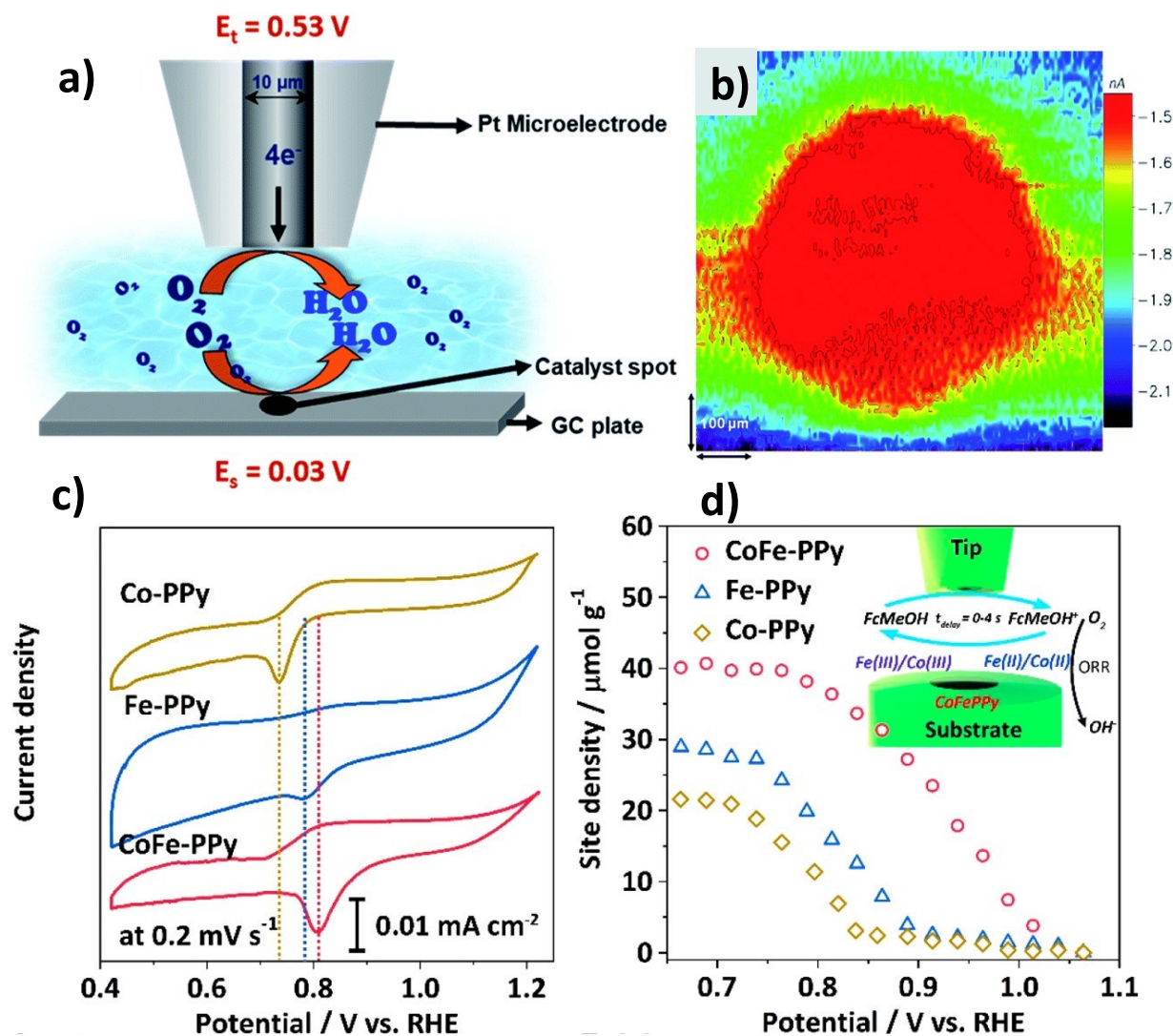


Figure 2.3. a) RC-SECM schematic and b) the corresponding image of localized ORR activity of nitrogen containing carbon sphere catalyst spot in 0.1 M NaOH electrolyte. Potentials were converted to RHE scale. Reproduced with permission from Tiwari *et al.*, 2017. Copyright 2017 the Royal Society of Chemistry. SI-SECM analysis showing c) cyclic voltammograms of ORR in N_2 saturated KOH electrolyte and d) titrated gravimetric site density of monometallic and bimetallic catalysts. Reproduced with permission from Li *et al.*, 2019. Copyright 2019 American Chemical Society.

2.4.2. Hydrogen Oxidation Reaction (HOR)

The various modes of SECM enabled the investigation of Pt nanoparticles (NPs) (Kim *et al.*, 2016), Pt decorated gold (Selva *et al.*, 2023), polycrystalline Pt (Wang et Wipf, 2020), and amorphous alloys based on Pt and Pd (Hasannaemi et Mukherjee, 2019) catalytic activity towards the anodic HOR reaction in proton-exchange membrane fuel cells. Here a fundamental understanding of the structure-activity relationship of electrocatalysts is sought to achieve higher efficiencies. The Bard group explored separately the topography and activity of individual Pt NPs in HOR with nanometer spatial resolution SECM as well as the fast electron transfer kinetics (Kim *et al.*, 2016). Wang et.al visualized for the first time the heterogenous HOR activity on high index single crystal Pt catalysts using SG/TC mode SECM and compared it to their crystallographic orientation (**Figure 2.4a, b**) (Wang et Wipf, 2020). Grains with (111) and (110) terrace orientations showed higher activity than those with (100) orientation (**Figure 2.4b**). As substrate potential increased from -0.75 to +0.8 V vs MSE, both the HOR activity and tip current decreased due to the blocking effect of anion adsorption and surface oxide growth (**Figure 2.4b-i**). However, the tip current increased when the potential was varied from +0.1 to -0.5 V vs MSE, suggesting a reversible reduction of Pt/O species (**Figure 2.4j, k**) (Wang et Wipf, 2020).

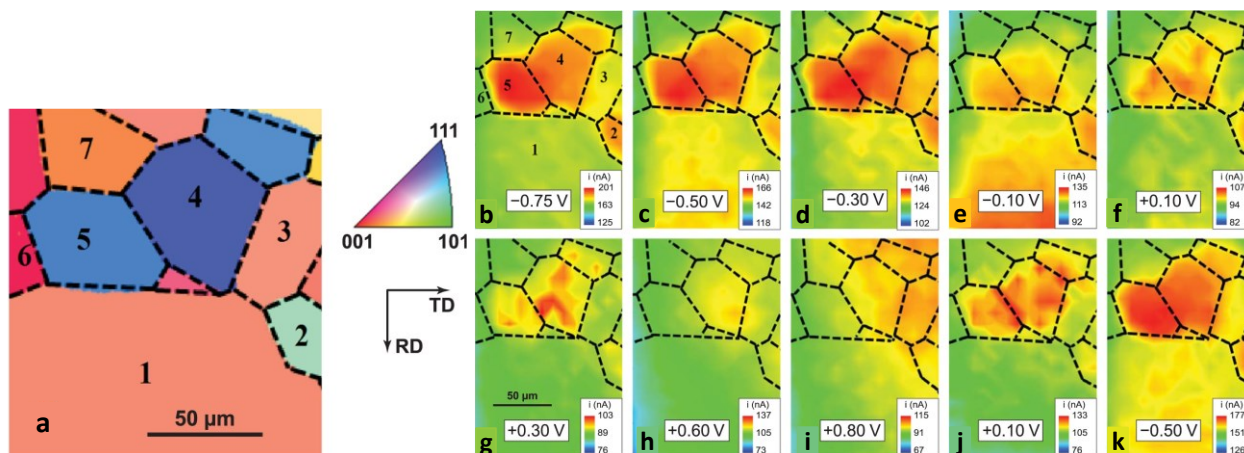


Figure 2.4. a) Image of electron backscatter diffraction inverse pole figure (IPF) b-k) SECM HOR current map at the corresponding grain boundaries of the polycrystalline platinum substrate biased at different potentials vs MSE in 10 mM H₂SO₄ + 0.1 M K₂SO₄ solution ($E_{tip} = -1.5$ V).

Normal direction (ND) was represented by a color triangle whereas the transverse and rolling direction axes by TD and RD respectively. Reproduced with permission from Wang et Wipf, 2020. Copyright 2020 the Electrochemical Society.

2.4.3. Membranes

The number of SECM reports on ion exchange membranes is limited (Ben Jadi *et al.*, 2020 ; Mareev *et al.*, 2018 ; Moghaddam et Peljo, 2021 ; Shi et A. Baker, 2015), despite of their vital role in determining the efficiency of fuel cells. Notable exceptions include, the Baker group use of a combination of SECM and scanning ion conductance microscopy (SICM) to examine the relation between membrane leakage and surface defects in Nafion (Shi et A. Baker, 2015). Similarly, the Peljo team found by FB-SECM the oxygen absorption in the electrocatalyst layer due to the catalyst's support (carbon black) combined with the Nafion ionomer (Moghaddam et Peljo, 2021).

2.5. Supercapacitors

The supercapacitors have not been investigated extensively with SECM. However, in the last decade, the handful of studies conducted mainly focus on the electrochemical reactivity, and kinetics of electrodes such as carbon-based materials (Franklin *et al.*, 2023 ; Liu *et al.*, 2022b ; Park *et al.*, 2017), conducting polymers (Dufil *et al.*, 2023 ; Sumboja *et al.*, 2015), metal oxides (Dey *et al.*, 2017 ; Zheng *et al.*, 2020) and dichalcogenides (Ghosh *et al.*, 2020, 2022 ; Ritzert *et al.*, 2018). The analysis of charge transfer kinetics at the electrode-electrolyte interface is essential as it facilitates rapid charge-discharge processes and thereby the performance of supercapacitors. For example, the heterogeneous charge transfer constant was quantified using FB-SECM for carbon-hydroquinone (Park *et al.*, 2017) and polyaniline-based electrodes (Sumboja *et al.*, 2015). In addition to the kinetics study, SECM has been found useful in understanding the heterogeneity in localized electrochemical reactivity of electrodes that could affect the charge transfer processes (Ritzert *et al.*, 2018 ; Zheng *et al.*, 2020).

2.6. Conclusion and Perspectives

SECM has become indispensable to the study of various processes in EESC devices such as LIBs, fuel cells, and supercapacitors, and to improve their performance. SECM has been

successfully applied to SEI, CEI, and ion transport in LIBs, the HOR, ORR, and membrane transport in fuel cells, and the electrochemical reactivity and kinetics in supercapacitors at the microscale. However, understanding is still lacking in many aspects of these devices. In LIBs, more insight is needed into the formation mechanism of CEI, its stability and side reactions whereas in fuel cells, the studies should focus on HOR catalysts other than Pt to reduce the cost and into the performance of other components like the ion exchange membranes, bipolar plates, *etc.* In general, supercapacitors were explored less with SECM. Consequently, there are many opportunities for future discoveries in supercapacitors exploring more electrode materials and electrolytes using SECM. Furthermore, though a few hyphenated techniques such as SECM-AFM, SECM-SICM and SECM-Raman have been developed these have yet to be widely applied despite their clear advantages. Though the scope of this review includes LIBs, the recent applications of SECM in Li-O₂ (Krueger *et al.*, 2022), Lithium-Sulfur (Lang *et al.*, 2023 ; Thangavel *et al.*, 2022), and Li metal batteries (Weber *et al.*, 2023) demonstrate its potential in future battery fields. The flexibility of SECM to hyphenate with other techniques, non-requirement of substrate conductivity, diversity in probe geometry, multiple measurement modes, along with the nanoscale electrochemical data, broadens its scope beyond EESC devices and make it distinct from other *in situ* techniques based on scanning probe microscopies and X-ray based methods.

2.7. Acknowledgments

The financial support from the Natural Sciences and Engineering Research Council (NSERC) is gratefully acknowledged. The authors would also like to acknowledge Elliot Howell, for his assistance during the literature search for supercapacitors.

CHAPTER III

INVESTIGATING MASS TRANSPORT IN LI-ION BATTERY ELECTRODES USING SECM AND SICM

Improving Li^+ ion transport within the electrode through the electrolyte-filled voids is key for optimizing power density and enabling future applications. In this work, we report for the first time a unique comparison between scanning electrochemical microscopy (SECM) and scanning ion conductance microscopy (SICM) in the context of LIBs. Employing SICM and SECM, we investigated the effect of porosities on the mass transport in $\text{Li}_4\text{Ti}_5\text{O}_{12}$ (LTO) anodes and observed an increased current with an increased film porosity. We also demonstrated the capability of SICM and SECM to detect the LTO film's heterogeneity and validated their complementary nature as they yielded comparable MacMullin numbers (N_M).

We anticipate that N_M obtained from these techniques can be used as a powerful tool to improve modeling studies and, thereby, the design of future batteries. In addition, these techniques can be extended to tune the transport properties of other porous structures in fuel cells, supercapacitors, *etc.*

This chapter has been just accepted as a research article in the journal, *DeCarbon* (In press, 2024). Anjana Raj Raju, Dr. Andrew Danis, and Prof. Steen B. Schougaard, are co-authors of this article.

The contributions of the authors of the article are listed below:

- Anjana Raj Raju: Scope of the review, collected articles, redaction of manuscript
- Dr. Andrew Danis: Initial investigation with SICM
- Prof. Steen B. Schougaard: Discussion, supervision and redaction of manuscript.

3.1. Abstract

Li-ion batteries (LIBs) are indispensable as global energy production transitions to sustainable production. Nevertheless, the use of LIBs in renewable energy storage applications is challenging due to their limited power densities. To comprehend the origin of this limitation, it is crucial to investigate the effect of electrode architecture on the Li^+ ion transport within their pores (solution-phase). In this work, the solution phase transport in various porous $\text{Li}_4\text{Ti}_5\text{O}_{12}$ (LTO) films was investigated using scanning ion conductance microscopy (SICM) and scanning electrochemical microscopy (SECM). When the porosity of LTO film increases, SECM and SICM approach curves show an increase in current. This is attributed to the ion transport through the film pores. The 2D topographical mapping using both techniques shows their ability to detect the LTO film's heterogeneity. Most importantly, this work gives insight into the complementary nature of the two scanning probe techniques as demonstrated by the comparable MacMullin numbers.

3.2. Introduction

Escalating energy demands and concerns about climate change drive the global transition towards renewable energy technology. During this transition, energy storage devices such as lithium-ion batteries (LIBs) are imperative due to their energy density, power density, and large scale availability (Pouraghajan *et al.*, 2018). Despite the merits, the limited capacity, safety concerns, and high production costs of LIBs hinder their extensive application (Pouraghajan *et al.*, 2018). As the energy market currently focuses on transportation sectors such as electric vehicles, hybrid electric vehicles, and plug-in hybrid vehicles, developing LIBs with high power density is critical. The composite electrode of LIBs has two phases: the solid phase consisting of the active material, polymeric binder, and carbon; and the solution phase of liquid electrolyte that occupies the pores. The Li^+ ion transport through these solid and solution phases is crucial for the overall performance of LIBs. Specifically optimizing solution phase mass transport which depends on microstructural parameters such as porosity and tortuosity, is key to achieving high power densities (Cornut *et al.*, 2015 ; DuBeshter *et al.*, 2014 ; Fongy *et al.*, 2010 ; Heubner *et al.*, 2020a ; Pouraghajan *et al.*, 2018 ; Vijayaraghavan *et al.*, 2012 ; Zheng *et al.*, 2012b). Porosity translates into the volume fraction of electrolyte within the electrode (Newman, 1995), whereas tortuosity is the ratio of the convoluted path to the straight line distance inside the electrode

representing an additional barrier to facile Li⁺ transport (Usseglio-Viretta *et al.*, 2018). Therefore, a fundamental understanding of the effect of these parameters on the Li⁺ ion transport through the solution phase is pivotal when designing batteries with higher power density.

The mass transport parameter for Li⁺ ion transport kinetics is the bulk electrolyte's ionic conductivity (κ_0) or diffusivity (D_0). The effect of the solid obstructing the transport in the solution phase within the electrode is captured in the effective conductivity (κ_{eff}) and effective diffusivity (D_{eff}). The dependence of these transport parameters on the electrode's porosity (ε) and tortuosity (τ) is represented commonly by the MacMullin number (N_M) defined as (Landesfeind *et al.*, 2016 ; Liu *et al.*, 2022a ; Patel *et al.*, 2003 ; Pouraghajan *et al.*, 2018):

$$N_M = \frac{\kappa_0}{\kappa_{eff}} = \frac{D_0}{D_{eff}} = \frac{\tau}{\varepsilon} \quad (3.1)$$

N_M has been used in transport model studies as this does not require any assumptions about the porosity (Liu *et al.*, 2022a). In this study, the effective transport in porous structures is represented in terms of N_M .

Several strategies have been aimed at comprehending the impact of electrode architecture on the mass transport of composite electrodes (Cornut *et al.*, 2015 ; Fongy *et al.*, 2010 ; Tran *et al.*, 2012 ; Yu *et al.*, 2006 ; Zheng *et al.*, 2012b). Two widely employed techniques, the electrochemical impedance spectroscopy (Andre *et al.*, 2011 ; Landesfeind *et al.*, 2016 ; Zahn *et al.*, 2017), and galvanostatic intermittent titration techniques (Cabañero *et al.*, 2018 ; Gao *et al.*, 2018), measure the mass transport in terms of ionic conductivity and diffusion coefficients, respectively. Nonetheless, these techniques cannot easily distinguish between solid and solution phase transport, and therefore only provide a general macroscopic understanding of the Li⁺ transport in the electrodes. Another approach, the polarization interrupt method, measures the transverse transport of Li⁺ ions in terms of D_{eff} , requires free-standing electrodes and a special cell geometry (Thorat *et al.*, 2009). Moreover, a detailed mathematical model is essential to elucidate the results obtained from this method. Although numerical simulations can be used as an alternative tool to study the mass transport phenomena and thereby predict battery

performance, they are computationally expensive (Heubner *et al.*, 2020a ; Nguyen *et al.*, 2020 ; Perry et Mamlouk, 2021 ; Stephenson *et al.*, 2007, 2011 ; Usseglio-Viretta *et al.*, 2018). Additionally, they often rely on assumptions like electrode homogeneity, spherical shape for active material, *etc.* which may not represent the real condition of battery electrodes.

Despite numerous techniques being employed, it is still challenging to obtain micro scale information, which is essential for improving battery design including power density. In this regard, *in situ* scanning probe techniques such as scanning electrochemical microscopy (SECM) and scanning ion conductance microscopy (SICM) emerge as a promising solution (Eidenschink et Matysik, 2024 ; Lipson *et al.*, 2011 ; Polcari *et al.*, 2016 ; Raju *et al.*, 2024 ; Takahashi *et al.*, 2023 ; Zhu *et al.*, 2021). Typically, SICM employs an electrolyte filled nanopipette to monitor the ion current generated between the working electrode inside the pipette and the counter electrode in the bulk solution (Hansma *et al.*, 1989 ; Takahashi *et al.*, 2023). Conversely, SECM has a microelectrode to monitor the electrochemical processes occurring at the electrode-electrolyte interphase (Bard *et al.*, 1989). Recent studies using these techniques showed their ability to independently measure the solution phase transport in battery cathodes (Hossain *et al.*, 2020 ; Payne *et al.*, 2019). For porous LiFePO_4 cathodes, Hossain *et al.* used SECM to investigate the effective diffusivity with an irreversible molecule, anthracene (Hossain *et al.*, 2020), whereas Payne *et al.* used SICM to measure the Li^+ ion conductivity of aqueous electrolyte (Payne *et al.*, 2019).

Here the focus is to analyze *anodes*. Specifically, $\text{Li}_4\text{Ti}_5\text{O}_{12}$ (LTO), which shows remarkable cycling stability at high charge-discharge rates (Odziomek *et al.*, 2017). The fast Li^+ ion kinetics and zero strain nature possessed by LTO, as well as its high lithiation potential (1.5 V vs Li/Li^+) help to elude lithium plating issues, making it an appealing high power anode (Ishihara *et al.*, 2014 ; Zhang *et al.*, 2020). In this study, we compared SECM and SICM techniques in the context of LIBs for the first time to understand the solution phase mass transport in battery electrodes.

3.3. Experimental

3.3.1. Preparation of Partially Delithiated LiFePO₄ (pd-LFP) Electrodes

The partial delithiation of LFP was performed based on a previous procedure with minor modifications (Lepage *et al.*, 2014). 3 g LFP (GELON) was partially delithiated using 99 μ l each of glacial acetic acid (ACS grade, Fisher Scientific) and hydrogen peroxide (H₂O₂, 30%, ACS grade, Fisher Chemical) in an Erlenmeyer flask containing 90 ml nanopure water. The suspension was stirred at 450 rpm for 24 h, filtered, and rinsed with nanopure water. Then the pd-LFP was dried under vacuum at 90°C for 24 h.

A homogenous slurry consisting of 80 wt% pd-LFP, 7 wt% carbon black (Super C65, IMERYS), and 13 wt% polyvinylidene fluoride (PVDF, Kynar HSV1810) in 1.3 ml N-methyl pyrrolidone (NMP, Gelon) was prepared by mixing mechanically with ceramic beads over 24 h. Then the slurry was coated on an aluminum wire (0.25 mm diameter, 99.5% purity, Goodfellow) and dried at 120°C in the oven for 5 min. This step was repeated three times to ensure a uniform coating. All the prepared pd-LFP coated Al wires have a coating thickness of approximately 180 μ m. These pd-LFP coated Al wire was used as working and quasi-reference counter electrodes for SICM measurements. The open circuit potential shows the stability of these wires (**Figure A.1**) and the cyclic voltammetry was performed to test the electrochemistry (**Figure A.7**).

3.3.2. Preparation of Micropipettes

Pipettes were pulled from borosilicate capillaries (1.2 mm o.d., 0.69 mm i.d., filamented, Sutter Instrument Co.) using a laser pipette puller (P-2000, Sutter Instrument Co.) with a three-step pulling procedure: (1) Heat=300, Fil=2, Vel=20, Del=100, Pull=Nil; (2) Heat=300, Fil=2, Vel=24, Del=200, Pull=Nil; (3) Heat=300, Fil=0, Vel=24, Del=200, Pull=120. Using a multi-line procedure provides greater control over pipette tip size and shape, resulting in pipettes with more reproducible characteristics. Using a JEOL-6000 scanning electron microscope (SEM, SE detector, accelerating voltage =10 and 15 keV), the pipettes were imaged before the experiments (**Figure A.2a, b**). The radii of the micropipettes used in this study varied from 1.05 μ m to 1.53 μ m.

3.3.3. Preparation of Microelectrodes

The microelectrode was prepared using a previously reported procedure (Danis *et al.*, 2015). In brief, soda lime capillaries were pulled using the laser puller with the following pulling program: (1) Heat=240, Fil=5, Vel=60, Del=140, Pull=70. A 1 cm long platinum (Pt) wire (0.025 mm diameter, 99.99%, Goodfellow) was inserted into the end of the pulled micropipette and heat sealed under vacuum. Later a copper wire with a conductive silver epoxy (EPO-TEK® H20E, Epoxy Technology) was inserted to make the connection with the Pt wire. Finally, a gold pin was soldered with the copper wire to complete the microelectrode assembly. It was kept at 120°C for 10 min for the epoxy to cure. The electroactive surface of the microelectrode was exposed using a polishing machine (Strugers Tegrapol 23). A SiC grinding paper with grit P320 and P1200 was used respectively to polish the microelectrode. The prepared microelectrodes were cleaned using water under sonication, dried at 100 °C, and imaged using an inverted microscope (Zeiss Axio Vert.A1) (**Figure A.2c, d**). All the fabricated microelectrodes have an RG (R/a) ≈ 2.5 , where R is the outer radius of the microelectrode and a is the radius of the Pt wire.

3.3.4. SICM and SECM Measurements

A commercial $\text{Li}_4\text{Ti}_5\text{O}_{12}$ (LTO, Nanomyte BE 10-CE, NEI Corporation) coated on a copper current collector with the composition LTO: carbon black (super P): PVDF = 90:5:5 wt% was used as the porous substrate. The LTO films were calendered with Hot Roller MTI Corp. HR01 to different porosities. Moreover, the calendering process reduces the surface roughness of the porous film (**Figure A.3**). The films were cut with a diameter of 1.5 cm and dried in a vacuum oven at 100 °C overnight before use. The film thickness was measured using a thickness gauge (Mitutoyo 547-526S) and it varied from 77 to 56 μm . The film porosity values range from 50% to 63%, which was calculated based on the component's densities (see Appendix A).

The experiments were conducted using a plastic petri dish, with a plastic disc placed on top to keep the film in place while immersed in the electrolyte (**Figure A.4**). The disc had two holes, one positioned above the LTO film and the other above the surface of the petri dish, to allow the probe to make contact with both substrates. The insulating nature of the petri dish was utilized as the internal control before approaching each LTO film. This provides information about the current contribution from the misalignment of probes (micropipette or microelectrode) with the

substrate. Similarly, in the case of porous LTO films, the approach curves were recorded by allowing the probe to make gentle contact with them, which was identified by a small increase in current following a drastic current decrease. This helps to determine the exact tip-substrate distance and reject any measurement where the pipette is misaligned, so the measured current reflects exclusively the transport from the porous films.

All SECM and SICM measurements were carried out using an ELProscan 3 system (HEKA, Lambrecht/Pfalz, Germany; potentiostat model, PG340) in an Argon-filled glove box ($\text{H}_2\text{O} < 1\text{ ppm}$, $\text{O}_2 < 1\text{ ppm}$). The speed was set at $1\ \mu\text{m s}^{-1}$ for all the approach curve measurements.

For SICM, a two-electrode configuration of pd-LFP was used. The electrolyte was 0.3 M LiPF_6 (Gotion) in propylene carbonate (PC, anhydrous, 99.7%, Sigma-Aldrich). The electrolyte-filled pipette with the pd-LFP coated wire serves as the probe. The counter-reference electrode is a ring-shaped pd-LFP wire, which provides uniform current distribution throughout the cell.

The three-electrode cell in SECM consists of a Pt disk microelectrode as the working electrode, a Pt wire as the counter, and an Ag/Ag₂O as the reference electrode. In studies that involve highly purified organic solvents, using a silver wire with an oxide coating as a quasi-reference electrode offers convenience when making the electrode assembly as well as compatibility with the highly anhydrous glovebox environment and little risk of contaminating the electrolyte. The solution contained 2 mM anthracene (purified, 98%, Sigma Aldrich) in 0.1 M tetraethylammonium tetrafluoroborate ($\text{TEABF}_4 \geq 99.0\%$ electrochemical grade, Sigma-Aldrich) in PC. Cyclic voltammetry (CV) was performed using a Pt microelectrode before the approach toward the substrate to find the steady-state potential (**Figure A.5a**). The irreversible nature of anthracene was confirmed with the help of CV using a Pt macroelectrode (1.6 mm diameter, 99.95% purity, BASi Research Products) (**Figure A.5b**) and approach curves using a copper film as the conductor (**Figure A.6**). In addition, the reproducibility of this technique was verified by approaching the insulator multiple times (**Figure A.8**).

For the 2D surface map measurement, SICM was carried out initially using 0.1 M TEABF_4 / PC electrolyte followed by SECM measurement in 2 mM anthracene containing the same electrolyte to determine the variation in normalized current across the LTO film surface. Both the SICM and

SECM surface maps were generated by recording approach curves at each position on the LTO. These approach curves were measured in a specific pattern to ensure that the distance between adjacent measurements is at least 100 μm , thereby preventing the overlap of the diffusion profile from previous measurements. Similarly, a total of 25 approach curves covering an area of 200 $\mu\text{m} \times 200 \mu\text{m}$ was recorded in each SICM and SECM map. The details of the porous LTO films (**Table A.1**) used for 2D surface map measurements and their transport properties in terms of N_M (**Figure A.9**) are given in SI.

3.3.5. Data Analysis

All the data analysis was performed using the Origin version 2024. All the confidence intervals were calculated at a 95% confidence level using Student-t-statistics for four observations.

3.4. Results and Discussion

3.4.1. SICM: Ion Current Measurement

In this study, we employed a partially delithiated LFP as a working electrode in SICM for the first time. The lithiation/delithiation reactions in LFP have been extensively studied, showing a remarkably flat equilibrium potential at 3.4 V vs Li/Li^+ within the lithiation level of $x= 0.1$ to 0.8 in Li_xFePO_4 (Padhi *et al.*, 1997 ; Zheng *et al.*, 2012a). As such partially delithiated LFP has been used as a reference/counter electrode in previous studies (Payne *et al.*, 2019).

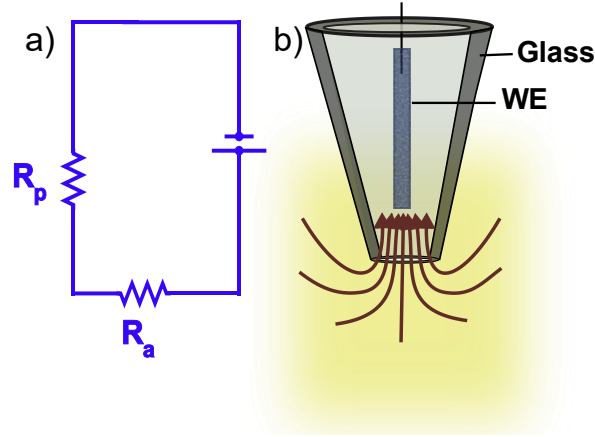


Figure 3.1. (a) Equivalent circuit for the electrochemical cell in SICM; (b) schematic of SICM set up when the micropipette is unaffected by an insulating or porous substrate (Arrows represent the ion current)

SICM works by measuring the ionic current generated at the pipette electrode due to the applied potential between the pipette and reference electrodes. In general, the electrochemical cell in SICM is described by an equivalent circuit with resistors connected in series (**Figure 3.1a**). The micropipette current is influenced by both the pipette resistance (R_p) and the distance-dependent access resistance (R_a). The substrate does not affect the ion flow when the tip-substrate distance is very large (**Figure 3.1b**). At this distance, maximum ion flow occurs at the pipette resulting in a steady state ion current (I^0), which is solely dependent upon R_p (Zhu *et al.*, 2021). At high tip-substrate distances, R_a is negligible due to the larger area between the working and counter electrode.

$$I^0 = \frac{V}{R_p} ; \quad R_p \approx \frac{1}{\kappa_0 \pi r_i \tan \alpha} \quad (3.2)$$

Where V is the imposed potential (V), κ_0 is the ionic conductivity of the electrolyte (Sm^{-1}), r_i and α are the inner radius (m) and the cone angle (degree) of the pipette, respectively. However, as the pipette moves closer to the substrate, the ion flow becomes restricted due to the presence of the substrate. R_a dominates at this point, so the ion current near the substrate (I^*) decreases (Zhu *et al.*, 2021). For an insulator substrate, I^* is given by (Zhu *et al.*, 2021):

$$I^* = \frac{V}{R_p + R_a} ; R_a \approx \frac{\frac{3}{2} \ln \left(\frac{r_o}{r_i} \right)}{\kappa_0 \pi d} \quad (3.3)$$

Where d is the tip-substrate distance and r_o is the outer radius of the micropipette.

In the case of a porous substrate, R_a is a combination of two components in parallel: resistance through the porous film (R_{por}) and the solution resistance in the gap between the pipette and the substrate (R_{gap}) (**Figure 3.2a**).

$$\frac{1}{R_a} = \frac{1}{R_{por}} + \frac{1}{R_{gap}} \quad (3.4)$$

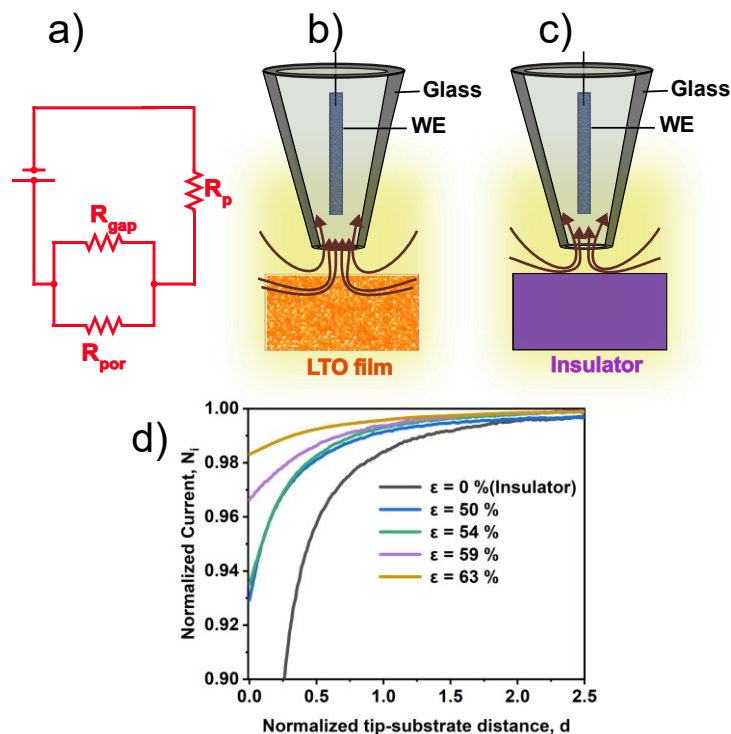


Figure 3.2. (a) Equivalent circuit diagram for the porous substrate; SICM schematic demonstrates the ion current due to migration (brown color arrows) (b) inside porous LTO films when the pipette is positioned on the LTO surface; (c) restricted current flow when the micropipette is near the insulator; (d) experimental SICM approach curves of LTO films (sample number 1-4) with different porosity (ϵ)

| LTO films used in SICM | | | | |
|-----------------------------|----------------|----------------|----------------|----------------|
| Sample Number | 1 | 2 | 3 | 4 |
| Porosity, ϵ (%) | 50.0 ± 1.4 | 54.3 ± 1.5 | 58.6 ± 0.1 | 63.2 ± 3.2 |
| Thickness (μm) | 57.4 ± 1.6 | 56.6 ± 1.6 | 62.0 ± 0.1 | 77.2 ± 3.9 |

Table 3.1. LTO films used for SICM measurements (95 % confidence interval)

As the pipette tip to porous substrate distance decreases, the ionic current becomes increasingly restricted due to the narrowing of the gap. Thus, R_{gap} increases, and the “squeezing” effect of the ionic current causes an increasing fraction of current to travel through the porous electrode path with the parallel resistance (R_{por}) (Bhushan et Fuchs, 2006 ; Payne *et al.*, 2019) (**Figure**

3.2b). Therefore, I^* for a porous substrate is a function of R_{gap} , and R_{por} . In contrast for an insulator, I^* depends only on the high resistance path (R_a) that does not have the R_{por} contribution. Therefore, as the micropipette approaches a distance (d) similar to the pipette opening diameter, the current flow is drastically affected (**Figure 3.2c**). Finally this current flow is completely blocked when the pipette tip touches the insulator's surface.

As the SICM technique is well established for an insulator, approach curves were performed on this substrate first before approaching the LTO films with various porosities (**Table 3.1**). Comparing the approach curves of insulator and porous films, a significant current decrease was only observed when the tip-substrate distance reaches the order of the tip radius (**Figure 3.2d**). As expected the presence of substrates impedes the ion flow toward the tip, the presence of pores in LTO films creates an alternate pathway for ion flow to the pipette tip and results in a higher current in contrast to the insulator. This relationship between the effective ionic conductivity ($\kappa_{eff,Li}$), and ion current is given by:

$$N_i = \frac{I^*}{I^0} = \frac{\kappa_{eff,Li}}{\kappa_{0,Li}} \quad (3.5)$$

Where N_i is the normalized current.

3.4.2. SECM: Faradaic Current Measurement

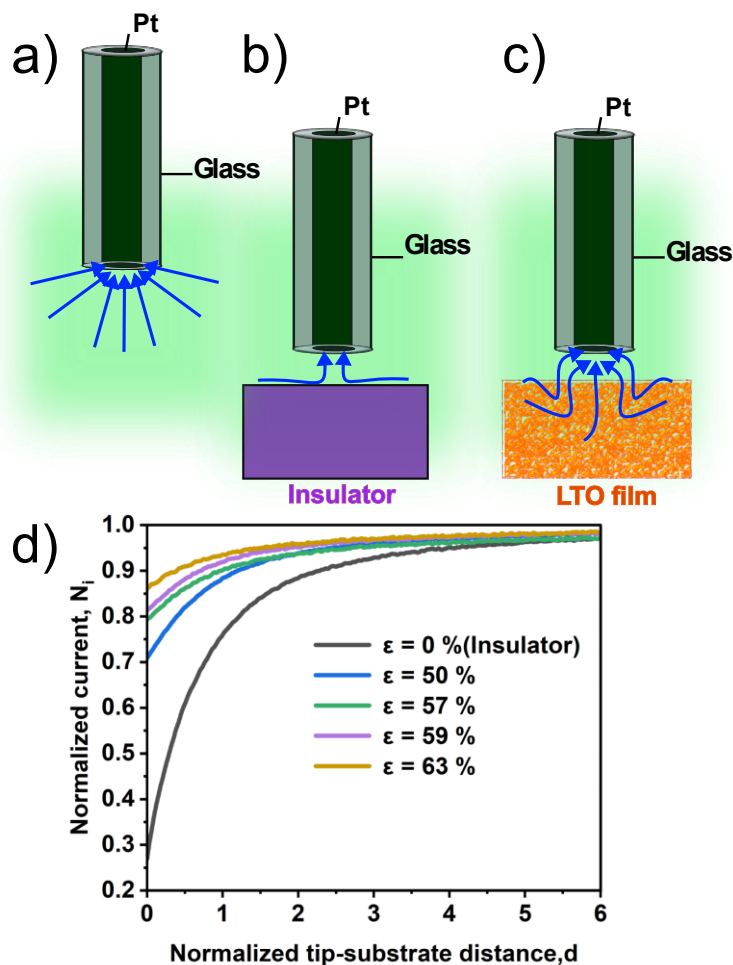


Figure 3.3. SECM schematic showing the Pt microelectrode detection of anthracene oxidation (a) in the bulk position; (b) near the insulator; (c) near the porous LTO film; (d) SECM experimental approach curves of LTO films (sample number 1-4) with various porosity (ϵ) (blue arrows represent the anthracene diffusion)

| | LTO films used in SECM | | | |
|-----------------------------|------------------------|----------------|----------------|----------------|
| Sample Number | 1 | 2 | 3 | 4 |
| Porosity, ϵ (%) | 49.9 ± 2.9 | 57.4 ± 1.2 | 59.4 ± 2.5 | 63.2 ± 2.1 |
| Thickness (μm) | 56.1 ± 3.3 | 61.0 ± 1.3 | 65.0 ± 2.7 | 75.8 ± 2.5 |

Table 3.2. LTO films used for SECM measurements (95 % confidence interval)

While SICM probes the solution phase transport based on the ionic conductivity of the electrolyte, SECM works by measuring the faradaic current generated at the poised microelectrode due to the redox reaction of a mediator. Here, SECM feedback mode was used to measure the current generated by the redox reaction of anthracene. The irreversible nature of anthracene results in negative feedback when the microelectrode approaches an insulating or conducting substrate. Consequently, though carbon additives are electronically conducting in the composite LTO, the approach curves always show negative feedback or hindered diffusion near the substrate. In binary electrolytes, such as LiPF_6 used in LIBs, the charge transport is governed by an expression similar to Fick's law (Newman et Balsara, 2004). The expression involves an implicit "diffusion coefficient" that combines both the anion and cation diffusion coefficients. Consequently, the diffusion process of binary electrolytes in batteries can be imitated using anthracene. Furthermore, the ratio (\mathcal{R}) of diffusion coefficients in bulk and near the porous structure remains constant despite the chemical nature of the diffusing species as the only variable between them is the porous architecture. Therefore,

$$\mathcal{R} = \frac{D_{eff,An}}{D_{0,An}} = \frac{D_{eff,LiPF_6}}{D_{0,LiPF_6}} \quad (3.6)$$

When the microelectrode is away from the substrate ($d > 10a$), no restriction is observed for the anthracene diffusion to the microelectrode (**Figure 3.3a**). Therefore, the current measured at the microelectrode due to anthracene oxidation attained the steady state given by (Lefrou et Cornut, 2010):

$$I^0 = 4nF\beta D_{0,An} C_{An} a \quad (3.7)$$

Where n is the number of electrons involved in anthracene oxidation, F is the Faraday constant, β is the correction factor that varies as a function of RG, $D_{0,An}$ is the bulk anthracene diffusion coefficient (m^2s^{-1}), C_{An} is the anthracene concentration (M), a is the radius of the microelectrode (m). When the microelectrode reaches the surface, anthracene diffusion depends on the nature of the substrate. If the substrate is an insulator, the diffusion to the microelectrode gets largely restricted (**Figure 3.3b**). Ideally, no diffusion takes place and the faradaic current becomes zero

as the microelectrode touches the insulating surface. However, if the substrate is porous, diffusion occurs through the pores and anthracene molecules can reach the microelectrode (**Figure 3.3c**).

SECM approach curves showed a similar trend to the SICM ones (**Figure 3.3d**). Owing to the porosities of the LTO film (**Table 3.2**), the anthracene diffuses towards the microelectrode and hence a higher current was measured near the porous films compared to an insulator.

Additionally, as the porosity of the films increases, the current also increases due to the increase in the number of anthracene molecules reaching the microelectrode through diffusion inside the porous networks. This effective diffusion coefficient of anthracene ($D_{eff,An}$) is expressed in terms of the faradaic current as (Hossain *et al.*, 2020, 2021):

$$N_i = \frac{I^*}{I^0} = \frac{D_{eff,An}}{D_{0,An}} = \frac{D_{eff,LiPF_6}}{D_{0,LiPF_6}} \quad (3.8)$$

3.4.3. 2D Surface Mapping and MacMullin Number

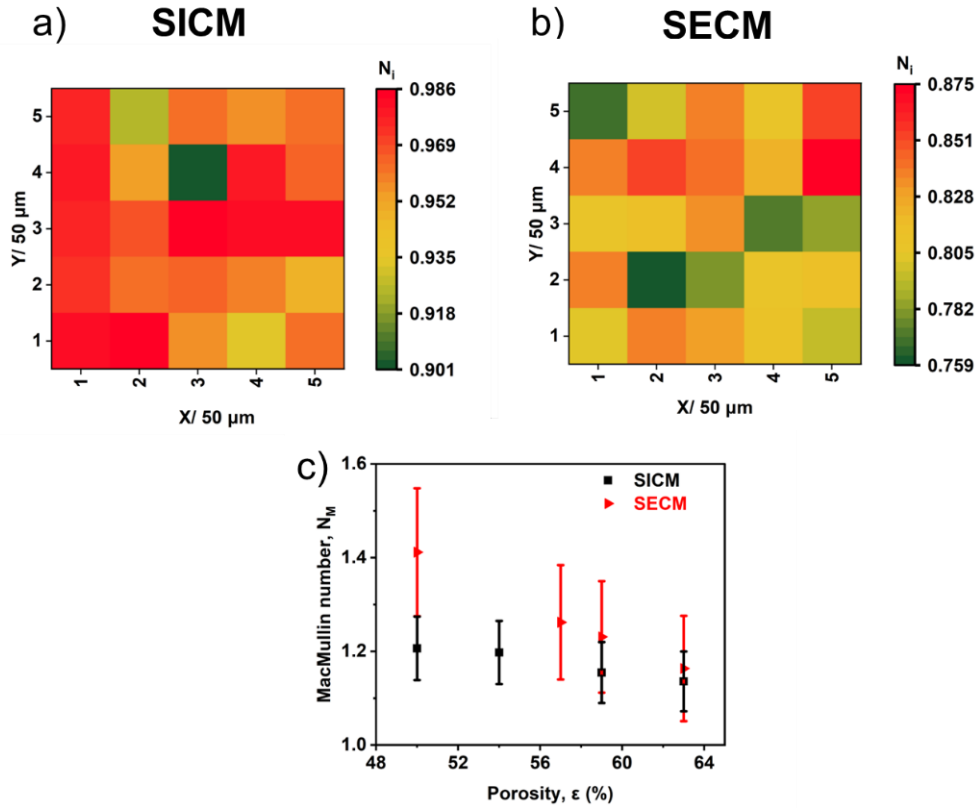


Figure 3.4. (a) SICM and (b) SECM 2D surface mapping of LTO film with a porosity, $\epsilon = 63.2 \pm 3.2$ % and thickness = 77.2 ± 3.9 μm ; (c) N_M values calculated for porous LTO films tested with SECM and SICM

The 2D surface mapping of LTO film using SICM and SECM revealed that the surface current is strongly dependent on the substrate's topography (**Figure 3.4a, b**). The contribution of surface roughness of the LTO films used in this study was significantly reduced by calendaring as demonstrated in the SEM images (**Figure A.3**). Therefore, the observed topography effect stems from the heterogeneity within the porous architecture encompassing the local tortuosity and porosity. While SICM surface mapping showed an 8% change in current (**Figure 3.4a**), SECM demonstrated a 12% variation for the same LTO film (**Figure 3.4b**). To compare the results obtained by SECM and SICM based on the effective mass transport parameters, we calculated N_M as follows by comparing equations (3.1), (3.5), and (3.7):

$$N_M = \frac{I^0}{I^*} = \frac{\kappa_{0,Li}}{\kappa_{eff,Li}} = \frac{D_{0,An}}{D_{eff,An}} = \frac{\tau}{\varepsilon} \quad (3.9)$$

The normalized current values from SECM and SICM were converted to N_M values (**Figure 3.4c**). The calculated N_M values demonstrated that the two techniques are complementary to each other when it comes to the measurement of transport in the solution phase. The 2D mapping along with the N_M data comparison of SECM and SICM demonstrated their capability to probe the microporous surface heterogeneity in battery electrodes and provide valuable information about the solution phase transport parameters. These microscopic details are advantageous for optimizing the transport properties of porous composite electrodes, and thereby the high power battery designs.

3.5. Conclusion and Perspectives

A comprehensive understanding of the mass transport within the porous battery electrode especially through the electrolyte filled pores is critical to attaining high power densities in rechargeable batteries including LIBs. Importantly, mass transport depends on the electrode architectural parameters like porosity and tortuosity. For the first time, SECM and SICM techniques were compared to investigate the solution phase mass transport in Li-ion battery anode films with different porosities. During both SECM and SICM measurements, current increased as the porosity of films increased as expected. The surface heterogeneity of LTO films was investigated with 2D surface mapping using SICM and SECM, demonstrating an 8% and a 12% change in the normalized current, respectively, for the same film. Furthermore, N_M determination from SECM and SICM validated the complementarity.

Although SECM and SICM techniques are individually robust in measuring the solution phase transport, each has its advantages and challenges. In SICM, the glass/quartz micropipettes used are easy to fabricate, less expensive, and possess tunable pore size, however, air bubbles can easily form at the orifice when filled with electrolyte. If the LFP coating on the wire (within the micropipette) is not uniformly distributed or is overly thick, the LFP particles can peel off from the wire causing the clogging of the pipette orifice and affecting the ion current measurements. More importantly, the pipette opening must be in the single-digit-micrometer range to provide

sufficient restriction for generating a measurable resistance. In contrast, microelectrodes in SECM do not face these issues and provide great reproducibility in terms of probe geometry. However, SECM tip fabrication procedure is more time-consuming in part due to the need for polishing to obtain a known geometry. Moreover, an irreversible mediator that is not prone to cause fouling is required. To improve the modeling studies and design high power batteries, N_M values derived from these techniques should become a powerful tool. Additionally, these scanning electrochemical probe methodologies can be extended to other porous materials, providing avenues to tailor their transport characteristics in fuel cells, supercapacitors, and fields not associated with energy such as in drug delivery and bio-sensing.

3.6. Acknowledgment

The financial support received from the Natural Sciences and Engineering Research Council (NSERC) for Grant No. RGPIN-2019-07200 is gratefully acknowledged. The authors would like to acknowledge Prof. Janine Mauzeroll (McGill University) for providing the lab facilities for microelectrode preparation.

CHAPTER IV

MICROPOROUS SUBSTRATE EFFECT ON SECM STEADY STATE CURRENTS – A 3D MODELING STUDY CRITICAL TO BATTERY ELECTRODE PERFORMANCE

Scanning electrochemical microscopy (SECM) is a powerful technique for investigating mass transport in porous structures, like lithium-ion battery electrodes, with microscale spatial resolution. As the porous substrate's architecture plays a crucial role in controlling mass transport, it is imperative to understand its role in enhancing the performance. In this chapter, we used 3D SECM modeling to compare the impact of substrate geometry on transport in three microporous structures: superposition (SP), and two high-fidelity (HF-1, HF-2) models. We found that increasing geometric complexity resulted in a lower steady-state current for a given thickness and porosity. The MacMullin number (N_M) comparison showed the order: HF-2 > HF-1 > SP, indicating the presence of more tortuous paths in HF-2 compared to HF-1 and SP. Our findings also revealed significant N_M deviation from the Bruggeman model, particularly at low porosities. This suggests that relying on the Bruggeman model for analyzing commercial porous battery electrodes with low porosity can lead to errors, emphasizing the importance of explicitly modeling transport in porous substrates with different geometries.

This chapter has been submitted as a research article in the *Journal of The Electrochemical Society* and is currently under revision. Anjana Raj Raju, Dr. Bastian Krueger, and Prof. Steen B. Schougaard are co-authors of this article.

The contributions of the authors of the article are listed below:

- Anjana Raj Raju: Modeling, data analysis, figures, discussion, redaction of manuscript
- Dr. Bastian Krueger: Design of porous substrates
- Prof. Steen B. Schougaard: Discussion, supervision and redaction of manuscript.

4.1. Abstract

Scanning electrochemical microscopy (SECM) enables the study of mass transport in porous substrates with microscale spatial resolution, which is profoundly influenced by the substrate's architecture. Here, a 3D SECM modeling was used to compare the impact of substrate geometry on transport in three porous structures: a superposition (SP) model with average porosity and two high fidelity (HF-1 and HF-2) models with explicit pore geometries. It was found that the steady-state current decreases with an increase in the geometric complexity from SP to HF-1 to HF-2, indicating the presence of more tortuous paths in HF-2. Despite having the same porosity and thickness values, the disparity between the SP and the two HF substrates shows the effect of microporous geometry. Our findings also demonstrated the deviation of all three substrates from Bruggeman's predictions, which highlights the significance of modeling to rationalize the transport properties in commercial battery electrodes.

4.2. Introduction

The performance of microporous structures used in energy storage devices, catalysis, sensing, gas storage, and biomedical applications is determined by the material chemistry *and* the mass transport processes occurring within them.(Chen *et al.*, 2022) These transport processes get complicated as the geometry of porous structures becomes complex, with numerous interfaces between different components. For instance, for energy storage devices such as lithium-ion batteries, the sluggish liquid phase Li^+ ion transport within the thick, composite porous electrodes limits them from achieving high power density.(Cornut *et al.*, 2015 ; Fongy *et al.*, 2010 ; Heubner *et al.*, 2020a ; Pouraghajan *et al.*, 2018) The ion transport depends on the electrode architectural parameters such as porosity, tortuosity, and thickness.(Boyce *et al.*, 2022 ; Vijayaraghavan *et al.*, 2012 ; Zheng *et al.*, 2012b) Therefore, it is essential to study the impact of these architectural parameters on mass transport in the micro- to nanoscale to optimize battery performance.

In this regard, localized measurement techniques on porous substrates are imperative. Although many methods have been previously reported to measure ion transport, they provide information on the macroscale rather than localized information.(Andre *et al.*, 2011 ; Cabañero *et al.*, 2018 ; Gao *et al.*, 2018 ; Landesfeind *et al.*, 2016 ; Zahn *et al.*, 2017) In recent years, scanning

electrochemical microscopy (SECM) has demonstrated its ability to effectively monitor and quantify the transport processes in numerous types of porous substrates with microscale spatial resolution.(Bath *et al.*, 1998 ; Haensch *et al.*, 2019 ; Hossain *et al.*, 2020 ; Kuss *et al.*, 2016 ; Macpherson *et al.*, 2002 ; McKelvey *et al.*, 2011 ; Nugues et Denuault, 1996 ; Scott *et al.*, 1991) SECM operates by tracking the flux of the redox molecule which undergoes either oxidation or reduction at the microelectrode tip when it emerges from the porous structure. During the ion transport measurements, a reversible mediator is not preferred in feedback mode SECM, as it can regenerate with the help of electronically conducting components in the porous substrates (eg: conductive carbon in the battery electrodes). This regeneration can adversely affect the positioning of the tip relative to the substrate and the mass transport measurements. Recently, SECM methodologies have been developed using irreversible molecules such as anthracene and ascorbic acid to study mass transport regardless of the nature of the porous substrates.(Haensch *et al.*, 2019 ; Hossain *et al.*, 2020) With the help of approach curves, the mass transport in porous substrates was measured in terms of the effective diffusion coefficient (D_{eff}) relative to the bulk electrolyte diffusivity (D). In experimental studies, controlling the actual porous substrate geometry is challenging. For example, changing the substrate's porosity readily changes its thickness, and therefore investigating the effect of porosity on steady-state current without the impact of thickness is difficult.

Numerical modeling offers an alternative solution to explore independently the effect of the above parameters on mass transport and validate the experimental observations (Hossain *et al.*, 2021). Nevertheless, the models based on SECM generally use an average value to represent the porosity of the entire substrate (Hossain *et al.*, 2020, 2021). As a result, they may not reflect the heterogeneity in porosity within the substrate geometries. To the best of our knowledge, no SECM modeling studies have been conducted to compare and understand the magnitude of the difference in steady-state current when using average porosity values vs explicitly modeling the porosity based on substrate geometry in the microscale.

In this work, we conducted a systematic study using 3D COMSOL simulations to understand the impact of substrate geometry with interconnected pores on the steady-state current. By simulating approach curves, we compared the steady-state currents obtained in a superposition

(SP) model substrate with an average porosity to two high-fidelity (HF) porous substrates with porosities defined by explicit geometric constraints.

4.3. Methods

Model Geometry

A 3D finite element model was built with COMSOL Multiphysics 6.1 using the “Transport of Diluted Species in Porous Media (TDS)” module to simulate the SECM tip and steady-state diffusion of an irreversible molecule, anthracene. The detailed information about the implemented governing equations along with the boundary conditions, mesh, *etc.* can be found in Appendix B (Figures B.1 and B.2, Table B.1).

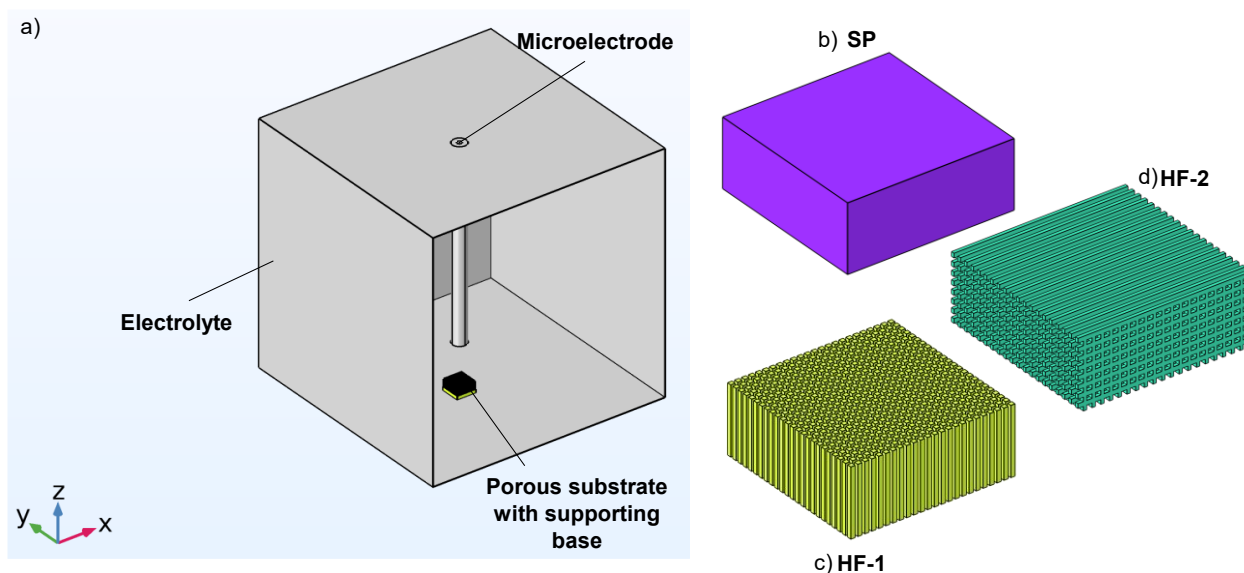


Figure 4.1. a) SECM 3D COMSOL model geometry, a zoomed-in view of porous substrates b) SP c) HF-1, d) HF-2

The model geometry consists of a disk microelectrode with a radius, $a = 12.5 \mu\text{m}$ and an $\text{RG} = 3$ along with a cubic electrolyte domain of size $1250 \mu\text{m} \times 1250 \mu\text{m} \times 1250 \mu\text{m}$ ($x \times y \times z$) and a porous substrate domain (**Figure 4.1a**). Three porous substrates were generated: two HF models with well-defined geometry and porosity, and one SP model with an average porosity. The SP model substrate was represented with a single rectangular slab of size $100 \mu\text{m} \times 100 \mu\text{m}$ (**Figure**

4.1b), HF -1 model substrate with an array of rectangular pillars equally spaced in the x and y directions (**Figure 4.1c**). The size of these pillars was $2.5\ \mu\text{m} \times 2.5\ \mu\text{m}$ (**Figure B.3a**). SP and HF-1 substrates were generated on top of a $20\ \mu\text{m}$ thick supporting rectangular base domain ($100\ \mu\text{m} \times 100\ \mu\text{m}$). HF-2 substrate was created using an array of equally spaced repeating units (**Figure B.3b**) of size $5\ \mu\text{m} \times 5\ \mu\text{m} \times 5\ \mu\text{m}$ in the x, y, and z directions in Autodesk Fusion software (**Figure 4.1d**). The initial substrate thickness for all porous substrates was $40\ \mu\text{m}$.

An average porosity was applied to the SP substrate using the “porous media” node of the TDS COMSOL module. For HF-1 and HF-2 model substrates, the spacing between the pillars was adjusted to assign a specific porosity value. The pore sizes in HF-1 and HF-2 are given in Appendix B (**Table B.2** and **Table B.3**) and the effect of substrate lateral size of HF-1 is discussed (**Figures B.4, B.5, and B.6**). The microelectrode z position was parametrized to automate the approach toward the porous substrate. All the responses were simulated at a tip-substrate distance (d) of $100\ \text{nm}$ and a bulk anthracene concentration of $2\ \text{mM}$ (**Table 4.1**).

| Parameter | Value | Description |
|--|---|--|
| a | 12.5 [μm] | Radius of microelectrode |
| R | 37.5 [μm] | Radius of glass sheath |
| RG | 3 | R/a |
| L_{Elec} | 1250 [μm] | Electrolyte domain length |
| L_{UME} | 1000 [μm] | Length of the microelectrode |
| C_{An} | 2 [mM] | Bulk anthracene concentration |
| D_{An} (Hossain <i>et al.</i> , 2021) | 1.4×10^{-9} [$\text{m}^2 \text{s}^{-1}$] | Bulk diffusion coefficient of anthracene |
| n | 1 | No: of electrons transferred |
| R | 8.314 [$\text{J mol}^{-1} \text{K}^{-1}$] | Universal gas constant |
| F | 96485 [C mol^{-1}] | Faraday's constant |
| k^0 | 0.112 [m s^{-1}] | Heterogeneous rate constant |
| κ | 1000 | Normalized heterogeneous rate constant: $(k^{0*a})/ D_{\text{An}}$ |
| η | 0.25 [V] | Overpotential: $E_{\text{app}} - E^0$ |
| α | 0.5 | Transfer coefficient |
| T | 293 [K] | Temperature |
| L | d/a | Normalized tip-substrate distance |
| τ | 1 | Tortuosity in SP model |

Table 4.1. Model parameters

4.4. Results and Discussion

4.4.1. Effect of Substrate Thickness (h)

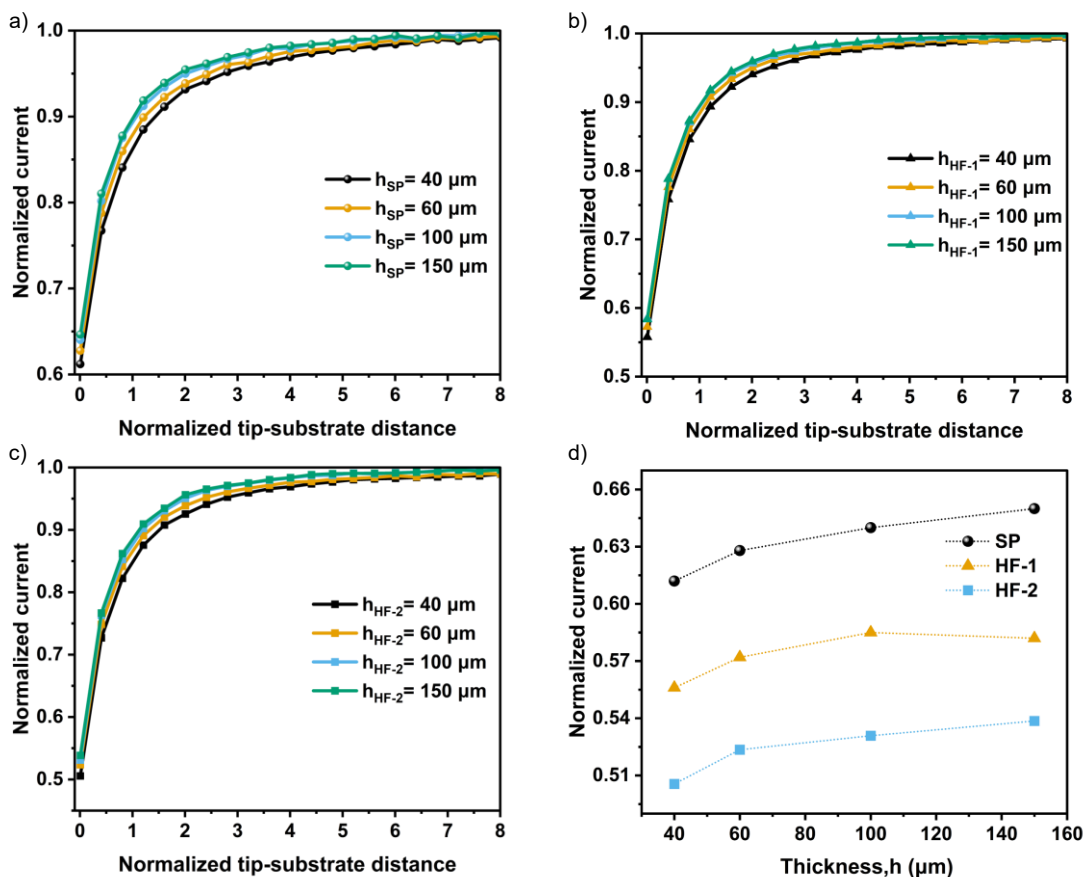


Figure 4.2. Approach curves show the effect of thickness in a) SP, b) HF-1 c) HF-2 substrates, and d) a comparison of thickness effect between HF and SP substrates with $\varepsilon = 63.3\%$ at $L = 0.008$

The approach curves were simulated to systematically investigate the effect of various microstructural parameters on the normalized current (Ni) at the HF and SP model porous substrates. The impact of substrate thickness in HF-1, HF-2, and SP models was studied in the range from 40 to 150 μm (**Figure 4.2a, b, c**). In all cases, an increase in substrate thickness results in increased current. This is attributed to the ability of anthracene molecules to reach the microelectrode tip through the substrate pores. When comparing the current values obtained from the three models, SP exhibited a higher current for all simulated thickness values (**Figure 4.2d**).

For a given thickness, the simulated current between SP and HF-1 exhibited a difference of approximately 6%, while the difference between SP and HF-2 was approximately 10%. These variations highlight the significance of the porous geometry, given that the same modeling parameters, including the RG of the microelectrode and substrate porosity, were used.

4.4.2. Impact of Porosity (ϵ)

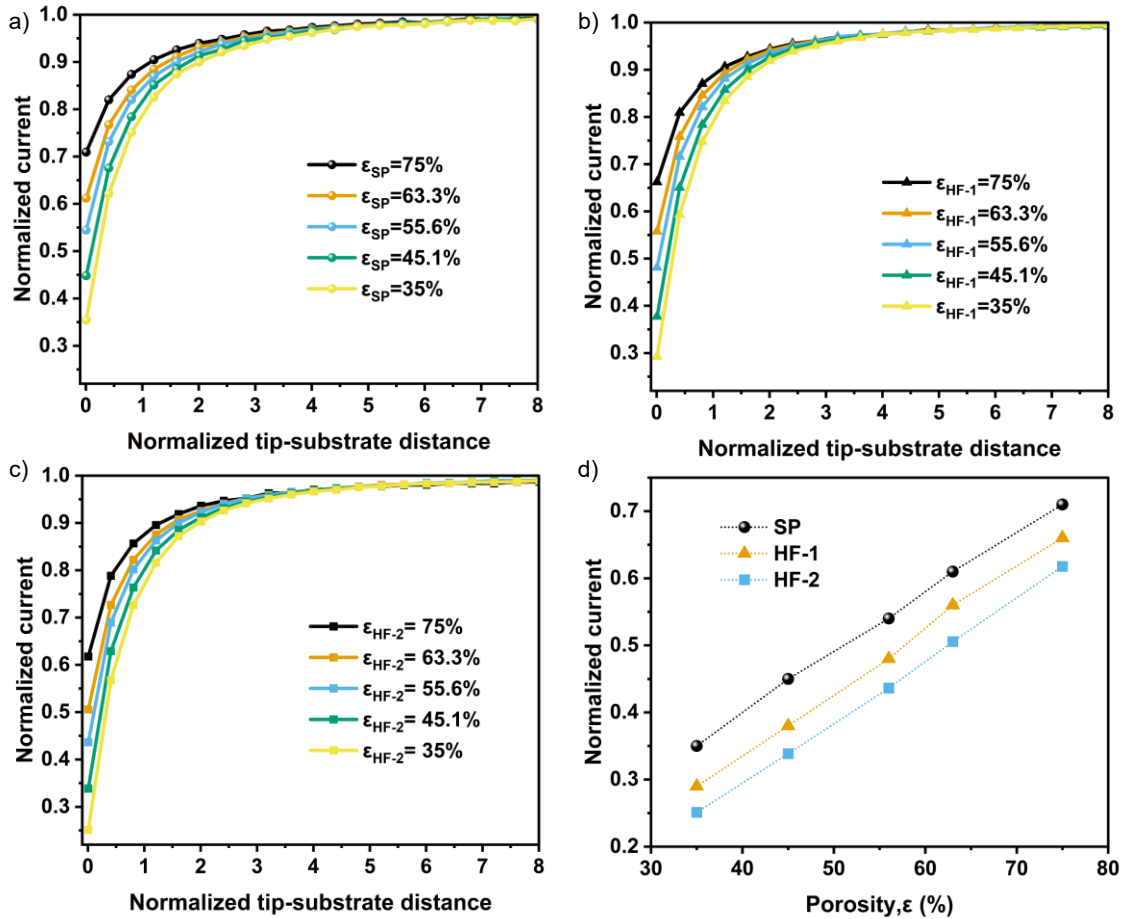


Figure 4.3. Approach curves showing the effect of porosities in a) SP, b) HF-1 c) HF-2 substrates with $h = 40 \mu\text{m}$, and d) comparison of normalized current obtained in all three models at $L = 0.008$

Porosity plays a crucial role in controlling ion transport in porous substrates used in batteries, fuel cells, *etc.* Consequently, optimizing the porosity values enhances the performance of these

devices. Here, we examined the effect of porosities ranging from 35% to 75% in HF and SP models (**Figure 4.3a, b, c**). In all three models, the normalized current increased with an increase in substrate porosities, as expected given the fact that more ions reach the microelectrode through the substrate pores. Interestingly, for the same porosity, the current observed for the SP model was approximately 6% and 10% higher than that of the HF-1 and HF-2 models respectively, highlighting the disparity between the three models (**Figure 4.3d**). Hence for a given porosity and thickness, any obstruction to the ion transport is solely due to the microporous substrate geometry.

4.4.3. MacMullin Number of Modeled Substrates

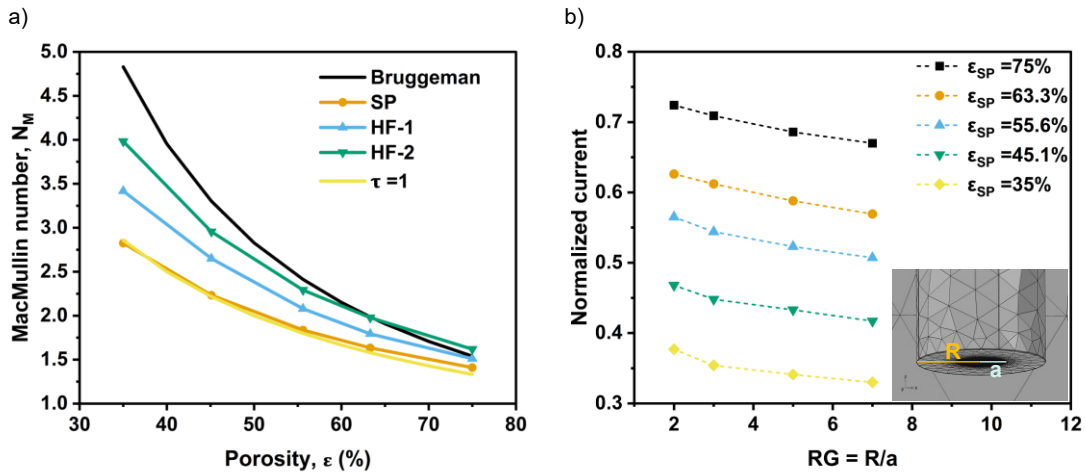


Figure 4.4. a) Comparison of N_M of three modeled substrates ($h = 40 \mu\text{m}$) with Bruggeman relation, b) shows the effect of RG on current for various porosities of the SP substrate at $L = 0.008$ and inset shows the meshed geometry of the microelectrode with the surrounding glass sheath

MacMullin number (N_M) was used in this study to represent the mass transport properties in terms of the diffusion coefficient. It is an important parameter that describes the relation between the porosity (ϵ) and tortuosity (τ) of the porous structures to the diffusion coefficients and is given as (Bruggeman, 1935 ; Hossain *et al.*, 2020, 2021 ; Pouraghajan *et al.*, 2018):

$$N_M = \frac{D}{D_{eff}} = \frac{\tau}{\varepsilon} \quad \text{Eq. (5.1)}$$

In addition, the microelectrode current at bulk electrolyte (I) and near the porous substrate (I*) is determined by the ratio of the corresponding diffusion coefficients of the electrolyte as the diffusion coefficient is the only parameter that changes between the bulk and the porous structure. Therefore, N_M becomes (Hossain *et al.*, 2020),

$$N_M = \frac{I}{I^*} = \frac{D}{D_{eff}} = \frac{\tau}{\varepsilon} \quad \text{Eq. (5.2)}$$

However, in the case of thin porous substrates ($h \leq 3a$), the above relation is not valid as the hemispherical diffusion front can change to cylindrical (Hossain *et al.*, 2021). In this study, as the substrate thickness ($h = 40 \mu\text{m}$) is greater than 3 times the radius of the microelectrode ($a = 12.5 \mu\text{m}$), Eq. (5.2) holds and was used to calculate N_M (**Figure 4.4a**) and effective diffusion coefficients (**Figure B.7**) for all three model substrates based on the normalized current obtained for various porosities. As expected, when porosity increases, N_M decreases for all the substrates and follows the order: SP < HF-1 < HF-2 (**Figure 4.4a**). This suggests that HF-2 has more tortuous paths compared to HF-1 and SP substrates, which arises due to its complex microporous grid-like geometry. Additionally, the difference in N_M between the three porous structures decreases as porosity increases, indicating that the substrate geometry has a predominant effect at low porosities by contributing more tortuous paths for mass transport.

The other important finding was the N_M deviation of the SP model from theory ($\tau = 1$) for $\varepsilon > 50\%$. Its N_M values are overestimated by 2-5% compared to theory. This underscores the challenges of using an SP porosity model at high porosities for simulating the experimental data. In general, N_M values of SP, HF-1, and HF-2 model substrates are consistently lower than those predicted by the widely adopted Bruggeman model ($\tau = \varepsilon^{-0.5}$) for porous structures (Bruggeman, 1935 ; Landesfeind *et al.*, 2016). The observed deviation of three models from Bruggeman's model and the inter-model differences validate the hypothesis of the effect of geometric complexity on mass transport.

4.4.4. Effect of RG

To further examine the discrepancy in normalized current obtained from the theory and SP model, we investigated the effect of RG on the approach curve current at the substrate. The RG was varied between 2 and 7 for each porosity value used in the SP model (**Figure 4.4b**). For all porosities, there was a decrease in current as RG increased, indicating that the glass sheath surrounding the electroactive metal hindered the diffusion of anthracene molecules. Furthermore, to follow the superposition theory ($\tau = 1$), the value of Ni should be equal to ε . However, the data suggests that increasing the RG resulted in an increased deviation of the SP model from theoretical predictions.

4.4.5. Concentration Profiles

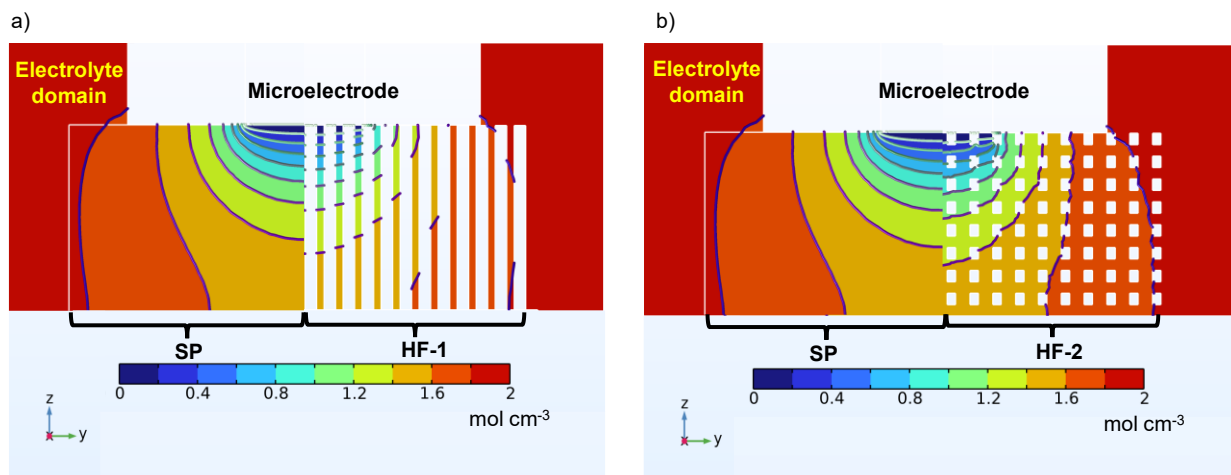


Figure 4.5. Cross-sectional view of anthracene concentration profile showing the comparison between a) SP and HF-1, b) SP and HF-2 substrates with $h = 40 \mu\text{m}$, $\varepsilon = 63.3\%$, $\text{RG} = 3$

The anthracene concentration profile shows that its concentration within individual HF-1 and SP model substrates is not uniform (**Figure 4.5a**). Here, we assumed that the transport of anthracene is exclusively carried out by diffusion. The concentration of the anthracene directly below the microelectrode is zero as it quickly undergoes oxidation. This creates a localized concentration gradient within the substrate which combined with a second constraint originating from the geometry, accounts for the transport.

Comparing the concentration profiles in HF-1 and SP models (**Figure 4.5a**) provides valuable insights into the observed differences. It was evident from the concentration profile that the diffusion of anthracene within the two models was not identical, despite both possessing the same porosity ($\varepsilon = 63.3\%$) and thickness ($h = 40 \mu\text{m}$). Using the same porosity, and thickness as in the other two substrates, the concentration profile for the HF-2 model was simulated and compared to the SP model. HF-2 also showed a non-uniform diffusion profile within the substrate (**Figure 4.5b**). Furthermore, the corresponding diffusive flux visualization of anthracene in SP, HF-1, and HF-2 substrates was analyzed (**Figure B.8**). A non-uniform flux distribution (represented by contour lines) was observed in all three substrates due to the anthracene oxidation. As the geometric complexity increases from SP, flux distribution within the substrate becomes distorted in HF-1 and HF-2. The distortions in flux distribution were more pronounced in HF-2 compared to HF-1. Most importantly, flux visualization helped confirm the dissimilarity in anthracene mass transport between the three porous substrates.

The concentration profile of anthracene in HF-2 and SP models (**Figure 4.5b**) showed dissimilarities, indicating that geometric constriction plays a critical role in addition to other parameters such as thickness, porosity, and RG. Hence, this result suggests that the differences in the normalized current observed in the two HF substrates and SP are due to the geometric orientation of pillars blocking the facile transport resulting in various tortuosity.

When utilizing the SP or HF models to replicate experimental data, it is crucial to take a meticulous approach in modeling porous substrates as the current depends not only on the porosity of the substrate but also on its geometry. The rationale behind the deviation of the SP model from the theory remains an unresolved question, possibly related to the proprietary and secret calculation algorithm of COMSOL. However, it is worth noting that the deviation is within 5% at high porosities for an $RG = 3$.

4.5. Conclusion

Recently, SECM has emerged as a powerful technique for studying mass transport in porous structures with microscale resolution. In this work, a comparative study using 3D SECM modeling was conducted to investigate the mass transport occurring in porous structures (SP, HF-

1, and HF-2) with different geometries. It showed that increasing the intricacy of substrate geometry at a specific porosity led to higher values of tortuosity and N_M . Accordingly, N_M varies *qualitatively* in the following order: SP < HF-1 < HF-2 as intuitively expected. Moreover, the N_M of all the substrates was lower than what was predicted by the Bruggeman model, and this disparity was predominant at low porosities. For instance, at $\varepsilon = 35\%$, the Bruggeman model overestimates N_M by 1.2 times compared to the HF-3 model. This discrepancy can lead to significant errors in the investigation of mass transport in commercial battery electrodes with a porosity of around 30%. Therefore, this work emphasizes the necessity of modeling the porous structure to gain a better understanding of the experimental data. Moreover, the dissimilar diffusion profile and the normalized current variation observed between SP and the two HF substrates demonstrated the impact of substrate geometry. As porous substrates are indispensable in applications beyond energy storage, this study underscores the importance of their geometry and the need for caution when modeling them.

4.6. Acknowledgment

The financial support from the Natural Sciences and Engineering Research Council (NSERC) is gratefully acknowledged.

CHAPTER V

INVESTIGATING THE IMPACT OF SURFACE ROUGHNESS ON MASS TRANSPORT IN POROUS SUBSTRATES

The efficacy of mass transport within porous structures is governed by the transport processes occurring in the solution-filled pores present in the micro to the nanoscale, which in turn depends on various structural parameters such as porosity, thickness, tortuosity, and surface roughness. Numerical modeling studies are a great tool to investigate the effect of structural parameters on mass transport independently, as these parameters are often tricky to control in experimental studies. Therefore, this chapter discusses a 3D modeling study based on scanning electrochemical microscopy to investigate the effect of surface roughness and porosity on high-fidelity porous structures with various surface roughness values.

This chapter has been prepared for submission as a research article in the *Journal of The Electrochemical Society*. Anjana Raj Raju, Dr. Bastian Krueger, and Prof. Steen B. Schougaard are co-authors of this article.

The individual contributions of the authors are:

- Anjana Raj Raju: Modeling, data analysis, figures, discussion, manuscript writing.
- Dr. Bastian Krueger: Design of porous substrates.
- Prof. Steen B. Schougaard: Discussions, supervision and manuscript editing.

5.1. Abstract

Surface roughness plays a critical role in the performance of porous structures in many fields including batteries and corrosion. In corrosion, surface roughness can lead to increased corrosion rates and more localized damages. In the case of batteries, surface roughness can result in the incomplete utilization of active material, capacity fade, *etc.* In this work, we employed numerical modeling based on scanning electrochemical microscopy (SECM) to study the effect of surface roughness. A 3D modeling study has been conducted with two types of high-fidelity (HF) porous

structures with smooth and rough surfaces where the effect of porosity has been studied independently. Our findings demonstrated that HF structures with rough surfaces exhibited higher probe currents for all studied porosities compared to those with smooth surfaces. This suggests that the probe current is influenced by both porosity and surface roughness, affecting the mass transport measurement using SECM. Consequently, this study necessitates the determination of the surface roughness of the porous structure before conducting SECM experimental studies.

5.2. Introduction

Scanning electrochemical microscopy (SECM), owing to its versatility and non-invasiveness, has garnered considerable attention in various fields including energy, corrosion, biology, surface modification, catalysis, instrumental development, *etc.* (Polcari *et al.*, 2016 ; Raju *et al.*, 2024). SECM utilizes a microelectrode as the scanning probe or tip to monitor electrochemical reactions occurring at the electrode-electrolyte interfaces with high spatial resolution, determined by the tip size (Amphlett et Denuault, 1998). One notable application of SECM is its ability to visualize and quantify localized mass transport through porous structures, which often contain complex interfaces and interconnected pores of different sizes (Bath *et al.*, 1998 ; Nugues et Denuault, 1996 ; Shen *et al.*, 2012). The mass transport properties of porous structures vary on the microscale and are greatly influenced by structural parameters such as porosity, and tortuosity (Boyce *et al.*, 2022 ; Vijayaraghavan *et al.*, 2012). Consequently, analyzing the contribution of these factors to the localized transport characteristics of porous substrates helps to optimize their performance, highlighting the significance of SECM.

Recently, SECM has been utilized to measure mass transport in porous substrates, including battery electrodes and nanoporous gold substrates (Haensch *et al.*, 2019 ; Hossain *et al.*, 2020). These studies have focused on determining diffusive mass transport in the respective substrates using the microelectrode current generated due to the irreversible reaction of the mediator molecule. The effect of porosities was investigated and the mass transport through the electrolyte-filled pores (solution-phase) was exclusively measured. This methodology is particularly relevant to the battery research community as it helps to measure the solution-phase transport, which is the predominant rate-limiting factor in batteries during the charge-discharge

process (Fongy *et al.*, 2010 ; Pouraghajan *et al.*, 2018 ; Stephenson *et al.*, 2007). Moreover, the previously reported techniques measure the mass transport in the mesoscale and could not distinguish the differences in transport through the solid particles and the electrolyte-filled pores within the substrate (Cabañero *et al.*, 2018 ; Gao *et al.*, 2018 ; Landesfeind *et al.*, 2016).

In addition to porosity, another important aspect that needs to be considered is the surface roughness of the substrates. Surface roughness is an important parameter in fields such as batteries (Chen *et al.*, 2019b ; Jang *et al.*, 2021 ; Zeng *et al.*, 2020b) and corrosion (Hilbert *et al.*, 2003 ; Walter et Kannan, 2011). For example, in batteries, studies have shown that surface roughness affects electrode performance and can promote undesirable phenomena like lithium dendrite growth, leading to the capacity fade of lithium-ion batteries (Gao et Guo, 2021). In the field of corrosion, increased surface roughness can accelerate the rate of corrosion by increasing the effective surface area (Nguyen *et al.*, 2012). Therefore, while adopting the SECM methodology to investigate the transport through porous substrates, the effect of surface roughness should be studied as it can affect the microelectrode current, which is informative about the diffusive mass transport in pore networks.

While investigating the effect of different parameters such as porosity, thickness, tortuosity, and surface roughness, it is worth noting that these parameters are interconnected. Consequently, studying one parameter at a time by controlling other parameters is experimentally challenging. In such situations, numerical modeling studies are a great tool for modeling complex geometries and independently investigating the effect of multiple parameters on mass transport (Hossain *et al.*, 2021). Moreover, it helps to validate the experimental data. However, modeling studies generally assume a smooth surface and adopt an average porosity value to represent the entire porous structure (Hossain *et al.*, 2021). This is because incorporating the asymmetry arising from the surface roughness requires a three-dimensional (3D) model which is computationally expensive. Nevertheless, 3D models can capture the true nature of the electrochemical system under investigation and explore transport in more complex substrate geometries.

In this work, we report an extensive 3D modeling study of SECM for the first time to investigate the effect of surface roughness in high-fidelity (HF) structures with various porosities. Finite

element simulations using COMSOL Multiphysics were employed to model the feedback mode SECM steady-state current in HF porous substrates with smooth and rough surfaces.

5.3. Methods

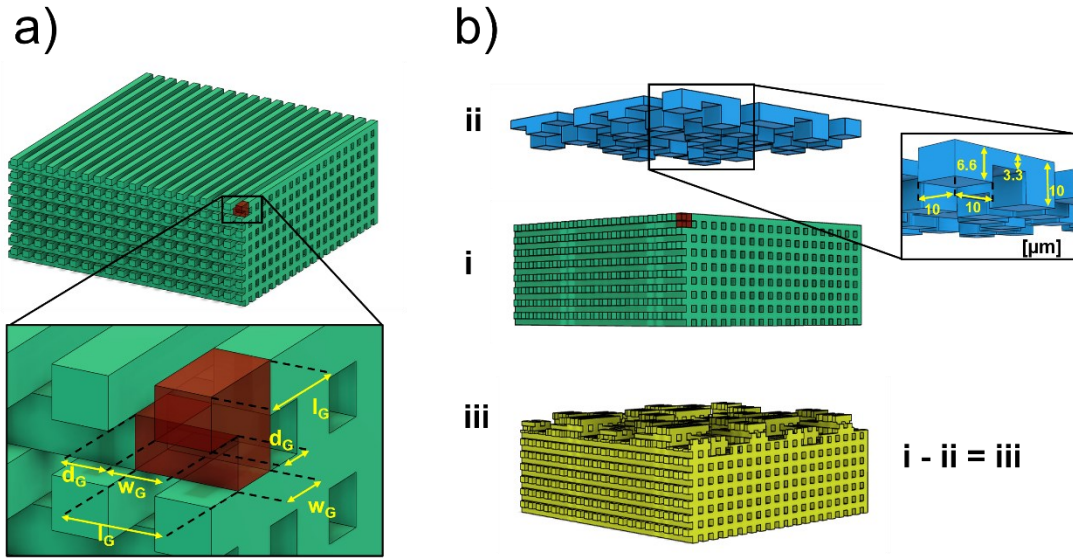


Figure 5.1. Grid geometry of a) smooth substrate with the repeating unit (brown color) and b) rough substrate (iii) with the building units i) and ii)

| Porosity (%) | Distance, d_G (μm) | Width, w_G (μm) | Length, l_G (μm) | Height, h_G (μm) |
|--------------|-----------------------------------|--------------------------------|---------------------------------|---------------------------------|
| 20 | 1 | 4 | 5 | 2.5 |
| 40 | 2 | 3 | 5 | 2.5 |
| 60 | 3 | 2 | 5 | 2.5 |
| 80 | 4 | 1 | 5 | 2.5 |

Table 5.1. Geometric dimensions of smooth and rough grid porous structures

The high-fidelity grid geometry of porous substrates with smooth (**Figure 5.1a**) and rough (**Figure 5.1b**) surfaces were generated using Autodesk Fusion 360 (2.0.16490, Autodesk) software. In rough substrates, surface roughness was attained by subtracting structure (ii) from structure (i). For structure (ii), each porous tower was generated with a 10 x 10 μm size and different heights. There were 24 towers with 6.6 μm height, 28 towers with 3.3 μm height, and 24 towers with 10 μm height, randomly distributed over the surface (**Figure 5.1b**). The surface

roughness (Ra) calculated for all rough substrates is 3.25 μm . Four different porosities (20%, 40%, 60%, and 80%) were created for both smooth and rough substrates. The dimensions used for building the porosity differences in the smooth and rough substrates are given in **Table 5.2**. In total, 8 porous substrates were created in a cubic grid geometry of size 100 $\mu\text{m} \times 100 \mu\text{m} \times 100 \mu\text{m}$ ($x \times y \times z$). These substrate files (.stl format) were then imported into the COMSOL Multiphysics 6.2 for SECM modeling.

| Parameter | Value | Description |
|--|---|---|
| a | 12.5 [μm] | Radius of microelectrode |
| R | 37.5 [μm] | Radius of glass sheath |
| RG | 3 | R/a |
| L_{Elec} | 1250 [μm] | Electrolyte domain length |
| L_{UME} | 1000 [μm] | Length of the microelectrode |
| C_{An} | 2 [mM] | Bulk anthracene concentration |
| D_{An} (Hossain <i>et al.</i> , 2021) | 1.4×10^{-9} [$\text{m}^2 \text{s}^{-1}$] | Bulk diffusion coefficient of anthracene |
| n | 1 | No: of electrons transferred |
| R | 8.314 [$\text{J mol}^{-1} \text{K}^{-1}$] | Universal gas constant |
| F | 96485 [C mol^{-1}] | Faraday's constant |
| k⁰ | 0.112 [m s^{-1}] | Heterogeneous rate constant |
| κ | 1000 | Normalized heterogeneous rate constant: $(k^0 \cdot a) / D_{\text{An}}$ |
| η | 0.25 [V] | Overpotential: $E_{\text{app}} - E^0$ |
| α | 0.5 | Transfer coefficient |
| T | 293 [K] | Temperature |
| L | d/a | Normalized tip-substrate distance |

Table 5.2. Model parameters

A 3D finite element SECM model was developed in COMSOL Multiphysics 6.2 using the “Transport of Diluted Species in Porous Media (TDS)” module. The SECM model geometry consisted of a microelectrode of radius 12.5 μm with a surrounding glass sheath (RG=3), an electrolyte of size 1250 $\mu\text{m} \times 1250 \mu\text{m} \times 1250 \mu\text{m}$ ($x \times y \times z$), and the imported porous substrate (see appendix C, **Figure C.1**). Here, the transport of an irreversible mediator, anthracene (An) was modeled using SECM in the feedback mode. The parameters used in the model are given in **Table 5.2**. The microelectrode z position approach to the porous substrate was automated with 29.98 steps and a step size of 5 μm . Simulations were carried out for all responses with the

microelectrode at a tip-substrate distance (d) of 100 nm from the substrate. Detailed information regarding the COMSOL model is given in Appendix C.

5.4. Results And Discussion

5.4.1. Steady State Concentration Map of Anthracene

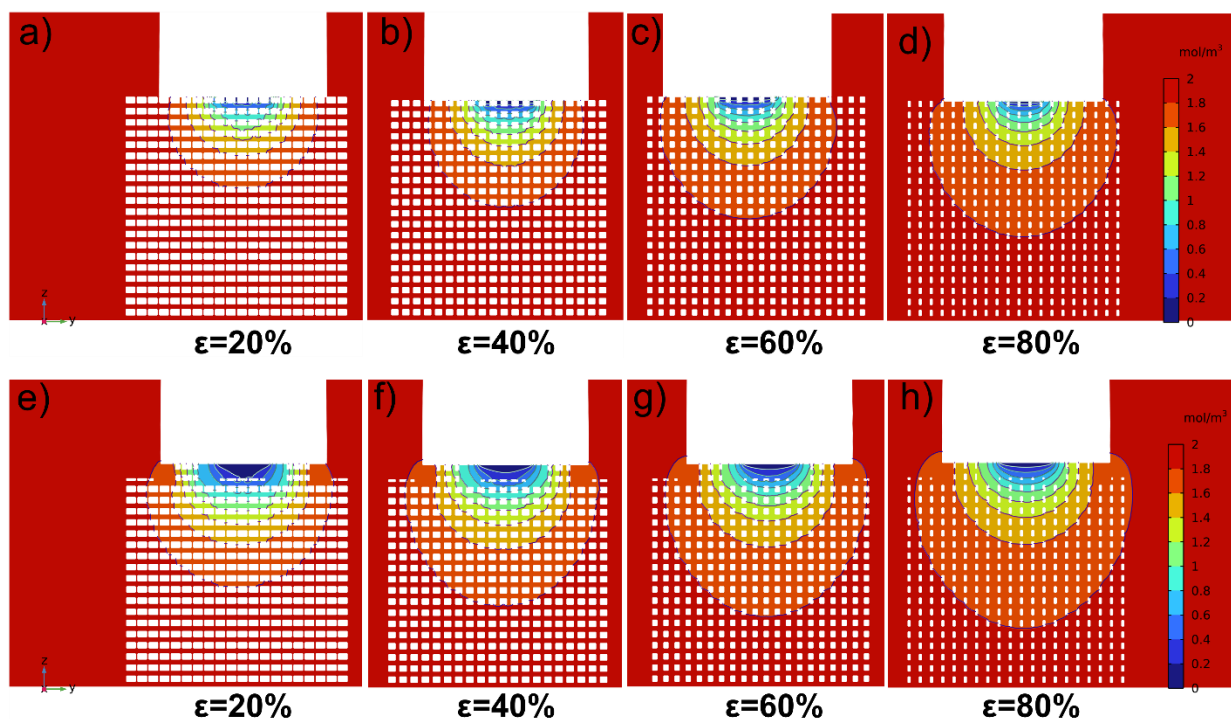


Figure 5.2. 2D cross-sectional concentration map of anthracene in a, b, c, d) smooth and e, f, g, h) rough substrates with various porosities at a normalized tip-substrate distance, $L = 0.008$

A systematic modeling approach was used to analyze the disparities in mass transport between smooth and rough substrates, both with porosities of 20%, 40%, 60%, and 80%. The microelectrode was positioned at a distance of $L = 0.008$, and the diffusion profile of anthracene was studied for all porous substrates (**Figure 5.2**). In this modeling study, anthracene was selected as the mediator as previous SECM experimental studies have demonstrated its unique advantages in studying the transport properties of substrates regardless of their nature (Hossain *et al.*, 2020 ; Lhenry *et al.*, 2013).

The anthracene concentration at the center of the microelectrode is essentially zero, due to the large overpotentials applied when probing porous media using SECM (Hossain *et al.*, 2021). This creates a mass transport constraint near the tip when it is far from the substrate. As a consequence, a non-uniform anthracene concentration is observed, leading to a hemispherical diffusion profile as anthracene molecules must diffuse from the bulk. A second limitation to mass transport arises due to the porosity and tortuosity of the substrate when the tip is positioned closer to it. This leads to a non-uniform anthracene diffusion profile within the substrate as well (Figure 5.2). The diffusion layer grows as the porosity increases in both smooth and rough substrates, as evidenced by the concentration gradient profiles.

5.4.2. Impact of Porosity and Surface Roughness

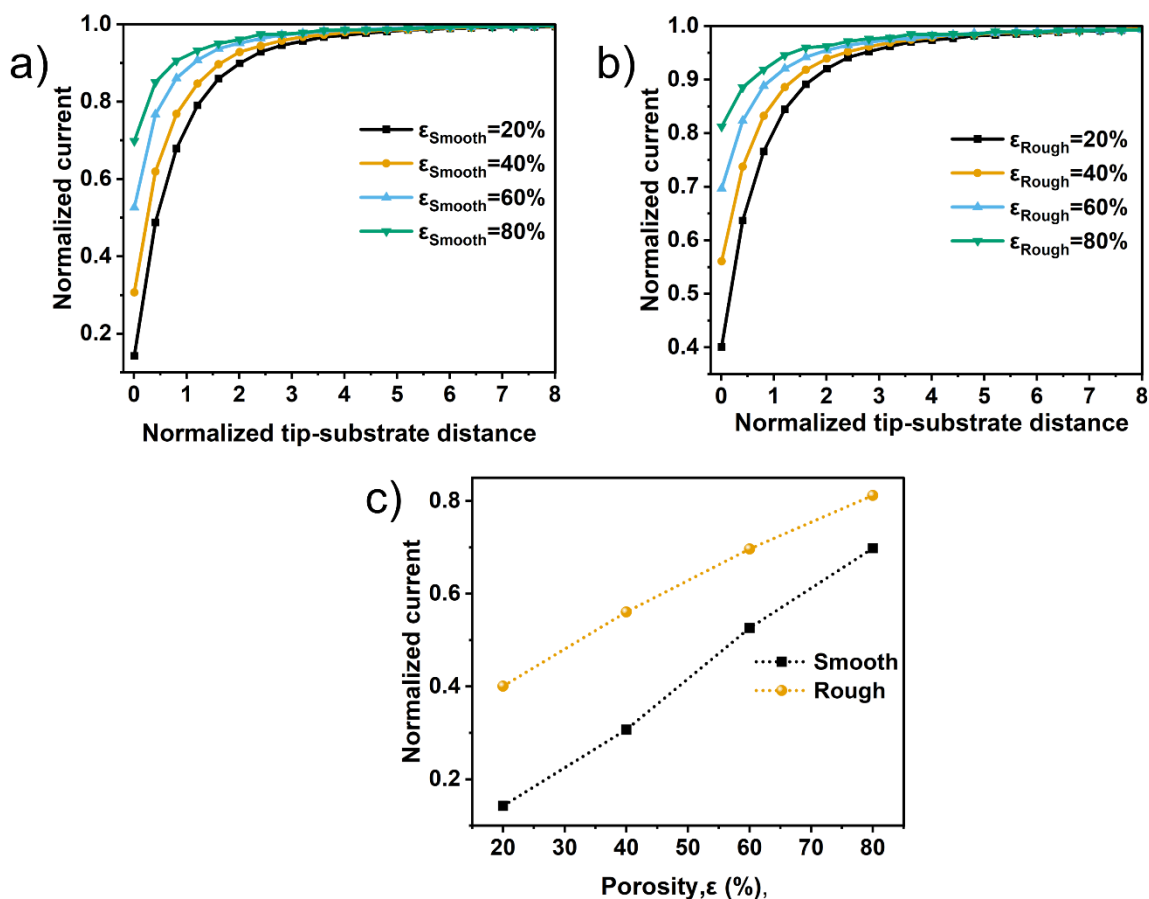


Figure 5.3. Approach curves showing the effect of porosities (ϵ) in a) smooth substrates, b) rough substrates with a thickness of 100 μm , and c) comparison of porosity effect in smooth and rough substrates at normalized tip substrate distance, $L= 0.008$

The impact of the substrate's porosity (ϵ) was studied by simulating approach curves in the feedback mode (**Figure 5.3a, b**). The current generated due to the irreversible anthracene oxidation at the microelectrode was calculated for all tip-substrate distances using equation C.5 provided in Appendix C. When the microelectrode (ME) is positioned far from the substrate (*i.e.*, bulk position), anthracene undergoes oxidation at the ME tip and a maximum diffusion-limited current is attained. However, as the tip approaches the substrate's surface, the current decreases due to the hindrance of anthracene diffusion toward the ME by the presence of the substrate. The current begins to decrease at a normalized tip-substrate distance, $L=2$, and drastically decreases for $L < 2$. Unlike the situation with an insulator, the observed current does not reduce to zero owing to the presence of porous pathways within the substrate, which provide an alternate pathway for anthracene diffusion. Consequently, an increasing porosity facilitates more molecules reaching the tip through the pores within the substrate. The modeled approach curve data showed that increasing porosity leads to increased normalized current at a normalized tip-substrate distance, $L = 0.008$, for both smooth and rough substrates (**Figure 5.3a, b**).

When the ME is close to the smooth porous substrate, the only available path for anthracene diffusion is *through* the pores within the substrates. Conversely, when the ME approaches the rough substrates, although the substrate impedes the diffusion towards the ME, it is not as effective compared to the smooth substrates due to the additional path. This results in a higher normalized current near rough substrates compared to smooth substrates for all studied porosities (**Figure 5.3c**). For instance, at a porosity of 40%, the normalized current value obtained is 0.31 for the smooth substrate whereas it is 0.56 for the rough substrate.

5.4.3. Comparing the Diffusion Profile of Anthracene

The comparison of concentration gradient profiles between smooth and rough surfaces across all porosities reveals the impact of surface topography, specifically roughness, on mass transport as measured by the tip (**Figure 5.4a**). For instance, the rough substrate with a porosity of 40% shows a larger diffusion front compared to those with a smooth surface. This suggests that the tip gets partially covered by the rough substrates and resulted in an increased flux of anthracene molecules towards the tip. Regardless of porosity values, this effect of surface roughness contributes to higher normalized currents, as demonstrated by the approach curves of the rough

substrates. Therefore, the current in rough substrates becomes a combination of the effect of porosity and the surface topography, whereas for smooth surfaces, it depends solely on the substrate's porosity or the effective diffusion of anthracene.

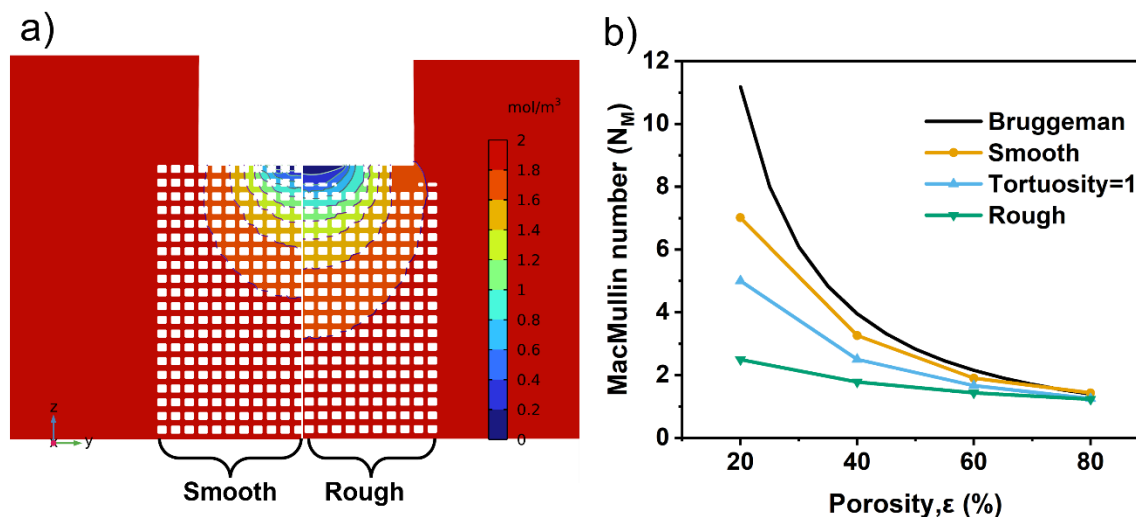


Figure 5.4. a) Concentration map of anthracene shows the comparison of diffusion in smooth and rough substrates with a thickness of 100 μm and porosity, $\epsilon=40\%$, b) MacMullin number comparison of the modeled substrates with the Bruggeman's relation

5.4.4. Determining MacMullin Number

The Macmullin number (N_M) is a crucial parameter that characterizes the interplay between porosity, tortuosity (τ), and the effective diffusivity of molecules within a porous substrate. It is a vital tool in transport modeling studies, as it does not rely on any assumptions about porosity (Liu *et al.*, 2022a). Previously reported studies have utilized N_M to represent the SECM current relationship to the effective transport characteristics (Hossain *et al.*, 2020, 2021). N_M relates the ratio of currents at the bulk (I) and near the porous substrates (I^*) to the ratio of bulk diffusivity (D) and the effective diffusivity (D_{eff}) as follows (Hossain *et al.*, 2020 ; Thorat *et al.*, 2009):

$$N_M = \frac{I}{I^*} = \frac{D}{D_{eff}} = \frac{\tau}{\epsilon} \quad \text{Eq. (5.1)}$$

In this study, as the only factor that affects the transport in the substrate compared to the bulk is the microstructural parameters such as the porosity and tortuosity of the substrate, the ratio of the currents and the diffusion coefficients ratio remains the same. Utilizing the above definition, N_M was determined for both smooth and rough surfaces with porosities 20%, 40%, 60%, and 80% (**Figure 5.4b**). For all these substrates, N_M decreases as porosity increases, suggesting that highly porous substrates lead to an increased flux of anthracene towards the tip through their pores. Compared to smooth substrates, rough substrates exhibit smaller N_M values, indicating the presence of less tortuous paths. However, when compared to the ideal value of tortuosity ($\tau=1$), all rough substrates showed a tortuosity value of less than one, which is unrealistic. This is predominantly due to the current contribution caused by the high surface roughness in addition to the porosity of the substrate.

While prior SECM experimental studies have used equation (5.1) to calculate N_M in porous substrates, the influence of surface roughness on current has not taken into account in this definition, indicating that this relationship is only valid for smooth substrates. Consequently, this skews the SECM data analysis in experimental mass transport studies using porous substrates with high surface roughness. A proper understanding of surface roughness is necessary before adopting SECM for tortuosity or mass transport studies in rough samples.

Furthermore, a widely adopted model to predict the tortuosity of porous substrates known as Bruggeman's relation was employed in this work to validate the modeling data. The Bruggeman's relation is given by (Bruggeman, 1935 ; Tjaden *et al.*, 2016):

$$\tau = \varepsilon^{(1-\alpha)} \quad \text{Eq. (5.2)}$$

Where α is the Bruggeman exponent. Typically, $\alpha= 1.5$ is used in most studies and predicts well the porosity dependence of tortuosity. Therefore, for Bruggeman, $N_M = \varepsilon^{-1.5}$. Comparing the N_M values of all modeled substrates with Bruggeman's model demonstrated a deviation at all porosities, raising questions about using this relationship to predict transport in porous structures. Without proper modeling data, using this relationship leads to significant errors in predicting the transport characteristics of porous structures. For example, as the observed deviation from

Bruggeman is more prominent at low porosities, utilizing this relation will be particularly problematic in predicting the performance of low porous substrates (eg: commercial battery electrodes possessing 30% porosity).

5.5. Conclusion and Perspectives

This study investigated the impact of surface roughness on mass transport in different porous substrates using 3D SECM modeling for the first time. The approach curve simulations demonstrated that an increase in porosity resulted in an increase in the tip current for all the smooth and rough surfaces. Additionally, N_M deviation of all substrates from Bruggeman's model highlights the importance of modeling studies in optimizing transport characteristics in porous substrates.

More importantly, rough substrates exhibited lower N_M and unrealistic tortuosity values compared to smooth ones, indicating the increased tip current contribution by the high surface roughness. In this SECM mass transport analysis with a microelectrode of $RG = 3$, the results were significantly impacted by the modeled substrates, which had a roughness of $3.25 \mu\text{m}$. Therefore, when examining porous substrates with high surface roughness, using probes with an RG greater than the surface roughness would be beneficial for averaging out the roughness effect on the probe current as bigger probes can cover a large area of the substrate. Furthermore, probe measurements should be performed at different spots on the substrate to average out the impact of roughness.

We anticipate that the findings of this study can be used as a reference for future experimental studies when analyzing rough substrates by SECM. It may also be useful to optimize the surface roughness of substrates to make them suitable for this methodology. Furthermore, the study suggests the potential need for measurements involving real porous samples with well-defined geometries created using 3D printing for in-depth analysis of experimental artifacts and surface roughness effects.

5.6. Acknowledgment

The financial support from the Natural Sciences and Engineering Research Council (NSERC) is gratefully acknowledged.

CHAPTER VI

CONCLUSIONS & PERSPECTIVES

This chapter aims to recapitulate the various analyses and studies conducted in chapters I to V and highlight their potential for future research.

6.1. Summary

Mass transport is a critical parameter that affects the reaction kinetics, material performance, and efficiency in all electrochemical systems. Consequently, understanding and optimizing mass transport is imperative for designing future electrochemical systems with optimized performance. As such, this dissertation primarily focuses on the mass transport process in porous structures, specifically with potential applications in battery technology. In LIBs, the sluggish Li^+ ion transport through the electrolyte and within the electrode causes large concentration gradients, leading to deterioration of power performance, especially at high current densities. This concern is particularly significant for the application of LIBs in electric vehicles, where fast charging, high power and energy densities, safety, high cycle life, and cost-effectiveness are crucial requirements. Therefore, this dissertation primarily focused on studying the mass transport of Li^+ ions through composite battery electrodes to enhance the power performance of next-generation LIBs.

Chapter I provided a fundamental review of the significance of mass transport phenomena in the performance of batteries, the architectural parameters affecting transport, and the existing techniques to determine the transport properties of the electrodes at the mesoscale to the microscale. Among the methods discussed in Chapter I, scanning probe microscopies (SPMs) like scanning ion conductance microscopy (SICM) and scanning electrochemical microscopy (SECM) are the effective tools used in this dissertation to investigate the mass transport in various porous structures. The utilization of scanning probe microscopes (SPMs) is essential for advancing our understanding of battery materials and interfaces, as they have the capability to uncover intricate transport processes and quantify the effective transport properties at the microscale, which cannot be obtained using bulk measurement techniques including EIS, CV,

GITT, *etc.* This microscale information plays a pivotal role in shaping the design of future batteries, enhancing their performance, and prolonging their lifecycle. Given the escalating challenges posed by climate change and increasing energy demands, we are in dire need of effective solutions. Hence, the employment and development of SPMs in battery research during this period are of utmost importance.

Given the significance of SPMs in this dissertation, **Chapter II** summarizes the trends of SECM in EESC devices such as batteries, fuel cells, and supercapacitors over the last decade. It discusses the indispensable use of SECM to provide the microscale information about the solid-electrolyte interphase, cathode-electrolyte interphase, and ion transport in LIBs, as well as the hydrogen oxidation reaction, oxygen reduction reaction, and membrane transport in fuel cells, and the electrochemical reactivity and kinetics in supercapacitors. Additionally, this review of SECM gives an idea of the various operating modes, such as feedback (FB), generation-collection (GC), surface interrogation (SI), and redox competition, which are relevant to the energy research community.

One interesting SECM application using FB mode was used in **Chapter III** to determine the mass transport in a battery anode, $\text{Li}_4\text{Ti}_5\text{O}_{12}$ (LTO), with different porosities. More importantly, SICM was also employed for the same purpose, to compare the transport measurement results. The probe currents measured were converted to Macmullin numbers (N_M), which represent the transport through the solution-filled pores in LTO films depending on the porosity and tortuosity of the films. Throughout this dissertation, the effective transport properties were described in terms of N_M . The study presented in Chapter III established the complementary nature of SECM and SICM in measuring solution-phase transport in battery electrodes for the first time, in terms of effective conductivity and diffusivity, respectively. In addition, this research used an irreversible mediator like anthracene to evaluate the transport properties in LTO films with conductive carbon. This helped to eliminate the impact of carbon on the probe current, which could otherwise cause errors in SECM measurements.

While the above experimental approach helps to understand the dynamics of the real porous substrates, it is often challenging to control one structural parameter of these substrates without affecting the other parameters. Therefore, in **Chapter IV**, a finite element modeling study of

SECM in three-dimension (3D) was conducted to independently investigate the effect of thickness, and porosity in three types of porous structures with different substrate geometries. The steady-state current at the probe due to the irreversible oxidation of anthracene in the FB mode was simulated using all three types of microporous substrates, such as superposition (SP), high-fidelity (HF)-1, and HF-2. SP is one of the commonly adopted models in SECM studies to represent the porous structure with an average porosity, whereas the other two porous structures have a well-defined geometry. The interesting observation was the decrease in steady state current as the substrate's geometric complexity increases at a given porosity and thickness. N_M follows the order: HF-2 > HF-1 > SP, indicating more tortuous paths in HF-2 regardless of the same porosity and thickness used for all substrates. Another finding is the deviation of N_M of all studied substrates from Bruggeman's relationship, which is the widely adopted model for porous substrates. As this deviation becomes large at lower porosities, relying on Bruggeman to predict the transport results in inaccurate values especially for commercial battery electrodes having 30% porosity. Therefore, this study highlights the significance of substrate geometry in mass transport, emphasizing the need to model actual porous structures rather than relying solely on the Bruggeman model if the geometry is known.

Although Chapters III and IV explored the experimental and modeling aspects of the SECM methodology to measure the mass transport in distinct porous structures, an aspect that is still not fully understood is the surface roughness importance when studying these structures. **Chapter V** focuses on the surface roughness effect, acknowledging its importance across disciplines such as battery technology and corrosion studies. The control of surface roughness during experimental investigations poses a challenge and necessitates a computationally expensive 3D model to comprehend its influence on transport properties.

The research outlined in Chapter V includes a comparative study using a 3D SECM model with anthracene to analyze the effect of surface roughness on mass transport in high-fidelity substrates with smooth and rough surfaces. The investigation involved analyzing the change in steady-state current in relation to the different porosities of two substrates with varying surface roughness. The research revealed that porous substrates with higher surface roughness consistently exhibited greater tip currents, resulting in tortuosity values of less than one. This indicates that when using

SECM to study substrates with higher surface roughness, the precision of mass transport measurements is adversely affected due to the influence of both roughness and porosity on the probe current. Furthermore, similar to the findings in Chapter IV, N_M deviates drastically from Bruggeman's model for both smooth and rough, porous substrates. The lower N_M values obtained for all the rough substrates and the unrealistic tortuosity values compared to the smooth substrates verify the contribution of surface roughness to the probe current in addition to the porosity beneath the probe.

In conclusion, Chapter I provides the significance of mass transport in LIBs and reviews the existing techniques for probing transport properties. Chapter II then advances the discussion to highlight the recent trends of SECM in the field of EESC devices. The subsequent chapters, III to V, add new knowledge to the field by extending the investigation using SPMs to include the impact of various structural parameters, substrate geometry, and topography on mass transport processes in porous structures through experimental approaches and modeling.

6.2. Outlook

The mass transport properties described in terms of N_M in this dissertation, obtained using SPMs such as SECM and SICM, are critical in improving the modeling and design of future batteries with high-power densities. In general, knowing the transport properties further helps in selecting appropriate electrode materials, optimizing various structural parameters such as porosity and thickness, as well as predicting and preventing battery degradation.

The complementary nature of SICM and SECM techniques discussed in Chapter III can extend to fields beyond batteries, such as corrosion studies, electrocatalysis, nanoporous materials, nanomedicine, and biological systems, where a nanoscale spatial resolution is essential for determining the mass transport. SICM can be employed in these cases as the nanopipette probes in SICM can be easily fabricated compared to nanoelectrode probes in SECM. In addition, it is difficult to find a porous substrate with a known tortuosity to serve as a reference to validate the experimental mass transport measurements. In such cases, either of these SPMs can be used to verify the results obtained through other techniques.

During battery cycling, solid electrolyte interphases and cathode electrolyte interphases can develop on the anodes and cathodes, respectively. Therefore, the next step forward is to adopt the SICM and SECM methodology to battery electrodes before and after cycling to understand the differences in overall mass transport properties. Additionally, temperature plays a significant role in the mass transport of batteries. Low temperature impede transport, while high temperature enhances it. This factor should be taken into account in future measurements using SICM and SECM methodologies outlined in this dissertation. Although the discussion is centered on LIBs, these two future lines of research are critical for other next-generation batteries, such as Li-O₂, and Li-S batteries.

The modeling studies discussed in Chapters IV and V have plenty of room for improvement. These studies focused on a simple 3D model for porous structures with substrates featuring uniform pore size or geometry. However, the exploration of non-uniform pore sizes is still pending, as real porous substrates exhibit a complex geometry with diverse interfaces and pore sizes. Additionally, the adsorption of redox mediators or their interaction with the substrate presents an important avenue for future research although it adds complexity to the numerical modeling studies.

Another aspect to consider in the future using the scanning probe methodologies is how the variation in the size of the probes affects the mass transport measurements. The experimental studies in Chapter III utilized only one probe dimension: a 12.5 μm radius Pt microelectrode with an RG ≈ 2.5 and a micropipette with a radius of $\approx 1.5 \mu\text{m}$. Therefore, it is particularly interesting to investigate the effect of dimensions of probe geometry on mass transport measurements in cases where the surface roughness is similar to the probe size and plays a significant role.

Chapter IV discussed an SECM modeling study demonstrating the effect of surface roughness on the probe current measured at the porous substrates. When conducting experimental studies of any substrates, integrating SECM with AFM is an option to deconvolute the effect of topography from the mass transport contribution at different spots on the substrates simultaneously, as SECM has already been proven to be flexible in integrating with various techniques like Raman, AFM, *etc.*

We anticipate that the numerical modeling studies presented in Chapters IV and V can serve as a reference for future experimental SECM mass transport studies in porous substrates. Chapter IV discussed the differences in mass transport in the superposition model substrates, a widely used geometry used in the COMSOL modeling study to represent a substrate with an average porosity. As such, the results can be used to validate the experimental results obtained using any real porous structures (eg: battery electrodes) to understand the underlying artifacts that may arise during the experiments.

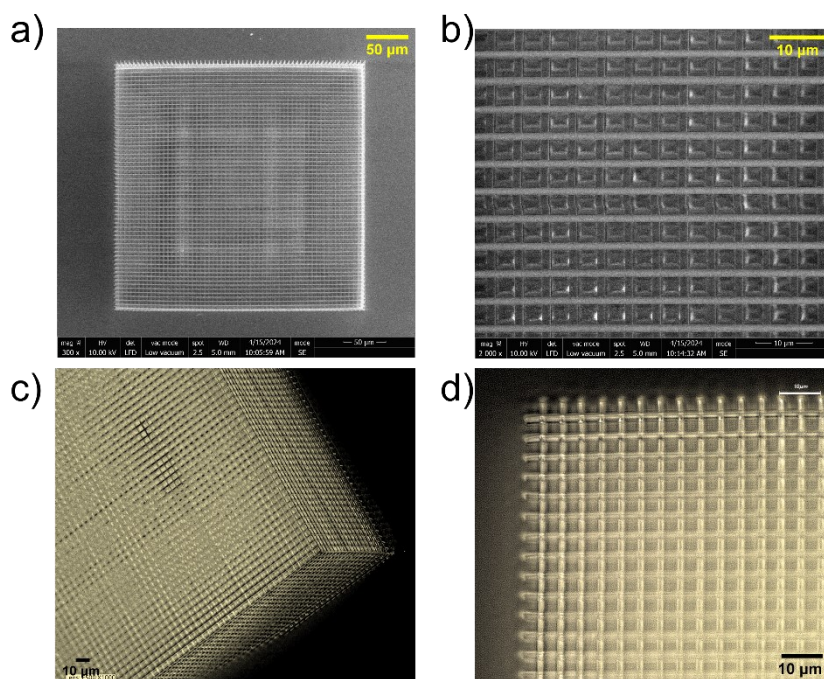


Figure 6.1. Smooth substrate with 80% porosity imaged using a), b) scanning electron microscopy, and c), d) optical microscopy

In addition to the 3D modeling results discussed, experimental data is also critical for understanding the challenges related to SECM transport measurement in real porous samples, especially with a large surface roughness. The meticulously uniform porous model geometries discussed in Chapters IV and V can be fabricated with the aid of high-resolution 3D printing techniques. The scope of this idea is currently under investigation in our laboratory. For example, a smooth substrate with 80% porosity was successfully fabricated with microscale precision using 3D printing (**Figure 6.1**). Scanning electron microscopy (**Figure 6.1a, b**) and optical

microscopy (**Figure 6.1c, d**) images illustrate the effectiveness of 3D printing in fabricating substrates with microscale precision. Future work involves experimental SECM investigation of mass transport in these 3D-printed microstructure geometries to validate the results obtained through modeling and to identify any experimental challenges.

While looking for future avenues for research based on SECM, an interesting aspect that can be considered is the development of electroanalytical probes sensitive to Li^+ ions. Although mercury (Hg)-based SECM probes are successfully developed for Li^+ detection in non-aqueous electrolytes, the toxicity of Hg creates a major drawback, necessitating the development of alternative probes. For example, we have fabricated an alternate probe based on gallium for Li^+ ion detection in non-aqueous electrolytes (Appendix D). This work can serve as a reference for future research related to gallium-lithium systems as it discusses the challenges and efforts undertaken to address them.

APPENDIX A

SUPPORTING INFORMATION TO INVESTIGATING MASS TRANSPORT IN LI-ION BATTERY ELECTRODES USING SECM AND SICM

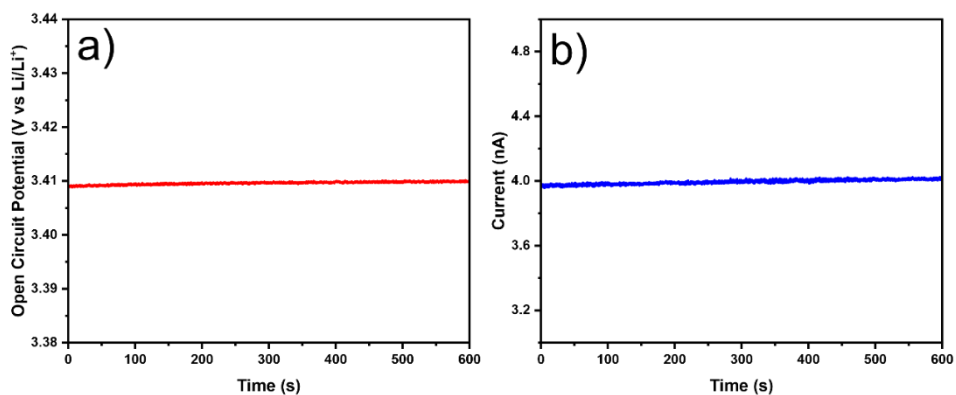


Figure A.1. a) Measurement of open circuit potential of the pd-LFP coated Al wire showing its stability, b) chronoamperometry (applied potential = 3.5 V vs Li/Li⁺) of the pd-LFP coated Al wire immersed within micropipette; Electrolyte: 0.1 M LiPF₆ in PC and QRCE: Li metal

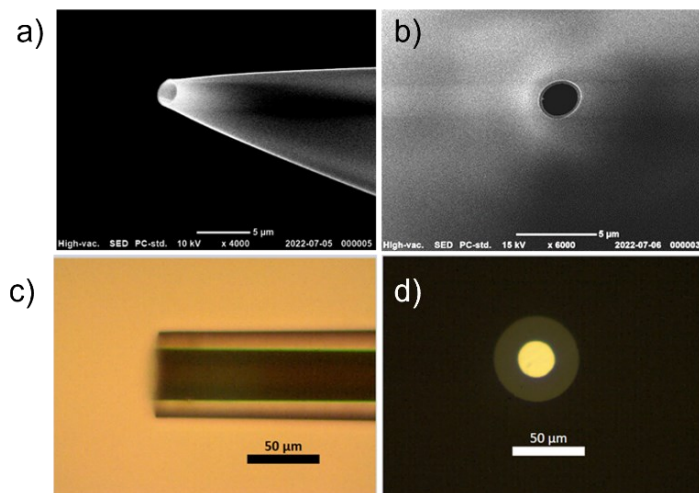


Figure A.2. SEM images of the micropipette a) side view, b) top view; and optical microscopy images of the Pt microelectrode c) side view, d) top view

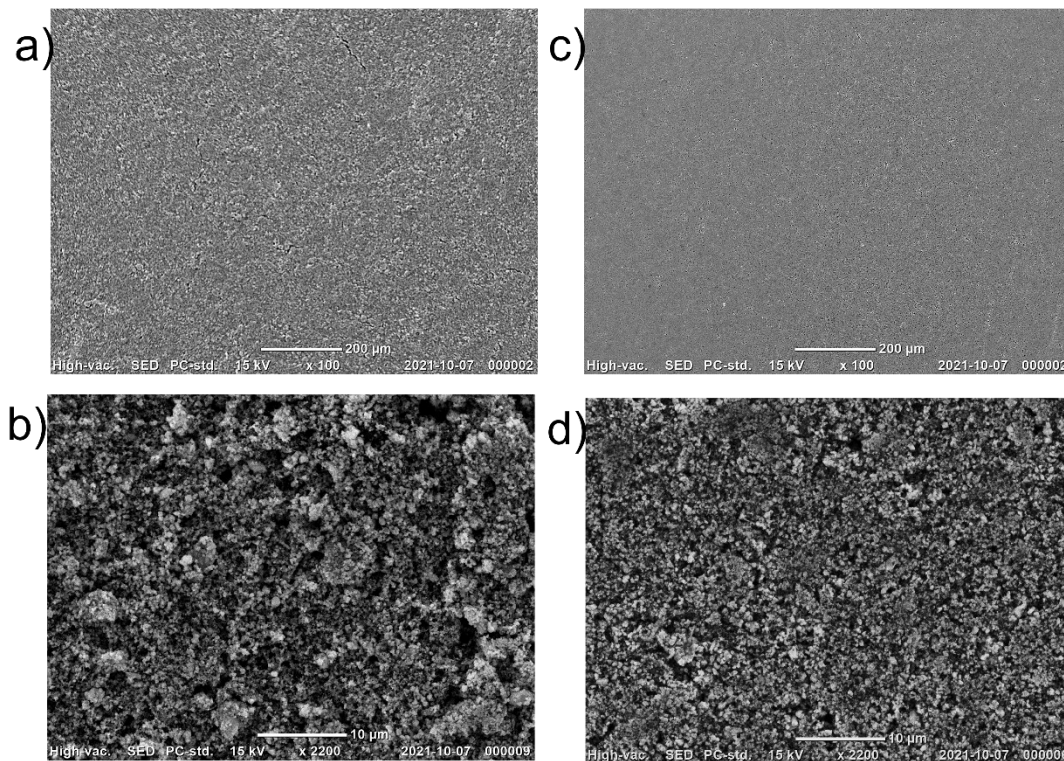


Figure A.3. SEM images of LTO films a, b) before and c, d) after calendaring

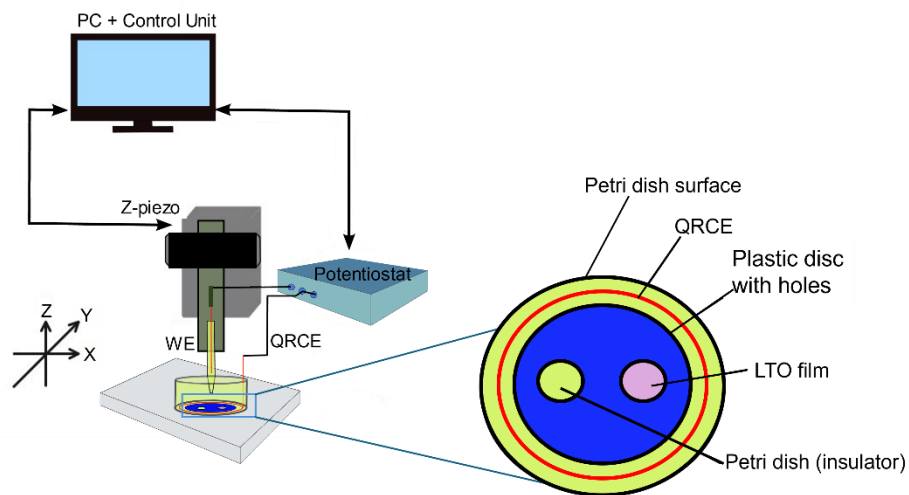


Figure A.4. Schematic of two-electrode configuration for SICM with the zoomed-in view of the electrochemical cell filled with electrolyte. A similar cell was used for SECM in three-electrode configuration with a microelectrode

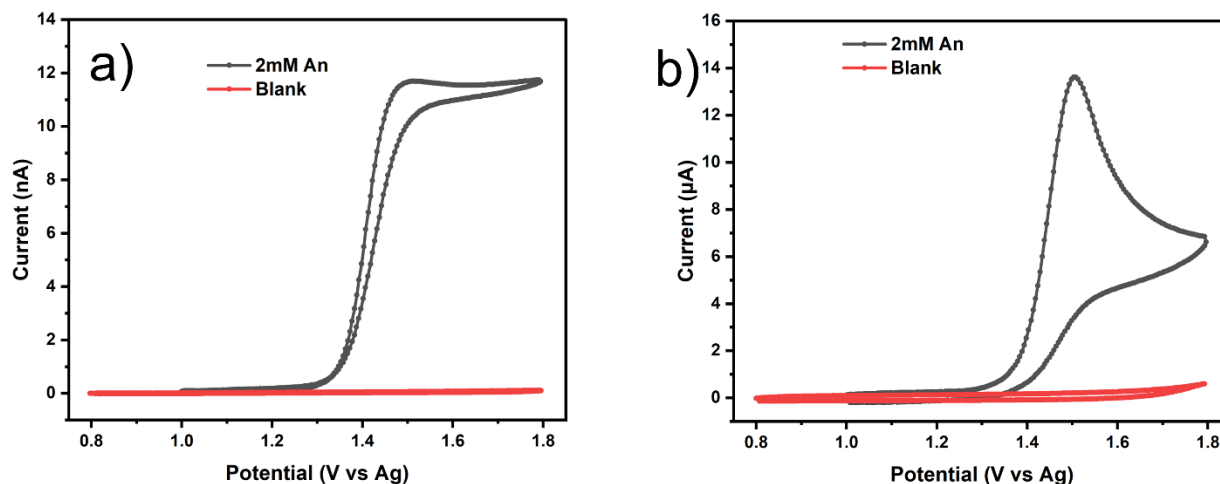


Figure A.5. Cyclic voltammetry (CV) of anthracene using a) 25 μm Pt microelectrode, b) 1.6 mm diameter Pt macroelectrode at a scan rate= 100 mVs^{-1} in 0.1 M TEABF₄/PC

A steady-state current of, $I^0 = 11.7 \times 10^{-9} \text{ A}$ is obtained from the CV of microelectrode (**Figure A.5a**). The electroactive radius (a) of the microelectrode can be calculated from (I^0) as follows:

$$I^0 = 4nF\beta D_{0,An} C_{An} a \quad \text{Eq. (A.1)}$$

For anthracene oxidation, $n=1$, $F=96485 \text{ Cmol}^{-1}$, $C_{An}=2 \times 10^{-6} \text{ mol cm}^{-3}$, $D_{0,An}=1.1 \times 10^{-5} \text{ cm}^2 \text{ s}^{-1}$, $\beta=1.09$ for an RG=2.5 (Lefrou et Cornut, 2010). Using these values, the calculated a is 12.5 μm .

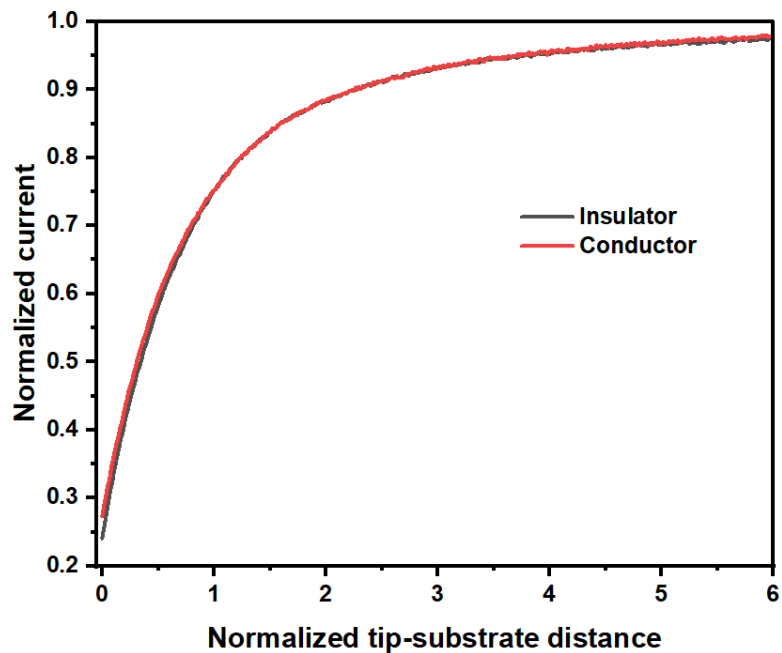


Figure A.6. SECM approach curves on insulator and conductor showing the hindered diffusion using anthracene

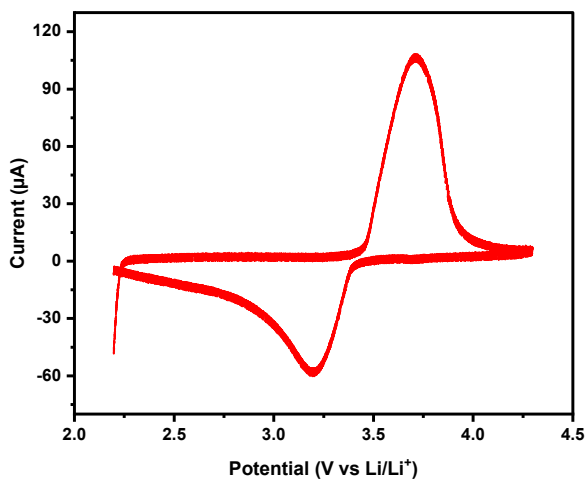


Figure A.7. Cyclic voltammetry using partially delithiated LFP ($\text{Li}_{(1-x)}\text{FePO}_4$) at a scan rate of 0.1 mVs^{-1} in $0.1 \text{ M LiPF}_6/\text{PC}$, counter/ reference electrode: Li metal. The area under the oxidation/reduction curves is the same and equals $41 \text{ } \mu\text{A V}$

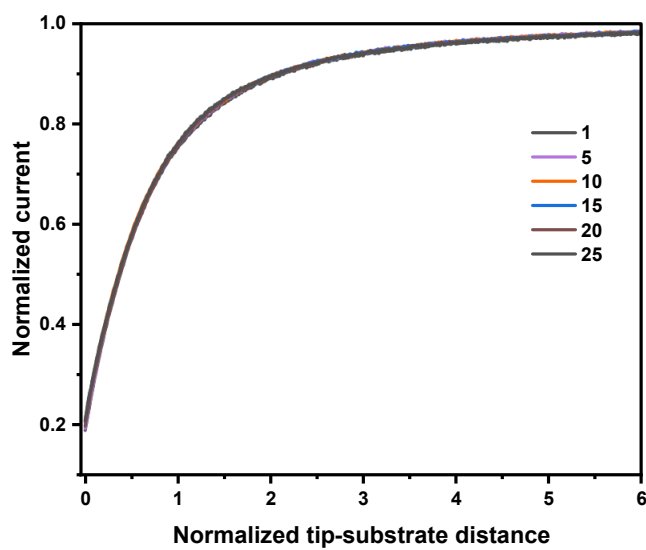


Figure A.8. SECM approach curves on the insulator repeated 25 times showing the reproducibility of the technique

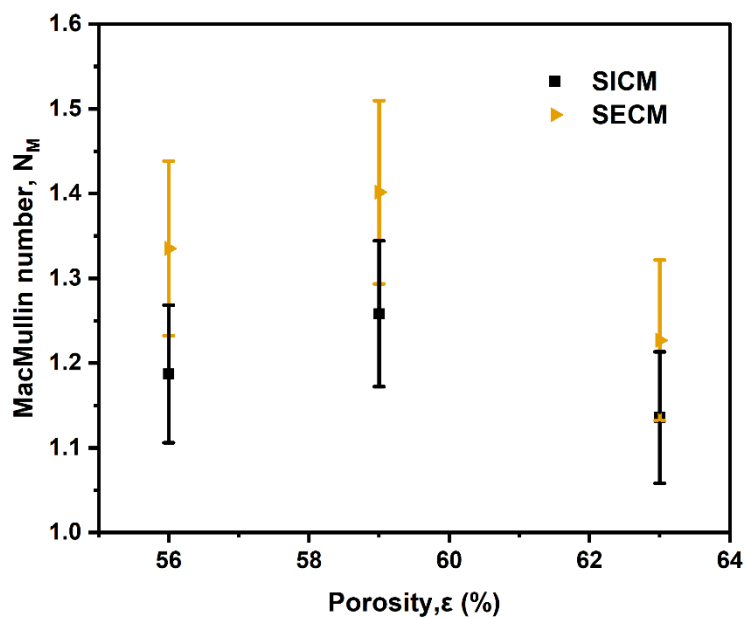


Figure A.9. MacMullin number calculated from SECM and SICM measurements conducted on the same LTO films

In **Figure A.9**, the MacMullin numbers obtained from SECM and SICM measurements show slight differences. These discrepancies arise from conducting the measurements at two different

locations on the same film, as well as from the variations in probe sizes used in the two techniques.

| LTO films used in SECM and SICM | | | |
|---------------------------------|----------------|----------------|----------------|
| Porosity, ε (%) | 55.9 ± 1.2 | 59.4 ± 2.5 | 63.2 ± 2.1 |
| Thickness (μm) | 59.4 ± 1.6 | 65.0 ± 2.7 | 75.8 ± 2.5 |

Table A.1. The film parameters used for MacMullin number calculations in Figure A.9

A.1. Porosity Calculation

To determine the porosities of the LTO films with a diameter of 1.5 cm, the following calculations are conducted.

The total volume of the film can be calculated by multiplying the area by its thickness (l),

$$V_T = \pi r^2 \cdot l \quad \text{Eq. (A.2)}$$

Where r is the radius of the film. The theoretical volume of the material is calculated by considering the mass fraction (m) and densities (ρ) of each of the individual components (LTO, C : carbon black, B : binder) of the composite film.

$$V_{mat} = m_T \cdot \left[\frac{m_{LTO}}{\rho_{LTO}} + \frac{m_C}{\rho_C} + \frac{m_B}{\rho_B} \right] \quad \text{Eq. (A.3)}$$

Where m_T is the mass of the LTO film without the mass of the copper current collector. Porosity (ε) is defined as the volume fraction of voids present inside the film:

$$\varepsilon = \frac{V_{void}}{V_T} \quad \text{Eq. (A.4)}$$

Total volume V_T constitutes both the volume of the material (V_{mat}) and volume of the voids (V_{void}). Therefore, ε can be expressed in terms of V_{mat} as follows:

$$\varepsilon = 1 - \frac{V_{mat}}{V_T}$$

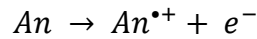
Eq. (A.5)

APPENDIX B

SUPPORTING INFORMATION TO MICROPOROUS SUBSTRATE EFFECT ON SECM STEADY STATE CURRENT-A 3D MODELING STUDY CRITICAL TO BATTERY ELECTRODE PERFORMANCE

B.1. Simulation Details

The irreversible oxidation of anthracene (An) at the microelectrode in bulk and near the porous substrate was simulated.



The total mass transfer of a species to the electrode is governed by the Nernst Planck equation. In 3D, it is given as:

$$J_{An} = -D_{An}\nabla C_{An} - \frac{z_{An}F}{RT}D_{An}C_{An}\nabla\phi + \nu C_{An} \quad \text{Eq. (B.1)}$$

Where J_{An} represents the flux of anthracene species, D_{An} the diffusion coefficient, ∇C_{An} the concentration gradient, C_{An} the concentration of anthracene, z_{An} the dimensionless charge, $\nabla\phi$ the electrostatic potential gradient, ν the solution velocity. As such, the three terms on the right side of equation (B.1) correspond to diffusion, migration, and convection, respectively.

In this work, a steady-state study was conducted to solve the Nernst Planck equation in 3D assuming negligible contribution from migration and convection. Hence the general form of the Nernst-Planck equation (equation (B.1)) is reduced to Fick's first law, which depends only on the diffusion and is given by,

$$J_{An} = -D_{An} \nabla C_{An} \quad \text{Eq. (B.2)}$$

The oxidation reaction occurring at the electrode surface acts as a driving force for generating a localized concentration gradient between the electrode-electrolyte interface. The second mass transport constraint in the superposition (SP) model comes from the porous substrate domain. The diffusion coefficient of anthracene inside the substrate ($D_{eff,An}$) depends on the microstructural parameters such as the porosity (ϵ) and tortuosity (τ). Hence the flux becomes,

$$J_{An} = -D_{eff,An} \nabla C_{An} \quad \text{Eq. (B.3)}$$

Where

$$D_{eff,An} = \frac{\epsilon}{\tau} D_{An} = \epsilon D_{An} \text{ (for SP model with } \tau = 1\text{)}$$

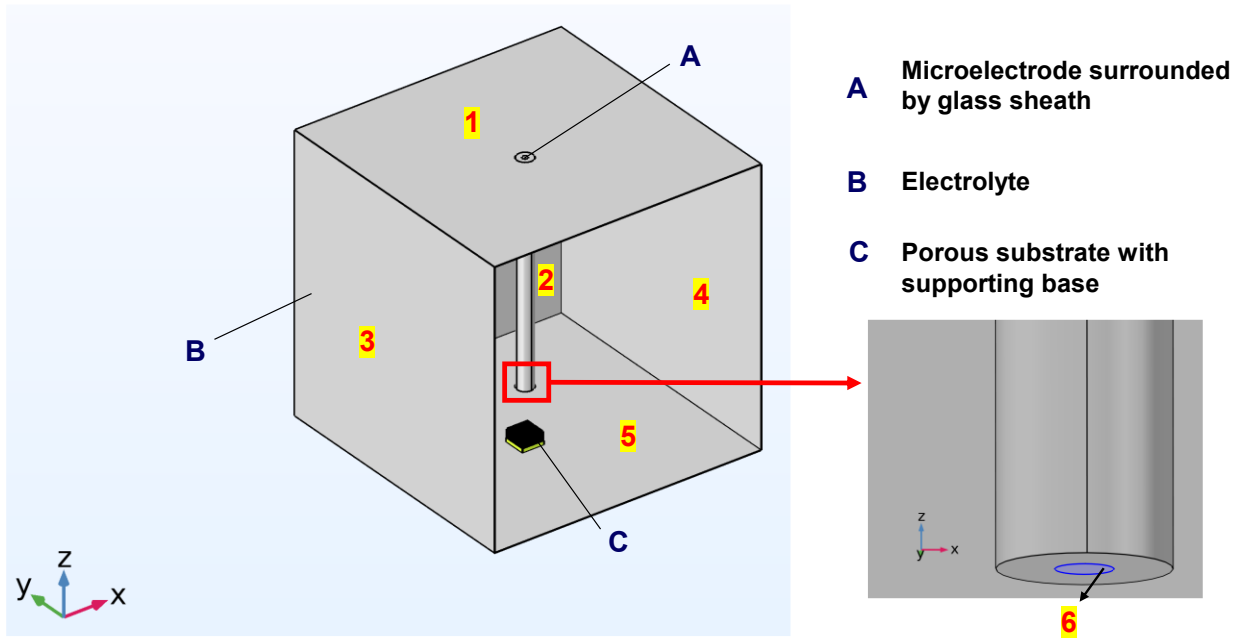


Figure B.1. Model geometry with domains (A, B, C), boundaries of electrolyte (1-5), and microelectrode (6)

In the Transport of Diluted Species in Porous Media physics of COMSOL, both porosity and tortuosity were set to *one* to impose the diffusion solely based on the high fidelity structure of the porous substrate. All domains (A, B, C) had an initial concentration of 2 mM anthracene.

B.2. Boundary Conditions

- 1) A no flux boundary condition was applied to all the surface boundaries of the porous substrate, supporting base, glass sheath, and at boundary 5 of the electrolyte.
- 2) A concentration boundary condition was applied to all the electrolyte boundaries (1-4) except boundary 5 (**Figure B.1**) where the porous substrate was located.

$$C_{An} = 2 \text{ mM}$$

- 3) The flux boundary condition at the microelectrode (boundary 6 in Figure B.1) was calculated with the help of forward and backward rate constants, κ_f and κ_b , respectively.

$$J_{An} = -[(\kappa_f \times C_{An}) - (\kappa_b \times C_{An^{*+}})] \quad \text{Eq. (B.4)}$$

As anthracene shows an irreversible kinetics, the flux becomes:

$$J_{An} = -[(\kappa_f \times C_{An})] \quad \text{Eq. (B.5)}$$

Where

$$\kappa_f = \kappa^0 \exp\left[\frac{(1 - \alpha)nF\eta}{RT}\right]$$

B.3. Meshing

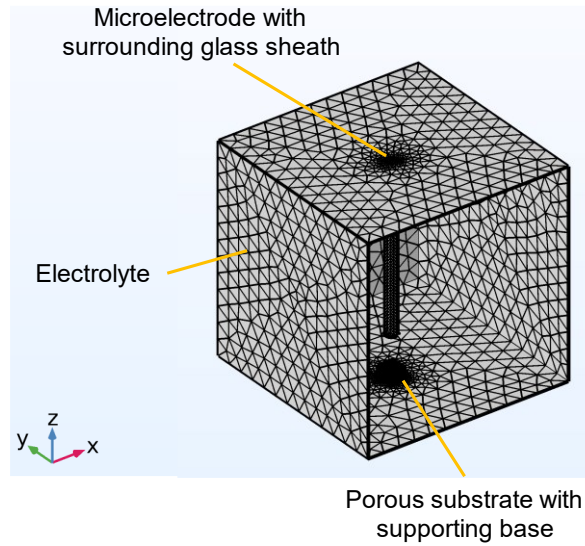


Figure B.2. Model geometry with tetrahedral mesh

A tetrahedral mesh was used to discretize the model geometry (**Figure B.2**). In general, higher mesh density leads to more accurate numerical computation results. Hence, an increased mesh density was applied for the microelectrode tip, glass sheath, and porous substrate regimes where a significant concentration gradient was expected (**Table B.1**). For the remaining geometry, a *fine* built-in mesh was applied.

| Domain | | Max: element size (μm) | Min: element size (μm) | Max: element growth rate | Curvature factor | Resolution |
|------------------|------|-------------------------------------|-------------------------------------|--------------------------|------------------|------------|
| Microelectrode | SP | 0.09 | 0.05 | 1.3 | 0.2 | 1 |
| | HF-1 | 0.09 | 0.05 | 1.2 | 0.2 | 1 |
| | HF-2 | 0.09 | 0.05 | 1.4 | 0.4 | 0.7 |
| Porous substrate | SP | 3.75 | 0.25 | 1.3 | 0.2 | 1 |
| | HF-1 | 3 | 0.25 | 1.3 | 0.2 | 1 |
| | HF-2 | 2 | 0.25 | 1.4 | 0.4 | 0.7 |
| Glass sheath | | 68.8 | 5 | 1.4 | 0.4 | 0.7 |

Table B.1. Shows the meshing parameters

B.4. Post Processing

The current formed at the microelectrode tip (boundary 6 in **Figure B.1**) was calculated by integrating the total normal flux across its surface area (A).

$$I = nFD \int_0^A \left[\frac{\partial C_{An}}{\partial z} \right] dA \quad \text{Eq. (B.6)}$$

Where z is the distance from the electrode surface and $z = 0$ refers to the electrode/electrolyte interface.

The ratio between the currents formed near the substrate (I^*) and at the bulk electrolyte (I) gives the normalized current (Ni) which is given as,

$$Ni = \frac{I^*}{I} \quad \text{Eq. (B.7)}$$

B.5. Dimensions of HF-1 and HF-2 Structures

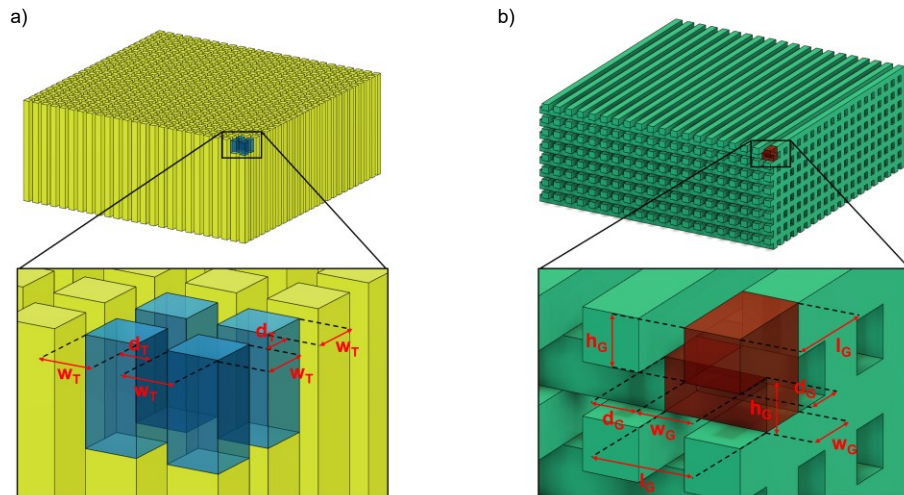


Figure B.3. a) Schematic of rectangular pillars in HF-1 b) repeating units in HF-2 substrates

| Porosity [%] | Distance d_T [μm] | Width w_T [μm] |
|--------------|----------------------------------|-------------------------------|
| 35.0 | 0.600 | 2.500 |
| 45.1 | 0.875 | 2.500 |
| 55.6 | 1.250 | 2.500 |
| 63.3 | 1.625 | 2.500 |
| 75.0 | 2.500 | 2.500 |

Table B.2. Geometric dimensions of HF-1 structure

| Porosity [%] | Distance d_G [μm] | Width w_G [μm] | Length l_G [μm] |
|--------------|----------------------------------|-------------------------------|--------------------------------|
| 35.0 | 1.750 | 3.250 | 5.000 |
| 45.1 | 2.255 | 2.745 | 5.000 |
| 55.6 | 2.780 | 2.220 | 5.000 |
| 63.3 | 3.165 | 1.835 | 5.000 |
| 75.0 | 3.750 | 1.250 | 5.000 |

Table B.3. Geometric dimensions of HF-2 structure

B.6. Effect of Size (w_T) in HF-1 Substrate

The effect of rectangular pillar size in HF-1 substrate was studied by varying the size from 1 μm to 10 μm while keeping the substrate thickness ($h = 40 \mu\text{m}$) and porosity ($\varepsilon = 63.3\%$) constant (**Figure B.4**). As the pillar size increased from 1 to 3.5 μm , the current near the HF-1 model substrate remained nearly constant. However, the current started to vary as the size changed from 4 to 10 μm , indicating an error in the model development. The approach curve suggests that a pillar size of 3.5 μm or less should be used to model the HF-1 substrate.

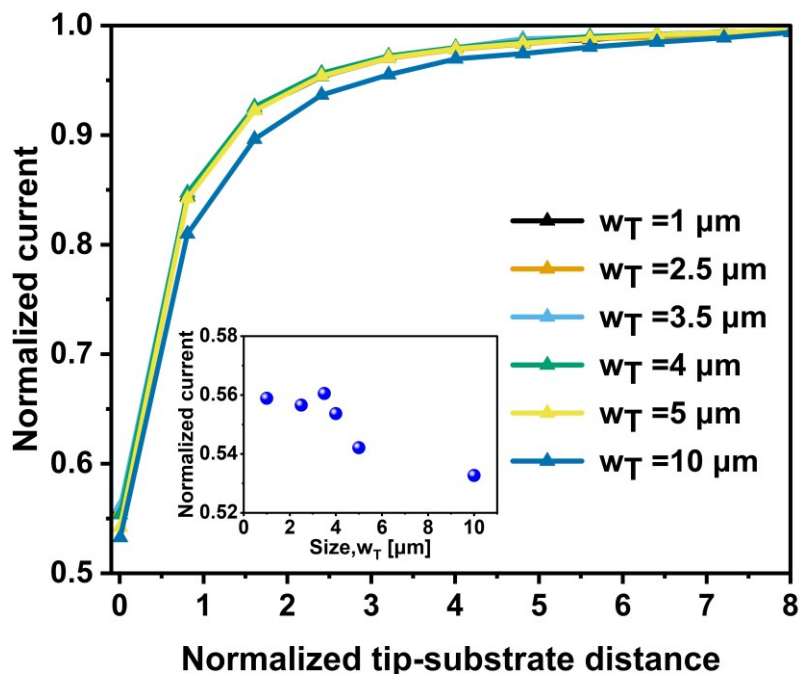


Figure B.4. Approach curves show the impact of the pillar size (w_T) of the HF-1 substrate on the current (inset shows the normalized current values at normalized tip-substrate distance = 0.008, for different pillar sizes)

In addition to the approach curve result, the diffusive flux in HF-1 substrates with various lateral pillar sizes was also investigated. For all modeled substrates, the flux is non-uniform due to the anthracene oxidation, and the flux is more confined beneath the microelectrode as the pillar size increases from 1 μm to 10 μm (**Figure B.5**). This result suggests that anthracene transport to the microelectrode gets increasingly impeded in the boundary between the solution and the substrate at $L=0.008$, as the lateral size of the substrate increases. As a consequence, the position of the microelectrode on the porous substrate determines the mass transport towards it if the substrate's lateral size is in the order of the radius of the microelectrode (12.5 μm). For instance, in HF-1 substrates with $w_T=10 \mu\text{m}$, the impact of pillar size on diffusive flux towards the microelectrode was more pronounced. Two representative cases of microelectrode position were considered for HF-1 substrate with $w_T=10 \mu\text{m}$. In the first case, the electroactive center of the tip was positioned above the pillar (**Figure B.6a**), and in the second case, it was positioned above a pore (**Figure B.6b**). The results showed a difference in the diffusive flux beneath the center of the tip indicating variations in mass transport measurement at different spots due to the large pillar size.

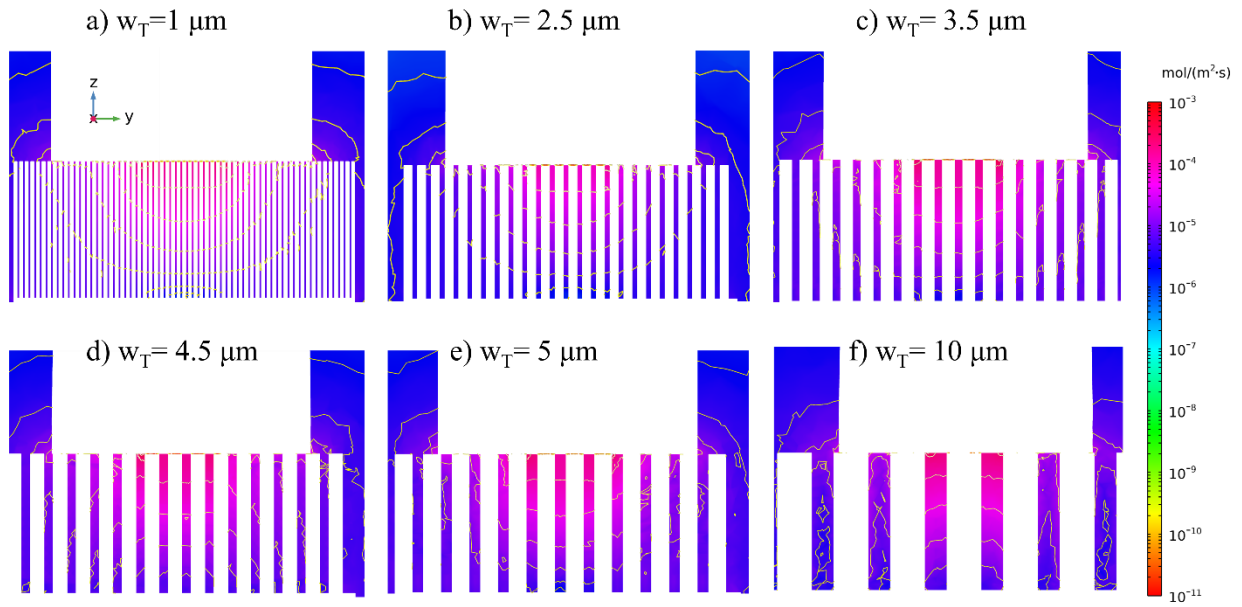


Figure B.5. Diffusive flux visualization within HF-1 substrate ($h = 40 \mu\text{m}$ and $\varepsilon = 63.3\%$) at a normalized tip-substrate distance, $L = 0.008$ for various lateral pillar sizes (w_T)

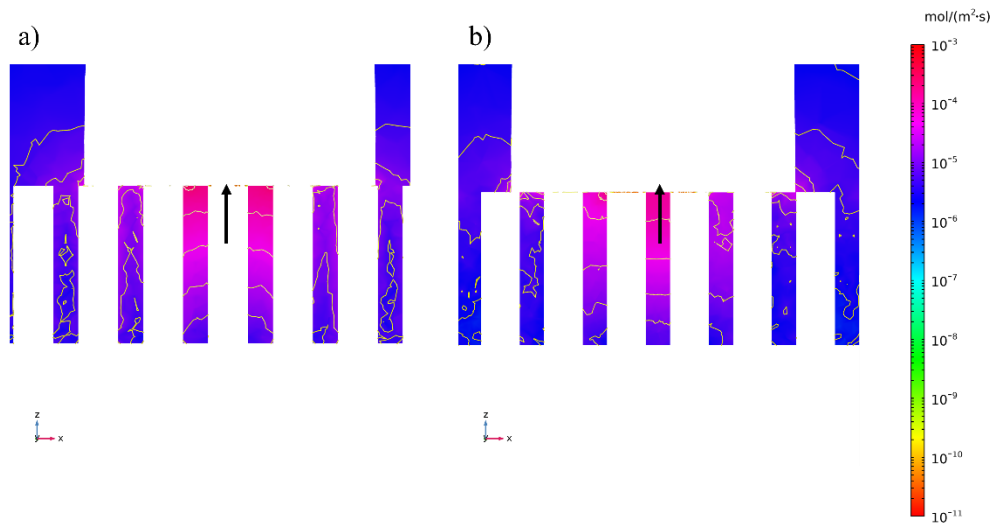


Figure B.6. Differences in diffusive flux visualized within HF-1 substrate at a normalized tip-substrate distance, $L = 0.008$ for pillar size, $w_T = 10 \mu\text{m}$ when the microelectrode center is positioned a) above the pillar and b) above the pore (Black arrows indicate the microelectrode centre)

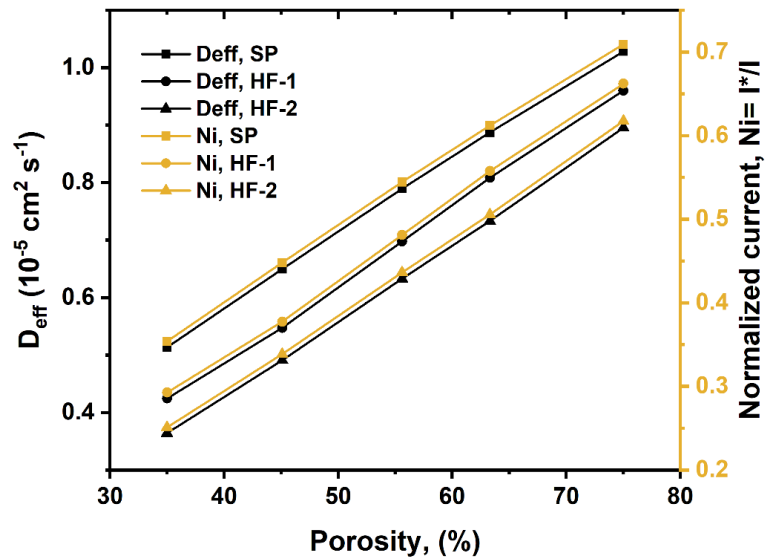


Figure B.7. Shows the calculated effective diffusion coefficients for all modeled substrates from the normalized currents when the microelectrode is positioned at a normalized tip-substrate distance, $L = 0.008$

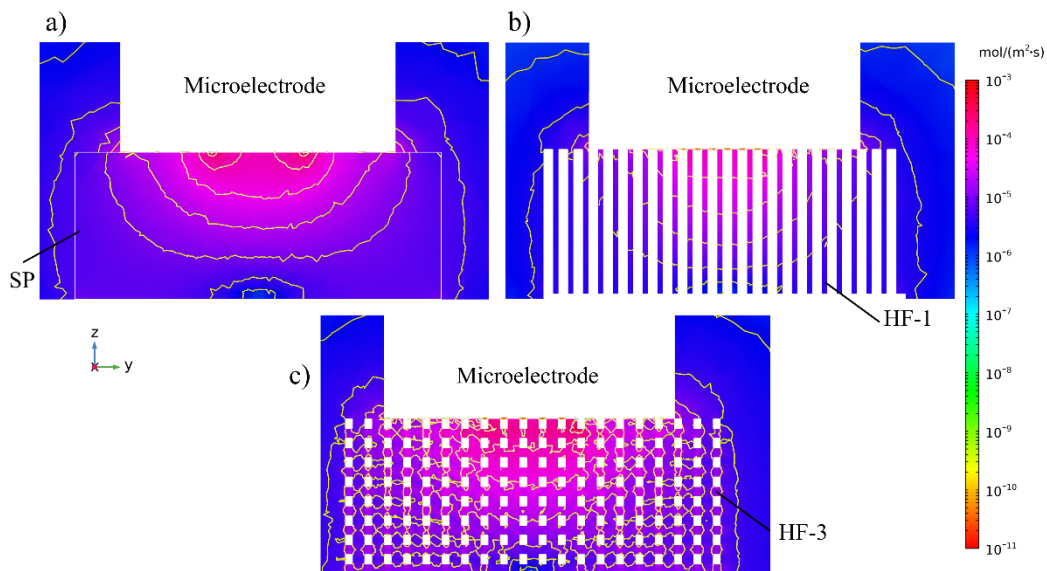


Figure B.8. Diffusive flux visualization in a) SP, b) HF-1, and c) HF-2 substrates with $h=40 \mu\text{m}$, $\varepsilon=63.3\%$, $\text{RG}=3$

APPENDIX C

SUPPORTING INFORMATION TO INVESTIGATING THE IMPACT OF SURFACE ROUGHNESS ON MASS TRANSPORT IN POROUS SUBSTRATES

This appendix discusses the simulation steps adopted for building the 3D COMSOL model used in Chapter V.

C.1. SECM: 3D COMSOL Simulation

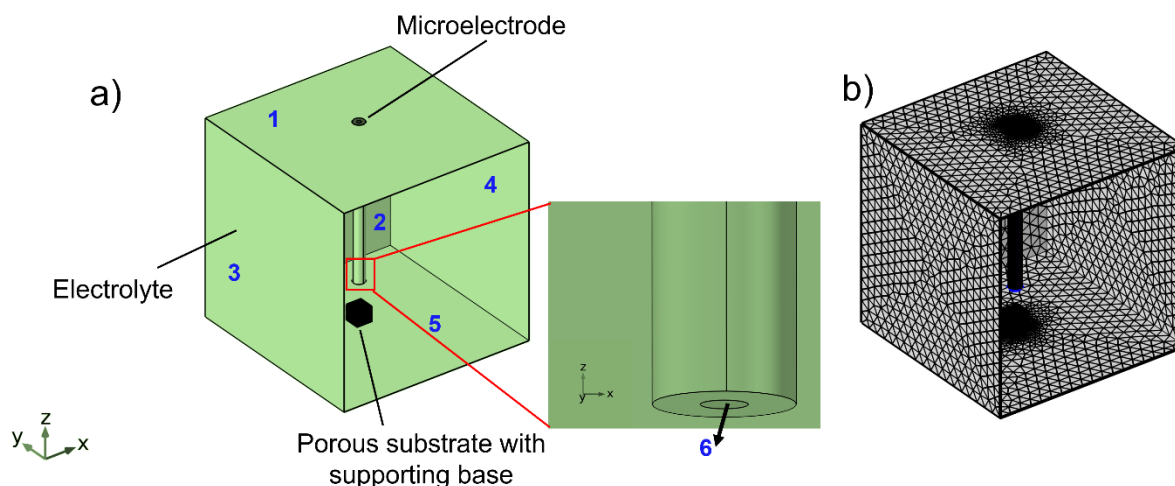


Figure C.1. a) Model geometry with domains (boundaries of electrolyte (1-5), and microelectrode (6), and b) with tetrahedral mesh

Using COMSOL Multiphysics 6.2, the irreversible oxidation of anthracene (An) was simulated at the SECM microelectrode surface to study the transport through high-fidelity porous structures with smooth and rough surfaces. Firstly, the model parameters (**Table 5.2**) were defined as given in Chapter V. Subsequently, the model geometry was constructed that represents the SECM probing of anthracene transport through porous substrates. As such, the geometry consists of three domains: 1) microelectrode, 2) electrolyte, and 3) porous substrate. The size of these domains was given in the methods section of Chapter V. After building the geometry, the appropriate governing equation has to be selected from ‘Physics.’ In this research, the physics

used was the Transport of Diluted Species in Porous Media (TDS), to model the transport of anthracene through porous substrates.

By using the TDS physics, we can describe the total mass transport of anthracene with the Nernst-Planck equation, which includes diffusion, migration, and convection terms in 3D as follows:

$$J_{An} = -D_{An}\nabla C_{An} - \frac{z_{An}F}{RT}D_{An}C_{An}\nabla\phi + v C_{An} \quad \text{Eq. (C.1)}$$

Where J_{An} represents the flux, D_{An} the diffusion coefficient, ∇C_{An} the concentration gradient, C_{An} the concentration of anthracene, z_{An} the dimensionless charge, F is the Faraday constant (96485 C mol⁻¹), R is the gas constant (8.314 Jmol⁻¹K⁻¹), T is the temperature (298K), $\nabla\phi$ the electrostatic potential gradient, and v the solution velocity.

A study was carried out to analyze the Nernst Planck equation in three dimensions under steady-state conditions. In this context, the mass transport contribution from diffusion was only taken into account. Typically, the effect of migration is negligible as SECM involves the use of a large amount of supporting electrolyte. Additionally, the microelectrode approaches the substrate at a low speed without disrupting the solution, minimizing the impact of convection. As a result, the general form of the Nernst-Planck equation (equation (C.1)) is simplified to Fick's first law, which is solely based on diffusion. This is expressed as:

$$J_{An} = -D_{An}\nabla C_{An} \quad \text{Eq. (C.2)}$$

A localized concentration gradient between the electrode-electrolyte interface is generated as the anthracene get oxidized at the microelectrode surface. When the microelectrode reaches the surface of the porous substrates, the anthracene oxidation at the microelectrode is determined by the anthracene diffusivity within the substrate, depending on the porosity (ϵ) and tortuosity (τ) of the substrate. This constitutes a flux,

$$J_{An} = -\frac{\varepsilon}{\tau} D_{An} \nabla C_{An} \quad \text{Eq. (C.3)}$$

For establishing the diffusion exclusively depending on the high-fidelity porous structure, the porosity (ε), and tortuosity (τ) were assigned a value of *one* in the COMSOL model.

C.2. Boundary Conditions

- 1) For surface boundaries of the porous substrate, supporting base, glass sheath, and at boundary 5 of the electrolyte, a no flux boundary condition was applied.
- 2) A concentration, $C_{An} = 2 \text{ mM}$ was applied to all electrolyte boundaries (1-4) (**Figure C.1a**)
- 3) As the kinetics of anthracene is irreversible, the flux at the microelectrode (boundary 6 in **Figure C.1a**) depends only on the forward rate constant, κ_f and is given by,

$$J_{An} = -[(\kappa_f \times C_{An})] \quad \text{Eq. (C.4)}$$

Where $\kappa_f = \kappa^0 \exp\left[\frac{(1-\alpha)nF\eta}{RT}\right]$

C.3. Meshing

The differential equations were solved by discretizing the model geometry into mesh or finite elements. A free tetrahedral mesh was used in this finite element simulation study (**Figure C.1b**). An increased mesh density was applied to microelectrode tip, glass sheath, and porous substrate regimes where a significant concentration change occurs (**Table C.1**). A *finer* built-in mesh was applied to the remaining geometry (bulk solution).

| Domain | | Max: element size (μm) | Min: element size (μm) | Max: element growth rate | Curvature factor | Resolution |
|---------------------|--------|------------------------------|------------------------------|--------------------------------|---------------------|------------|
| Microelectrode | | 0.09 | 0.05 | 1.4 | 0.4 | 0.7 |
| Porous substrate | Smooth | 2 | 0.25 | 1.4 | 0.4 | 0.7 |
| | Rough | 2 | 0.15 | 1.4 | 0.4 | 0.7 |
| Glass sheath | Smooth | 68.8 | 5 | 1.4 | 0.4 | 0.7 |
| | Rough | 68.8 | 3 | 1.4 | 0.4 | 0.7 |
| Electrolyte | Smooth | 68.8 | 5 | 1.4 | 0.4 | 0.7 |
| | Rough | 68.8 | 3 | 1.4 | 0.4 | 0.7 |

Table C.1. Shows the meshing parameters used in the model

C.4. Calculating the Current

At each simulated tip-substrate distance, integrating the total normal concentration flux across the microelectrode surface area (A) provides the current at the tip (boundary 6 in **Figure C1a**).

$$I = nFD \int_0^A \left[\frac{\partial C_{An}}{\partial z} \right]_{z=0} dA \quad \text{Eq. (C.5)}$$

Where $\left(\frac{\partial C_{An}}{\partial z}\right)$ is the concentration gradient along the z-direction of the microelectrode and $z = 0$ refers to the microelectrode/electrolyte interface.

For the approach curve simulation, the current was normalized to the current obtained at the bulk, and the tip-distance distance was normalized to the microelectrode radius. Here we are particularly interested in the ratio (*i.e.*, normalized current (Ni)) of the currents formed near the substrate (I^*) and at the bulk electrolyte (I).

$$Ni = \frac{I^*}{I} \quad \text{Eq. (C.6)}$$

APPENDIX D

DEVELOPING GALLIUM-COATED MICROELECTRODE FOR LITHIUM-ION DETECTION IN SOLUTION

This appendix summarizes the efforts of developing a gallium-coated microelectrode for detecting lithium (Li^+) ions in electrolyte solution. Although much effort has been undertaken for this project, the results received are not satisfactory for detecting Li^+ ions in electrolytes with different concentrations. However, we expect this appendix may be a reference for future researchers when trying to develop liquid microelectrodes. This appendix mainly includes the challenges we faced and the possible efforts to solve them.

D.1. Introduction

Microelectrodes (ME) are the critical component of scanning electrochemical microscopy (SECM). While the microelectrode size is important for achieving high resolution, the choice of microelectrode composition and shape is also crucial for the suitable application of SECM in various fields including energy storage, electrocatalysis, corrosion, biomedical research, *etc.* (Polcari *et al.*, 2016).

One of the most popular liquid metal-based probes is the mercury (Hg)-based ME due to its ability to monitor simultaneously the redox and ionic reactivity in complex systems (Barton et Rodríguez-López, 2014). Moreover, the liquid nature of these probes offers unique properties such as flexible probe geometry and improved contact with substrates having rough or irregular surfaces. This leads to a significant advancement in the field of SECM, especially in the ion detection studies of alkali metal ions including Li^+ , Na^+ , and K^+ (Barton et Rodríguez-López, 2014, 2017). For instance, a mercury (Hg)-sphere capped ME was developed for the Li^+ ion quantification in non-aqueous solutions (Barton et Rodríguez-López, 2014). This study also demonstrated that the amalgamation of lithium at the probe can be used to determine the probe-substrate distance. Although Hg-based probes have several advantages, one of the greatest drawbacks of this probe is the toxicity of mercury, which demands special handling requirements and safe disposal procedures. This necessitates of a liquid metal-based ME that is less toxic, easy

to handle, and environmentally friendly compared to Hg-based probes if the probe is to be used extensively outside a narrow community of academic researchers. As such, gallium (Ga) is a good alternative to Hg, as it meets the previous requirements and possesses a melting point of 29.68 °C. Therefore, in this work, our objective was to develop a Ga-coated platinum ME capable of detecting Li⁺ ions from a non-aqueous liquid electrolyte solution. With the help of cyclic voltammetry, the plating and stripping of Li⁺ ions from this probe were investigated.

D.2. Experimental Methods

D.2.1. Fabrication of platinum (Pt) microelectrodes

Pt MEs were fabricated first following a reported procedure (Danis *et al.*, 2015). Using a P-2000 laser puller (Sutter Instrument Co.), the soda lime capillaries were pulled into two pipettes with the program: Heat=240, Fil=5, Vel=60, Del=140, Pull=70. Then a 1 cm long Pt wire (25 μm diameter, 99.99% purity, Goodfellow) was inserted into the tip of the pulled pipettes and sealed the tip using the heating coil with the other end of the pipette connected to the vacuum. Later a copper wire of 10 cm in length with the conductive silver epoxy (EPO-TEK® H20E, Epoxy Technology) was used to create a connection to the Pt wire. The final assembly was completed by soldering a gold pin to the end of the copper wire. Later, the assembled microelectrode was kept under 120 °C for 10 min to cure the silver epoxy and was polished using SiC grinding paper with grit P320 and P1200 to get an RG of 2.5. Before coating gallium, MEs were cleaned with nanopure water using sonication.

D.2.2. Coating Pt ME with gallium

The following is a representative example of the probe fabrication procedure.

The liquid gallium (Sigma Aldrich, 99.99%) was stored in a 50 °C oven before use. The gallium was then transferred to a borosilicate capillary (1.2 mm o.d., 0.69 mm i.d., filamented, Sutter Instrument Co.) and placed into the coating setup consisting of a heater with the temperature set at 45 °C (**Figure D.1**). With the help of the dinolite camera (Dino-Lite Pro-AM411T, Microscope.com), Pt ME was aligned on top of the gallium containing capillary and successfully coated with gallium. After imaging the Ga-coated Pt ME using an optical microscope (Nikon Eclipse 50i), it was transferred immediately into the Argon-filled glove box (H₂O < 1ppm, O₂ <

1ppm) for measurements using an ELProscan 3 system (HEKA, Lambrecht/Pfalz, Germany; potentiostat model, PG340).

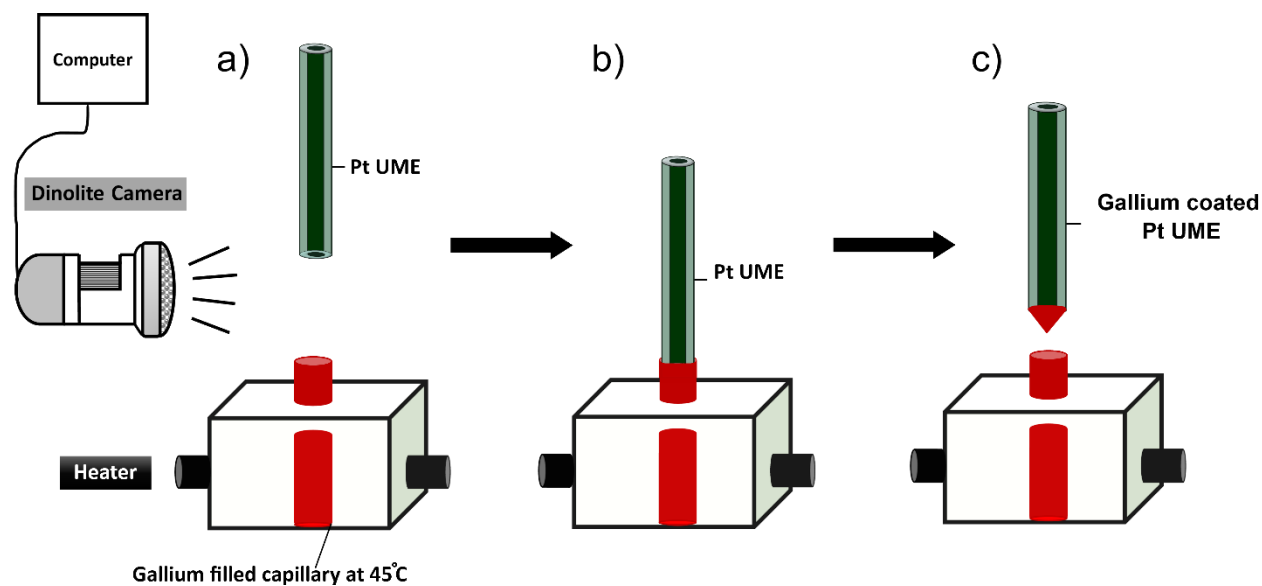


Figure D.1. Steps in the fabrication of gallium microelectrode

D.2.3. Experimental setup

The experimental setup consists of a two-electrode configuration, where Ga-coated ME acts as the working electrode and a $\text{Li}_{(1-x)}\text{FePO}_4$ film (thickness= 55 μm) as the quasi-reference counter electrode (**Figure D.2**). Detailed information regarding the preparation of delithiated $\text{Li}_{(1-x)}\text{FePO}_4$ and the slurry fabrication was provided in Chapter 3. The experimental setup also has a heater and a dinolite camera (Dino-Lite AM73915MT8, Dunwell Tech) attached near the quartz vial containing the electrolyte. The electrolyte is lithium hexafluorophosphate (LiPF_6 , $\geq 99.99\%$ battery grade, Sigma Aldrich) in a 50:50 volume ratio of ethylene carbonate (EC, Gotion) and dimethyl carbonate (DMC, Sigma Aldrich). Cyclic voltammetry measurements were performed at a scan rate of 50 mVs^{-1} for plating and stripping lithium ions. All the potentials mentioned in this work are relative to $\text{Li}_{(1-x)}\text{FePO}_4$.

X-ray diffraction (XRD) was carried out for a Ga-coated Pt macroelectrode after performing the electrochemistry inside the glove box. With the help of a diffractometer (XRD, Bruker D8

Advance) with copper $K\alpha$ radiation, the crystal structure was analyzed for 2θ ranging from 15 to 60 degrees.

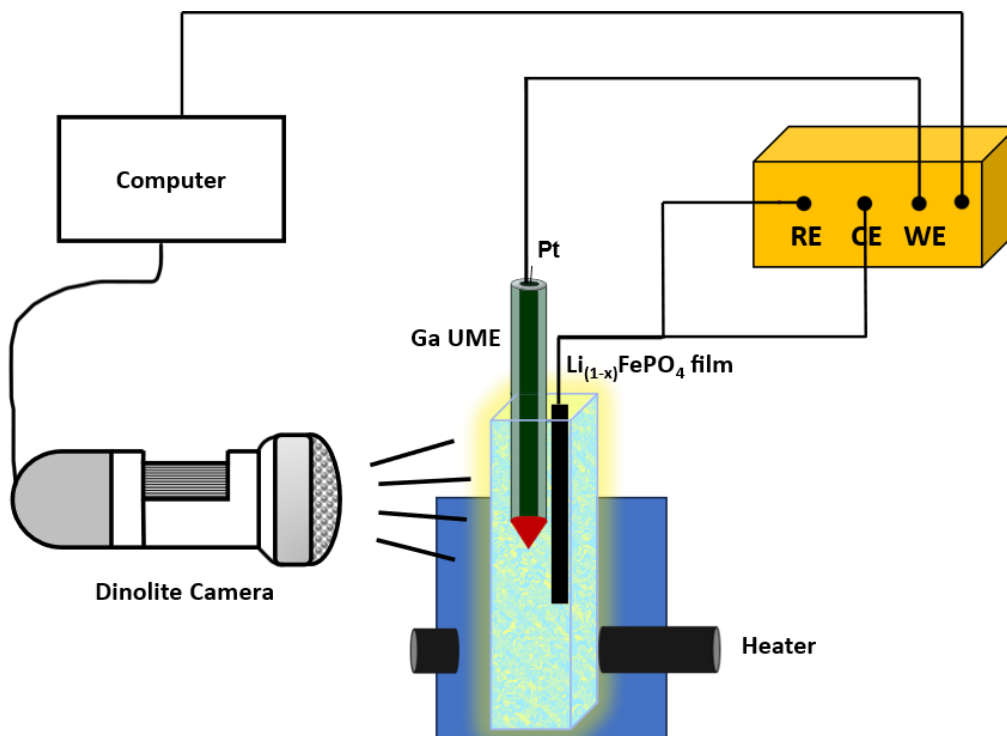


Figure D.2. Schematic of the experimental setup with Ga-coated ME as working electrode and partially delithiated $\text{Li}_{(1-x)}\text{FePO}_4$ film as quasi-reference counter electrode

D.3. Results and Discussion

All the fabricated Ga-coated MEs have a conical tip when imaged outside the glove box (**Figure D.3a**). However, the small perturbations in the antechamber of the glove box as well as their immersion in liquid electrolyte can affect this conical shape, as demonstrated by the dinolite images (**Figure D.3b**).

The liquid gallium readily forms a thin layer of oxides (in the order of nanometer) when exposed to oxygen ($>1\text{ppm}$) (Daeneke *et al.*, 2018 ; Syed *et al.*, 2019). To remove these gallium oxides (Ga_2O_3) from the gallium ME surface, cyclic voltammetry was carried out between -1 V and -2.55 V vs $\text{Li}_{(1-x)}\text{FePO}_4$ for 6 cycles in a 0.1 M LiPF_6 in EC: DMC electrolyte at room temperature (29°C) (**Figure D.3c**). The initial cycle for the negative potential scan showed a peak at -1.85 V

corresponding to the reduction of gallium oxide. After cycle 1, there is no peak formation, which indicates the effective removal of oxide layers from the Ga-coated ME. Moreover, the current in the negative direction at potential -2.55 V keeps decreasing over the cycles, possibly due to the changes in the gallium surface. This procedure was conducted for all the tested Ga-coated MEs and macroelectrodes used in this study.

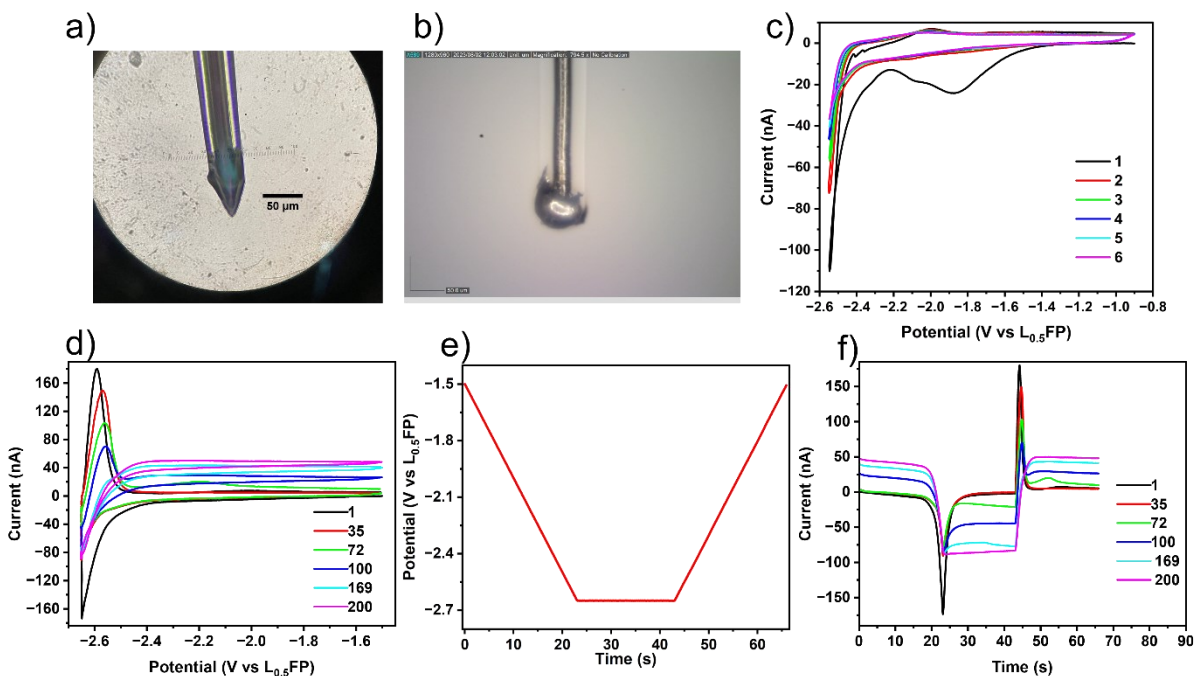


Figure D.3. a) Optical microscopy images of Ga-coated ME taken outside glove box, b) camera images of Ga-coated ME immersed in electrolyte taken inside the glove box, c) cyclic voltammogram for surface activation of Ga-coated ME, d) cyclic voltammogram during plating and stripping of Li^+ ions at 50 mVs^{-1} , e) the corresponding potential vs time plot, and f) current vs time plot

After removing the gallium oxides, the plating and stripping of Li^+ ions were conducted for 200 cycles to test the stability of the Ga-coated ME (**Figure D.3d**). In this study, a minimum potential (-2.65 V) for Li^+ ion plating was used to avoid the formation of multiple solid gallium-lithium alloy phases (Deshpande *et al.*, 2011). First, the Li^+ ion was plated onto Ga-coated ME by scanning the potential from -1.5 V to -2.65 V (**Figure D.3e**). Then the ME potential was held at -2.65 V for 20 s. During the initial cycles, this helps the plating current to reach zero and

promotes the gallium-lithium alloy formed at the ME to reach equilibrium. However, over time, the current behavior at this constant potential regime changes.

Upon reversing the scan direction, a sharp peak formation was observed at -2.6 V, corresponding to Li^+ stripping from the ME (**Figure D.3d**). Over the cycles, the current decreased at the plating potential of -2.65 V, and similarly, the stripping current was also reduced, indicating the instability of the gallium microelectrode. This instability stems from the difficulty of Ga-coated ME to release completely the previously plated Li^+ ions. We speculate that the Li^+ ions are either consumed in a parasitic reaction or remain in the Ga-coated ME as a solid lithium-gallium alloy. To gain a better understanding of the potential solid alloys that could form at the Ga-coated ME, it is important to analyze the phase diagram of Ga-Li systems. The phase diagram indicates that above 17.6 atomic % of Li into Ga, multiple solid alloys such as $\text{Li}_3\text{Ga}_{14}$, Li_2Ga_7 , *etc.* can form (Azza *et al.*, 2017). Additionally, a previous study showed the formation of Li_2Ga_7 alloy based on X-ray diffraction data of the Ga-Li coin cells at the minimum plating potential of -2.65 V (Deshpande *et al.*, 2011). Based on the reported studies, we expect the formation of these solid alloys over the cycles.

Another important observation in this study was the sudden change in the current behavior during the constant potential regime at cycle 72 (**Figure D.3f**). This is possibly an indication of the beginning of a nucleation process within Ga-coated ME. After cycle 72, the Li^+ stripping peak decreased rapidly, and eventually, the peak disappeared. This suggests that the continuous addition of Li_2Ga_7 alloy into the Ga-coated ME after each cycle may have resulted in more solid phases, isolating the liquid gallium core from further plating reactions with the electrolyte.

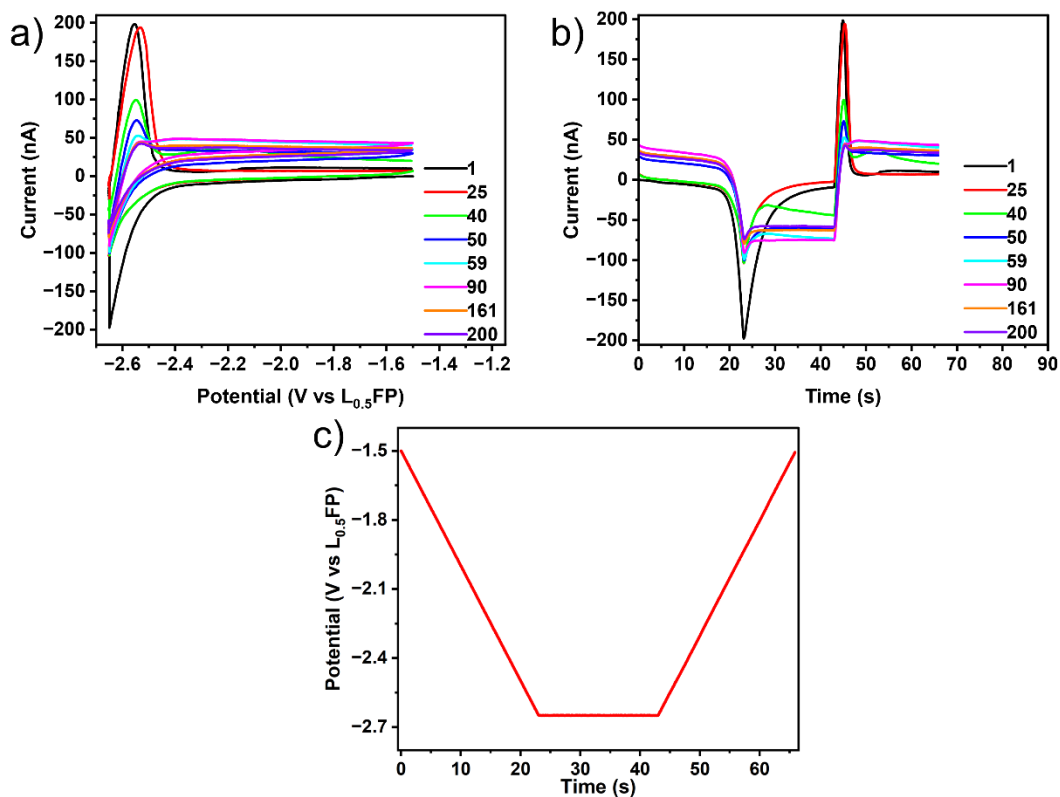


Figure D.4. a) Cyclic voltammogram during plating and stripping of Li⁺ ions at 50 mVs⁻¹, b) the corresponding current vs time plot, and c) potential vs time plot at 40 °C

A similar voltammetry procedure was conducted with other Ga-coated ME by heating the electrolyte to 40 °C to investigate the influence of temperature on the plating and stripping process (**Figure D.4**). The trend of plating and stripping current is similar to the experiment conducted at room temperature. However, a sharp decrease in current was observed earlier *i.e.*, at cycle 40. The analysis of the corresponding current-time plot demonstrated the variation in current behavior at cycle 40 from previous cycles at the constant plating potential regime. Finally, the Li⁺ stripping peak disappeared. This underscores our previous hypothesis (**Figure D.3e**) of nucleation sites within gallium ME, which causes the liquid gallium core isolation. As temperature facilitates the diffusion of Li⁺ ions, this nucleation state can be achieved faster compared to the room temperature measurements. As a result, further measurements were conducted at room temperature to decrease the rate of nucleation.

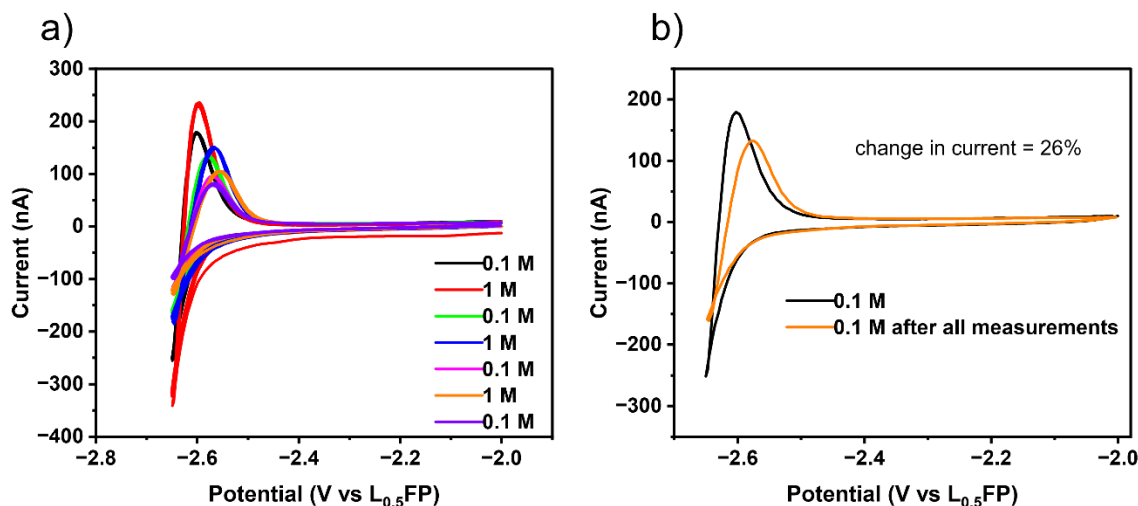


Figure D.5. a) Cyclic voltammogram of gallium tip with different concentrations of LiPF₆ in EC: DMC, and b) Variation of current at the gallium tip for the 0.1 M electrolyte before and after testing different concentrations, scan rate= 50 mVs⁻¹

To assess the instability of the Ga-coated ME, we studied its electrochemical behavior using two different concentrations of the LiPF₆ in EC: DMC electrolyte (**Figure D.5a**). Initially, the gallium ME was tested in 0.1 M solution by scanning the potential from -2 V to -2.65 V and back. Subsequently, the same ME was tested with a 1 M solution. This process was repeated three times, and the plating and stripping current for the 0.1 M was tested again. During this procedure, an increase in stripping peak current from 180 nA to 233 nA was observed when switching from the 0.1 M to 1 M solution. However, comparing the initial current observed for the 0.1 M solution with the third dataset demonstrated a decrease in current as well as a shift in peak current. A similar trend was seen in the case of 1 M solution. These results demonstrate the challenge of effectively quantifying Li⁺ ions in various concentrated solutions using Ga-coated ME. Moreover, the difference in stripping peak current obtained for the 0.1 M solution between the initial and final data set is nearly 26% (**Figure D.5a**), which indicates that the surface of Ga-coated ME was not adequately healing after each plating and stripping cycle, resulting in the loss

of its original metallic liquid surface properties. Therefore, we need to focus on the surface chemistry of gallium during the plating and stripping reactions.

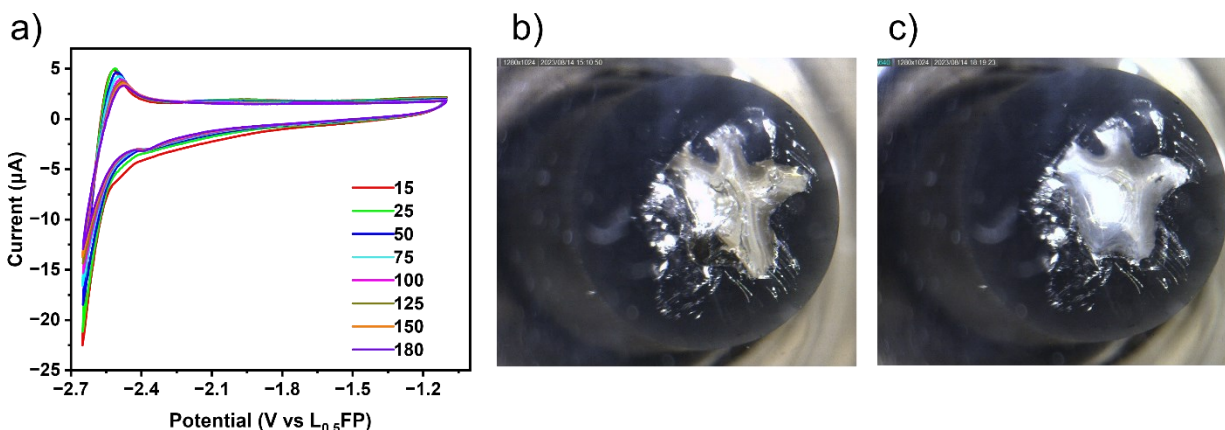


Figure D.6. a) Cyclic voltammogram of Ga-coated macroelectrode during plating and stripping of Li^+ ions in 0.1 M LiPF_6 electrolyte at 50 mVs^{-1} , dinolite camera images of Ga-coated macroelectrode b) before and c) after 180 cycles

The changes occurring at the gallium surface during plating and stripping on an ME are quite challenging to observe as the amount of gallium at the ME tip is limited. Therefore, to further investigate the variation of the Ga-coated ME surface, a Pt macroelectrode was coated with gallium. The larger size of the macroelectrode in comparison to the ME resulted in a larger amount of gallium on the macroelectrode surface. As a result, during the cyclic voltammetry, a current in the range of μA was observed compared to the nA currents observed in the case of ME (**Figure D.6a**). Here, the potential was swept to -2.65 V for plating Li^+ ions to Ga macroelectrode, and the stripping was performed by reversing the potential scan for 180 cycles. Although a significant change in current was not observed, it is worth noting that the stripping and plating current gradually decreased, indicating that as the size of the gallium surface is increased, the nucleation takes longer time to contribute to a noticeable change in current. The optical images of Ga macroelectrode before and after 180 cycles displayed the surface changes of gallium during the cycling (**Figure D.6b, c**). The ME image after 180 cycles showed a matte surface due to the presence of lithium remaining on the gallium surface even after the stripping procedure.

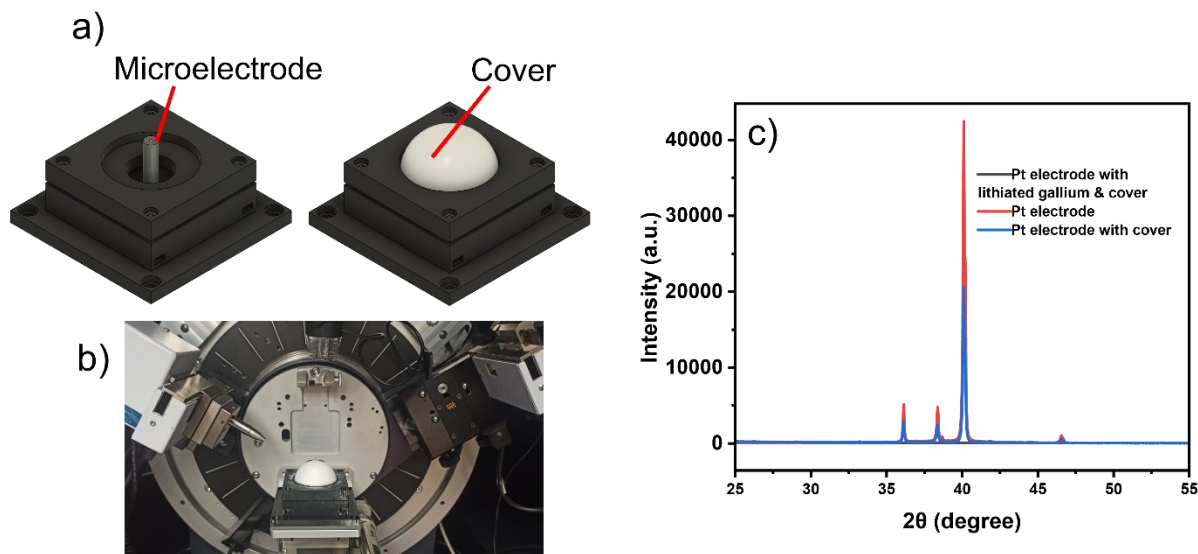


Figure D.7. a) Schematic of X-ray diffraction sample holder containing microelectrode with and without air-tight cover, b) sample holder in the diffraction set up, and c) comparison of XRD of the sample holder and Ga-coated ME containing lithium-gallium alloy

Another effort has been undertaken to understand the lithium-gallium alloy formation occurring on the surface of Ga-coated macroelectrode. Due to the air-sensitivity of the samples, performing XRD measurements posed a challenge. To address this, we designed a custom sample holder to enable XRD measurements on the macroelectrode containing lithium-gallium alloys (**Figure D.7a**). Before measuring the macroelectrode with gallium-lithium alloy, the sample holder was tested using the X-ray diffractometer (**Figure D.7b**) to examine its contribution to the diffractogram. The first XRD measurement was conducted on the Pt macroelectrode by placing it on the sample holder without the air-tight cover. Subsequently it was tested with the cover. The diffractogram shows three peaks corresponding to the Pt metal (**Figure D.7c**). The peak intensities decreased during the XRD measurements with the air-tight cover. Given the successful measurement of sample holder with XRD, we proceeded with diffraction measurements of the Ga-coated macroelectrode immediately after performing the plating and stripping of Li^+ ions. Despite multiple attempts, no peaks corresponding to lithium-gallium alloys were observed (**Figure D.7c**). This suggests that a sufficient amount of solid crystalline alloy was not formed within the gallium macroelectrode to be detectable by the X-rays.

D.4. Conclusion

In this study, a Ga-coated ME was fabricated through controlled immersion into a gallium reservoir. The resulting Ga-coated microelectrodes demonstrated the capability to detect Li^+ ions in a liquid electrolyte. However, the reliability of *quantifying* Li^+ ions in different electrolyte concentrations is questionable due to the poor self-healing of gallium during extended measurements. We have observed a significant variation in the stripping peak current over time, indicating changes in the surface properties of liquid gallium metal. Additionally, the abrupt decrease in peak current suggests the blockage of the liquid gallium surface by the formation of solid lithium-gallium alloys over time. The Ga macroelectrode demonstrated the retention of lithium on the gallium surface even after the stripping process. As a result, the application of Ga-coated ME for liquid electrolytes is limited or unsuitable. We anticipate that this study could serve as a reference point for future research related to the lithium-gallium system.

BIBLIOGRAPHY

- Amin, R., Delattre, B., Tomsia, A. P. et Chiang, Y.-M. (2018). Electrochemical Characterization of High Energy Density Graphite Electrodes Made by Freeze-Casting. *ACS Applied Energy Materials*, 1(9), 4976-4981. <https://doi.org/10.1021/acsaem.8b00962>
- Amphlett, J. L. et Denuault, G. (1998). Scanning Electrochemical Microscopy (SECM): An Investigation of the Effects of Tip Geometry on Amperometric Tip Response. *The Journal of Physical Chemistry B*, 102(49), 9946-9951. <https://doi.org/10.1021/jp982829u>
- Andre, D., Meiler, M., Steiner, K., Wimmer, Ch., Soczka-Guth, T. et Sauer, D. U. (2011). Characterization of high-power lithium-ion batteries by electrochemical impedance spectroscopy. I. Experimental investigation. *Journal of Power Sources*, 196(12), 5334-5341. <https://doi.org/10.1016/j.jpowsour.2010.12.102>
- Antartis, D., Dillon, S. et Chasiotis, I. (2015). Effect of porosity on electrochemical and mechanical properties of composite Li-ion anodes. *Journal of Composite Materials*, 49(15), 1849-1862. <https://doi.org/10.1177/0021998314568653>
- Aurbach, D., Levi, M. D., Levi, E., Teller, H., Markovsky, B., Salitra, G., Heider, U. et Heider, L. (1998). Common Electroanalytical Behavior of Li Intercalation Processes into Graphite and Transition Metal Oxides. *Journal of The Electrochemical Society*, 145(9), 3024. <https://doi.org/10.1149/1.1838758>
- Azza, H., Selhaoui, N., Iddaoudi, A. et Bouriden, L. (2017). Thermodynamic Reassessment of the Gallium–Lithium Phase Diagram. *Journal of Phase Equilibria and Diffusion*, 38(5), 788-795. <https://doi.org/10.1007/s11669-017-0567-2>
- Bard, A. J., Denuault, Guy., Friesner, R. A., Dornblaser, B. C. et Tuckerman, L. S. (1991a). Scanning electrochemical microscopy: theory and application of the transient (chronoamperometric) SECM response. *Analytical Chemistry*, 63(13), 1282-1288. <https://doi.org/10.1021/ac00013a019>
- Bard, A. J., Fan, F. R. F., Kwak, Juhyoun. et Lev, Ovidia. (1989). Scanning electrochemical microscopy. Introduction and principles. *Analytical Chemistry*, 61(2), 132-138. <https://doi.org/10.1021/ac00177a011>
- Bard, A. J., Fan, F.-R. F., Pierce, D. T., Unwin, P. R., Wipf, D. O. et Zhou, F. (1991b). Chemical Imaging of Surfaces with the Scanning Electrochemical Microscope. *Science*, 254(5028), 68-74. <https://doi.org/10.1126/science.254.5028.68>
- Bard, A. J. et Faulkner, L. R. (2000). *Electrochemical Methods: Fundamentals and Applications* (2nd Edition). Wiley. <https://www.wiley.com/en-us/Electrochemical+Methods%3A+Fundamentals+and+Applications%2C+2nd+Edition-p-9780471043720>

- Bard, A. J., Mirkin, M. V., Unwin, P. R. et Wipf, D. O. (1992). Scanning electrochemical microscopy. 12. Theory and experiment of the feedback mode with finite heterogeneous electron-transfer kinetics and arbitrary substrate size. *The Journal of Physical Chemistry*, 96(4), 1861-1868. <https://doi.org/10.1021/j100183a064>
- Barton, Z. J. et Rodríguez-López, J. (2014). Lithium Ion Quantification Using Mercury Amalgams as in Situ Electrochemical Probes in Nonaqueous Media. *Analytical Chemistry*, 86(21), 10660-10667. <https://doi.org/10.1021/ac502517b>
- Barton, Z. J. et Rodríguez-López, J. (2017). Fabrication and Demonstration of Mercury Disc-Well Probes for Stripping-Based Cyclic Voltammetry Scanning Electrochemical Microscopy. *Analytical Chemistry*, 89(5), 2716-2723. <https://doi.org/10.1021/acs.analchem.6b04022>
- Bath, B. D., Lee, R. D., White, H. S. et Scott, E. R. (1998). Imaging Molecular Transport in Porous Membranes. Observation and Analysis of Electroosmotic Flow in Individual Pores Using the Scanning Electrochemical Microscope. *Analytical Chemistry*, 70(6), 1047-1058. <https://doi.org/10.1021/ac971213i>
- Ben Jadi, S., El Guerraf, A., Kiss, A., El Azrak, A., Bazzaoui, E. A., Wang, R., Martins, J. I. et Bazzaoui, M. (2020). Analyses of scanning electrochemical microscopy and electrochemical impedance spectroscopy in direct methanol fuel cells: permeability resistance and proton conductivity of polyaniline modified membrane. *Journal of Solid State Electrochemistry*, 24(7), 1551-1565. <https://doi.org/10.1007/s10008-020-04659-2>
- Bhushan, B. et Fuchs, H. (dir.). (2006). *Applied Scanning Probe Methods II: Scanning Probe Microscopy Techniques* (1^{re} éd.). Springer-Verlag. <https://doi.org/10.1007/b139097>
- Billaud, J., Bouville, F., Magrini, T., Villevieille, C. et Studart, A. R. (2016). Magnetically aligned graphite electrodes for high-rate performance Li-ion batteries. *Nature Energy*, 1(8), 1-6. <https://doi.org/10.1038/nenergy.2016.97>
- Boyce, A. M., Lu, X., Brett, D. J. L. et Shearing, P. R. (2022). Exploring the influence of porosity and thickness on lithium-ion battery electrodes using an image-based model. *Journal of Power Sources*, 542, 231779. <https://doi.org/10.1016/j.jpowsour.2022.231779>
- Bruggeman, D. A. G. (1935). Berechnung verschiedener physikalischer Konstanten von heterogenen Substanzen. I. Dielektrizitätskonstanten und Leitfähigkeiten der Mischkörper aus isotropen Substanzen. *Annalen der Physik*, 416(7), 636-664. <https://doi.org/10.1002/andp.19354160705>
- Bülter, H., Peters, F., Schwenzel, J. et Wittstock, G. (2014). Spatiotemporal Changes of the Solid Electrolyte Interphase in Lithium-Ion Batteries Detected by Scanning Electrochemical Microscopy. *Angewandte Chemie International Edition*, 53(39), 10531-10535. <https://doi.org/10.1002/anie.201403935>

- Bülter, H., Peters, F., Schwenzel, J. et Wittstock, G. (2015a). Investigation of Electron Transfer Properties of the SEI on Metallic Lithium Electrodes by SECM at Open Circuit. *ECS Transactions*, 66(9), 69. <https://doi.org/10.1149/06609.0069ecst>
- Bülter, H., Peters, F. et Wittstock, G. (2016). Scanning Electrochemical Microscopy for the In Situ Characterization of Solid–Electrolyte Interphases: Highly Oriented Pyrolytic Graphite versus Graphite Composite. *Energy Technology*, 4(12), 1486-1494. <https://doi.org/10.1002/ente.201600071>
- Bülter, H., Sternad, M., Sardinha, E. dos S., Witt, J., Dosche, C., Wilkening, M. et Wittstock, G. (2015b). Investigation of the Electron Transfer at Si Electrodes: Impact and Removal of the Native SiO₂ Layer. *Journal of The Electrochemical Society*, 163(3), A504. <https://doi.org/10.1149/2.0731603jes>
- Cabañero, M. A., Boaretto, N., Röder, M., Müller, J., Kallo, J. et Latz, A. (2018). Direct Determination of Diffusion Coefficients in Commercial Li-Ion Batteries. *Journal of The Electrochemical Society*, 165(5), A847. <https://doi.org/10.1149/2.0301805jes>
- Chen, B., Perry, D., Page, A., Kang, M. et Unwin, P. R. (2019a). Scanning Ion Conductance Microscopy: Quantitative Nanopipette Delivery–Substrate Electrode Collection Measurements and Mapping. *Analytical Chemistry*, 91(3), 2516-2524. <https://doi.org/10.1021/acs.analchem.8b05449>
- Chen, J. C.-M., Yang, J. et Cheng, M. M.-C. (2019b). Induced nanoscale roughness of current collectors enhances lithium ion battery performances. *Journal of Power Sources*, 430, 169-174. <https://doi.org/10.1016/j.jpowsour.2019.05.026>
- Chen, L., He, A., Zhao, J., Kang, Q., Li, Z.-Y., Carmeliet, J., Shikazono, N. et Tao, W.-Q. (2022). Pore-scale modeling of complex transport phenomena in porous media. *Progress in Energy and Combustion Science*, 88, 100968. <https://doi.org/10.1016/j.pecs.2021.100968>
- Chen, Z., Danilov, D. L., Raijmakers, L. H. J., Chayambuka, K., Jiang, M., Zhou, L., Zhou, J., Eichel, R.-A. et Notten, P. H. L. (2021). Overpotential analysis of graphite-based Li-ion batteries seen from a porous electrode modeling perspective. *Journal of Power Sources*, 509, 230345. <https://doi.org/10.1016/j.jpowsour.2021.230345>
- Cho, Y.-B., Lee, C. et Lee, Y. (2015). Study of Porosity-Dependent Oxygen Reduction at Porous Platinum Tips Using Scanning Electrochemical Microscopy. *Journal of The Electrochemical Society*, 162(10), H792. <https://doi.org/10.1149/2.0841510jes>
- Churikov, A. V., Ivanishchev, A. V., Ivanishcheva, I. A., Sycheva, V. O., Khasanova, N. R. et Antipov, E. V. (2010). Determination of lithium diffusion coefficient in LiFePO₄ electrode by galvanostatic and potentiostatic intermittent titration techniques. *Electrochimica Acta*, 55(8), 2939-2950. <https://doi.org/10.1016/j.electacta.2009.12.079>
- Clancy, T. M. et Rohan, J. F. (2018). Ultra-Fast Cycling of Nanoscale Thin-Film LiCoO₂ Electrodes in Aqueous Electrolytes. *ChemElectroChem*, 5(21), 3273-3278. <https://doi.org/10.1002/celec.201800822>

- Cornut, R., Lepage, D. et Schougaard, S. B. (2015). Interpreting Lithium Batteries Discharge Curves for Easy Identification of the Origin of Performance Limitations. *Electrochimica Acta*, 162, 271-274. <https://doi.org/10.1016/j.electacta.2014.11.035>
- Daeneke, T., Khoshmanesh, K., Mahmood, N., Castro, I. A. de, Esrafilzadeh, D., J. Barrow, S., D. Dickey, M. et Kalantar-zadeh, K. (2018). Liquid metals: fundamentals and applications in chemistry. *Chemical Society Reviews*, 47(11), 4073-4111. <https://doi.org/10.1039/C7CS00043J>
- Danis, L., Polcari, D., Kwan, A., Gateman, S. M. et Mauzeroll, J. (2015). Fabrication of Carbon, Gold, Platinum, Silver, and Mercury Ultramicroelectrodes with Controlled Geometry. *Analytical Chemistry*, 87(5), 2565-2569. <https://doi.org/10.1021/ac503767n>
- Danis, L., Snowden, M. E., Tefashe, U. M., Heinemann, C. N. et Mauzeroll, J. (2014). Development of Nano-Disc electrodes for Application as Shear Force Sensitive Electrochemical Probes. *Electrochimica Acta*, 136, 121-129. <https://doi.org/10.1016/j.electacta.2014.05.047>
- Dees, D. W., Kawauchi, S., Abraham, D. P. et Prakash, J. (2009). Analysis of the Galvanostatic Intermittent Titration Technique (GITT) as applied to a lithium-ion porous electrode. *Journal of Power Sources*, 189(1), 263-268. <https://doi.org/10.1016/j.jpowsour.2008.09.045>
- Deng, J., Bae, C., Denlinger, A. et Miller, T. (2020). Electric Vehicles Batteries: Requirements and Challenges. *Joule*, 4(3), 511-515. <https://doi.org/10.1016/j.joule.2020.01.013>
- Deshpande, R. D., Li, J., Cheng, Y.-T. et Verbrugge, M. W. (2011). Liquid Metal Alloys as Self-Healing Negative Electrodes for Lithium Ion Batteries. *Journal of The Electrochemical Society*, 158(8), A845. <https://doi.org/10.1149/1.3591094>
- Dey, M. K., Sahoo, P. K. et Satpati, A. K. (2017). Electrochemically deposited layered MnO₂ films for improved supercapacitor. *Journal of Electroanalytical Chemistry*, 788, 175-183. <https://doi.org/10.1016/j.jelechem.2017.01.063>
- Dobrzaniecka, A., Zeradjanin, A. R., Masa, J., Blicharska, M., Wintrich, D., Kulesza, P. J. et Schuhmann, W. (2016). Evaluation of kinetic constants on porous, non-noble catalyst layers for oxygen reduction—A comparative study between SECM and hydrodynamic methods. *Catalysis Today*, 262, 74-81. <https://doi.org/10.1016/j.cattod.2015.07.043>
- dos Santos Sardinha, E., Sternad, M., R. Wilkening, H. M. et Wittstock, G. (2019). Nascent SEI-Surface Films on Single Crystalline Silicon Investigated by Scanning Electrochemical Microscopy. *ACS Applied Energy Materials*, 2(2), 1388-1392. <https://doi.org/10.1021/acsaem.8b01967>
- DuBeshter, T., Sinha, P. K., Sakars, A., Fly, G. W. et Jorne, J. (2014). Measurement of Tortuosity and Porosity of Porous Battery Electrodes. *Journal of The Electrochemical Society*, 161(4), A599. <https://doi.org/10.1149/2.073404jes>

- Dufil, Y., Dietrich, M., Zigah, D., Favier, F., Sadki, S., Gentile, P. et Fontaine, O. (2023). Local Degradation of PEDOT:PSS on Silicon Nanostructures Using Scanning Electrochemical Microscopy. *Small*, 19(10), 2206789. <https://doi.org/10.1002/sml.202206789>
- Edwards, M. A., Williams, C. G., Whitworth, A. L. et Unwin, P. R. (2009). Scanning Ion Conductance Microscopy: a Model for Experimentally Realistic Conditions and Image Interpretation. *Analytical Chemistry*, 81(11), 4482-4492. <https://doi.org/10.1021/ac900376w>
- Eidenschink, J. et Matysik, F.-M. (2024). Simultaneous Scanning Ion Conductance and Electrochemical Microscopy in Lithium-Ion Battery Research. *ChemElectroChem*, 11(6), e202300577. <https://doi.org/10.1002/celec.202300577>
- Elango, R., Demortière, A., De Andrade, V., Morcrette, M. et Seznec, V. (2018). Thick Binder-Free Electrodes for Li-Ion Battery Fabricated Using Templating Approach and Spark Plasma Sintering Reveals High Areal Capacity. *Advanced Energy Materials*, 8(15), 1703031. <https://doi.org/10.1002/aenm.201703031>
- Engstrom, R. C. et Pharr, C. M. (1989). Scanning Electrochemical Microscopy. *Analytical Chemistry*, 61(19), 1099A - 1104. <https://doi.org/10.1021/ac00194a735>
- Fan, F. R. F., Mirkin, M. V. et Bard, A. J. (1994). Polymer Films on Electrodes. 25. Effect of Polymer Resistance on the Electrochemistry of Poly(vinylferrocene): Scanning Electrochemical Microscopic, Chronoamperometric, and Cyclic Voltammetric Studies. *The Journal of Physical Chemistry*, 98(5), 1475-1481. <https://doi.org/10.1021/j100056a018>
- Filice, F. P., Li, M. S. M., Henderson, J. D. et Ding, Z. (2015). Three-Dimensional Electrochemical Functionality of an Interdigitated Array Electrode by Scanning Electrochemical Microscopy. *The Journal of Physical Chemistry C*, 119(37), 21473-21482. <https://doi.org/10.1021/acs.jpcc.5b05568>
- Fong, K. D., Self, J., Diederichsen, K. M., Wood, B. M., McCloskey, B. D. et Persson, K. A. (2019). Ion Transport and the True Transference Number in Nonaqueous Polyelectrolyte Solutions for Lithium Ion Batteries. *ACS Central Science*, 5(7), 1250-1260. <https://doi.org/10.1021/acscentsci.9b00406>
- Fongy, C., Gaillot, A.-C., Jouanneau, S., Guyomard, D. et Lestriez, B. (2010). Ionic vs Electronic Power Limitations and Analysis of the Fraction of Wired Grains in LiFePO₄ Composite Electrodes. *Journal of the Electrochemical Society*, 157(7), A885-A891. <https://doi.org/10.1149/1.3432559>
- Franklin, G., Halim, E.-M., Merlet, C., Taberna, P.-L. et Simon, P. (2023). Insights into the effect of oxygen functional groups on the heterogeneous electron transfer at activated carbons from scanning electrochemical microscopy. *Electrochimica Acta*, 465, 142944. <https://doi.org/10.1016/j.electacta.2023.142944>

- Friedl, J. et Stimming, U. (2017). Determining Electron Transfer Kinetics at Porous Electrodes. *Electrochimica Acta*, 227, 235-245. <https://doi.org/10.1016/j.electacta.2017.01.010>
- Fu, K., Wang, Y., Yan, C., Yao, Y., Chen, Y., Dai, J., Lacey, S., Wang, Y., Wan, J., Li, T., Wang, Z., Xu, Y. et Hu, L. (2016). Graphene Oxide-Based Electrode Inks for 3D-Printed Lithium-Ion Batteries. *Advanced Materials*, 28(13), 2587-2594. <https://doi.org/10.1002/adma.201505391>
- Fu, K., Yao, Y., Dai, J. et Hu, L. (2017). Progress in 3D Printing of Carbon Materials for Energy-Related Applications. *Advanced Materials*, 29(9), 1603486. <https://doi.org/10.1002/adma.201603486>
- Gao, H., Wu, Q., Hu, Y., Zheng, J. P., Amine, K. et Chen, Z. (2018). Revealing the Rate-Limiting Li-Ion Diffusion Pathway in Ultrathick Electrodes for Li-Ion Batteries. *The Journal of Physical Chemistry Letters*, 9(17), 5100-5104. <https://doi.org/10.1021/acs.jpcllett.8b02229>
- Gao, L. T. et Guo, Z.-S. (2021). Effects of Optimized Electrode Surface Roughness and Solid Electrolyte Interphase on Lithium Dendrite Growth. *Energy Technology*, 9(7), 2000968. <https://doi.org/10.1002/ente.202000968>
- Gasteiger, H. A., Panels, J. E. et Yan, S. G. (2004). Dependence of PEM fuel cell performance on catalyst loading. *Journal of Power Sources*, 127(1), 162-171. <https://doi.org/10.1016/j.jpowsour.2003.09.013>
- Ghosh, K., Ng, S., Iffelsberger, C. et Pumera, M. (2020). ReS₂: A High-Rate Pseudocapacitive Energy Storage Material. *ACS Applied Energy Materials*, 3(10), 10261-10269. <https://doi.org/10.1021/acsaem.0c02187>
- Ghosh, K., Ng, S., Iffelsberger, C. et Pumera, M. (2022). 2D MoS₂/carbon/polylactic acid filament for 3D printing: Photo and electrochemical energy conversion and storage. *Applied Materials Today*, 26, 101301. <https://doi.org/10.1016/j.apmt.2021.101301>
- Gmitter, A. J., Badway, F., Rangan, S., Bartynski, R. A., Halajko, A., Pereira, N. et Amatucci, G. G. (2010). Formation, dynamics, and implication of solid electrolyte interphase in high voltage reversible conversion fluoride nanocomposites. *Journal of Materials Chemistry*, 20(20), 4149. <https://doi.org/10.1039/b923908a>
- Gossage, Z. T., Hui, J., Sarbapalli, D. et Rodríguez-López, J. (2020). Coordinated mapping of Li⁺ flux and electron transfer reactivity during solid-electrolyte interphase formation at a graphene electrode. *Analyst*, 145(7), 2631-2638. <https://doi.org/10.1039/C9AN02637A>
- Haensch, M., Balboa, L., Graf, M., Silva Olaya, A. R., Weissmüller, J. et Wittstock, G. (2019). Mass Transport in Porous Electrodes Studied by Scanning Electrochemical Microscopy: Example of Nanoporous Gold. *ChemElectroChem*, 6(12), 3160-3166. <https://doi.org/10.1002/celec.201900634>

- Hansma, P. K., Drake, B., Marti, O., Gould, S. A. C. et Prater, C. B. (1989). The Scanning Ion-Conductance Microscope. *Science*, 243(4891), 641-643. <https://doi.org/10.1126/science.2464851>
- Hasannaemi, V. et Mukherjee, S. (2019). Noble-Metal based Metallic Glasses as Highly Catalytic Materials for Hydrogen Oxidation Reaction in Fuel Cells. *Scientific Reports*, 9(1), 12136. <https://doi.org/10.1038/s41598-019-48582-7>
- Henrotte, O., Boudet, A., Limani, N., Bergonzo, P., Zribi, B., Scorsone, E., Joussetme, B. et Cornut, R. (2020). Steady-State Electrocatalytic Activity Evaluation with the Redox Competition Mode of Scanning Electrochemical Microscopy: A Gold Probe and a Boron-Doped Diamond Substrate. *ChemElectroChem*, 7(22), 4633-4640. <https://doi.org/10.1002/celec.202001088>
- Heubner, C., Nickol, A., Seeba, J., Reuber, S., Junker, N., Wolter, M., Schneider, M. et Michaelis, A. (2019). Understanding thickness and porosity effects on the electrochemical performance of $\text{LiNi}_{0.6}\text{Co}_{0.2}\text{Mn}_{0.2}\text{O}_2$ -based cathodes for high energy Li-ion batteries. *Journal of Power Sources*, 419, 119-126. <https://doi.org/10.1016/j.jpowsour.2019.02.060>
- Heubner, C., Nikolowski, K., Reuber, S., Schneider, M., Wolter, M. et Michaelis, A. (2020a). Recent Insights into Rate Performance Limitations of Li-ion Batteries. *Batteries & Supercaps*, 4, 268-285. <https://doi.org/10.1002/batt.202000227>
- Heubner, C., Schneider, M. et Michaelis, A. (2020b). Diffusion-Limited C-Rate: A Fundamental Principle Quantifying the Intrinsic Limits of Li-Ion Batteries. *Advanced Energy Materials*, 10(2), 1902523. <https://doi.org/10.1002/aenm.201902523>
- Heubner, C., Voigt, K., Marcinkowski, P., Reuber, S., Nikolowski, K., Schneider, M., Partsch, M. et Michaelis, A. (2021). From Active Materials to Battery Cells: A Straightforward Tool to Determine Performance Metrics and Support Developments at an Application-Relevant Level. *Advanced Energy Materials*, 11(46), 2102647. <https://doi.org/10.1002/aenm.202102647>
- Hilbert, L. R., Bagge-Ravn, D., Kold, J. et Gram, L. (2003). Influence of surface roughness of stainless steel on microbial adhesion and corrosion resistance. *International Biodeterioration & Biodegradation*, 52(3), 175-185. [https://doi.org/10.1016/S0964-8305\(03\)00104-5](https://doi.org/10.1016/S0964-8305(03)00104-5)
- Hossain, Md. S., Stephens, L. I., Hatami, M., Ghavidel, M., Chhin, D., Dawkins, J. I. G., Savignac, L., Mauzeroll, J. et Schougaard, S. B. (2020). Effective Mass Transport Properties in Lithium Battery Electrodes. *ACS Applied Energy Materials*, 3(1), 440-446. <https://doi.org/10.1021/acsaem.9b01695>
- Hossain, Md. S., Stephens, L. I., Mauzeroll, J. et Schougaard, S. B. (2021). Structural dependence of effective mass transport properties in lithium battery electrodes. *Journal of Power Sources*, 504, 230069. <https://doi.org/10.1016/j.jpowsour.2021.230069>

- Huang, D., Engtrakul, C., Nanayakkara, S., Mulder, D. W., Han, S.-D., Zhou, M., Luo, H. et Tenent, R. C. (2021). Understanding Degradation at the Lithium-Ion Battery Cathode/Electrolyte Interface: Connecting Transition-Metal Dissolution Mechanisms to Electrolyte Composition. *ACS Applied Materials & Interfaces*, *13*(10), 11930-11939. <https://doi.org/10.1021/acscami.0c22235>
- Hui, J., Burgess, M., Zhang, J. et Rodríguez-López, J. (2016). Layer Number Dependence of Li⁺ Intercalation on Few-Layer Graphene and Electrochemical Imaging of Its Solid–Electrolyte Interphase Evolution. *ACS Nano*, *10*(4), 4248-4257. <https://doi.org/10.1021/acsnano.5b07692>
- Hui, J., Gossage, Z. T., Sarbapalli, D., Hernández-Burgos, K. et Rodríguez-López, J. (2019). Advanced Electrochemical Analysis for Energy Storage Interfaces. *Analytical Chemistry*, *91*(1), 60-83. <https://doi.org/10.1021/acs.analchem.8b05115>
- Hui, J., Schorr, N. B., Pakhira, S., Qu, Z., Mendoza-Cortes, J. L. et Rodríguez-López, J. (2018). Achieving Fast and Efficient K⁺ Intercalation on Ultrathin Graphene Electrodes Modified by a Li⁺ Based Solid-Electrolyte Interphase. *Journal of the American Chemical Society*, *140*(42), 13599-13603. <https://doi.org/10.1021/jacs.8b08907>
- Hwang, S., Kim, D.-H., Shin, J. H., Jang, J. E., Ahn, K. H., Lee, C. et Lee, H. (2018). Ionic Conduction and Solution Structure in LiPF₆ and LiBF₄ Propylene Carbonate Electrolytes. *The Journal of Physical Chemistry C*, *122*(34), 19438-19446. <https://doi.org/10.1021/acs.jpcc.8b06035>
- IPCC. (2022). *Global Warming of 1.5°C: IPCC Special Report on Impacts of Global Warming of 1.5°C above Pre-industrial Levels in Context of Strengthening Response to Climate Change, Sustainable Development, and Efforts to Eradicate Poverty* (1^{re} éd.). Cambridge University Press. <https://doi.org/10.1017/9781009157940>
- Ishihara, Y., Miyazaki, K., Fukutsuka, T. et Abe, T. (2014). Kinetics of Lithium-Ion Transfer at the Interface between Li₄Ti₅O₁₂ Thin Films and Organic Electrolytes. *ECSS Electrochemistry Letters*, *3*(8), A83-A86. <https://doi.org/10.1149/2.0011408eel>
- Ivanov, A. P., Actis, P., Jönsson, P., Klenerman, D., Korchev, Y. et Edel, J. B. (2015). On-Demand Delivery of Single DNA Molecules Using Nanopipets. *ACS Nano*, *9*(4), 3587-3595. <https://doi.org/10.1021/acsnano.5b00911>
- Jang, T., Kang, J.-H., Kim, S., Shim, M., Lee, J., Song, J., Kim, W., Ryu, K. et Byon, H. R. (2021). Nanometer-Scale Surface Roughness of a 3-D Cu Substrate Promoting Li Nucleation in Li-Metal Batteries. *ACS Applied Energy Materials*, *4*(3), 2644-2651. <https://doi.org/10.1021/acsaem.0c03210>
- Jaouen, F., Proietti, E., Lefèvre, M., Chenitz, R., Dodelet, J.-P., Wu, G., Taek Chung, H., Marie Johnston, C. et Zelenay, P. (2011). Recent advances in non-precious metal catalysis for oxygen - reduction reaction in polymer electrolyte fuel cells. *Energy & Environmental Science*, *4*(1), 114-130. <https://doi.org/10.1039/C0EE00011F>

- Jia, M., Zhang, W., Cai, X., Zhan, X., Hou, L., Yuan, C. et Guo, Z. (2022). Re-understanding the galvanostatic intermittent titration technique: Pitfalls in evaluation of diffusion coefficients and rational suggestions. *Journal of Power Sources*, 543, 231843. <https://doi.org/10.1016/j.jpowsour.2022.231843>
- Jiao, Y., Zhuang, J., Zheng, Q. et Liao, X. (2020). A High Accuracy Ion Conductance Imaging Method Based on the Approach Curve Spectrum. *Ultramicroscopy*, 215, 113025. <https://doi.org/10.1016/j.ultramicro.2020.113025>
- Jiyane, N., García-Quismondo, E., Ventosa, E., Schuhmann, W. et Santos, C. S. (2023). Elucidating Degradation Mechanisms of Silicon-graphite Electrodes in Lithium-ion Batteries by Local Electrochemistry. *Batteries & Supercaps*, 6(8), e202300126. <https://doi.org/10.1002/batt.202300126>
- Ju, Z., Zhu, Y., Zhang, X., Lutz, D. M., Fang, Z., Takeuchi, K. J., Takeuchi, E. S., Marschilok, A. C. et Yu, G. (2020). Understanding Thickness-Dependent Transport Kinetics in Nanosheet-Based Battery Electrodes. *Chemistry of Materials*, 32(4), 1684-1692. <https://doi.org/10.1021/acs.chemmater.9b05396>
- Kang, M., Perry, D., Bentley, C. L., West, G., Page, A. et Unwin, P. R. (2017). Simultaneous Topography and Reaction Flux Mapping at and around Electrocatalytic Nanoparticles. *ACS Nano*, 11(9), 9525-9535. <https://doi.org/10.1021/acsnano.7b05435>
- Katemann, B. B. et Schuhmann, W. (2002). Fabrication and Characterization of Needle-Type. *Electroanalysis*, 14(1), 22-28. [https://doi.org/10.1002/1521-4109\(200201\)14:1<22::AID-ELAN22>3.0.CO;2-F](https://doi.org/10.1002/1521-4109(200201)14:1<22::AID-ELAN22>3.0.CO;2-F)
- Kim, J., Park, S., Hwang, S. et Yoon, W.-S. (2022). Principles and Applications of Galvanostatic Intermittent Titration Technique for Lithium-ion Batteries. *Journal of Electrochemical Science and Technology*, 13(1), 19-31. <https://doi.org/10.33961/jecst.2021.00836>
- Kim, J., Renault, C., Nioradze, N., Arroyo-Currás, N., Leonard, K. C. et Bard, A. J. (2016). Electrocatalytic Activity of Individual Pt Nanoparticles Studied by Nanoscale Scanning Electrochemical Microscopy. *Journal of the American Chemical Society*, 138(27), 8560-8568. <https://doi.org/10.1021/jacs.6b03980>
- Kim, T., Choi, W., Shin, H.-C., Choi, J.-Y., Kim, J. M., Park, M.-S. et Yoon, W.-S. (2020). Applications of Voltammetry in Lithium Ion Battery Research. *Journal of Electrochemical Science and Technology*, 11(1), 14-25. <https://doi.org/10.33961/jecst.2019.00619>
- Klenerman, D., Korchev, Y. E. et Davis, S. J. (2011). Imaging and characterisation of the surface of live cells. *Current Opinion in Chemical Biology*, 15(5), 696-703. <https://doi.org/10.1016/j.cbpa.2011.04.001>
- Korchev, Y. E., Bashford, C. L., Milovanovic, M., Vodyanoy, I. et Lab, M. J. (1997). Scanning ion conductance microscopy of living cells. *Biophysical Journal*, 73(2), 653-658. [https://doi.org/10.1016/S0006-3495\(97\)78100-1](https://doi.org/10.1016/S0006-3495(97)78100-1)

- Krueger, B., Balboa, L., Dohmann, J. F., Winter, M., Bieker, P. et Wittstock, G. (2020). Solid Electrolyte Interphase Evolution on Lithium Metal Electrodes Followed by Scanning Electrochemical Microscopy Under Realistic Battery Cycling Current Densities. *ChemElectroChem*, 7(17), 3590-3596. <https://doi.org/10.1002/celec.202000441>
- Krueger, B., Rücker, K. K. et Wittstock, G. (2022). Redox Mediators for Faster Lithium Peroxide Oxidation in a Lithium–Oxygen Cell: A Scanning Electrochemical Microscopy Study. *ACS Applied Energy Materials*, 5(3), 3724-3733. <https://doi.org/10.1021/acsaem.2c00172>
- Krumov, M. R., Lang, S., Johnson, L. et Abruña, H. D. (2023). Operando Investigation of Solid Electrolyte Interphase Formation, Dynamic Evolution, and Degradation During Lithium Plating/Stripping. *ACS Applied Materials & Interfaces*, 15(40), 47692-47703. <https://doi.org/10.1021/acsaami.3c08485>
- Kuang, Y., Chen, C., Kirsch, D. et Hu, L. (2019). Thick Electrode Batteries: Principles, Opportunities, and Challenges. *Advanced Energy Materials*, 9(33), 1901457. <https://doi.org/10.1002/aenm.201901457>
- Kuss, C., Payne, N. A. et Mauzeroll, J. (2016). Probing Passivating Porous Films by Scanning Electrochemical Microscopy. *Journal of The Electrochemical Society*, 163(4), H3066-H3071. <https://doi.org/10.1149/2.0131604jes>
- Kwak, Juhyoun. et Bard, A. J. (1989). Scanning electrochemical microscopy. Theory of the feedback mode. *Analytical Chemistry*, 61(11), 1221-1227. <https://doi.org/10.1021/ac00186a009>
- Landesfeind, J., Hattendorff, J., Ehrl, A., Wall, W. A. et Gasteiger, H. A. (2016). Tortuosity Determination of Battery Electrodes and Separators by Impedance Spectroscopy. *Journal of The Electrochemical Society*, 163(7), A1373-A1387. <https://doi.org/10.1149/2.1141607jes>
- Lang, S., Colletta, M., Krumov, M. R., Seok, J., Kourkoutis, L. F., Wen, R. et Abruña, H. D. (2023). Multidimensional visualization of the dynamic evolution of Li metal via in situ/operando methods. *Proceedings of the National Academy of Sciences*, 120(7), e2220419120. <https://doi.org/10.1073/pnas.2220419120>
- Laschuk, N. O., Easton, E. B. et Zenkina, O. V. (2021). Reducing the resistance for the use of electrochemical impedance spectroscopy analysis in materials chemistry. *RSC Advances*, 11(45), 27925-27936. <https://doi.org/10.1039/D1RA03785D>
- Lasia, A. (2022). The Origin of the Constant Phase Element. *The Journal of Physical Chemistry Letters*, 13(2), 580-589. <https://doi.org/10.1021/acs.jpcllett.1c03782>
- Latz, A. et Zausch, J. (2011). Thermodynamic consistent transport theory of Li-ion batteries. *Journal of Power Sources*, 196(6), 3296-3302. <https://doi.org/10.1016/j.jpowsour.2010.11.088>

- Lazanas, A. Ch. et Prodromidis, M. I. (2023). Electrochemical Impedance Spectroscopy—A Tutorial. *ACS Measurement Science Au*, 3(3), 162-193. <https://doi.org/10.1021/acsmesuresciau.2c00070>
- Lefrou, C. et Cornut, R. (2010). Analytical Expressions for Quantitative Scanning Electrochemical Microscopy (SECM). *ChemPhysChem*, 11(3), 547-556. <https://doi.org/10.1002/cphc.200900600>
- Leitão, S. M. (2015). *Design and construction of a scanning Ion conductance microscope* [Master's Thesis, Instituto Superior Técnico, University of Lisbon]. <https://scholar.tecnico.ulisboa.pt/records/xFqgvky0dJeaRxMP4bTEqECI4UumOOdgFoR2>
- Lepage, D., Sobh, F., Kuss, C., Liang, G. et Schougaard, S. B. (2014). Delithiation kinetics study of carbon coated and carbon free LiFePO₄. *Journal of Power Sources*, 256, 61-65. <https://doi.org/10.1016/j.jpowsour.2013.12.054>
- Lhenry, S., Leroux, Y. R. et Hapiot, P. (2013). Chemically Irreversible Redox Mediator for SECM Kinetics Investigations: Determination of the Absolute Tip–Sample Distance. *Analytical Chemistry*, 85(3), 1840-1845. <https://doi.org/10.1021/ac303226e>
- Li, G. (2021). Regulating Mass Transport Behavior for High-Performance Lithium Metal Batteries and Fast-Charging Lithium-Ion Batteries. *Advanced Energy Materials*, 11(7), 2002891. <https://doi.org/10.1002/aenm.202002891>
- Li, M., Feng, M., Luo, D. et Chen, Z. (2020a). Fast Charging Li-Ion Batteries for a New Era of Electric Vehicles. *Cell Reports Physical Science*, 1(10), 100212. <https://doi.org/10.1016/j.xcrp.2020.100212>
- Li, M. S. M., Filice, F. P. et Ding, Z. (2016). Determining live cell topography by scanning electrochemical microscopy. *Journal of Electroanalytical Chemistry*, 779, 176-186. <https://doi.org/10.1016/j.jelechem.2016.02.042>
- Li, P., Jin, Z., Qian, Y., Fang, Z., Xiao, D. et Yu, G. (2019). Probing Enhanced Site Activity of Co–Fe Bimetallic Subnanoclusters Derived from Dual Cross-Linked Hydrogels for Oxygen Electrocatalysis. *ACS Energy Letters*, 4(8), 1793-1802. <https://doi.org/10.1021/acsenergylett.9b00893>
- Li, P., Jin, Z., Qian, Y., Fang, Z., Xiao, D. et Yu, G. (2020b). Supramolecular confinement of single Cu atoms in hydrogel frameworks for oxygen reduction electrocatalysis with high atom utilization. *Materials Today*, 35, 78-86. <https://doi.org/10.1016/j.mattod.2019.10.006>
- Li, X.-R., Meng, X.-Z., Zhang, Q.-H., Wu, L.-K., Sun, Q.-Q., Deng, H.-Q., Sun, S.-J. et Cao, F.-H. (2023). Insight into oxygen reduction activity and pathway on pure titanium using scanning electrochemical microscopy and theoretical calculations. *Journal of Colloid and Interface Science*, 643, 551-562. <https://doi.org/10.1016/j.jcis.2023.03.127>

- Limani, N., Boudet, A., Scorsone, E., Derycke, V., Jusselme, B. et Cornut, R. (2023). Low loading ORR selectivity evaluation of Pt-free catalysts with scanning electrochemical microscopy. *Electrochemistry Communications*, 153, 107538. <https://doi.org/10.1016/j.elecom.2023.107538>
- Lipson, A. L., Ginder, R. S. et Hersam, M. C. (2011). Nanoscale In Situ Characterization of Li-ion Battery Electrochemistry Via Scanning Ion Conductance Microscopy. *Advanced Materials*, 23(47), 5613-5617. <https://doi.org/10.1002/adma.201103094>
- Liu, B., Prugue, K., Nikpour, M., Ward, K., Mazzeo, B. A. et Wheeler, D. R. (2022a). Heterogeneity in MacMullin Number of Li-Ion Battery Electrodes Studied by Means of an Aperture Probe. *Journal of The Electrochemical Society*, 169(1), 010517. <https://doi.org/10.1149/1945-7111/ac4542>
- Liu, D., Yu, Q., Liu, S., Qian, K., Wang, S., Sun, W., Yang, X.-Q., Kang, F. et Li, B. (2019a). Evolution of Solid Electrolyte Interface on TiO₂ Electrodes in an Aqueous Li-Ion Battery Studied Using Scanning Electrochemical Microscopy. *The Journal of Physical Chemistry C*, 123(20), 12797-12806. <https://doi.org/10.1021/acs.jpcc.9b01412>
- Liu, D., Zeng, X., Liu, S., Wang, S., Kang, F. et Li, B. (2019b). Application of Alternating Current Scanning Electrochemical Microscopy in Lithium-Ion Batteries: Local Visualization of the Electrode Surface. *ChemElectroChem*, 6(18), 4854-4858. <https://doi.org/10.1002/celec.201901431>
- Liu, S., Liu, D., Wang, S., Cai, X., Qian, K., Kang, F. et Li, B. (2019c). Understanding the cathode electrolyte interface formation in aqueous electrolyte by scanning electrochemical microscopy. *Journal of Materials Chemistry A*, 7(21), 12993-12996. <https://doi.org/10.1039/C9TA03199E>
- Liu, X., Lu, Z., Pan, H., Cheng, J., Dou, J., Huang, X. et Chen, X. (2022b). Investigation of functionalization effect of carbon nanotubes as supercapacitor electrode material on hydrogen evolution side-reaction by scanning electrochemical microscopy. *Electrochimica Acta*, 429, 141056. <https://doi.org/10.1016/j.electacta.2022.141056>
- Liu, Y., Zhu, Y. et Cui, Y. (2019d). Challenges and opportunities towards fast-charging battery materials. *Nature Energy*, 4(7), 540-550. <https://doi.org/10.1038/s41560-019-0405-3>
- Lu, L.-L., Lu, Y.-Y., Xiao, Z.-J., Zhang, T.-W., Zhou, F., Ma, T., Ni, Y., Yao, H.-B., Yu, S.-H. et Cui, Y. (2018). Wood-Inspired High-Performance Ultrathick Bulk Battery Electrodes. *Advanced Materials*, 30(20), 1706745. <https://doi.org/10.1002/adma.201706745>
- Macpherson, J. V., Jones, C. E., Barker, A. L. et Unwin, P. R. (2002). Electrochemical Imaging of Diffusion through Single Nanoscale Pores. *Analytical Chemistry*, 74(8), 1841-1848. <https://doi.org/10.1021/ac0157472>
- Manthiram, A. (2017). An Outlook on Lithium Ion Battery Technology. *ACS Central Science*, 3(10), 1063-1069. <https://doi.org/10.1021/acscentsci.7b00288>

- Mareev, S. A., Butylskii, D. Yu., Pismenskaya, N. D., Larchet, C., Dammak, L. et Nikonenko, V. (2018). Geometric heterogeneity of homogeneous ion-exchange Neosepta membranes. *Journal of Membrane Science*, 563, 768-776. <https://doi.org/10.1016/j.memsci.2018.06.018>
- Markevich, E., Levi, M. D. et Aurbach, D. (2005). Comparison between potentiostatic and galvanostatic intermittent titration techniques for determination of chemical diffusion coefficients in ion-insertion electrodes. *Journal of Electroanalytical Chemistry*, 580(2), 231-237. <https://doi.org/10.1016/j.jelechem.2005.03.030>
- Masias, A., Marcicki, J. et Paxton, W. A. (2021). Opportunities and Challenges of Lithium Ion Batteries in Automotive Applications. *ACS Energy Letters*, 6(2), 621-630. <https://doi.org/10.1021/acsenergylett.0c02584>
- Mauzeroll, J., Hueske, E. A. et Bard, A. J. (2003). Scanning Electrochemical Microscopy. 48. Hg/Pt Hemispherical Ultramicroelectrodes: Fabrication and Characterization. *Analytical Chemistry*, 75(15), 3880-3889. <https://doi.org/10.1021/ac0340881>
- McKelvey, K., Kinnear, S. L., Perry, D., Momotenko, D. et Unwin, P. R. (2014). Surface Charge Mapping with a Nanopipette. *Journal of the American Chemical Society*, 136(39), 13735-13744. <https://doi.org/10.1021/ja506139u>
- McKelvey, K., Snowden, M. E., Peruffo, M. et Unwin, P. R. (2011). Quantitative Visualization of Molecular Transport through Porous Membranes: Enhanced Resolution and Contrast Using Intermittent Contact-Scanning Electrochemical Microscopy. *Analytical Chemistry*, 83(17), 6447-6454. <https://doi.org/10.1021/ac201489c>
- Mishra, A., Lin, J.-W., Zahiri, B., Braun, P. V. et Rodríguez-López, J. (2024). In Situ Investigation of Lattice Oxygen Loss from Preferentially Faceted Electrodeposited LiCoO₂ via Scanning Electrochemical Microscopy. *Journal of The Electrochemical Society*, 171(5), 056510. <https://doi.org/10.1149/1945-7111/ad4f22>
- Mishra, A., Sarbapalli, D., Hossain, M. S., Gossage, Z. T., Li, Z., Urban, A. et Rodríguez-López, J. (2022). Highly Sensitive Detection and Mapping of Incipient and Steady-State Oxygen Evolution from Operating Li-Ion Battery Cathodes via Scanning Electrochemical Microscopy. *Journal of The Electrochemical Society*, 169(8), 086501. <https://doi.org/10.1149/1945-7111/ac857e>
- Moghaddam, M. et Peljo, P. (2021). Oxygen Absorption in Electrocatalyst Layers Detected by Scanning Electrochemical Microscopy. *ChemElectroChem*, 8(15), 2950-2955. <https://doi.org/10.1002/celec.202100702>
- Momotenko, D., McKelvey, K., Kang, M., Meloni, G. N. et Unwin, P. R. (2016). Simultaneous Interfacial Reactivity and Topography Mapping with Scanning Ion Conductance Microscopy. *Analytical Chemistry*, 88(5), 2838-2846. <https://doi.org/10.1021/acs.analchem.5b04566>

- Nebel, M., Erichsen, T. et Schuhmann, W. (2014). Constant-distance mode SECM as a tool to visualize local electrocatalytic activity of oxygen reduction catalysts. *Beilstein Journal of Nanotechnology*, 5(1), 141-151. <https://doi.org/10.3762/bjnano.5.14>
- Nebel, M., Neugebauer, S., Eckhard, K. et Schuhmann, W. (2013). Ring-disk microelectrodes for simultaneous constant-distance and constant-current mode scanning electrochemical microscopy. *Electrochemistry Communications*, 27, 160-163. <https://doi.org/10.1016/j.elecom.2012.11.028>
- Neubauer, J., Pesaran, A., Bae, C., Elder, R. et Cunningham, B. (2014). Updating United States Advanced Battery Consortium and Department of Energy battery technology targets for battery electric vehicles. *Journal of Power Sources*, 271, 614-621. <https://doi.org/10.1016/j.jpowsour.2014.06.043>
- Newman, J. (1995). Optimization of Porosity and Thickness of a Battery Electrode by Means of a Reaction-Zone Model. *Journal of the Electrochemical Society*, 142(1), 97. <https://doi.org/10.1149/1.2043956>
- Newman, J. et Balsara, N. P. (2004). *Electrochemical Systems* (3rd ed.). John Wiley & Sons, Inc.
- Nguyen, T. L., Blanquet, A., Staiger, M. P., Dias, G. J. et Woodfield, T. B. F. (2012). On the role of surface roughness in the corrosion of pure magnesium in vitro. *Journal of Biomedical Materials Research Part B: Applied Biomaterials*, 100B(5), 1310-1318. <https://doi.org/10.1002/jbm.b.32697>
- Nguyen, T.-T., Demortière, A., Fleutot, B., Delobel, B., Delacourt, C. et Cooper, S. J. (2020). The electrode tortuosity factor: why the conventional tortuosity factor is not well suited for quantifying transport in porous Li-ion battery electrodes and what to use instead. *npj Computational Materials*, 6(1), 1-12. <https://doi.org/10.1038/s41524-020-00386-4>
- Nugues, S. et Denuault, G. (1996). Scanning electrochemical microscopy: Amperometric probing of diffusional ion fluxes through porous membranes and human dentine. *Journal of Electroanalytical Chemistry*, 408(1), 125-140. [https://doi.org/10.1016/0022-0728\(96\)04523-8](https://doi.org/10.1016/0022-0728(96)04523-8)
- Odziomek, M., Chaput, F., Rutkowska, A., Świerczek, K., Olszewska, D., Sitarz, M., Lerouge, F. et Parola, S. (2017). Hierarchically structured lithium titanate for ultrafast charging in long-life high capacity batteries. *Nature Communications*, 8, 15636. <https://doi.org/10.1038/ncomms15636>
- Ogihara, N., Itou, Y., Sasaki, T. et Takeuchi, Y. (2015). Impedance Spectroscopy Characterization of Porous Electrodes under Different Electrode Thickness Using a Symmetric Cell for High-Performance Lithium-Ion Batteries. *The Journal of Physical Chemistry C*, 119(9), 4612-4619. <https://doi.org/10.1021/jp512564f>
- Padhi, A. K., Nanjundaswamy, K. S. et Goodenough, J. B. (1997). Phospho-olivines as Positive-Electrode Materials for Rechargeable Lithium Batteries. *Journal of The Electrochemical Society*, 144(4), 1188. <https://doi.org/10.1149/1.1837571>

- Page, A., Perry, D. et Unwin, P. R. (2017). Multifunctional scanning ion conductance microscopy. *Proceedings of the Royal Society A: Mathematical, Physical and Engineering Sciences*, 473(2200), 20160889. <https://doi.org/10.1098/rspa.2016.0889>
- Parikh, D., Christensen, T. et Li, J. (2020). Correlating the influence of porosity, tortuosity, and mass loading on the energy density of $\text{LiNi}_{0.6}\text{Mn}_{0.2}\text{Co}_{0.2}\text{O}_2$ cathodes under extreme fast charging (XFC) conditions. *Journal of Power Sources*, 474, 228601. <https://doi.org/10.1016/j.jpowsour.2020.228601>
- Park, J., Kumar, V., Wang, X., Lee, P. S. et Kim, W. (2017). Investigation of Charge Transfer Kinetics at Carbon/Hydroquinone Interfaces for Redox-Active-Electrolyte Supercapacitors. *ACS Applied Materials & Interfaces*, 9(39), 33728-33734. <https://doi.org/10.1021/acsami.7b06863>
- Patel, K. K., Paulsen, J. M. et Desilvestro, J. (2003). Numerical simulation of porous networks in relation to battery electrodes and separators. *Journal of Power Sources*, 122(2), 144-152. [https://doi.org/10.1016/S0378-7753\(03\)00399-9](https://doi.org/10.1016/S0378-7753(03)00399-9)
- Payne, N. A., Dawkins, J. I. G., Schougaard, S. B. et Mauzeroll, J. (2019). Effect of Substrate Permeability on Scanning Ion Conductance Microscopy: Uncertainty in Tip–Substrate Separation and Determination of Ionic Conductivity. *Analytical Chemistry*, 91(24), 15718-15725. <https://doi.org/10.1021/acs.analchem.9b03907>
- Perry, D. et Mamlouk, M. (2021). Probing mass transport processes in Li-ion batteries using electrochemical impedance spectroscopy. *Journal of Power Sources*, 514, 230577. <https://doi.org/10.1016/j.jpowsour.2021.230577>
- Polcari, D., Dauphin-Ducharme, P. et Mauzeroll, J. (2016). Scanning Electrochemical Microscopy: A Comprehensive Review of Experimental Parameters from 1989 to 2015. *Chemical Reviews*, 116(22), 13234-13278. <https://doi.org/10.1021/acs.chemrev.6b00067>
- Pouraghajan, F., Knight, H., Wray, M., Mazzeo, B., Subbaraman, R., Christensen, J. et Wheeler, D. (2018). Quantifying Tortuosity of Porous Li-Ion Battery Electrodes: Comparing Polarization-Interrupt and Blocking-Electrolyte Methods. *Journal of The Electrochemical Society*, 165(11), A2644-A2653. <https://doi.org/10.1149/2.0611811jes>
- Raju, A. R., Schougaard, S. B. et Mauzeroll, J. (2024). Current trends in SECM for energy storage devices: Reaching the microstructure level to tune devices and performance. *Current Opinion in Electrochemistry*, 45, 101522. <https://doi.org/10.1016/j.coelec.2024.101522>
- Ramachandran, T., Sana, S. S., Kumar, K. D., Kumar, Y. A., Hegazy, H. H. et Kim, S. C. (2023). Asymmetric supercapacitors: Unlocking the energy storage revolution. *Journal of Energy Storage*, 73, 109096. <https://doi.org/10.1016/j.est.2023.109096>
- Rheinlaender, J. et Schäffer, T. E. (2017). An Accurate Model for the Ion Current–Distance Behavior in Scanning Ion Conductance Microscopy Allows for Calibration of Pipet Tip

- Geometry and Tip–Sample Distance. *Analytical Chemistry*, 89(21), 11875-11880.
<https://doi.org/10.1021/acs.analchem.7b03871>
- Ritzert, N. L., Szalai, V. A. et Moffat, T. P. (2018). Mapping Electron Transfer at MoS₂ Using Scanning Electrochemical Microscopy. *Langmuir*, 34(46), 13864-13870.
<https://doi.org/10.1021/acs.langmuir.8b02731>
- Robertson, D. C., Flores, L., Dunlop, A. R., Trask, S. E., Usseglio-Viretta, F. L. E., Colclasure, A. M., Yang, Z. et Bloom, I. (2021). Effect of Anode Porosity and Temperature on the Performance and Lithium Plating During Fast-Charging of Lithium-Ion Cells. *Energy Technology*, 9(1), 2000666. <https://doi.org/10.1002/ente.202000666>
- Sa, N., Lan, W.-J., Shi, W. et Baker, L. A. (2013). Rectification of Ion Current in Nanopipettes by External Substrates. *ACS Nano*, 7(12), 11272-11282. <https://doi.org/10.1021/nn4050485>
- Santos, C. S., Botz, A., Bandarenka, A. S., Ventosa, E. et Schuhmann, W. (2022). Correlative Electrochemical Microscopy for the Elucidation of the Local Ionic and Electronic Properties of the Solid Electrolyte Interphase in Li-Ion Batteries. *Angewandte Chemie International Edition*, 61(26), e202202744. <https://doi.org/10.1002/anie.202202744>
- Schorr, N. B., Jiang, A. G. et Rodríguez-López, J. (2018). Probing Graphene Interfacial Reactivity via Simultaneous and Colocalized Raman–Scanning Electrochemical Microscopy Imaging and Interrogation. *Analytical Chemistry*, 90(13), 7848-7854.
<https://doi.org/10.1021/acs.analchem.8b00730>
- Schulte, W., Liu, S., Plettenberg, I., Kuhri, S., Lüke, W., Lehnert, W. et Wittstock, G. (2017). Local Evaluation of Processed Membrane Electrode Assemblies by Scanning Electrochemical Microscopy. *Journal of The Electrochemical Society*, 164(7), F873.
<https://doi.org/10.1149/2.0061709jes>
- Scott, E. R., White, H. S. et Bradley Phipps, J. (1991). Scanning electrochemical microscopy of a porous membrane. *Journal of Membrane Science*, 58(1), 71-87.
[https://doi.org/10.1016/S0376-7388\(00\)80638-9](https://doi.org/10.1016/S0376-7388(00)80638-9)
- Seiffarth, G., Steimecke, M., Walther, T., Kühhirt, M., Rümmler, S. et Bron, M. (2016). Mixed Transition Metal Oxide Supported on Nitrogen Doped Carbon Nanotubes – a Simple Bifunctional Electrocatalyst Studied with Scanning Electrochemical Microscopy. *Electroanalysis*, 28(10), 2335-2345. <https://doi.org/10.1002/elan.201600254>
- Selva, J. S. G., Sukeri, A., Bacil, R. P., Serrano, S. H. P. et Bertotti, M. (2023). Electrocatalysis of the hydrogen oxidation reaction on a platinum-decorated nanoporous gold surface studied by scanning electrochemical microscopy. *Journal of Electroanalytical Chemistry*, 934, 117294. <https://doi.org/10.1016/j.jelechem.2023.117294>
- Shen, M., Ishimatsu, R., Kim, J. et Amemiya, S. (2012). Quantitative Imaging of Ion Transport through Single Nanopores by High-Resolution Scanning Electrochemical Microscopy. *Journal of the American Chemical Society*, 134(24), 9856-9859.
<https://doi.org/10.1021/ja3023785>

- Shi, W. et A. Baker, L. (2015). Imaging heterogeneity and transport of degraded Nafion membranes. *RSC Advances*, 5(120), 99284-99290. <https://doi.org/10.1039/C5RA20291D>
- Silva, S. M., Aguiar, L. F., Carvalho, R. M. S., Tanaka, A. A., Damos, F. S. et Luz, R. C. S. (2016). A glassy carbon electrode modified with an iron N4-macrocycle and reduced graphene oxide for voltammetric sensing of dissolved oxygen. *Microchimica Acta*, 183(3), 1251-1259. <https://doi.org/10.1007/s00604-016-1750-6>
- Singh, V., Tiwari, A. et Nagaiah, T. C. (2018). Facet-controlled morphology of cobalt disulfide towards enhanced oxygen reduction reaction. *Journal of Materials Chemistry A*, 6(45), 22545-22554. <https://doi.org/10.1039/C8TA06710D>
- Sklyar, O., Träuble, M., Zhao, C. et Wittstock, G. (2006). Modeling Steady-State Experiments with a Scanning Electrochemical Microscope Involving Several Independent Diffusing Species Using the Boundary Element Method. *The Journal of Physical Chemistry B*, 110(32), 15869-15877. <https://doi.org/10.1021/jp062619e>
- Sklyar, O. et Wittstock, G. (2002). Numerical Simulations of Complex Nonsymmetrical 3D Systems for Scanning Electrochemical Microscopy Using the Boundary Element Method. *The Journal of Physical Chemistry B*, 106(30), 7499-7508. <https://doi.org/10.1021/jp020301q>
- Spahr, M. E. (2009). Carbon-Conductive Additives for Lithium-Ion Batteries. Dans M. Yoshio, R. J. Brodd et A. Kozawa (dir.), *Lithium-Ion Batteries: Science and Technologies* (p. 117-154). Springer. https://doi.org/10.1007/978-0-387-34445-4_5
- Stanley, J. et Pourmand, N. (2020). Nanopipettes—The past and the present. *APL Materials*, 8(10), 100902. <https://doi.org/10.1063/5.0020011>
- Stephenson, D. E., Hartman, E. M., Harb, J. N. et Wheeler, D. R. (2007). Modeling of Particle-Particle Interactions in Porous Cathodes for Lithium-Ion Batteries. *Journal of The Electrochemical Society*, 154(12), A1146. <https://doi.org/10.1149/1.2783772>
- Stephenson, D. E., Walker, B. C., Skelton, C. B., Gorzkowski, E. P., Rowenhorst, D. J. et Wheeler, D. R. (2011). Modeling 3D Microstructure and Ion Transport in Porous Li-Ion Battery Electrodes. *Journal of The Electrochemical Society*, 158(7), A781. <https://doi.org/10.1149/1.3579996>
- Sumboja, A., Tefashe, U. M., Wittstock, G. et Lee, P. S. (2015). Investigation of Charge Transfer Kinetics of Polyaniline Supercapacitor Electrodes by Scanning Electrochemical Microscopy. *Advanced Materials Interfaces*, 2(1), 1400154. <https://doi.org/10.1002/admi.201400154>
- Sun, K., Wei, T.-S., Ahn, B. Y., Seo, J. Y., Dillon, S. J. et Lewis, J. A. (2013). 3D Printing of Interdigitated Li-Ion Microbattery Architectures. *Advanced Materials*, 25(33), 4539-4543. <https://doi.org/10.1002/adma.201301036>

- Sun, P., Zhang, Z., Guo, J. et Shao, Y. (2001). Fabrication of Nanometer-Sized Electrodes and Tips for Scanning Electrochemical Microscopy. *Analytical Chemistry*, 73(21), 5346-5351. <https://doi.org/10.1021/ac010474w>
- Sun, W., Li, Q. M., Xiao, P. et Carbone, P. (2024). Determination of the tortuosity of a Li-ion battery separator. *Journal of Energy Storage*, 97, 112940. <https://doi.org/10.1016/j.est.2024.112940>
- Syed, N., Zavabeti, A., Messalea, K. A., Della Gaspera, E., Elbourne, A., Jannat, A., Mohiuddin, M., Zhang, B. Y., Zheng, G., Wang, L., Russo, S. P., Esrafilzadeh, D., McConville, C. F., Kalantar-Zadeh, K. et Daenke, T. (2019). Wafer-Sized Ultrathin Gallium and Indium Nitride Nanosheets through the Ammonolysis of Liquid Metal Derived Oxides. *Journal of the American Chemical Society*, 141(1), 104-108. <https://doi.org/10.1021/jacs.8b11483>
- Takahashi, Y., Shevchuk, A. I., Novak, P., Murakami, Y., Shiku, H., Korchev, Y. E. et Matsue, T. (2010). Simultaneous Noncontact Topography and Electrochemical Imaging by SECM/SICM Featuring Ion Current Feedback Regulation. *Journal of the American Chemical Society*, 132(29), 10118-10126. <https://doi.org/10.1021/ja1029478>
- Takahashi, Y., Takamatsu, D., Korchev, Y. et Fukuma, T. (2023). Correlative Analysis of Ion-Concentration Profile and Surface Nanoscale Topography Changes Using Operando Scanning Ion Conductance Microscopy. *JACS Au*, 3(4), 1089-1099. <https://doi.org/10.1021/jacsau.2c00677>
- Taleghani, S. T., Marcos, B., Zaghbi, K. et Lantagne, G. (2017). A Study on the Effect of Porosity and Particles Size Distribution on Li-Ion Battery Performance. *Journal of The Electrochemical Society*, 164(11), E3179. <https://doi.org/10.1149/2.0211711jes>
- Tarnev, T., Wilde, P., Dopilka, A., Schuhmann, W., Chan, C. K. et Ventosa, E. (2020). Surface Properties of Battery Materials Elucidated Using Scanning Electrochemical Microscopy: The Case of Type I Silicon Clathrate. *ChemElectroChem*, 7(3), 665-671. <https://doi.org/10.1002/celec.201901688>
- T. Gossage, Z., Hui, J., Zeng, Y., Flores-Zuleta, H. et Rodríguez-López, J. (2019). Probing the reversibility and kinetics of Li⁺ during SEI formation and (de)intercalation on edge plane graphite using ion-sensitive scanning electrochemical microscopy. *Chemical Science*, 10(46), 10749-10754. <https://doi.org/10.1039/C9SC03569A>
- Thangavel, N. K., Mahankali, K. et Arava, L. M. R. (2022). Nanoscale Visualization of Reversible Redox Pathways in Lithium-Sulfur Battery Using In Situ AFM-SECM. *Journal of The Electrochemical Society*, 169(6), 060501. <https://doi.org/10.1149/1945-7111/ac70ff>
- Thorat, I. V., Stephenson, D. E., Zacharias, N. A., Zaghbi, K., Harb, J. N. et Wheeler, D. R. (2009). Quantifying tortuosity in porous Li-ion battery materials. *Journal of Power Sources*, 188(2), 592-600. <https://doi.org/10.1016/j.jpowsour.2008.12.032>

- Tiwari, A., Singh, V., Mandal, D. et Nagaiah, T. C. (2017). Nitrogen containing carbon spheres as an efficient electrocatalyst for oxygen reduction: Microelectrochemical investigation and visualization. *Journal of Materials Chemistry A*, 5(37), 20014-20023. <https://doi.org/10.1039/C7TA05503J>
- Tjaden, B., Brett, D. J. L. et Shearing, P. R. (2018). Tortuosity in electrochemical devices: a review of calculation approaches. *International Materials Reviews*, 63(2), 47-67. <https://doi.org/10.1080/09506608.2016.1249995>
- Tjaden, B., Cooper, S. J., Brett, D. J., Kramer, D. et Shearing, P. R. (2016). On the origin and application of the Bruggeman correlation for analysing transport phenomena in electrochemical systems. *Current Opinion in Chemical Engineering*, 12, 44-51. <https://doi.org/10.1016/j.coche.2016.02.006>
- Tran, H. Y., Greco, G., Täubert, C., Wohlfahrt-Mehrens, M., Haselrieder, W. et Kwade, A. (2012). Influence of electrode preparation on the electrochemical performance of $\text{LiNi}_{0.8}\text{Co}_{0.15}\text{Al}_{0.05}\text{O}_2$ composite electrodes for lithium-ion batteries. *Journal of Power Sources*, 210, 276-285. <https://doi.org/10.1016/j.jpowsour.2012.03.017>
- Unwin, P. R. et Bard, A. J. (1991). Scanning electrochemical microscopy. 9. Theory and application of the feedback mode to the measurement of following chemical reaction rates in electrode processes. *The Journal of Physical Chemistry*, 95(20), 7814-7824. <https://doi.org/10.1021/j100173a049>
- Usseglio-Viretta, F. L. E., Colclasure, A., Mistry, A. N., Claver, K. P. Y., Pouraghajan, F., Finegan, D. P., Heenan, T. M. M., Abraham, D., Mukherjee, P. P., Wheeler, D., Shearing, P., Cooper, S. J. et Smith, K. (2018). Resolving the Discrepancy in Tortuosity Factor Estimation for Li-Ion Battery Electrodes through Micro-Macro Modeling and Experiment. *Journal of The Electrochemical Society*, 165(14), A3403-A3426. <https://doi.org/10.1149/2.0731814jes>
- Vadhva, P., Hu, J., Johnson, M. J., Stocker, R., Braglia, M., Brett, D. J. L. et Rettie, A. J. E. (2021). Electrochemical Impedance Spectroscopy for All-Solid-State Batteries: Theory, Methods and Future Outlook. *ChemElectroChem*, 8(11), 1930-1947. <https://doi.org/10.1002/celec.202100108>
- Vassiliev, S. Yu., Levin, E. E. et Nikitina, V. A. (2016). Kinetic analysis of lithium intercalating systems: cyclic voltammetry. *Electrochimica Acta*, 190, 1087-1099. <https://doi.org/10.1016/j.electacta.2015.12.172>
- Ventosa, E., Madej, E., Zampardi, G., Mei, B., Weide, P., Antoni, H., La Mantia, F., Muhler, M. et Schuhmann, W. (2017). Solid Electrolyte Interphase (SEI) at TiO_2 Electrodes in Li-Ion Batteries: Defining Apparent and Effective SEI Based on Evidence from X-ray Photoemission Spectroscopy and Scanning Electrochemical Microscopy. *ACS Applied Materials & Interfaces*, 9(3), 3123-3130. <https://doi.org/10.1021/acsami.6b13306>
- Ventosa, E., Wilde, P., Zinn, A.-H., Trautmann, M., Ludwig, A. et Schuhmann, W. (2016). Understanding surface reactivity of Si electrodes in Li-ion batteries by in operando

- scanning electrochemical microscopy. *Chemical Communications*, 52(41), 6825-6828. <https://doi.org/10.1039/C6CC02493A>
- Verma, P., Maire, P. et Novák, P. (2010). A review of the features and analyses of the solid electrolyte interphase in Li-ion batteries. *Electrochimica Acta*, 55(22), 6332-6341. <https://doi.org/10.1016/j.electacta.2010.05.072>
- Vijayaraghavan, B., Ely, D. R., Chiang, Y.-M., García-García, R. et García, R. E. (2012). An Analytical Method to Determine Tortuosity in Rechargeable Battery Electrodes. *Journal of The Electrochemical Society*, 159(5), A548. <https://doi.org/10.1149/2.jes113224>
- Waldmann, T., Hogg, B.-I. et Wohlfahrt-Mehrens, M. (2018). Li plating as unwanted side reaction in commercial Li-ion cells – A review. *Journal of Power Sources*, 384, 107-124. <https://doi.org/10.1016/j.jpowsour.2018.02.063>
- Walter, R. et Kannan, M. B. (2011). Influence of surface roughness on the corrosion behaviour of magnesium alloy. *Materials & Design*, 32(4), 2350-2354. <https://doi.org/10.1016/j.matdes.2010.12.016>
- Wang, C.-Y., Xu, T., Ge, S., Zhang, G., Yang, X.-G. et Ji, Y. (2016). A Fast Rechargeable Lithium-Ion Battery at Subfreezing Temperatures. *Journal of The Electrochemical Society*, 163(9), A1944. <https://doi.org/10.1149/2.0681609jes>
- Wang, W., Xu, L., Sun, H., Li, X., Zhao, S. et Zhang, W. (2015). Spatial resolution comparison of AC-SECM with SECM and their characterization of self-healing performance of hexamethylene diisocyanate trimer microcapsule coatings. *Journal of Materials Chemistry A*, 3(10), 5599-5607. <https://doi.org/10.1039/C5TA00529A>
- Wang, Y. et Wipf, D. O. (2020). Visualizing Hydrogen Oxidation Reaction Activity of Polycrystalline Platinum by Scanning Electrochemical Microscopy. *Journal of The Electrochemical Society*, 167(14), 146502. <https://doi.org/10.1149/1945-7111/abbf28>
- Weber, F. M., Graff, K. M., Kohlhaas, I. et Figgemeier, E. (2023). Effective Lithium Passivation through Graphite Coating for Lithium Metal Batteries. *ACS Applied Energy Materials*, 6(6), 3413-3421. <https://doi.org/10.1021/acsaem.2c04128>
- Weiss, M., Ruess, R., Kasnatscheew, J., Levartovsky, Y., Levy, N. R., Minnmann, P., Stolz, L., Waldmann, T., Wohlfahrt-Mehrens, M., Aurbach, D., Winter, M., Ein-Eli, Y. et Janek, J. (2021). Fast Charging of Lithium-Ion Batteries: A Review of Materials Aspects. *Advanced Energy Materials*, 11(33), 2101126. <https://doi.org/10.1002/aenm.202101126>
- Wu, H., Jia, H., Wang, C., Zhang, J.-G. et Xu, W. (2021). Recent Progress in Understanding Solid Electrolyte Interphase on Lithium Metal Anodes. *Advanced Energy Materials*, 11(5), 2003092. <https://doi.org/10.1002/aenm.202003092>
- Xin, S., Liu, Z., Ma, L., Sun, Y., Xiao, C., Li, F. et Du, Y. (2016). Visualization of the electrocatalytic activity of three-dimensional MoSe₂@reduced graphene oxide hybrid

- nanostructures for oxygen reduction reaction. *Nano Research*, 9(12), 3795-3811.
<https://doi.org/10.1007/s12274-016-1249-9>
- Xiong, H., Gross, D. A., Guo, J. et Amemiya, S. (2006). Local Feedback Mode of Scanning Electrochemical Microscopy for Electrochemical Characterization of One-Dimensional Nanostructure: Theory and Experiment with Nanoband Electrode as Model Substrate. *Analytical Chemistry*, 78(6), 1946-1957. <https://doi.org/10.1021/ac051731q>
- Xiong, H., Guo, J. et Amemiya, S. (2007). Probing Heterogeneous Electron Transfer at an Unbiased Conductor by Scanning Electrochemical Microscopy in the Feedback Mode. *Analytical Chemistry*, 79(7), 2735-2744. <https://doi.org/10.1021/ac062089i>
- Xu, K. (2014). Electrolytes and Interphases in Li-Ion Batteries and Beyond. *Chemical Reviews*, 114(23), 11503-11618. <https://doi.org/10.1021/cr500003w>
- Ye, J., Baumgaertel, A. C., Wang, Y. M., Biener, J. et Biener, M. M. (2015). Structural Optimization of 3D Porous Electrodes for High-Rate Performance Lithium Ion Batteries. *ACS Nano*, 9(2), 2194-2202. <https://doi.org/10.1021/nn505490u>
- Yoo, H. D., Liang, Y., Dong, H., Lin, J., Wang, H., Liu, Y., Ma, L., Wu, T., Li, Y., Ru, Q., Jing, Y., An, Q., Zhou, W., Guo, J., Lu, J., Pantelides, S. T., Qian, X. et Yao, Y. (2017). Fast kinetics of magnesium monochloride cations in interlayer-expanded titanium disulfide for magnesium rechargeable batteries. *Nature Communications*, 8(1), 339. <https://doi.org/10.1038/s41467-017-00431-9>
- Yu, D. Y. W., Donoue, K., Inoue, T., Fujimoto, M. et Fujitani, S. (2006). Effect of Electrode Parameters on LiFePO₄ Cathodes. *Journal of The Electrochemical Society*, 153(5), A835. <https://doi.org/10.1149/1.2179199>
- Yu, D. Y. W., Fietzek, C., Weydanz, W., Donoue, K., Inoue, T., Kurokawa, H. et Fujitani, S. (2007). Study of LiFePO₄ by Cyclic Voltammetry. *Journal of The Electrochemical Society*, 154(4), A253. <https://doi.org/10.1149/1.2434687>
- Zahn, R., Lagadec, M. F. et Wood, V. (2017). Transport in Lithium Ion Batteries: Reconciling Impedance and Structural Analysis. *ACS Energy Letters*, 2(10), 2452-2453. <https://doi.org/10.1021/acseenergylett.7b00740>
- Zampardi, G., Klink, S., Kuznetsov, V., Erichsen, T., Maljusch, A., La Mantia, F., Schuhmann, W. et Ventosa, E. (2015a). Combined AFM/SECM Investigation of the Solid Electrolyte Interphase in Li-Ion Batteries. *ChemElectroChem*, 2(10), 1607-1611. <https://doi.org/10.1002/celec.201500085>
- Zampardi, G., La Mantia, F. et Schuhmann, W. (2015b). In-operando evaluation of the effect of vinylene carbonate on the insulating character of the solid electrolyte interphase. *Electrochemistry Communications*, 58, 1-5. <https://doi.org/10.1016/j.elecom.2015.05.013>

- Zampardi, G., Mantia, F. L. et Schuhmann, W. (2015c). Determination of the formation and range of stability of the SEI on glassy carbon by local electrochemistry. *RSC Advances*, 5(39), 31166-31171. <https://doi.org/10.1039/C5RA02940F>
- Zampardi, G., Trocoli, R., Schuhmann, W. et Mantia, F. L. (2017). Revealing the electronic character of the positive electrode/electrolyte interface in lithium-ion batteries. *Physical Chemistry Chemical Physics*, 19(41), 28381-28387. <https://doi.org/10.1039/C7CP05453J>
- Zampardi, G., Ventosa, E., Mantia, F. L. et Schuhmann, W. (2013). In situ visualization of Li-ion intercalation and formation of the solid electrolyte interphase on TiO₂ based paste electrodes using scanning electrochemical microscopy. *Chemical Communications*, 49(81), 9347-9349. <https://doi.org/10.1039/C3CC44576C>
- Zeng, X., Liu, D., Wang, S., Liu, S., Cai, X., Zhang, L., Zhao, R., Li, B. et Kang, F. (2020a). In Situ Observation of Interface Evolution on a Graphite Anode by Scanning Electrochemical Microscopy. *ACS Applied Materials & Interfaces*, 12(33), 37047-37053. <https://doi.org/10.1021/acsami.0c07250>
- Zeng, Y., Gossage, Z. T., Sarbapalli, D., Hui, J. et Rodríguez-López, J. (2022). Tracking Passivation and Cation Flux at Incipient Solid-Electrolyte Interphases on Multi-Layer Graphene using High Resolution Scanning Electrochemical Microscopy. *ChemElectroChem*, 9(5), e202101445. <https://doi.org/10.1002/celec.202101445>
- Zeng, Z., Barai, P., Lee, S.-Y., Yang, J., Zhang, X., Zheng, W., Liu, Y.-S., Bustillo, K. C., Ercius, P., Guo, J., Cui, Y., Srinivasan, V. et Zheng, H. (2020b). Electrode roughness dependent electrodeposition of sodium at the nanoscale. *Nano Energy*, 72, 104721. <https://doi.org/10.1016/j.nanoen.2020.104721>
- Zhang, D., Haran, B. S., Durairajan, A., White, R. E., Podrazhansky, Y. et Popov, B. N. (2000). Studies on capacity fade of lithium-ion batteries. *Journal of Power Sources*, 91(2), 122-129. [https://doi.org/10.1016/S0378-7753\(00\)00469-9](https://doi.org/10.1016/S0378-7753(00)00469-9)
- Zhang, W., Seo, D.-H., Chen, T., Wu, L., Topsakal, M., Zhu, Y., Lu, D., Ceder, G. et Wang, F. (2020). Kinetic pathways of ionic transport in fast-charging lithium titanate. *Science*, 367(6481), 1030-1034. <https://doi.org/10.1126/science.aax3520>
- Zhang, X., Ju, Z., Zhu, Y., Takeuchi, K. J., Takeuchi, E. S., Marschilok, A. C. et Yu, G. (2021). Multiscale Understanding and Architecture Design of High Energy/Power Lithium-Ion Battery Electrodes. *Advanced Energy Materials*, 11(2), 2000808. <https://doi.org/10.1002/aenm.202000808>
- Zheng, H., Chai, L., Song, X. et Battaglia, V. (2012a). Electrochemical cycling behavior of LiFePO₄ cathode charged with different upper voltage limits. *Electrochimica Acta*, 62, 256-262. <https://doi.org/10.1016/j.electacta.2011.12.019>
- Zheng, H., Li, J., Song, X., Liu, G. et Battaglia, V. S. (2012b). A comprehensive understanding of electrode thickness effects on the electrochemical performances of Li-ion battery

- cathodes. *Electrochimica Acta*, 71, 258-265.
<https://doi.org/10.1016/j.electacta.2012.03.161>
- Zheng, H., Tan, L., Liu, G., Song, X. et Battaglia, V. S. (2012c). Calendering effects on the physical and electrochemical properties of Li[Ni_{1/3}Mn_{1/3}Co_{1/3}]O₂ cathode. *Journal of Power Sources*, 208, 52-57. <https://doi.org/10.1016/j.jpowsour.2012.02.001>
- Zheng, Z., Yu, Q., Chen, Z., Zhu, W., Hu, Q., Liu, Y., Gui, L. et Song, Y. (2020). Investigation of localized electrochemical reactivity on a β -PbO₂ electrode using scanning electrochemical microscopy. *Journal of Electroanalytical Chemistry*, 878, 114699. <https://doi.org/10.1016/j.jelechem.2020.114699>
- Zhou, F., Unwin, P. R. et Bard, A. J. (1992). Scanning electrochemical microscopy. 16. Study of second-order homogeneous chemical reactions via the feedback and generation/collection modes. *The Journal of Physical Chemistry*, 96(12), 4917-4924. <https://doi.org/10.1021/j100191a036>
- Zhu, C., Huang, K., Siepser, N. P. et Baker, L. A. (2021). Scanning Ion Conductance Microscopy. *Chemical Reviews*, 121(19), 11726-11768. <https://doi.org/10.1021/acs.chemrev.0c00962>
- Zhu, C., Zhou, L., Choi, M. et Baker, L. A. (2018). Mapping Surface Charge of Individual Microdomains with Scanning Ion Conductance Microscopy. *ChemElectroChem*, 5(20), 2986-2990. <https://doi.org/10.1002/celec.201800724>
- Zhu, P., Slater, P. R. et Kendrick, E. (2022). Insights into architecture, design and manufacture of electrodes for lithium-ion batteries. *Materials & Design*, 223, 111208. <https://doi.org/10.1016/j.matdes.2022.111208>
- Zubi, G., Dufo-López, R., Carvalho, M. et Pasaoglu, G. (2018). The lithium-ion battery: State of the art and future perspectives. *Renewable and Sustainable Energy Reviews*, 89, 292-308. <https://doi.org/10.1016/j.rser.2018.03.002>